THE UNIVERSITY OF ILLINOIS AT CHICAGO
Graduate College
CERTIFICATE OF APPROVAL

March 3, 1994

I hereby recommend that the thesis prepared under my supervision by

Rurngsheng Guo

entitled The Study of Bose-Einstein Correlations in Deep-inelastic U-Nucleon and U-Nucleus Scattering at 465 GeV/c

be accepted in partial fulfillment of the requirements for the degree of

Doctor of Philosophy

Mark R. Adams
Adviser (Chairperson of Defense Committee)

I concur with this recommendation

Uday Sukhatme
Department Head/Chair

Recommendation concurred in:

Donald W. McZeal
C. Halliwell
Wai Yee Keung
Jin-Chieh Peng

Members of Thesis or Dissertation Defense Committee

UIC The University of Illinois at Chicago

FERMILAB LIBRARY

gift Thesis AA F4933

ACKNOWLEDGEMENTS

I would like to thank the members of my thesis committee; Professor Mark Adams, Professor Clive Halliwell, Professor Donald McLeod, and Professor Y. E. Kueng, of the University of Illinois at Chicago; and Dr. Jen-Chieh Peng of the Los Alamos National Laboratory; for their time spent reviewing this thesis and their helpful comments which have been incorporated. Especially I would like to thank my thesis advisor, Professor Mark Adams, for directing me to both software and hardware projects which kept me focussed on the steps necessary for bringing this analysis to completion.

I shall acknowledge all of the people whom I have worked with for these years in muonlab. My classmate, Timothy Carroll; I'll remember his "hanging time" while we fixed the PSA detector and the discussion of the analysis. My volleyball teammate , Spentzouris Panagiotis; who always made me feel good when we played volleyball together. Ashutosh Kotwal, who always talk and eat a lot, Yin Fang Guang, Harsh Venkataramania, Patrick Madden, Arijit Banerjee, and Vassilios Papavassiliou, thanks for the discussions about the analysis. Let's go and have some drinks.

I learned many techniques of hardware and software for the experiment from Steve Wolbers, Harry Melanson, David Jaffe, John Ryan, and Steve Magill, Thanks to them. Thanks to Donald Geesaman and Heidi Schellman who ran the this experiment so succefully. Thanks to Carlos Salgado and Shuichi Kunori help me in Monte Carlo simulations, John Schell who spent lots of his dating time on helping the production.

I had a good time when worked with Uwe Bratzler and Tianchi Zhao for the PSC detector. Brian Lavoy, Goldie Gillespie, who gave me the technical support for fixing the detector. Thanks guys. Thanks for the Fermilab volleyball league gave me lots of fun to play with so many good guys and make my life easier.

Especially I will like to thank my parents, my wife Hsiu-i and two sweet daughters, Yu-chen and Ting-in, for their support and patience.

RSG

TABLE OF CONTENTS

CHAPTER PAGE

1 INTRODUCTION 1
1.1 The World of Scattering 1
1.2 Kinematics of Deep Inelastic Scattering 2
1.3 Amplitude Interference and Intensity Interference 5
1.4 Theoretical Phenomenology 6
1.5 The Chaoticity Parameter λ 9
1.5.1 Coherent and Incoherent Sources 9
1.5.2 Resonance Production 10
1.5.3 Final State Coulomb and Strong Interactions 11
1.5.4 Experimental effects 12
1.6 Models of Source Distribution 13
1.6.1 The Goldhaber Gaussian Source Model 13
1.6.2 The Kopylov-Podgorestskii Model 14
1.7 Experimental Methods and Results for Studying the BE Effect 16
1.7.1 Reference Selections 16
1.7.2 Monte-Carlo Correction 17
1.7.3 Evidence from Experiments 18
1.7.3.1 Results from hdron-hadron collision 18
1.7.3.2 Results from Nucleus-Nucleus collision 19
1.7.3.3 Results from e^+e^- annihilations 19
1.7.3.4 Results from Lepton-Nucleus interactions 20
1.8 The Bose-Einstein Correlation Study in E665 RUN90 21
1.8.1 Investigating the Shape and Dimension of Pion Production Source . . 22
1.8.2 Investigate the Model Dependence of BE Correlation 22
1.8.3 Investigate the A Dependence of BE Correlation 23
1.8.4 Investigate the BE Effect in Shadowing and Non-Shadowing Regions 23
1.8.5 Investigate the Dependence on Kinematical Variables 23

2 THE E665 EXPERIMENTAL APPARATUS 25
2.1 The Experiment 25
2.2 Coordinate System 26
2.3 Generation of Muon Beams 26
2.4 Beam Spectrometer 28
2.5 Targets 31
2.6 Experimental Apparatus 33
2.6.1 Vertex Drift Chambers (VDC) 34
2.6.2 Wide Angle Detectors 35

TABLE OF CONTENTS (continued)

CHAPTER PAGE

2.6.3 PC Chambers 35
2.6.4 PCF Chambers 36
2.6.5 PSC Chambers 36
2.6.6 DC Chambers 38
2.6.7 PSA Chambers and SSA Scintillator 38
2.6.8 Calorimeter 39
2.6.9 The Muon Detectors 39
2.7 Triggers 40

3 EVENT RECONSTRUCTION AND DATA REDUCTION 41
3.1 Decoding and Translating 41
3.2 Pattern Recognition(PR) 42
3.2.1 The Beam Spectrometer Pattern Recognition 42
3.2.2 The Muon Detector Pattern Recognition 43
3.2.3 Forward Spectrometer Pattern Recognition(FSPR) 44
3.2.3.1 DC Processor 44
3.2.3.2 PC processor 45
3.2.3.3 MA processor 45
3.2.3.4 PF processor 46
3.2.3.5 P2 and PS processors 46
3.2.3.6 M2 and MS Processors 47
3.2.3.7 SF Processor 47
3.2.3.8 SN Processor 48
3.2.3.9 CF Processor 48
3.2.3.10 MD Processor 48
3.2.3.11 PV and MV Processors 48
3.2.3.12 UN Processor 49
3.3 Track Fitting(TF) 49
3.4 VDC Pattern Recognition and Track Fitting 51
3.5 Muon Matching 52
3.6 Vertex Fitting 53
3.7 Electromagnetic Calorimeter 54
3.8 Alignment 54
3.9 Generation and Simulation of Monte-Carlo Events 56
3.10 RUN90 Filter 57
3.11 Data Reduction and Split 57

TABLE OF CONTENTS (continued)

CHAPTER PAGE

4 DATA ANALYSIS 60
4.1 Event Selection 61
4.1.1 Event Kinematics and Reconstruction Quality Cuts 61
4.1.2 The Rejection of Events Containing Exclusively Produced Mesons . . 68
4.2 Track Selection 71
4.2.1 Fitted and Close Tracks 72
4.2.2 Identical Track Remove and Track Quality Cuts 73
4.3 The Monte-Carlo Study 78
4.3.1 Acceptance and Reconstruction Efficiency 79
4.3.2 The Reconstruction of Physical Origins and Particle Types 95
4.3.3 The Reconstruction of Two Charged Tracks 97
4.4 The Final Statistics and The Comparison of Data and Monte-Carlo 102

5 THE BOSE-EINSTEIN CORRELATION ANALYSIS 109
5.1 The Reference Samples 109
5.1.1 Unlike-Sign Charged Pairs 110
5.1.2 Mixed Charged Pairs 116
5.2 The Correlation Function $R(q)$ 122
5.2.1 The Goldhaber Parametrization 127
5.3 The Kopylov-Podgoretskii Parametrization $R(q_t, q_0)$ 137
5.4 The Goldhaber and Kopylov-Podgoretskii Parametrizations 138
5.5 The A-Dependence of Bose-Einstein Correlation 141
5.5.1 A-Dependence of the Shape of the Pion Emission Source 145
5.6 The Dependence on the Event Kinematical Variables 151
5.6.1 The x_{bj} Dependence 151
5.6.2 The W^2 Dependence 157
5.6.3 The ν Dependence 161
5.6.4 The Q^2 Dependence 163
5.7 Conclusion 168

CITED LITERATURE 170

VITA 179

LIST OF TABLES

TABLE		PAGE
I	RESULTS FROM HADRON-HADRON INTERACTIONS	19
II	RESULTS FROM e^+e^- EXPERIMENTS	20
III	RESULTS FROM LEPTON-NUCLEAR EXPERIMENTS	21
IV	PROPERTIES OF E665 RUN90 TARGET MATERIAL	33
V	AVERAGE EFFICIENCY OF EACH PSC PLANE	38
VI	ONE-HADRON TAPES AND EVENTS FOR EACH RUN PERIOD	61
VII	EVENTS FAILED FOR EACH SELECTION REQUIREMENT	71
VIII	FRACTIONS OF PHYSICAL ORIGINS FOR "TRUE" AND "MC REC."	95
IX	ORIGINS FOR RECONSTRUCTED "FITTED" AND "CLOSE" TRACKS	96
X	PHYSICAL ORIGINS AND PARTICLE TYPES AFTER CUTS	98
XI	EVENTS AND TRACKS PASSED ALL SELECTION CRITERIA	102
XII	RESULTS FROM FITS FOR $R(q)$("MIXED" REFERENCE)	128
XIII	RESULTS FROM FITS FOR $R(q)$ ("UNLIKE" REFERENCE)	133
XIV	RESULTS OF FITS WITH (WITHOUT) THE LOWEST 4 q BINS	137
XV	FIT RESULTS FOR Kopylov-Podgoretskii PARAMETRIZATION	138

LIST OF FIGURES

FIGURE PAGE

1.1 Deep inelastic scattering. The First Born approximation Feynman diagram for deep inelastic muon scattering 3

1.2 Bose-Einstein Interference. Two identical bosons were emitted from separated sources and were detected at two separated points. 6

1.3 Probable interpretation of two source size result. 22

2.1 Fixed target beamline distributions in Fermi National Accelerator Laboratory. 27

2.2 Schematic view of NM Muon beamline 29

2.3 Front view of E665 RUN90 target system 31

2.4 Elevation view of liquid and solid target system. 32

2.5 The E665 Experimental Apparatus 33

2.6 The PSC chamber 37

3.1 Flow chart for the FSPR processors 50

3.2 Flow chart for E665 RUN90 production 60

4.1 X-position and Y versus Z position of primary vertex for liquid and solid targets before cuts. The lines and the "excluded region" indicate the cuts. . 63

4.2 Plots of $\delta\nu/\nu$ versus ν, $\delta Q^2/Q^2$ versus Q^2, and the acceptance of SAT versus $log(Q^2)$ for all targets before cuts. 64

4.3 Plots for Y_{bj}, $log(x_{bj})$, Y_{bj} versus $log(x_{bj})$, E_{cal}/ν versus $log(x_{bj})$, E_{cal}/ν, and the multiplicity for events passing the first six cuts. The "excluded region" indicates events in this region are excluded 66

4.4 Distributions of Y_{bj}, $log(x_{bj})$, and E_{cal}/ν for events passing all cuts except the cut on the variable shown, (a) to (c). Events yield as function of Q^2, ν, $log(x_{bj})$, Y_{bj}, E_{cal}/ν, and the multiplicity after all cuts, (d) to (i). 67

4.5 Z_{total} plot for two oppositely charged tracks events and the Z_{total} versus invariant masses of these two tracks. The plot at the lower-left is for Z_{total} versus invariant mass($M_{\pi\pi}$) and the lower-right is for Z_{total} versus invariant mass(M_{KK}) 69

4.6 The invariant mass ($M_{\pi\pi}$, M_{KK}) distributions of exclusive two oppositely charged tracks events. 70

LIST OF FIGURES (continued)

FIGURE PAGE

4.7 X-position difference between primary and secondary vertices for tracks which "fitted" to the secondary vertex. The negative value of difference indicates the primary vertex has been reconstructed upstream of the secondary vertex 72

4.8 Minimum distance(d) and d/σ_d distributions for all, "fitted", and "close" tracks and R=DATA/MC distribution as functions of d and d/σ_d. 74

4.9 The momentum dependence of the Y and Z slopes measured at the vertex for Forward Spectrometer (FS) and VDC-only tracks. Plots on the left are data and plots on the right are Monte-Carlo events. The bounded regions indicate the rejection area of tracks 76

4.10 $\delta P/P^2$ distributions for forward spectrometer (FS) and VDC-only tracks. . 77

4.11 $\delta P/P^2$ distributions for forward spectrometer (FS) and VDC-only tracks after track length cut. 77

4.12 Y versus Z position of track at the primary vertex for forward spectrometer (FS) and for VDC only tracks. 78

4.13 Geometrical acceptance, reconstruction efficiency, and full acceptance, as a function of momentum for positive and negative tracks. The arrow indicate the value of cut on momentum(4 GeV/c). 80

4.14 The momentum dependence of reconstruction efficiency (a) and full acceptance (b) for all, FS-only, and VDC-only tracks. The arrow indicate the value of cut on momentum(4 GeV/c). 81

4.15 Geometrical acceptance, reconstruction efficiency, and full acceptance as a function of Y position measured at primary vertex for positive and negative tracks. 83

4.16 Geometrical acceptance, reconstruction efficiency, and full acceptance as a function of Z position measured at primary vertex for positive and negative tracks. 84

4.17 Geometrical acceptance, reconstruction efficiency, and full acceptance as a function of dY/dx measured at primary vertex for positive and negative tracks. 85

4.18 Geometrical acceptance, reconstruction efficiency, and full acceptance as a function of dZ/dx measured at primary vertex for positive and negative tracks. 86

4.19 The momentum dependence of full acceptance for liquid and solid targets, (a) and (b). The ratio of solid and liquid target for full acceptance is shown in (c). 87

LIST OF FIGURES (continued)

FIGURE PAGE

4.20 The full acceptance as a function of Y and Z position measured at primary vertex for liquid and solid targets, (a) and (b). The ratio of solid and liquid target for full acceptance is shown in (c). 88

4.21 The full acceptance as a function of dY/dX and dY/dX measured at primary vertex for liquid and solid targets, (a) and (b). The ratio of solid and liquid target for full acceptance is shown in (c). 89

4.22 The "modified" momentum dependence of full acceptance for liquid and solid targets, (a) and (b). The ratio of solid and liquid target for full acceptance is shown in (c). 92

4.23 The "modified" full acceptance as function of Y and Z position measured at primary vertex for liquid and solid targets, (a) and (b). The ratio of solid and liquid target for full acceptance is shown in (c) 93

4.24 The "modified" full acceptance as function of dY/dX and dY/dX measured at primary vertex for liquid and solid targets, (a) and (b). The ratio of solid and liquid target for full acceptance is shown in (c) 94

4.25 Fraction of particle contamination as a function of P. 97

4.26 Reconstruction efficiency as a function of ΔYP, ΔZP, and q for two like-charged and unlike-charged tracks(Solid). 99

4.27 Reconstruction efficiency as a function of ΔYP, ΔZP, and q for two like-charged and unlike-charged tracks(Liquid). 100

4.28 Ratio (Solid/Liquid) of Reconstruction efficiency as a function of ΔYP, ΔZP, and q for like-charged and unlike-charged pairs. 101

4.29 Y_{bj} and ν distributions for data and reconstructed Monte-Carlo events. . . . 103

4.30 W^2 and Q^2 distributions for data and reconstructed Monte-Carlo events. . . 104

4.31 X-position of primary vertex for data and reconstructed Monte-Carlo events. The plot on the top is for liquid target and at the bottom is for solid target. 105

4.32 Data and MC REC comparisons for momentum at lab. frame, the momentum in photon-proton C.M.S. frame, and the X_f distributions. (b), (d), (f) are the ratio of DATA/MC REC. 107

LIST OF FIGURES (continued)

FIGURE PAGE

4.33 Data and MC REC comparisons for charge of track, longitudinal momentum related to virtual photon direction of lab and CMS frame. (b), (d), (f) are the ratio of DATA/MC REC. 108

5.1 Number of entries versus q distribution of like-sign charged pairs and unlike-sign charged pairs from events for data, reconstructed Monte-Carlo, and Monte-Carlo truth samples. 111

5.2 MTRU q distributions for inclusive decays, (a): ρ^0, (b): ω, (c): ϕ with pion masses, (d): K^{*0} with pion masses, (e): η', and (f): η. Plot (h) is sum of all decays and (g) is the sum excluding ρ^0 decay 113

5.3 q distributions of (a): all unlike charged pairs and unlike charged pairs from all decays. (b): unlike charged pairs and like charged pairs after removed all decays. (c): same as (b) but include ρ^0 decays 114

5.4 MC REC q distributions for inclusive decays, (a): ρ^0, (b): ω, (c): ϕ with pion masses, (d): K^{*0} with pion masses, (e): η', and (f): η. Plot (h) is sum of all decays and (g) is the sum excluding ρ^0 decay 115

5.5 Ratio of track momenta distribution between event and mixed event. The momenta are calculated in the CMS frame. 117

5.6 Number of entries versus the q distribution of mixed like-sign charged pairs and mixed unlike-sign charged pairs for "DATA", "MC REC", and "MC TRUE" events. 118

5.7 Ratios of mixed like-sign charged pairs over mixed unlike-sign charged pairs versus q distributions for "DATA", "MC REC.", "MC TRUE" samples. The bottom plot shows the ratio for data after correction from Monte-Carlo has been applied 119

5.8 Ratio of "MC REC."/"MC TRUE" versus q for mixed like-sign charged and mixed unlike-sign charged pairs. 121

5.9 The ratio of like-sign/unlike-sign charged pairs versus q, $R(q)$, from events for all "DATA", "MC REC.", "MC TRUE", and "DATA CORR.". 123

5.10 The ratio for like-sign/unlike-sign charged pairs versus q, $R(q)$, for "MC TRUE" and "DATA CORR." after removed all decays, (b) and (d). In (a) and (c) shows the $R(q)$ after removed all decays other than ρ^0 decay 124

LIST OF FIGURES (continued)

FIGURE PAGE

5.11 The ratio for like-sign/mixed like-sign charged pairs versus q, $R(q)$, for all "DATA", "MC REC.", "MC TRUE", and "DATA CORR.". 125

5.12 The ratio for like-sign/mixed unlike-sign charged pairs versus q, $R(q)$, for all "DATA", "MC REC.", "MC TRUE", and "DATA CORR.". 126

5.13 Goldhaber Parametrization fit for the ratio, $R(q)$, which obtained by using mixed like-sign, (a) and (b), and mixed unlike-sign, (c) and (d), charged pairs as references. (a), (c) are fitted with 1-Gaussian and (b), (d) are fitted with 2-Gaussian 129

5.14 Comparison of radius (r_g) extracted from the fit for different experiments which used the mixing method as reference. (a): one-Gaussian fit, (b): two-Gaussian fit. 130

5.15 Goldhaber Parametrization fits of $R(q)$ which obtained from using unlike-sign charged pairs as references. The fitting parameters are detailed in Table XIII. (a) and (c) are 1-Gaussian fit, (b) and (d) are 2-Gaussian fit 132

5.16 Same fits as Figure 5.7 for $R(q)$ with excluding the lowest 4 q bins. 134

5.17 Same fits as Figure 5.7 for $R(q)$ with excluding the lowest 4 q bi ns. 135

5.18 Comparison of the radius extracted from fitting all bins(all) and fitting without lowest 4 bins(exc 4) for both references. 1G: one Gaussian fit, 2G: two Gaussian fit, 1G+ρ: one Gaussian plus ρ fit. 2G+ρ: two Gaussian plus ρ fit 136

5.19 The ratio versus q_t and q_0 distributions for three q_0 and q_t regions. Plots on the left are as a function of q_t a nd plots on the right are as a function of q_0. 139

5.20 Schematic representation of the q_v^2 and q_0^2 dependence of the correlation function R as given by equations (5.7) and (5.6) with $\gamma = 1$ and $\lambda = 1$. The area of the boxes is proportional to the value of $R(q_v^2, q_0^2)$ 140

5.21 Schematic 2-dimensional representations of the correlation function $R(q_v^2, q_0^2)$ for "DATA CORR." The area of the boxes is proportional to the value of $R(q_v^2, q_0^2)$= Like/references. 141

5.22 Ratio (Like/Mixed like) as a function of q for four targets with one-Gaussian Goldhaber parametrization fit. 142

5.23 Ratio (Like-Unlike) versus q distributions for four targets with one-Gaussian Goldhaber parametrization fit. The decays effect are removed in the MTRU. 143

LIST OF FIGURES (continued)

FIGURE PAGE

5.24 Schematic plots of radius(r_g) and chaoticity(λ) versus target atomic mass obtained from the fits of $R(q) = Like/reference$. 144

5.25 Ratio versus $q_l(q_\top)$ distributions for each individual $q_\top(q_l)$ interval. 146

5.26 Ratio versus q_l distributions at $q_\top \leq 0.15GeV$ for all targets. The plots are fitted with the function $R = \gamma + \lambda exp(-r_l^2 q_l^2)$. 148

5.27 Ratio versus $q_\top$ distributions at $q_l \leq 0.2GeV$ for all targets. The plots are fitted with the function $R = \gamma + \lambda exp(-r_\top^2 q_\top^2)$. 149

5.28 The A-dependence of the "radius" and chaoticity "λ" in longitudinal and transverse directions. 150

5.29 Ratios of like-sign pairs over mixed like-sign versus q in three different x_{bj} intervals for All(includes C), D2+H2, and Ca+Pb target. 153

5.30 Plots for r_g and λ obtained from the fit of plots in previous figure for three x_{bj} intervals. The bottom two plots are the ratio of r_g and λ of "heavy" target over "light" target 154

5.31 Ratios (like/unlike) as function of q in three different x_{bj} intervals for All, D2+H2, and Ca+Pb target. 155

5.32 Plots for the r_g and λ obtained from the fit of previous plots in three x_{bj} intervals. Plots (e) and (f) are the ratios of heavy/light target for "radius(r_g)" and "λ" 156

5.33 Ratios (like/mixed) as function of q in three different W^2 intervals for All(includes C), D2+H2, and Ca+Pb target. 158

5.34 Radius and chaoticity "λ" obtained from the fit to the q plots in three W^2 intervals. Plots (e) and (f) are the ratios of heavy/light target for "radius(r_g)" and "λ". 159

5.35 Ratios (like/mixed) as function of q in three different ν intervals for All(includes C), D2+H2, and Ca+Pb target. 161

5.36 Radius and chaoticity "λ" obtained from the fit to the plots in three ν intervals. Plots (e) and (f) are the ratios of heavy/light target for "radius(r_g)" and "λ". 162

5.37 Ratios (like/mixed like) as function of q in three different Q^2 intervals for All(includes C), D2+H2, and Ca+Pb target. 164

LIST OF FIGURES (continued)

FIGURE PAGE

5.38 "Radius" and chaoticity "λ" obtained from the fit to the plots in Q^2 intervals. Plots (e) and (f) are the ratios of heavy/light target for "radius(r_g)" and "λ". 165

5.39 Radius(r_g) as a function of x_{bj} (a) and W^2 (b) for this analysis and other lepton-nucleon experiments. 166

5.40 Radius(r_g) as a function of ν (a) and Q^2 (b) for this analysis and other lepton-nucleon experiments. 167

SUMMARY

The Bose-Einstein correlation between two like-sign charged pions was studied in deep inelastic muon nucleon and nucleus interactions. The goals for this study were to measure nuclear effects on the size and shape of the pion emission source and the dependence of these values on the event kinematical variables. Two parametrization models (Goldhaber and Kopylov-Podgorestskii) have been used for this study.

The Goldhaber parametrization gives the radius of the pion emission region of $r_g = 0.63 \pm 0.04$ fm and for the chaoticity parameter $\lambda = 0.39 \pm 0.03$. Using the Kopylov-Podgorestskii parameterization yields $r_k = 1.8 \pm 0.72 \pm$, $\lambda = 0.34 \pm 0.05$ and for the pion source lifetime of $\tau = 0.75 \pm 0.18$ fm. A double enhancement which represents two source size distribution was observed with a smaller size of $0.51 \pm 0.06 \pm 0.04$ fm and a bigger second size of $1.53 \pm 0.39 \pm 0.28$ fm. The results of this analysis show the Goldhaber parametrization is preferable to explain the source distribution.

The Goldhaber parametrization was used for the further studies. The data are compatible with an oblate shape of the pion emission region with not any nuclear effect on the source size and the shape. A decreasing source size has been observed with increasing x_{bj} as well as with increasing Q^2. No dependence for Bose-Einstein effect on other kinematical variables, ν and W^2, is seen. No nuclear effect for the dependence on event kinematical variables, x_{bj}, W^2, ν, and Q^2 has been found.

This thesis is based on the data collected in the 1990-91 Fermilab experiment E665 fixed target run period and the reconstruction is completed in 1993. The organization of this thesis is as follow: The first chapter describes a brief introduction of experimental and theoretical approach for studying the Bose-Einstein correlation and the evidence from other experiments. Chapter two describes the experimental apparatus which used to gather the data for this analysis. The procedure used to reconstruct raw data into events with kinematical variables

SUMMARY(continued)

and the simulation of Monte-Carlo events is described in chapter three. Chapter four describes the selection of events and tracks used for the Bose-Einstein correlation analysis and the Monte-Carlo studies for understanding the quality of data. The analysis of Bose-Einstein correlation and the results of the analysis along with the conclusions are described in chapter five.

1. INTRODUCTION

1.1 The World of Scattering

At the beginning of this century Rutherford used alpha particles scattered off gold atoms and found the atom has nuclear substructure. This is the first time one used scattering to investigate the structure of fundamental particles. Since then scattering experiments have become a very powerful tool for probing the structure deep inside small objects, the nucleon and the nucleus. In the middle of this century, pions and electrons were being used as the projectiles to perform the scattering experiments and to study the results of these collisions.

In 1968 the SLAC-MIT experiment [1] used an electron beam scattered inelastically off the hydrogen target and found the point-like structures inside the nucleon interpreted as "partons" by Feynman [2]. From Bjorken's [3] point of view, this deep inelastic scattering(DIS) of electron from nucleon can be referred to as an elastic scattering of the electron off point-like constituents of the nucleon, the partons. Later the partons were identified with quarks and the concepts of the partons and the quarks were merged as the Naive Parton Model.

In order to deepen our understanding of the structure of nucleons, we need to use more energetic projectiles. Electrons are very good projectiles because they are very easy to create and to accelerate. They have no "structure" and can undergo a very "clean" interaction with target nucleons. Due to limits on the size of linear accelerators or energy lost in the circular accelerator, it is very difficult to reach electron beam energy of hundreds of GeV. Since the energy radiation is proportional to $1/m^2$ this is much less of an effect on protons, thus the energy of proton beams in circular accelerators can reach above the TeV level. Using an

energetic proton beam interacting with material can create high energy secondary intermediate particles and those secondary particles can then be used as the projectiles for the interaction. Some of the short lived secondaries will decay into leptons and their associated neutrinos, and those high energy leptons(mostly muons) can be collected and used as projectiles to perform the deep inelastic lepton-nucleus scattering to study nuclear structure at high energy.

The Fermilab E665 experiment is the world highest muon beam experiment with 465 GeV average muon incident energy. During the 87-88 fixed target run period, several physics results from muons interacting with deuterium and xenon targets have been published for data from RUN87-88. During the 1990-91 period, a set of different nuclear targets were used to interact with the muon beam and some new detectors were used to collect the data. The triggers were updated and improved to have better acceptance.

1.2 Kinematics of Deep Inelastic Scattering

In this section the kinematics of the lepton -nucleus deep inelastic scattering are described; in the rest of this thesis all kinematic variables will use the same notation as this section. For a scattering process, from the Quantum Electrodynamics(QED) point of view, the incident leptons interchange quanta with the target nucleus and the quanta carry the energy and momentum from the lepton to the target nucleus. If the target breaks up during the scattering then this process becomes a deep inelastic scattering(DIS), and the energy lost during the scattering is used to break the attractive bonds between the constituents of the target. The electromagnetic interactions are usually characterized by a small coupling constants, the fine structure constant, α. This implies that the perturbative expansions are valid and the exchange of quanta during DIS is dominated by the exchange of one virtual photon, the lowest-order electromagnetic scattering. The Feynman diagram of single photon exchange is shown in Figure 1.1 .

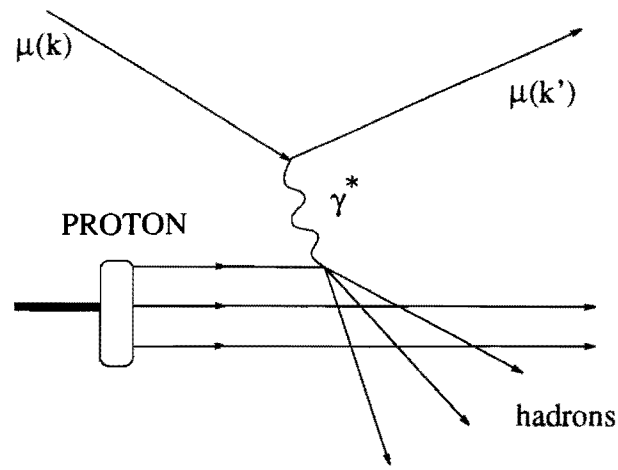

Figure 1.1: Deep inelastic scattering. The First Born approximation Feynman diagram for deep inelastic muon scattering

The incoming lepton has 4-momentum $k = (E, \vec{k})$ and the outgoing lepton, with scattering angle θ in lab-frame, has a 4-momentum $k' = (E', \vec{k'})$. The initial target nucleon 4-momentum is $P = (M; 0, 0, 0)$, where M is the nucleon mass which is initially at rest in the lab-frame. The 4-momentum transferred during the interaction is defined as $q = k' - k$, or $q = (\nu, \vec{k'} - \vec{k})$ where $\nu = E - E'$ is the energy transferred in the interaction. Since the value of q^2 is negative for the virtual process, it is useful to define a positive value $Q^2 \equiv -q^2$. In the laboratory frame the expression for Q^2 and ν are then

$$Q^2 = -2{m_\mu}^2 + 2EE' - 2|\vec{k}||\vec{k'}|cos\theta \approx 4EE'sin(\theta/2)^2 \text{ for } m_\mu \ll E, E' \tag{1.1}$$

and

$$\nu = \frac{P \cdot q}{M} = E - E' \tag{1.2}$$

where m_μ and M are the masses of the muon and the nucleon, and P is the four momentum of the nucleon before the interaction in the laboratory frame and θ is the muon scattering angle. The ν is the energy difference between incoming and scattering muons, also referred to as the energy carried by the virtual photon in the laboratory frame. The invariant mass of the hadronic final state is then given by

$$W^2 = (P + q)^2 = M^2 - Q^2 + 2M\nu. \tag{1.3}$$

In the case of elastic scattering, where $M^2 = W^2$, the square of the 4-momentum transfer will

then become $Q^2 = 2M\nu$. Other Lorentz scalars most often used to describe lepton-nucleon deep inelastic scattering are defined as

$$x_{bj} \equiv -\frac{q \cdot q}{2(P \cdot q)} = \frac{Q^2}{2M\nu} \tag{1.4}$$

and

$$Y_{bj} \equiv \frac{P \cdot q}{P \cdot k} = \frac{\nu}{E}. \tag{1.5}$$

Where x_{bj} can expresses the inelasticity of the interaction, when x_{bj} equals 1 then the interaction is an elastic scattering . From another point of view, in the infinite-momentum frame, this variable , x_{bj}, can present the fraction of total proton momentum carried by this parton. Other hadron variables are used to describe the hadrons produced in deep inelastic scattering, such as Feynman scaling variable, x_f, and Lorentz invariant variable Z are defined as

$$x_f \equiv \frac{p_{||}}{p_{||max}} \approx \frac{p_{||}}{W/2} \tag{1.6}$$

$$Z \equiv \frac{P_{target} \cdot P_{hadron}}{P_{target} \cdot q}. \tag{1.7}$$

where $p_{||}$ is the longitudinal momentum along the virtual photon direction carried by the hadron, and the maximum possible longitudinal momentum will be approximately equal to half of the available energy. In the laboratory frame the Z will become to the ratio of the energy carried by the hadron over the energy transfer in the event, $Z = E/\nu$.

1.3 Amplitude Interference and Intensity Interference

About hundred years ago, Michelson used amplitude interferometry to investigate the diameter of stars for the first time. But since amplitude interferometry depends on the path length and phase, the fluctuating atmosphere index of refraction modifies the observed signal by a random, rapidly varying, phase factor. This phase distortion is very serious in precise optical measurements and is responsible for the limitations that apply to the measurement of the stellar diameters.

On the other hand intensity interferometry, first introduced by Hanbury-Brown and Twiss (HBT) [4] in the 1950s, measuring the intensity interferences of two sources as a function of time at spatially separated points. The advantage of intensity interferometry is that the intensity varies slowly in comparison to the rapidly varying amplitude, and the phase factor appearing in amplitude interferometry is absent in intensity interferometry. Thus the phase distortions due to turbulence of the air, changes in the refraction index of the atmosphere, etc., do not have an effect on the intensity measurement whereas they may be intolerable for the classical Michelson amplitude interferometry. Another advantage of intensity interferometry is that much larger separation between detectors can resulted an increase in resolution power.

The same phenomenon as the HBT effect for the photons, can be used for measuring the correlation between bosons to determine the boson producing source size, shape, or taken a further step to investigate the possible interaction process. The first experimental observation of boson interference was shown by Goldhaber, Goldhaber, Lee, and Pais (GGLP) [5] in $p\bar{p}$ annihilations at 1.05 GeV/c. An enhancement of the ratio of probability for finding an identical pion pair over a non-identical pion pair at small relative momenta was observed; since then this correlation enhancement was referred to as the GGLP effect. For decades, the GGLP effect has been used to deduce the space-time structure by many theorists; meanwhile the experimental physicists have performed many different experiments to determine the spatial dimension of the interference sources.

1.4 Theoretical Phenomenology

Bose-Einstein (BE) correlation is based on quantum mechanical principles and is derived from the "ambiguity" in the paths of identical bosons coming from different parts of the source. The wave functions of two identical bosons are symmetric under exchange. The basis for BE correlation study is the measurement of the two-particle correlation function R defined as:

$$R(p_1, p_2) = \frac{P(p_1, p_2)}{P(p_1) \cdot P(p_2)} \tag{1.8}$$

where p_1, p_2 are particle four-momenta, $P(p_1, p_2)$ is the joint probability of two identical particles to be emitted and $P(p_1) \cdot P(p_2)$ is the product of single-particle probabilities of two particles without BE correlations.

Figure 1.2 shows two identical bosons emitted from two sources located at r_α and r_β and detected simultaneously at positions $A(r_1)$ and $B(r_2)$ with observed momenta p_1 and p_2. The separation of two sources is d and D is the distance from sources to the detectors.

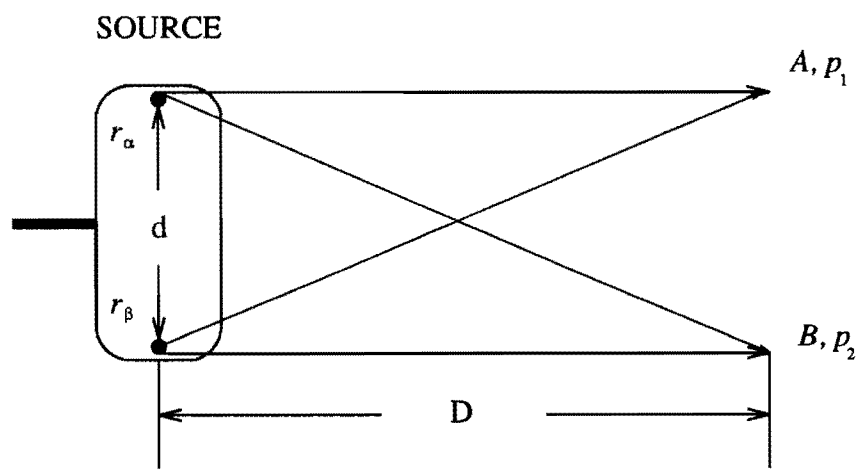

Figure 1.2: Bose-Einstein Interference. Two identical bosons emitted from separated sources and detected at two separated points.

The amplitude for observing the bosons can be written as

$$A = \frac{1}{\sqrt{2}}(\Psi_{1\alpha}\Psi_{2\beta}) \tag{1.9}$$

where $\Psi_{1(2)\alpha(\beta)} \propto exp\{ip_{1(2)} \cdot (r_{1(2)} - r_{\alpha(\beta)})\}$ are the plane wave functions for bosons produced at locations $r_{\alpha(\beta)}$ and detected at detectors $A(B)$ with four-momentum $p_{1(2)}$. According to quantum mechanics, the wave function which describes two identical bosons must be symmetric under exchange so the amplitude of detecting these two bosons at detectors A and B simultaneously is

$$A_{cor} = \frac{1}{\sqrt{2}}(\Psi_{1\alpha}\Psi_{2\beta} + \Psi_{2\alpha}\Psi_{1\beta}). \tag{1.10}$$

Assuming that the boson sources r_α and r_β are randomly distributed in a region of space with a normalized density distribution $\rho(r)$ then the correlation function R can be calculated by summing the probability(P) of finding bosons over the source distribution. For two identical bosons, the probability P_{iden} is

$$P_{iden}(p_1, p_2) \propto \int d^4r_\alpha \int d^4r_\beta \rho(r_\alpha)\rho(r_\beta)|A_{cor}|^2 \tag{1.11}$$

where

$$|A_{cor}|^2 = 1 + cos((p_1 - p_2) \cdot (r_\alpha - r_\beta)). \tag{1.12}$$

For non-identical pions the probability is simply the sum over the distribution of sources and turns out to be identity since the density distribution $\rho(r)$ has already been normalized.

Thus the correlation function R can then be written as

$$R = 1 + \int d^4r_\alpha \int d^4r_\beta \rho(r_\alpha)\rho(r_\beta) cosq(r_\alpha - r_\beta) \tag{1.13}$$

where $q = (p_1 - p_2)$. Replacing cosine function by $\frac{1}{2}(e^{iq(r_\alpha - r_\beta)} + e^{-iq(r_\alpha - r_\beta)})$ and rearranging the integral then

$$R = 1 + (1/2)\int d^4r_\alpha e^{iqr_\alpha}\rho(r_\alpha)\int d^4r_\beta \rho(r_\beta)e^{-iqr_\beta} + (1/2)\int d^4r_\alpha e^{-iqr_\alpha}\rho(r_\alpha)\int d^4r_\beta\rho(r_\beta)e^{iqr_\beta}. \tag{1.14}$$

Since r_α, r_β can be in anywhere within the source region, averaging over all possible coordinates then

$$R = 1 + |\int d^4r\rho(r)e^{iqr}|^2. \tag{1.15}$$

where $\rho(r) = \rho(\vec{r}, t)$ is the (normalized) distribution of the boson emission sources. Applying the Fourier transformation, $\rho(r) \rightarrow F(q)$, the modified correlation function R then becomes a function which depends only on the distribution of 4-momenta difference, q, of the two bosons

$$R(q) = 1 + |F(q)|^2. \tag{1.16}$$

The correlation equations (1.15) and (1.16) indicate that for independent single-particle boson sources the correlation is determined by the Fourier transform of the distribution of the sources in space-time. Therefore, accurate measurements of the two-particle correlations make it possible to obtain information about the source distribution. Unfortunately, to obtain an accurate measurement requires large statistics; this is not possible for current experiments. At the present time the most common approach is to parametrize the relation of equation (1.15) by specifying the distribution of $(\vec{r}_1 - \vec{r}_2)$ and $(t_1 - t_2)$ of definite models of the boson generation source. Then the correlation effect measured by experiments can be used both to determine the parameters $< \vec{r}^2 >$ and $< t^2 >$ and as an argument for or against particular models.

1.5 The Chaoticity Parameter λ

Equations (1.8) to (1.16) have assumed that the bosons were emitted totally incoherently, which gives the maximum interference effect R=2 at q=0 ($p_1 = p_2$). Note that the experiments have a finite resolution in measuring the momentum difference so the intercept extracted from data is usually an extrapolation to the point $q = 0$. However, the maximum effect observed in experiments are smaller than two, that is, the interference effect is partial. For this reason, a parameter called chaoticity (incoherence factor) λ with value between 0 and 1 was introduced by Deutschmann et al [6], which was interpreted as a measurement of the incoherence or chaoticity of the boson emitters. From theoretical understanding the interference effect among identical bosons can be smaller than its maximum because of several effects such as resonance productions, Coulomb and strong interactions between bosons, coherent production, and experimental biases.

1.5.1 Coherent and Incoherent Sources

The character of the particle source is the main influence on the final state boson interference. If we consider that the boson can be emitted from one of a number of discrete sources, and each has a probability amplitude $\rho_i(x)$, the probability of observing a particle with momentum p from those sources is the sum over i of the product of the source amplitude with the particle wave function $\Psi(x)$. In the case of a totally coherent source, the probability of observing the particle is $P_c(p) = |\sum_i \Psi(x_i)\rho_i|^2$ and $P_I(p) = \sum_i |\Psi(x_i)\rho_i|^2$ for the totally incoherent case.

If the source is continuously distributed in the space and the particle wave function is assumed to be a plane wave, then the sum can be replaced by the integral and thus the probability for coherent sources becomes $P_c(p) = |\int \Psi_p(x)\rho(x)d^3x|^2 = |F(p)|^2$. The momentum dependence of the probability is determined by the spatial dependence of the source distribution(the Fourier transformation of $\rho(x) \rightarrow F(p)$). On the other hand the probability to detect an incoherent source distribution is a simple non-momentum dependent function

$P_I(p) = \int |\Psi_p(x)\rho(x)|^2 d^3x = \int |\rho(x)|^2 d^3x$, where $|\Psi_p(x)|^2 = 1$.

For detecting two identical bosons with momenta p_1 and p_2 simultaneously, the probability for a totally coherent source $P_c(p_1, p_2)$ can then be written as

$$\begin{aligned} P_c(p_1, p_2) &= \frac{1}{2}|\int\int d^3x_1 d^3x_2 \Psi_{12}(x_1, x_2)\rho(x_1)\rho(x_2)|^2 \\ &= \frac{1}{2}|\int\int d^3x_1 d^3x_2 \frac{1}{\sqrt{2}}(e^{ip_1x_1}e^{ip_2x_2} + e^{ip_1x_2}e^{ip_1x_2})\rho(x_1)\rho(x_2)|^2. \end{aligned} \tag{1.17}$$

The factor of $\frac{1}{2}$ comes from the fact that the particles are indistinguishable. Applying the Fourier transformation, the probability becomes $P_c(p_1, p_2) = |F(p_1)F(p_2)|^2$, simply equal to the product of probabilities of two individual particles. Thus there is no correlation between these two identical boson, and the correlation function $R(p_1, p_2) = \frac{P_c(p_1,p_2)}{P_c(p_1)\cdot P_c(p_2)} = 1$, if they are emitted totally coherently. In the case of totally incoherent source, the integral of probability detecting two identical bosons becomes

$$P_I(p_1, p_2) = \int\int d^3x_1 d^3x_2 |\Psi_{12}(x_1, x_2)\rho(x_1)\rho(x_2)|^2. \tag{1.18}$$

Applying the same calculation and the Fourier transformation as for the coherent source, the probability for detecting two incoherently identical bosons becomes $P_I(p_1, p_2) = |F_I(0)|^2 + |F_I(p_1 - p_2)|^2$, where $F_I(0) = \rho^*(x)\rho(x)$. The correlation function becomes $R(p_1, p_2) = 1 + |F_I(p_1 - p_2)|^2/|F_I(0)|^2$, the same as equation (1.16) when the sources distribution are normalized to unit, $|F_I(0)|^2 = 1$.

If the sources contribute incoherently, they have a non-vanishing term in the correlation function, and this term depends on the 4-momentum different of the two bosons. On the other hand, the correlation term will vanish if the source distribute coherently.

1.5.2 Resonance Production

In an interaction, bosons (mostly pions in experiments) are produced either directly from the collision or via a short-lived or long-lived resonance decay. The two pion correlation measures the four-momenta difference between two final state pions and it can not identify from which

origin the pion was produced. Thus the pions from resonance decays(particular the short-lived resonance decays such as ρ decay with decay length within few fermi) will show interference with the directly produced pions as well as with the pions produced via other short-lived resonances. These kinds of interference pattern will give a larger source size between two pions and results with a narrow peak at the small q region.

Another influence on the correlation function is resonance pion productions such as ρ, η, ω etc.; their decays will give a large fraction of the reference (non-identical pion pairs) in the region near the invariant masses of the resonances. For example, a ρ decay will produce a $\pi^+\pi^-$ pair in the region around $q^2 = 0.5GeV^2$ and then cause a dip in the correlation function R(q^2). Other resonances which decay into non pion pairs but are misidentified as pions, such as ϕ decay into K^+K^- pairs, will also give similar effects.

1.5.3 Final State Coulomb and Strong Interactions

Final-state Coulomb interactions between produced pions will distort the two particle densities of like-sign and unlike-sign charged pion pairs at small q. The attractive force between unlike-sign charged pions will decrease the angle between these two pions and an enhancement of correlation function will be observed. The repulsive force between like-sign charged pion pairs will lead to a suppression. Gyulassy, Kauffmann, and Wilson [7] suggested that a correction factor, the Gamow factor, should be applied in the correlation function to produce a Coulomb-corrected correlation function.

$$R(p_1, p_2)_{Coulomb\ corrected} = W(p_1, p_2) R(p_1, p_2)_{non-Coulomb\ corrected} \tag{1.19}$$

where the Gamow factor is $W(p_1, p_2) = 2\pi\eta/[exp(2\pi\eta) - 1]$ with $\eta = \frac{\alpha m_\pi}{|p_1 - p_2|}$. This correction factor will suppress the correlation function in the small q region, and is only an approximation valid when the source size is much less than the Bohr radius of the pion pair.

Strong interaction in the final-state $\pi\pi$ rescattering also generates an effect on the correlation function. Suzuki [8] and others [9] estimated this effect and reported that these "strong"

final state interactions may reduce the measurement of the correlation function by as much as 20%. Very few two pion correlation experimental or theoretical analyses have performed this kind of correction of strong interaction.

1.5.4 Experimental effects

Usually experimentalists study the two bosons interference effect assuming that the two particles are pions unless a particle identification system is applied. In a collision, large fraction of particles other than pions are produced, a large portion are kaons and those kaons also have the same interference effects as pions. It has been proposed that kaons may "freeze out" at earlier times and higher temperatures than pions [10, 11] and this implies that the kaon correlation effect will give a smaller source size than obtained from the pion correlation effect. On the other hand, if we assume pions and kaons are produced at the same time, pions have a higher percentage from resonance decay than kaons have, thus the distortion from resonance decays for kaons is less than the distortion for pions [12]. From both assumptions above, using pion interferometry to measure the source size will result in a larger source size than using kaon interferometry and the contamination of kaons in the pion interference effect will decrease the "pure" pion produced source size. Other particles misidentified such as protons and electrons, even they are not a large fraction, also will influence the result of measurement of the two particles correlation effect.

Other effects originating from experimental uncertainty and reconstruction resolution are also give a significant effect on the correlation function. Detectors have finite resolution for two tracks which are very close to each other; detectors might recognize only one track instead of two tracks which have a Bose-Einstein effect. On the other hand, one might have only one true track and reconstructed as two tracks with very close momentum distribution. This will result in an enhancement at very small q. During the track reconstruction, track kinematics varied with the fitting resolution and thus the q distribution for two tracks varied as well. Those experimental biases can lead to a significant decrease of the parameter λ.

1.6 Models of Source Distribution

Initially, experimentalists studied the correlation of two identical pions in the framework of some particular models of single particle distribution such as;

- an uniform distribution of a disk with an exponential decay time.
- a surface of hemisphere distribution with an exponential decay time.
- an uniform distribution in a sphere with exponential decay time.
- a distribution uniformly fill the volume of ellipsoid.
- a Gaussian distribution for the space with an exponential decay time.

All these models assumed that the single particle sources were emitted simultaneously and decayed exponentially with mean lifetime τ.

At the present time the data are not precise enough to examine the shape of the particle source in detail, hence some parametrizations of the shape are chosen and characteristic parameters are determined by fitting the data. Usually two types of parameterizations, including the chaoticity parameter, which were introduced by Kopylov-Podgoretski [13] and Goldhaber [5] are used.

1.6.1 The Goldhaber Gaussian Source Model

The most extensively used parametrization corresponding to pion emission sources in experiments is the Gaussian distribution which was first proposed in investigations of the $p\overline{p}$ interaction by GGLP [5] as

$$\rho(x) = C \cdot exp(-\frac{1}{2}(x_{\perp}^2 r_{\perp}^2 + x_z^2 r_z^2 + t^2 \tau^2)). \tag{1.20}$$

Where $r_\top(r_z)$ is the transverse(longitudinal) radius along the particular direction z and the τ is the spread of production time. The correlation function with this source distribution thus becomes

$$R(q_\top, q_z, q_0) = 1 + \lambda exp(-q_\top^2 r_\top^2 - q_z^2 r_z^2 - q_0^2 \tau^2). \tag{1.21}$$

Note that this equation is not a Lorentz invariant. From the study of high energy hadronic jets correlation effect [14], when the correlation function was divided into a two dimensional array, $q_\top^2$ and q_l^2 where $q_l^2 = q_z^2 - q_0^2$, then the modified correlation function becomes

$$R(q_\top, q_l) = 1 + \lambda exp(-r_\top^2 q_\top^2 - r_l^2 q_l^2). \tag{1.22}$$

Result from the fit of the jet data obtained $r_\top^2 \approx r_l^2$ and implied that the variable q_l^2, $(q_z^2 - q_0^2)$, is a relevant combination to describe the data. The variable q_l^2 which conjugates to $t^2 - z^2$ can describes the source density in a one dimensional string and is related to the longitudinal development of the source.

Other experiments [27, 15] also showed that a single Gaussian can explain the data. Thus a single Lorentz invariant Gaussian variable, $q^2 = q_\top^2 + q_l^2$, was introduced and the parametrization is then referred to as the Goldhaber parameterization,

$$R(q^2) = 1 + \lambda exp(-r_g^2 q^2) \tag{1.23}$$

where $q^2 = (p_1 - p_2)^2 = M_{\pi\pi}^2 - 4m_\pi^2$, with $M_{\pi\pi}^2$ the invariant mass of pion pairs and m_π the mass of pion. This parameterization corresponds to a Gaussian shape of the source in the center of mass of the pion pair where q_0=0.

1.6.2 The Kopylov-Podgorestskii Model

Another commonly used model assumes that the source is uniformly distributed on either the surface or interior of an ellipsoid. This model assumes that the pion production has two steps, first the source is excited and moves with constant speed then it is deexcited by emitting pions.

Under the conditions that the sources are excited at the same time and move with constant speed, Kopylov and Podgorestskii suggested that the emitter position must be averaged over the source distribution.

A simplified parametrization for the Kopylov-Podgorestskii model is formed by assuming the sources are stationary and isotropic. Then the correlation function with this parametrization becomes

$$R(q_t, q_0) = 1 + \lambda[4J_1^2(q_t r_k)/(q_t r_k)^2]/[1 + (q_0\tau)^2], \tag{1.24}$$

where J_1 is the first order of Bessel function, with E_i, $\vec{p}_i$ are the pion energy and momentum, and $\vec{q} = \vec{p}_1 - \vec{p}_2$, $\vec{p} = \vec{p}_1 + \vec{p}_2$, $q_0 = |E_1 - E_2|$, then $q_t = |\vec{q} \times \vec{p}|/|\vec{p}|$. This parameterization then corresponds to a radiating spherical surface of radius r_k with an incoherent emitter with life time τ.

In order to provide a means of comparing extracted values r_k of the Kopylov-Podgorestskii parameterization with r_g of the Goldhaber parameterization, one can use the approximation (comparing the power-series expansions of each function)

$$|2J_1(a)/a|^2 \approx exp(-a^2/4) \tag{1.25}$$

and the equation (1.24) can be expressed as

$$R(q_t, q_0) = 1 + \lambda exp[-(r_k/2)^2 q_t^2 - (q_0\tau)^2]. \tag{1.26}$$

Formulae (1.23) and (1.26) turn out to be nearly indistinguishable in shape, and the parameter $r_k \approx 2r_g$ when $q_0 \approx 0$.

1.7 Experimental Methods and Results for Studying the BE Effect

The experimental challenge in studying the BE effect in multipion production is how to understand and to eliminate the correlated background which will affect the result. In this section, the experimental techniques for selecting references and the correction of the results along with results from various experimental collisions are described.

1.7.1 Reference Selections

The correlation function $R(q)$ measures the probability ratio between two identical pions and the references in the events. Ideally the reference samples, $P(p_1) \cdot P(p_2)$, should have the following properties,

I Absence of BE correlation.

II Presence of correlation due to energy-momentum and quantum number conservation.

III Presence of correlation due to the topology and the global properties of the events.

IV Absence of additional dynamical correlations due to resonances or long-lived particle decays.

In order to satisfy the reference sample requirements, the following are the three most commonly used reference samples selection criteria:

- The reference sample is formed from the pairs of unlike-sign charged pions in the events. This choice can satisfy the first 3 requirements but exhibits the additional correlations due to condition IV. Usually the number of unlike-sign charged pairs is greater than like-sign charged pairs, so the normalization between like-sign charged pairs and unlike-sign charged pairs should be applied to the correlation.

- The reference sample is formed by a so-called "mixed event" method, a pion from one event is combined with a pion randomly chosen from other events which have approximately the same characteristics. This choice can satisfy the condition IV but can lose the correlations due to energy-momentum and charge conservation.

- The reference sample is formed by a combination of unlike-sign charged pions from the same event with randomly interchanged $\vec{p}_t$ in the hadronic c.m.s.. This can satisfy 3-momentum conservation but not energy conservation.

These three methods of selecting the reference samples have their advantages and disadvantages. The EMC [16] and BEBC [17] experiments used the Monte Carlo technique to study the methods of forming the references and the results showed not much different between first two methods but with an enhancement at small q for third method. Most experiments have used the first two methods to select the references.

1.7.2 Monte Carlo Correction

The results of BE correlation function $R(q)$ obtained from the data must be corrected due to the experimental limitation of detecting two very close tracks. Mostly, experimentalists have used the Monte Carlo technique to correct for the experimental bias. The Monte Carlo generates and simulates events based on the experimental setup, then the same package of event reconstruction is applied. The comparison of BE effects between data and Monte Carlo events will reduce the effects which come from experimental acceptance and efficiency as well as the reference sample selection bias.

1.7.3 Evidence from Experiments

1.7.3.1 Results from hadron-hadron collision

In 1960 the first BE correlation experiment was done by using $p\bar{p}$ collisions[5]. Since then many hadron-hadron collision experiments have measured the two-pion correlation, and results were interpreted in terms of source geometry. The pion source sizes measured via different methods in hadron-hadron interactions ($\pi^{\pm}p$, $K^{\pm}p$,pp and $p\bar{p}$), are all close to 1 fm. The sizes extracted using the two parameterizations, Goldhaber and Kopylov-Podgorestskii, are similar and found to be not strongly dependent on the type of collision. Also, the results from Serpukhov [30] used pion reactions with H, D2, C, Cu and Pb targets to show the source size has no dependence on the target and is close to 1.1 fm.

Recent results from the UA1 [18] $p\bar{p}$ collision experiment show that the Gaussian distribution can describe the data very well in two and three pions correlations but not for higher order (four and five pions) correlations. They reported that a exponential distribution with a normalizing factor $(1 + \delta q^2)$,

$$\rho(q) \propto 1 + \lambda e^{-rq}, \tag{1.27}$$

has much better fit for all orders of data. Also they reported that the radius r is rising with higher order (three, four and five) pions correlation while the incoherence parameter λ is nearly constant for all orders. Other experimental results from E735 and AFS[21] had the same conclusion that the radius was dependent on the pion multiplicity density. This might correlate to the higher order correlation with bigger source size. No significant dependence of r and λ with the center-of-mass energy, $\sqrt{s}$, has been observed. Table I lists the recent results from UA1 [18], NA27 [19], NA22 [20], and E735 [21]. Results from other different hadron-hadron interactions not shown in this table are in reference [22].

TABLE I: RESULTS FROM HADRON-HADRON INTERACTIONS

Interaction	Reference	$\sqrt{s}(GeV)$	λ	r(fm)	Fit
UA1($p\bar{p}$)	mixed	630	0.168 ± 0.004	0.742 ± 0.009	Goldhaber
UA1($p\bar{p}$)	mixed	630	0.410 ± 0.015	1.264 ± 0.017	exponential
UA1($p\bar{p}$)	mixed	900	0.186 ± 0.006	0.814 ± 0.016	Goldhaber
UA1($p\bar{p}$)	mixed	900	0.531 ± 0.038	1.374 ± 0.018	exponential
NA27(pp)	mixed	27.4	0.44 ± 0.01	1.20 ± 0.03	Goldhaber
NA27(pp)	mixed	27.4	0.30 ± 0.01	1.69 ± 0.07	Kopylov
NA22(π^+p)	mixed	22.3	0.38 ± 0.02	0.83 ± 0.02	Goldhaber
NA22(π^+p)	mixed	22.3	0.29 ± 0.02	1.50 ± 0.07	Kopylov
NA22(π^+p)	unlike	22.3	0.41 ± 0.02	0.87 ± 0.02	Goldhaber
NA22(π^+p)	unlike	22.3	0.30 ± 0.02	1.51 ± 0.07	Kopylov
E735($p\bar{p}$)	mixed	1800	0.35 ± 0.06	1.06 ± 0.07	Kopylov

1.7.3.2 Results from Nucleus-Nucleus collisions

The results of Bose-Einstein correlation studies in Nucleus-Nucleus interactions found a bigger pion source, between 2 to 5 fm, which depends on two parameters: the projectile size (as well as the target size) and the particle multiplicity density. They showed the relation between r_g, the radius parameter from Gaussian fit, and the atomic number of the projectile(target), A_p. A line fit , r_g =0.7 $A_p{}^{1/3}$, can represent the data [23]. Also the data from nucleus-nucleus interactions show that the radius, r, has a slow rise with the pion multiplicity but no significant dependence on the projectile energy.

1.7.3.3 Results from e^+e^- annihilations

Results of Bose-Einstein study of e^+e^- collision experiments found an average source size approximately between 1.0-0.5 fm and the shape of source is spherically symmetric when viewed from collision c.m.s. frame [25, 24, 27, 26]. Results also showed that the parameters are not significant varying with collision energy, $\sqrt{s}$. Table II is the results from recent e^+e^- annihilation experiments in different energy regions. Other e^+e^- annihilation results not shown in this table are in reference [22].

TABLE II: RESULTS FROM e^+e^- EXPERIMENTS

Experiment	$\sqrt{s}(GeV)$	λ	r(fm)
ALEPH(mixed reference)	91.4	0.4 ± 0.02	0.5 ± 0.02
ALEPH(unlike reference)	91.4	0.62 ± 0.04	0.8 ± 0.04
OPAL(unlike reference)	91.4	1.08 ± 0.05	0.93 ± 0.02
TPC-PEP4(mixed reference)	29	0.61 ± 0.05	0.65 ± 0.04
Mark II(mixed reference)	29	0.45 ± 0.03	1.01 ± 0.09
Mark II(unlike reference)	29	0.50 ± 0.03	0.84 ± 0.06
TASSO(unlike reference)	34.4	0.35 ± 0.03	0.80 ± 0.06

1.7.3.4 Results from Lepton-Nucleus interactions

Results from μ-P interactions [28, 16] and ν-P [17] interaction obtained the parameters, r and λ, were about the same value as for e^+e^- interactions. The source shape has also been reported as spherically symmetric. A double enhancement was observed in E665 1987 data results [28] when using "mixed" like-sign charged pairs as references. This result can be fitted better if we use a two Gaussian fit is used instead of a one Gaussian fit. Equation (1.28) and Figure 1.3 are the representations of a two Gaussian fit:

$$R = 1 + \lambda_l exp(-r_l^2 q^2) + \lambda_s exp(-r_s^2 q^2) \tag{1.28}$$

where r_s indicates the short radius of the directed produced pions source and the r_l is the large radius for the more peak distribution which originated from the combination of decay length for the resonance and r_s. The E665 results with two Gaussian fit gave the small source size is about 0.35 fm and the large source size is about 1.72 fm. Table III lists the results from lepton-nucleus interactions.

TABLE III: RESULTS FROM LEPTON-NUCLEAR EXPERIMENTS

Experiment	Reference sample	λ	r(fm)	Fit Function
EMC(μp)	mixed	0.73 ± 0.06	0.46 ± 0.03	one gaussian
EMC(μp)	unlike	1.08 ± 0.10	0.84 ± 0.03	one gaussian
E180($\nu(\bar{\nu})p$)	mixed	0.70 ± 0.10	0.81 ± 0.09	one gaussian
E180($\nu(\bar{\nu})p$)	unlike	0.80 ± 0.11	0.89 ± 0.09	one gaussian
WA25($\nu(\bar{\nu})p$)	mixed	0.42 ± 0.05	0.57 ± 0.06	one gaussian
WA25($\nu(\bar{\nu})p$)	unlike	0.58 ± 0.05	0.74 ± 0.06	one gaussian
WA59($\nu(\bar{\nu})p$)	mixed	0.59 ± 0.07	0.80 ± 0.08	one gaussian
WA59($\nu(\bar{\nu})p$)	unlike	0.65 ± 0.12	0.75 ± 0.07	one gaussian
E665(μp)	mixed	0.33 ± 0.04	0.36 ± 0.05	one gaussian
E665(μp)	mixed	0.32 ± 0.02 0.27 ± 0.13	0.35 ± 0.03 1.75 ± 0.51	two gaussian
E665(μp)	mixed	0.58 ± 0.03	0.50 ± 0.06	exponential

1.8 The Bose-Einstein Correlation Study in E665 RUN90

The E665 muon DIS experiment during 1990-91 data taking has several advantages , the world highest average muon beam energy(465 GeV), a very good tracking system, an efficient trigger setup, and many different nuclear targets, which can be used to study the BE correlation in a way which no other experiments have done.

The BE correlation study on E665 Run 87 was limited by statistics and did not have enough information to investigate the energy dependence of longitudinal dimension. For Run 90, a new VDC detector has been installed which provides more track finding and improves the vertex finding resolution. Also, the data sample is about 10 times that of the Run 87 data.

Five different nuclear targets were used during E665 90-91 data taking, the targets were rotated randomly for each spill to provide good systematic comparison. No other DIS experiments have done A-dependent BE correlation studies before. The results of muon-nucleus DIS will be complementary to the proton-nuclear and the nuclear-nuclear results.

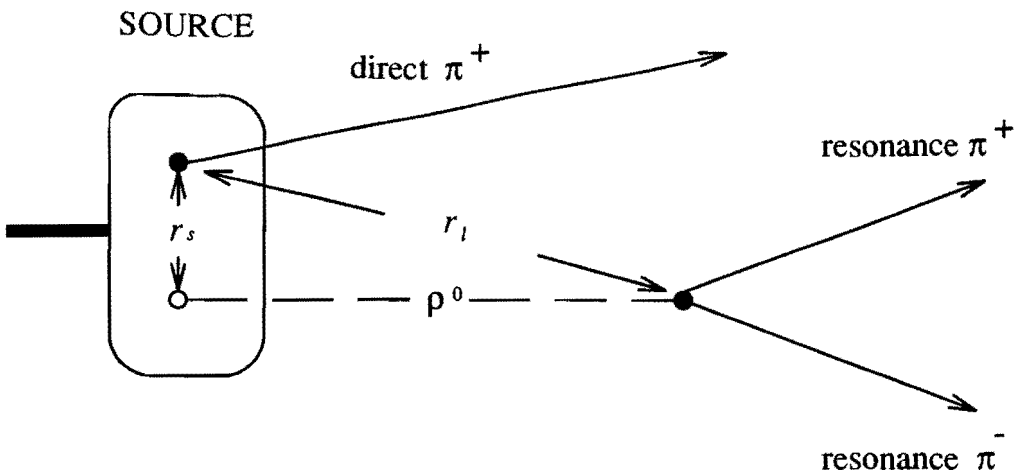

Figure 1.3: Probable interpretation of two source size result.

1.8.1 Investigating the Shape and Dimension of Pion Production Source

One of the main topic of this analysis is to investigate the source size and the space shape of the pion emission source. The pion emission is assumed to have a spherical distribution in the pion-pion center-of- mass system. In this system the energy difference $q_0 = 0$ and the r in equation (1.23) is interpreted as the rms source size of the pion pair in the $\pi\pi$ center-of-mass system. E665 muon DIS has a well defined jet(hadron fragmentation) direction which can provides a very good measurement for the source size in both longitudinal and transverse directions. The shape of the pion emission source can then be determined by a two dimensional fit to the equation (1.22).

1.8.2 Investigate the Model Dependence of BE Correlation

Most BE correlation studies were based on two parametrizations as described before, the Goldhaber and the Kopylov-Podgorestskii parametrizations. These two models turn out to be indistinguishable when q_0 approaches to zero, but when q_0 increases then which model can describe the data better becomes an important issue. The E665 results from RUN87 have been examined and found to be consistent with the Goldhaber parametrization. The model dependence is examined for RUN90 as well.

1.8.3 Investigate the A Dependence of BE Correlation

The results from 200 GeV proton reaction with different nuclear targets have shown that the radius of source has little dependence on the targets and is around 1.1 fm [29]. On the other hand, the results from 40 GeV pions for the reaction $\pi + C \rightarrow 2\pi + X$ has a larger radius, around 2.6 fm [30]. Also from the study of the relation of radius to pion pair momentum, the radius increases when the pion pairs momentum decreases [18].

In muon deep inelastic scattering, pions can either be created directly by the struck quark or by the excited state reinteracting with other nucleons inside the nucleus before they enter the free propagation region. Since the correlations between identical pions are determined by the relative positions of their last scattering points, there may be differences in size and shape(as well as the parameters) between scattering with different nuclear targets.

1.8.4 Investigate the BE Effect in Shadowing and Non-Shadowing Regions

In the region of low x_{bj}, where is called the shadowing region, the picture of virtual photon interact with a nucleus can be viewed as a hadron-hadron interaction. The E665 experiment has the ability to probe this shadowing region and the results of RUN87 showed that the σ_A, the cross section of nuclear target, is suppressed in the shadowing region. However hadronization appears remarkably similar in both shadowing and non-shadowing regions [31]. This Bose-Einstein correlation study for RUN90 data will investigate the dependence of the pion emission source size on x_{bj} , and the nuclear effects at both shadowing and non-shadowing regions for the source size.

1.8.5 Investigate the Dependence on Kinematical Variables

The results from neutrino-nucleus interactions [17] showed the studies of correlation dependence on the kinematical variables Q^2, W^2, and ν. They found that the source radius has no

dependence on these variables, but e^+e^- annihilation experiments showed that the radius increases at high energy. E665 has higher energy than these experiments and may resolve any discrepancies. The incoherence parameter λ also was not dependent on these variables but had dependence on the variable x_{bj}. The x_{bj} range probed by E665 has been greatly extended to a very low value $\leq 10^{-3}$, and this can provide more information about the λ dependence of x_{bj}.

The previous experimental results from e^+e^-, lepton-nucleon, and hadron-hadron collisions all agree that r is about 1 fm, whereas the nuclear-nuclear interaction has a bigger size. The parameters, r and λ, dependence on the target mass, kinematic variables and event characters are still under investigation. The E665 muon DIS experiment in the 90-91 data taking period has the capability to expand on those studies.

2. THE E665 EXPERIMENTAL APPARATUS

2.1 The Experiment

Fermilab Experiment-665(E665) was a muon-nucleon scattering experiment which was sitting at the end of a 1.5km muon beam-line. It consisted of about hundred physicists and graduate students from 18 institutions in United States, Germany, and Poland. The main experimental goals for E665 were to study the nucleon structure function and the hadron production in muon-nucleon deep inelastic scattering. This chapter describes the generation of high energy muon beam, the detection of muon beam, , the targets used for the interaction, and the apparatus used to collect the data for this analysis. A detailed description of E665 apparatus for early data taking periods, 1987-1988, can be found in [34]. Significant changes such as the new detectors and the upgrade of trigger system which were made for RUN 90-91, are described.

The description of the E665 experimental apparatus can be separated into two major sections: the Muon Beam Spectrometer and the Experimental Apparatus. Muons were created and focused in the muon beamline and the information provided by the Muon Beam Spectrometer was used to reconstruct the trajectories and momenta of muon tracks. The muon beam was injected into the target and the resulting charged particles from the interaction went through the experimental apparatus and left their "signals" on the experimental detectors. The muons, scattered or non-scattered, penetrated the hadron absorber and "fired" the Muon Spectrometer located at the end of apparatus. Comparing the reconstructed results between muon beam spectrometer and the forward muon detectors, one can obtain the scattering angle of the muon and calculate the kinematics for the event.

2.2 Coordinate System

The global coordinate system of E665 was a right-handed Cartesian system with the X-axis defined as the direction of the muon beam. The Y-axis was defined along the horizontal (parallel to experimental floor) direction with positive Y pointed to the left if looked along the beam direction. The Z-axis was defined as the perpendicular direction related to the X-Y plane with positive Z pointed "up" to the sky. The center of this system, Y=Z=0, was defined to be at the centering of the Chicago Cyclotron Magnet(CCM). The two powerful analysis magnets had the magnetic field along the Z-direction thus only bend the charged particles in the Y directions. For track reconstruction, the X-Y plane was then referred as the bending plane and X-Z plane was the non-bending plane.

The local coordinate system of each detector was defined by a vector Θ which was perpendicular to the plane wires (along the measuring direction). The Θ can be expressed as the global coordinates of each detector with the rotation angle (α) about the X-axis; for a detector with normal direction along the X-axis, $\Theta = Y \sin\alpha - Z \cos\alpha$ where β and γ were zero in this case. The chamber which measures the Z coordinate is defined to have $\alpha = \pi$ and a chamber which measures the Y coordinate is defined to have $\alpha = \pi/2$. Chambers with $0 < \alpha < \pi/2$ were called U-chambers and chambers with $-\pi/2 < \alpha < 0$ were the V-chambers.

2.3 Generation of Muon Beams

Protons were accelerated to the energy of 800 GeV at the Tevatron of Fermi National Accelerator Laboratory(FNAL), which is a dual purpose synchrotron with diameter 2 Km. Those 800 GeV protons were extracted to three fixed target experimental beam lines in a 23 seconds spill for every 59 seconds period. The 53 MHz radio frequency(RF) signals used to accelerate the proton in the Tevatron gave a discrete time structure of the proton beams. Each "pulse" of protons was separated with equal space, about 19 ns, by the RF frequency. Figure 2.1 shows the arrangement of fixed target experimental areas at FNAL.

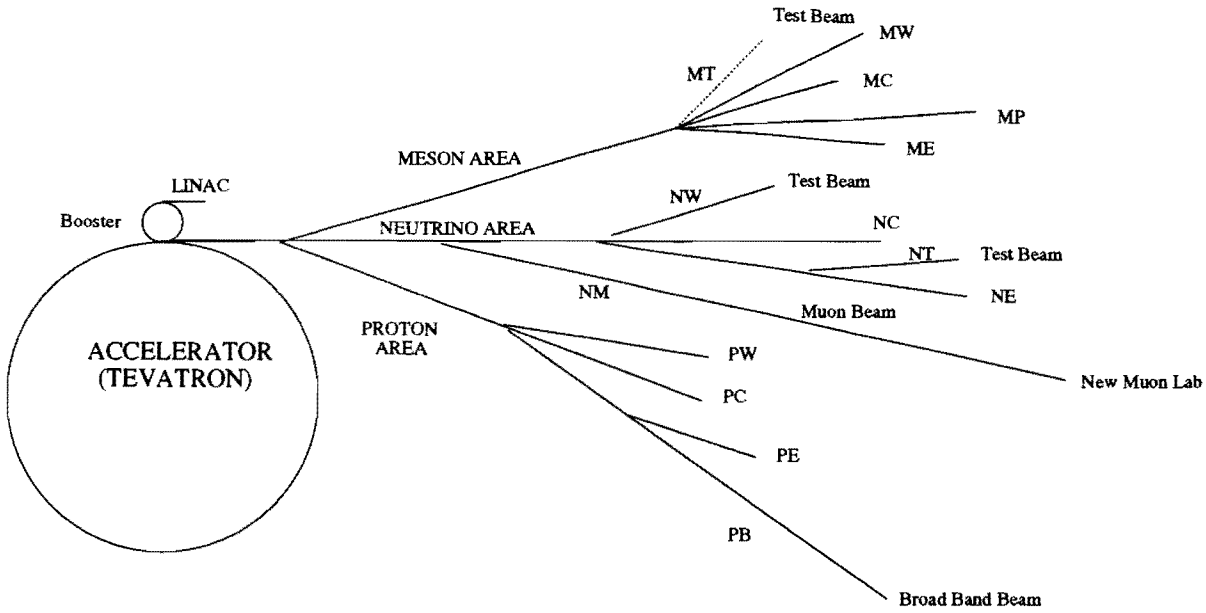

Figure 2.1: Fixed target beamline distributions in Fermi National Accelerator Laboratory.

The muon beam was a tertiary beam at Fermilab, 800 GeV protons were extracted to a 1.5 Km long channel which provided enough time to create and collect the muons into the experimental apparatus. During a Tevatron spill, about 4×10^{12} protons were extracted into the New Muon(NM) beamline, as showed in Figure 2.1, and the protons were focussed to a 48.5 cm long beryllium target. Collisions between protons and target nuclei produced many secondary particles, most of which were pions and kaons. Protons which did not interact with target were forced into a beam dump and stopped. Those secondary particles were steered into an about 1.1 km evacuated tube which was surrounded by several FOcus and DefOcus(FODO) quadrupole magnets. This long tube provided the decay flight path for these secondaries to decay into muons and associated neutrinos. The FODO quadrupole magnet sets focus the muons and force them into a very small cross section. The associated dipole magnets bent and swept the low momentum charged particles away from the main muon beam. At the end of the decay FODO channel, the "un-decayed" secondaries were absorbed in a beryllium dump. The muons penetrated the beryllium dump and passed a dipole momentum selecting magnet, the muons with certain momentum range were steered into another muon FODO tube.

The main purpose of the muon FODO system was to separate the halo muons from the

muon beam. As the decay FODO system, the muon FODO provided efficient transport for the muon beam past devices which removed a large portion of halo. A toroidal magnet which provided a very strong azimuthal magnetic field around the muon beam was applied. This toroidal magnetic field can deflect the halo which is just outside the radius of muon beam pipe and has no effect on the muon beam inside the beam pipe. The halo contamination in the muon beam after application of the muon-FODO and toroid magnets was reduced to about 20 % of the original contamination. More details about the muon beam line were described in [32]. Figure 2.2 shows the schematic of the NM Muon beamline.

The status of muon beam during the data taking was monitored by several sets of Segmented Wire Ionization Chambers(SWICs) which provided the profile integrated over time through the whole beam spill. A beam line scaler counting system provided the information for the muon to proton ratio, and the ratio of total muon beam count to acceptable muon beam count to check the beam tuning consistency. During run 90, an average about 2×10^7 muons per spill entered the experimental hall.

2.4 Beam Spectrometer

Before entered the experimental apparatus of E665, the muon beam has traversed a 55.5 meters long Muon Beam Spectrometer as shown in Figure 2.2. The beam spectrometer had two main purposes, to provide a fast signal for the trigger system and to gather the track information for off-line reconstruction of the beam muon trajectory. Four stations of multiwire proportional chambers(MWPCs) with small wire spacing (1 mm) and separated by an approximately 25 m distance were employed for the muon beam spectrometer system. This system provided very good spacial and momentum resolution. The associated scintillation counters in each station can provide fast trigger signals in a high rate environment.

The four beam spectrometer stations were divided into two groups with two stations each. These two groups were separated by a dipole horizontal bending magnet(NMRE) with long

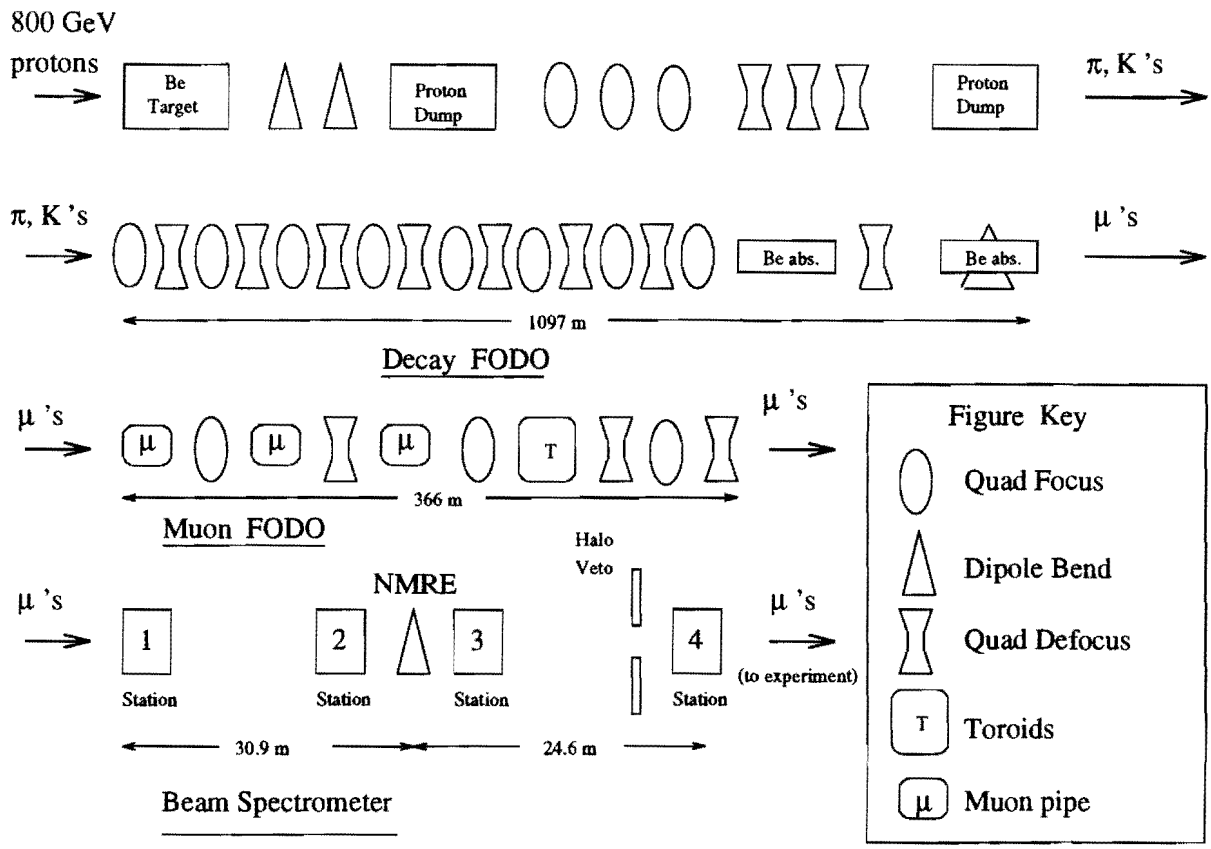

Figure 2.2: Schematic view of NM Muon beamline

level arm in each side. Each station of detectors contained a set of scintillator hodoscope for triggering information and a package of MWPC's for tracking information. The measurement of the bending angle of the track as it went through a defined bending magnet field (NMRE) was used to reconstruct the momentum of the muon. The NMRE was operated at altered currents depending on the beam momentum tune to ensure that the desired muon beam entered the experimental apparatus. For normal 500 GeV beam tune, the NMRE was operated at 3350 amperes and provided a horizontal momentum kick of 1.54 GeV/c.

Six high resolution Fermilab standard designed beam chambers[33] with wire spacing 1 mm were arranged in two packages (YZU, Y'Z'V) for each beam station(PBT). The active area of Y,Z planes was 12.8 cm $\times$ 12.8 cm (128 wires each) while the U and V planes had an approximate active area of 6.4 cm $\times$ 12.8 cm. The Z chambers (with horizontal wires) provided the non-bend tracking information in the pattern recognition, the Y chambers (with vertical wires) determined the momentum, and the U and V (with wire angle $\pm 30^o$) chambers are used to remove the ambiguities of multi-muon tracks reconstruction. The planes in each package were separated into two gas volumes (UYZ, and VY'Z') with independent high-voltage power supplies so that if one of them was not functioning then the other set still can provide a space point for reconstruction. The chamber was operated at -3.1 kV on the cathode planes and the anode wires were at ground potential. The gas mixing consisted of 50% argon and 50% ethane bubbled through ethanol at 0°. Signals from the chambers were amplified and discriminated at each chamber. Discriminated signals were transmitted through flat pair cable to delay and latch modules in CAMAC crates and read out for each trigger.

Each beam station consisted of 2 scintillator hodoscopes(Y and Z views) except station 2 which only had the Y view. All of the scintillator hodoscopes(SBT) consisted of thirteen small counters with the graded size (except the constant width segments of the Z plane of station 1) in order to have approximately equal rate in each counter. These hodoscopes were used to generate the experimental trigger logic, and to provide the information to mask the hits in the PBT's for eliminating the out of time beam tracks. Two beam halo monitor systems, SVJ and SVW, were employed to detect the halo muons which were very close to the muon beam or

spread over wide area separately. The in-time signals from these two scintillator hodoscopes were used as the veto of the triggers.

2.5 Targets

A new automatically control target system has been installed for RUN90 and RUN91 data-taking periods. The target system as is shown in Figure 2.3 and Figure 2.4, consisted of a motorized stand which was able to hold three identical cryogenic liquid targets and a number of solid disk targets.

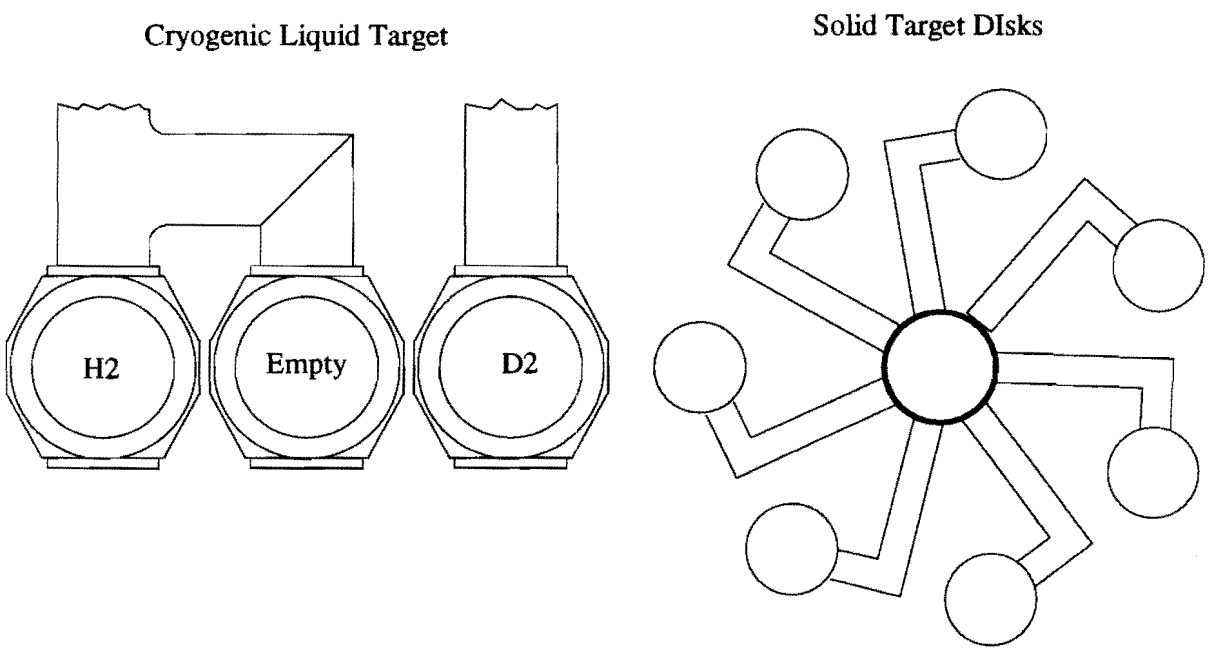

Figure 2.3: Front view of E665 RUN90 target system

This automatic target system was controlled by a software program associated with a special text file[35] which changed the target once every spill to reduce the time-dependent systematic errors. A manual control was also avaliable as a backup when the automatic control failed. The information of which target was in the spill was recorded, and an error was given when the target had an incorrect position which can be used to eliminate these events from the analysis.

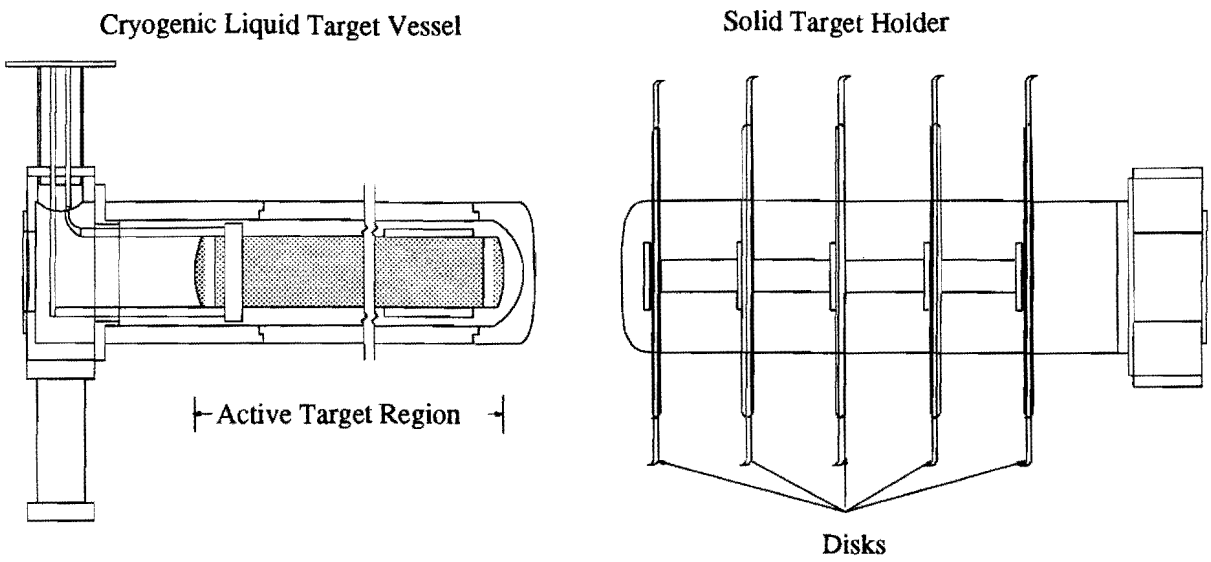

Figure 2.4: Elevation view of liquid and solid target system.

The liquid target system used for the RUN90 contained three identical cylindric vessels with 1.0 m long and 0.1 m in diameter. Three cryogenic materials were filled in these vessels, one was liquid hydrogen, one was liquid deuterium, and the other one was left evacuated. The saturated vapor pressure for each liquid target was monitored by a pressure-to-voltage transducer and was recorded in the data throughout the RUN90.

Each solid target system was mounted on a serial of five disk holders with a total of seven series mounted radially about a rotating axle. For RUN90, a set of lead targets, a set of copper and carbon targets, a set of calcium targets, a set of carbon targets with same thickness as others and a set of carbon targets with half of the thickness, and an empty target holder set were used. Each calcium target was sealed in stainless steel to prevent interaction with water in the atmosphere. Any one of these target was rotated to the beam one at a time with a random, automatically controlled file. Table IV lists the target material for RUN90.

TABLE IV: PROPERTIES OF E665 RUN90 TARGET MATERIAL

Target	Z/A	Length (cm)	Diameter (cm)	Thickness (g/cm^2)	Radiation length in %	Nuclear inter. length in %
H_2	1.0/1.01	100.03	10.	7.1	11.6	13.9
D_2	1.0/2.01	100.03	10.	16.2	13.2	29.6
Thick C	6.0/12.01	5 × 3.37	10.16	29.95	70.1	34.7
Thin C	6.0/12.01	5 × 1.67	10.26	15.07	35.3	17.5
Ca	20/40.08	5 × 2.54	6.96	19.50	99.7	16.6
Pb	82/207.19	5 × 0.1	10.16	5.37	84.3	2.7

2.6 Experimental Apparatus

The plan view of E665 experimental apparatus is shown in Figure 2.5. The apparatus extended a distance of around 35 meters from the target to muon detectors. The whole detector system was an open geometry design which can detect the scattering muon, the charged final state hadrons and some of the neutral particles which decay into charged particles with high momentum resolution.

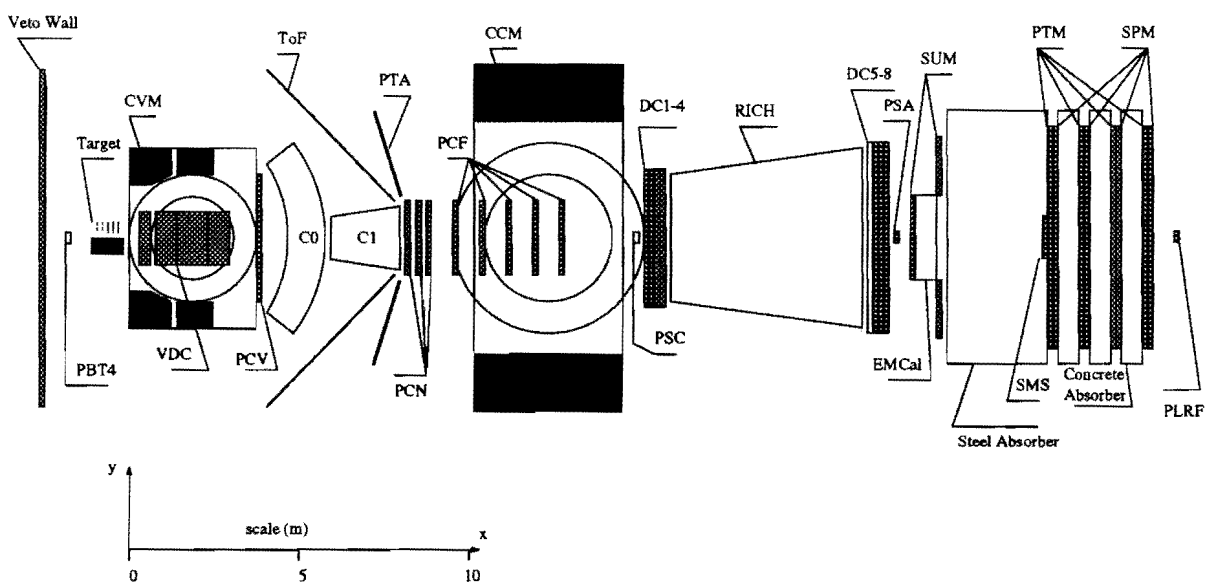

Figure 2.5: The E665 Experimental Apparatus

The detectors were built around or inside the two large superconducting dipole magnets which provided the momenta measurement of the charged particles. The first magnet, the CERN Vertex Magnet(CVM), was setting right after the target and contained the Vertex Drift Chamber (VDC) centered in the one meter gap between two magnet poles for measuring the slowly moving charged particles. The CVM was capable of running at 5000 amperes with a corresponding field of 1.5T(Tesla).

The second magnet was the Chicago Cyclotron Magnet(CCM) was original constructed for using as the magnet for the Chicago Cyclotron and was used as analyzing magnet for past experiments. At the time when New Muon Laboratory was built, the CCM was moved into place first and the Muon Laboratory was constructed around it, meanwhile this magnet was converted to a superconducting magnet. The CCM was a dipole magnet with a diameter of 3m for each pole and a gap of 1.3m between two poles. The superconducting coil was capable of carrying about 900 amperes which corresponds to a magnet field about 1.5T. For the RUN90-RUN91 these two magnets were operated with opposite field directions to provide a focussing condition. The corresponding field integrals, $\int B \cdot dl$, were 4.3 Tm(Tesla-meters) for CVM and 6.734Tm for CCM respectively. With this focussing, a scattered muon's downstream position depended only on the scattering angle and not on the muon energy.

2.6.1 Vertex Drift Chambers (VDC)

A new set of Vertex Drift Chambers(VDC) was installed between the gap of CVM magnet, immediately downstream of the target, for RUN90-91 to replace the streamer chamber(SC) used for RUN87-88. The VDC detector consisted of 13 planes with several different designs: the VCA for wide angle, the VCB for beam region and the VCZ for Z view detection, which covered the whole beam and wide angle regions. The arrangement of the planes along the positive X direction was as follows: BU, BV, ZZ, AV, AU, ZZ, BU, ZZ, AV, AU, ZZ, BV, and BU views. Since the VDC chambers were located inside the magnet field, the U and V view thus have tilted cell geometry to compensate for the Lorentz angle[36].

The VCA planes consisted of 14 cells each with 7.3 cm cell width and 45° of cell angle, and about an 18 cm dead center region through which the unscattered muon passed. The high voltage of VCA was operated at an average 1370 Volt/cm of field strength at the middle of the cell. The VCB planes consisted of 16 cells each with 1.27 cm width and about 11.537^o of cell angle and covered the dead region of the VCA planes. The field strength at the middle of the cell was about 1550 Volt/cm. The VCZ was separated into two sections, the beam region and the wide angle region with 8 cells each. The cell width were 1.27 cm and 7.0 cm and the field strengths were 1550 Volt/cm and 1175 Volt/cm for beam and wild angle region respectively. The whole chamber were strung on an aluminum channel frames with an inner area 69.8 cm $\times$ 120 cm and the coverage of the entire VDC package was about 65 cm $\times$ 100 cm. The gas used for VDC detector was 50 %-50 % Argon-Ethane mixing with the gas pressure at 15 psi during RUN90-91 and was monitored by the pressure gauges on the gas-mixing rack.

2.6.2 Wide Angle Detectors

The wide angle detectors included PCV MWPC's, Time-Of-Flight (TOF) hodoscope, and PTA proportional tubes. The combination of VDC, PCV, TOF, and PTA was designed to detect low momentum tracks of an interaction. The PCV, TOF, and PTA were located outside the CVM magnet and can provide the extrapolating information to match the low momentum tracks found in the VDC's. In this analysis only VDC and PCV were used for reconstructing the low momentum tracks.

2.6.3 PC Chambers

The PC multiwire proportional chambers (PC's) was the first set of the detectors for the Forward Spectrometers. The PC's consisted of three stations each with four wire planes and were located in the field free region between the CVM and CCM magnets. In each station the planes were arranged with the wire orientations in the order of Y, U(+28°), V(-28°), and Z

with the active area 2m × 2m. The anode wire spacing was 3 mm and the separation between adjacent anode planes in each module was 12 mm. A detailed description of PC chambers can be found in [37].

2.6.4 PCF Chambers

The PCF MWPC's were located inside the CCM magnet field which consisted of 5 sets of the 3 planes (wire rotations Z, U(+15°), and V(-15°)) combination with 85 cm separation along the beam direction between each set. The PCF's have an anode wire spacing of 2 mm and the anode wires share common cathode planes with the anode-cathode gap of 6.4 mm. The high voltage were run at an average 3.7 kV with a gas mixture of argon, CO_2, and freon.

2.6.5 PSC Chambers

The PSC chamber was a package of four low-mass 2-planes combinations MWPC with wire spacing 1 mm and was used to cover the DC1-DC4 deadened beam regions. It was located just downstream of the CCM magnet, about 15 cm in front of the first set of DC chambers. The PSC had an active area about 14.4 cm × 14.4 cm and with the wire orientations of chambers are Y, Z, Y', Z', U (+45°), V (-45°), U', and V'. The separation of the anode planes in each 2-planes combination is 1 cm and the distance between 2 combinations (center to center) is 2.3 cm in Z [38].

Signals from the detector were amplified and sent to the delay latches (LeCroy 2731A modules) which were gated by the LeCroy 2738 controller. The gas flow for the PSC was Ar-CO_2-Freon during the data taking period. Figure 2.6 shows the active region of the PSC chamber and Table V shows the average efficiency with high-voltage setting for each plane.

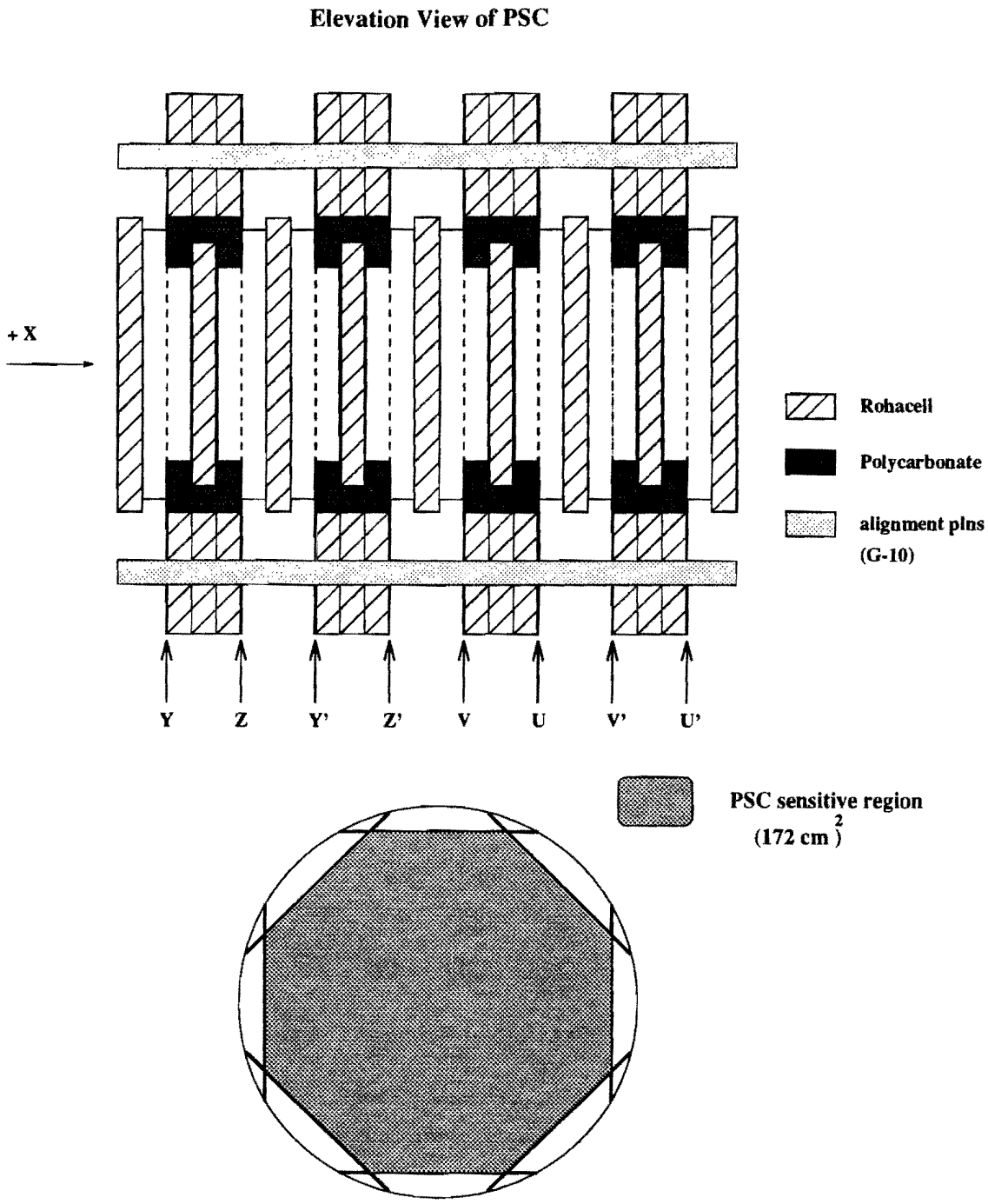

Figure 2.6: The PSC chamber

TABLE V: AVERAGE EFFICIENCY OF EACH PSC PLANE

Plane	High-Voltage (kV)	Efficiency
PSCZ1	2.40	0.05
PSCY1	2.45	0.15
PSCZ2	2.65	0.55
PSCY2	2.68	0.75
PSCV1	2.65	0.79
PSCU1	2.70	0.72
PSCV2	2.67	0.71
PSCU2	2.68	0.64

2.6.6 DC Chambers

The drift chambers(DC's) contained two identical sets of 8-plane detectors(DCA and DCB) with the orientations of Z, Z', U (+5.758^o), U', V (-5.758^o), V', Z, and Z'. The wire spacing of detector was 50.8 mm and the "primed" planes had a half cell offset respect to the "un-primed" planes. The active areas were 2 m $\times$ 4 m for DCA's and 2 m $\times$ 6 m for DCB's respectively. All planes were deadened in the beam region with an average 10 cm $\times$ 5 cm (Y $\times$ Z) which were covered by the PSC and PSA chambers. The electric field of DC's were operated at about 492 V/cm which yielded a drift velocity of 4.2 cm/μs and a drift time of 500 ns. The drift time have been calibrated for each run period[39, 40] and the average efficiency of each chamber was measured to be 90%.

2.6.7 PSA Chambers and SSA Scintillator

The PSA detector consisted of 8 planes standard Fermilab beamline MWPC with wire spacing 1 mm. The active area of PSA was 12.8 cm $\times$ 12.8 cm which used to cover the dead region of the DCB chambers. Thus, the combination of two small MWPCs, PSC and PSA, was able to cover the whole dead region of DCs. The arrange of PSA chambers was separated into two halves. The first half consisted 4 planes with wire orientations of Z, Y, Z', and Y' and the

second half consisted 4 planes with wire orientations of U (+45°), V (-45°), U', and V' along the beam direction, where the "primed" planes had half wire offset respect to the "unprimed" planes.

The SSA small angle scintillator was attached at the downstream face of the PSA chambers during RUN90-91 for improving the trigger efficiency. It contained two views of hodoscopes, Y and Z, with 12 counters each and an active area 13.2 cm × 13.2 cm [41]. The same PCOS III MWPC readout system as PSC chambers was used for PSA. The PSA chambers were operated at 3.1 kV with a gas mixture of 50 % argon and 50 % ethane. The average efficiency of each plane was about 75 %.

2.6.8 Calorimeter

An Electromagnetic Calorimeter was attached at most downstream end of the forward tracking chambers for providing the identification information of tracks. The calorimeter had an active area of 3 m × 3 m and composed of twenty 5 mm thick lead planes interspersed with twenty planes of proportional tubes. Each tube had 8 wires with an 1 cm spacing and was arranged in alternate Y and Z views. The tubes were read out in pairs which were commonly shown as "bi-tubes" in calorimeter documentation elsewhere[42]. More detail about the calibration and the alignment of electromagnetic calorimeter can be found in [43].

2.6.9 The Muon Detectors

The Muon Spectrometer was designed to search the scattered muons and to provide the triggering information. It was located at the downstream of a 3 meter-thick iron hadron absorber which provided a total about 18 interaction lengths for eliminating the contaminations of the hadron in the muon detectors. The muon spectrometer contained four stations with a 91.4 cm thick shielding block wall separating each station. Each station contained two complementary parts; the SPM scintillation counters which generated fast signals for the muon triggering and

the PTM proportional tubes provided the tracking information for the offline reconstruction. A small hodoscope scintillator(SMS) was used for recovering the dead beam region of the PTM's and SPM's. A detailed description about SPM, PTM, and SMS can be found in [14].

2.7 Triggers

Two levels of trigger logic were used for the E665, the level one and the level two triggers, which were defined by the timing with respect to the passage of the scattered muon. The level one trigger was used to generate the "gates" for the detector readout systems. The requirement of the level one trigger was as soon after the scattered muon passed the detector as possible, so it used information from the scintillators. The level two trigger was generated about 200 ns after level one trigger has been generated, and it initiated the data acquisition system of the experiment [44].

In RUN90 several experimental triggers were used for various purposes. The physics triggers (SAT and LAT) used for determining that the muon undergo a scattering with target, the halo trigger for the halo events which can be used to align the wide angle detectors, the prescaled trigger used for the normalization, and the calibration triggers for the calibration of detectors.

The small angle trigger(SAT) was designed to be fired when a beam muon did not go through the predicted unscattered trajectory in the forward spectrometer and the muon detectors[45]. The upgraded SAT trigger had an angular acceptance as low as 0.5 mradian and a minimum Q^2 of about 0.1 GeV^2 and the fraction of beam muon satisfied the SAT beam trigger requirement in RUN90 was about 70 % instead of 17 % for in the RUN87[46]. The large angle trigger(LAT) had a larger minimum scattering angle requirement (3 mradian) than SAT trigger and was the sum of the SVS and SWM triggers. A detailed description of the LAT trigger can be found in reference [44].

3. EVENT RECONSTRUCTION AND DATA REDUCTION

The event reconstruction is a procedure for reconstructing the signals left by charged particles when they passed through apparatus and determining the event kinematics from the trajectory and momentum of the muon. This chapter divides the descriptions of the event reconstruction into: Decoding and Translating, Pattern Recognition, Track Fitting, Muon Matching, Vertex Finding, Electromagnetic Calorimeter, and Alignment. A data reduction(DR) process which keeps the "good" physics events for further analysis and a split process which separates the data more advanced into several physical sub-samples were attached after the event reconstruction. At the end of this chapter, the generation and simulation of Monte Carlo events is described.

3.1 Decoding and Translating

When charged particles passed through the detectors, the "signals" left in the detectors were encoded by the readout system of each detector in specific format and stored in the magnetic tape via the online software system. The first step of event reconstruction is to decode "signals" into the list of wires in the planes which had registered "wire hits", due to the close passage of charged particles. The translating routine translates these "wire hits" into the E665 local coordinate system. The translation is based on the information from the detector, such as the position of the first active physical wire, the wire spacing, and the readout direction of the detector. A constant file(L1ACON) which contains the information for each detector is used for the translation.

The X position of a hit is the global physical plane position which is measured by survey. The Y and Z positions are represented by a combination of the "WIRE"(the first effected wire position), the wire spacing, and the "Θ" (the measurement direction of the plane) as:

$$\begin{pmatrix} \Theta \\ W \end{pmatrix} = \begin{pmatrix} sin\alpha & -cos\alpha \\ cos\alpha & sin\alpha \end{pmatrix} \begin{pmatrix} Y \\ Z \end{pmatrix} \tag{3.1}$$

where W is the wire number counting from the "WIRE" and α is the rotation angle of the detector as described in chapter 2.

3.2 Pattern Recognition(PR)

Only charged particles can leave "hits" in the detectors and only they can interact with magnetic field, so the goal for PR is to find the best combinations of those "hits" which can represent the trajectory of a charged particle. In the stage of PR, there is no momentum information for the tracks, the trajectories of charged particles are assumed to be straight lines in the magnet free regions and non-bending Z view, and to be helical lines in the bending view(Y direction) inside the magnetic field. In addition, a constraint "target pointing" is attached for eliminating the tracks with high potential of not originating from the interaction in the target. The constrained parameters for each sub-processor which have been studied with data and Monte Carlo events were stored in a adjustable control file (PRCUTS). The main body of pattern recognition is divided into three sections, the beam spectrometer, the muon spectrometer, and the forward spectrometer.

3.2.1 The Beam Spectrometer Pattern Recognition

In the beam spectrometer pattern recognition, the PB processor first used the Space-Point Finding algorithm[31] to find the space-point in each of the four beam stations. Then a straight-line fit was performed for these space-points at the non-bend Z view. If χ^2/NDF

of the fit passed the requirement (5.0 for all four stations) then the fit for the Y view (the bend-view) was performed. For the Y view fit, the beam stations were divided into upstream (station 1 and 2) and downstream sections(station 3 and 4), relative to bending-magnet NMRE, and straight line segments in each section were formed. The segments from each section were projected to the center of NMRE where they should intersect if they came from the valid particle trajectory. If the projection satisfies the fit then it saved as a track.

After the PB processor, the SB processor projected the line found in the PB to the four SBT phodoscopes to find the hits belong to the track. The hits from SBT phodoscopes and the associate PBT hits were combined to use for the determination of a track as an "in-time" or "out-of-time" beam track.

3.2.2 The Muon Detector Pattern Recognition

The muon PR was started with PM processor which used the Projection Finding algorithm(PTRACK) to find the muon track in the muon detectors. At least three PTM stations having hits in the Z view were required by the PM processor to find the Z-projection inside the PTM's. If several Z lines have been found then a checking of the share hits between lines was attached. If a line has less than four hits and has more than one hit shared with other lines then this line was eliminated. The Y-projection which associated with each Z-projection was performed after Z-projection has been found.

If the projections in both views passed the χ^2/NDF test then these two projections were merged into a space line and stored in LPML and LPRO standard banks. The muon PR processor contained three sub-processors which performed in series, the PM processor applied for the proportional tubs (PTM), the SM for the small hodoscope(SMS), and the OV reconstructed the track which share the remaining hits from both detectors. After all the full area of muon detectors was well covered.

3.2.3 Forward Spectrometer Pattern Recognition(FSPR)

The FSPR consists several sub-processors which were used to find the line segments in each forward detector or to link those line segments into a complete forward spectrometer track. In FSPR, two sets of parameters contained in PRCUTS for both muon and hadron phases were applied for each sub-processor. The muon phase has smaller acceptable windows for target position and the slopes of tracks for processors which use "target pointing" technique, and has narrow road widths for processors which use the "Projection Finding" algorithm to minimize the fraction of reconstructed tracks which did not originate from primary interaction. Then, the hadron phase which has wider road width, to allow pick up of the hits left in the detectors, was applied.

3.2.3.1 DC Processor

The first FSPR processor was the DC processor which used the Projection Finding algorithm to group hits from DC's into the space lines. In the muon phase, the DC processor extrapolated the Z-projections found in the PM processor into DC's to make the local window for each DC plane . The target pointing constraint was included to form the window. Then the Y-projections from the muon detectors were also extrapolated into DC's to search hits from U and V chambers which were consistent with the Z-projections.

In the hadron phase, the processor searched for all possible Z-projections and Y-projections for remaining hits in DC's. Since the Y coordinate of a hit was converted based on the hit from U and V chambers , a Y coordinate of hit might be attached to various Z-projections or several Y coordinates of hits were associated with same Z-projection. A routine to eliminate the degeneracy and share hits for DC tracks was attached. At the end of the DC processor, a minimum number of hits was required for both Y and Z projections before they were combined into a straight space line (LDCL); at least 4 DC hits for each projection and in each projection, each DC station (DCA and DCB) must have contributed at least two hits.

3.2.3.2 PC processor

The PC processor used the same Projection Finding algorithm as DC processor except the projection was inside the local PC's instead of external projection for DC. This processor used the first and the last PC station as the seed and target planes in each view (Y, Z, U, V). The full projection of each view was formed using hit combinations from seed and target planes and projecting them to the middle plane to pick up hits. The target pointing constrain was contained. A straight-line fit was imposed to determine the combination of the hits and a comparison was performed between the combinations to eliminate the multi-finding projections.

Following the projections have been found in 4 views, a combined projection algorithm was imposed. First, the combining of 4 views full-projection was performed. This was done by using hits in Y and Z planes to calculate the predicted values of the slopes and the intercepts in the other two views(U and V). If the comparison of the coordinates between prediction and projection satisfied the constrained limit, a 3-dimensional straight line fit was imposed. If the χ^2/NDF of fit satisfied the limitation then this track was saved as a temporary LPCL line. The same combining algorithm was applied for 3 views full-projection in which an additional hit from the non-projection view was required. At the end, the combining of 2 views full-projection was performed which included at least one additional hit from each non-projection view requirement. The first Z plane of PCF's, PCF1Z, was included for searching the Z-projection.

The efficiency of the processor as a function of detector hardware performance was detailed in [31]. The overall efficiency of PC processor for this analysis was about 88 % [47].

3.2.3.1 MA Processor

The MA processor which was used to link the lines found in PC's and DC's and to pick up hits from PCF's inside the magnet was applied after DC and PC processors. First, the MA processor attempted to match the DC and PC lines in both Y and Z views. Then it used the

extrapolated Y, Z coordinates at both upstream and downstream faces of the CCM magnet to make a possible band inside the magnet. This band was based on the Monte Carlo studies of charged tracks traversing the magnetic field. A comparison between the predictions and the hits of PCF's was performed, the closest PCF's hits from the predictions were picked up. If the hits picked from PCF's satisfied the constrained requirements , they were combined with hits from PC's and DC's into a valid line. Hits which used for this line were dropped to avoid the double usage later.

3.2.3.4 PF Processor

The PF processor extrapolated the line segments left in the PC's through the magnetic field to make a window for searching PCF's hits. First, a straight Z line from PC line to the last plane of PCF which has hits was extrapolated . Then a helical path inside the magnet in Y bend-view was reconstructed based on the straight PC lines outside the magnet and hits from the last plane of PCF's. Hits in other PCF planes which were located inside the constrained window along this interpolated path were picked up. If more than 8 PCF hits had been found then a DHFIT3 [31] model was imposed for each hit. If the χ^2/NDF of the fit was less than 2, then the original PC line was replaced by a new line (LPFL) which included the additional PCF hits. The efficiency of this processor was 96 % for this analysis.

3.2.3.5 P2 and PS processors

The P2 and PS processors used the Space-Point Finding algorithm [31] to construct the space-points in PSC and PSA detectors. The PSC and PSA had 8 planes in 4 views each and the minimum hits requirement of these processors were 3 hits which were originated from 3 different views. The hits from 3 different views were examined through the symmetric sum :

$$\delta = \Theta_1 sin(\alpha_2 - \alpha_3) + \Theta_2 sin(\alpha_3 - \alpha_1) + \Theta_3 sin(\alpha_1 - \alpha_2) \tag{3.2}$$

where Θ_i is coordinate of the wire hit and α_i is the angle of detector plane orientation, i runs from 1 to 3. If the δ was less then 1.5 σ , $\sigma = d/\sqrt{12}$ with d is the wire spacing, than this three-plane combination was kept.

After all possible three-plane combinations were found, the shared hits for each combination was examined. If two three-plane combinations shared two or more hits then these two combinations were combined. If more than one hits from same detector plane contributed to a combination then the hit with smaller δ was chosen. At the end of the processor, the X, Y, and Z coordinates of the space-point were calculated. The efficiencies of PS and P2 processor were 99 % and 98 % respectively.

3.2.3.6 M2 and MS Processors

The M2 processor extrapolated the LPFL line found in PC's and PCF's by using the DHFIT3 model to the PSC detector. The intercept and the error from the extrapolation were used to define a window in the PSC to search for a space-point. If a PSC space-point was located within this defined window then an extended LPFL line which contained PC, PCF, and PSC hits was upgraded. The efficiency of M2 processor is 96 %.

The MS processor used the same algorithm as M2 to link the LPFL lines which contain hits with the space-point found in the PSA detector. Once the PSA space-point had been picked up by the extrapolation, a final line (LLIN) which contains hits from all contributing detectors was formed. All detector hits and all temporary line segments used to form this line were dropped to avoid multiple usage. The efficiency of this processor was 95 %.

3.2.3.7 SF Processor

The SF processor used the Space-Point Finding algorithm to construct the space-point in each of five PCF detector stations. Then it searched for all possible five space-point, four space-point and three space-point combinations. In non-bend Z view, the space-points from each station were grouped into a straight line and the corresponding Y coordinates of the space-points inside the magnet field required to lie on a circular trajectory. The DHFIT3 model was applied to the hits if the space-points satisfied the Z and Y projections. Lines passing the test of DHFIT3 were saved as LSFL temporal lines.

3.2.3.8 SN Processor

The SN processor used the LSFL lines found in SF processor and projected them upstream to the PC chambers. The DHFIT3 model was used to extrapolate the LSFL lines to each PC station and to find the PC hits inside a defined window at each intercept. The hits found in PC's were combined with PCF hits and the DHFIT3 test for the hits was performed. Tracks passed the test were saved as temporal LSNL lines with. The combination of SF and SN processors was able to recover 78 % of the tracks which were missed by the pervious processors(PC, PF, MA).

3.2.3.9 CF Processor

The CF processor compared the hits of PC and PCF detectors for all LPFL and LSNL temporal lines to eliminate the possible duplicate tracks. If two temporal lines had identical PC, PCF hits, then one of the lines was kept if both lines have same detector hits, or keep the line which has additional hits from other detectors. All temporal lines, including LPFL and LSNL, were saved as new LPFL temporal lines after the comparison of this processor.

3.2.3.10 MD Processor

The MD processor which was used to link the LPFL lines and the DC hits. extrapolated the LPFL lines to each DC chamber searching for corresponding hits. It has two steps, first it extrapolated the existing LPFL and LDCL lines to the downstream face of CCM magnet and found the matching of these lines. Then, it extrapolated the LPFL lines to each DC chamber searching for corresponding hits inside the defined window. A DHFIT3 test was performed for the picked up hits and a final LLIN track was complete once the hits passed the test.

3.2.3.11 PV and MV Processors

The PV processor used the Space-Point Finding algorithm to reconstruct space-points in the PCV chamber. An internal space-line was constructed for a found space-point which

included the local coordinates of the space-point and the Y, Z slopes of the space-line. Then the MV processor projected all lines found in FSPR into the PCV's to match the space-lines. A straight-line fit (STFIT3) was imposed when the PCV space-point was located inside the constrained window. If the χ^2/NDF of the fit satisfied the minimum requirement, the PCV hits were included for the track.

3.2.3.12 UN Processor

At the end of the pattern recognition, the UN processor which was adjusted by a control file to decide what type of temporary line to be saved as a final line(LLIN) was applied. A comparison of PC-PCF hits between tracks was performed for eliminating the duplicate tracks.

The performance of the FSPR for RUN90 has been studied with both data and Monte Carlo events, detailed description can be found in [47]. Figure 3.1 shows the flow chart of the FS pattern recognition processors.

3.3 Track Fitting(TF)

Track Fitting is a processor which used to group the hits of the track found in pattern recognition into a fitted line and to estimate the trajectory and momentum of the track. The model for the track fitting was given in term of five parameters which were used to define the trajectory of a charged particle moved in a free space with a region of static magnetic field. The parameters are the three components of the vector momentum (p_x, p_y, p_z) and the two coordinates of track (Y and Z) at a given reference plane.

The track fitting program consisted of three independent packages which were executed sequentially, the beam, the forward spectrometer, and the wide angle track fitting. The beam track fitting used the spatial measurements of the track at upstream and downstream of NMRE magnet and the magnet field of NMRE. After the fit, the momentum and trajectory of beam track at the X-position of PBT4 was converted into five parameters (y, z, y', z', and $1/P$) and

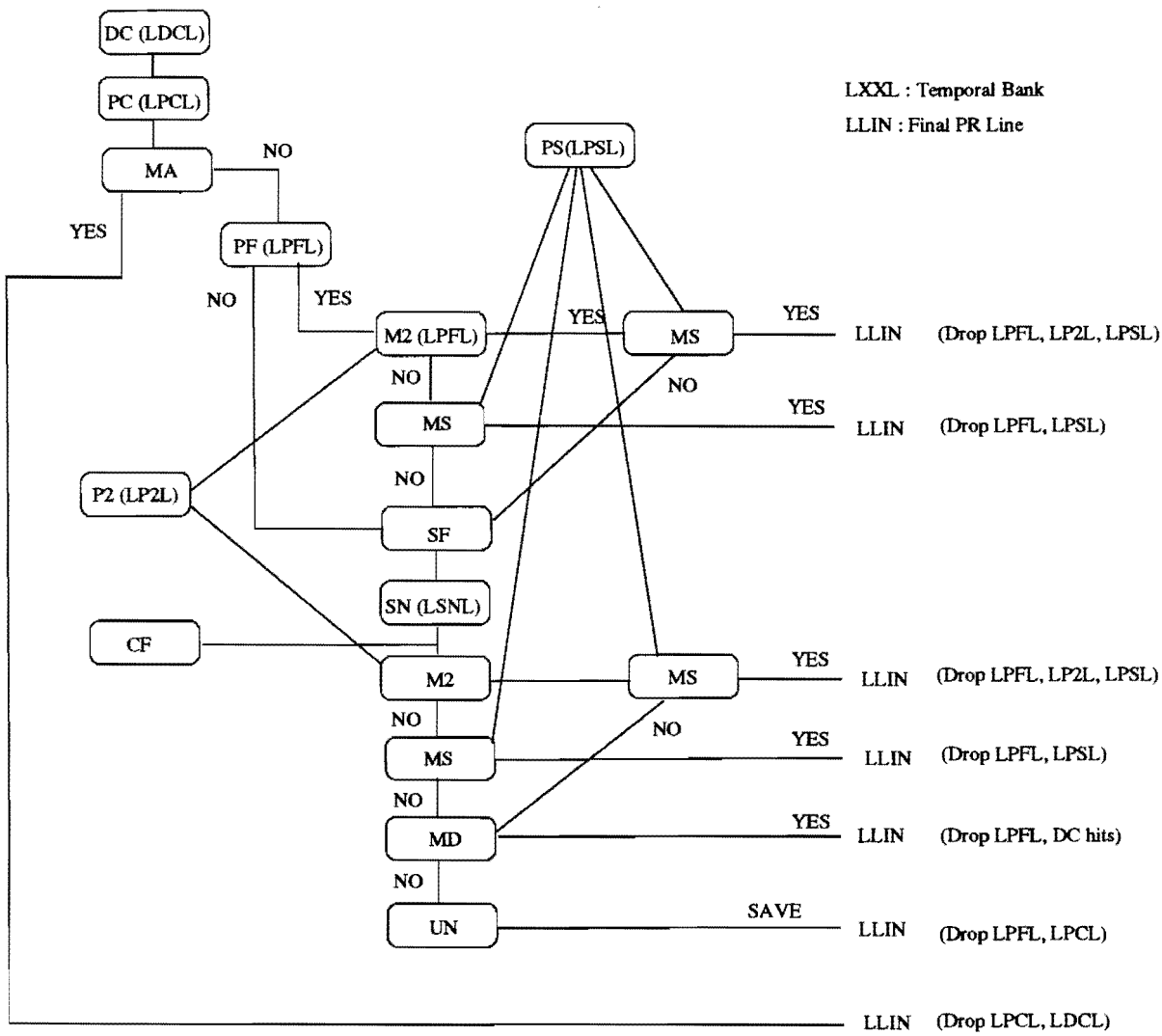

Figure 3.1: Flow chart for the FSPR processors

stored in the E665 standard bank. The fitting program for the forward spectrometers was a processor in three regions, upstream of the CCM magnet, inside the magnet and downstream of the magnet. The processor contained the information of the magnet field incorporated with the knowledge of the multiple scattering in the detectors. The deviation of the fitted trajectory from the measured space-point provided the knowledge to estimate the quality of the fit and confirm the track hypothesis. If the fitting passed the test then the errors of the momentum and position along the trajectory were obtained and stored in the standard bank. Detailed descriptions and studies of the track fitting procedure can be found in [48].

3.4 VDC Pattern Recognition and Track Fitting

In RUN90, a new set of VDC detector was installed covering the measurement of low momentum tracks, which were swept out of the apparatus before entering the FS, and improving the resolution of vertex finding. The pattern recognition and track fitting for VDC's were included in a package which performed after the FS PRTF have been done.

The VDC PRTF was a combination of three individual processors, VA, VB , and VD. The VA processor, the first step of VDC processor, used the Ray Trace method to swim the FS tracks along a helical segment with step length of 2 cm to each VDC layer. The track parameters, (positions, slopes, etc), at each layer were calculated based on the input track parameters. Also a window, which was used to pick up VDC hits in the layer, was formed based on the errors of the swim. The closest hit from the track, within the window, at each VDC layer was picked up and added to the track. At least 6 VDC hits were required and the track fitting which includes hits from VDC's and FS was applied. The fitted results of the track were stored in the standard bank (LSTF) as a complete final track. The VA processor was a processor which extended the FS tracks to the VDC's and improved the resolution of track. It did not change the final number of tracks.

After VA processor, the VB processor was used to pick up hits left in the VDC's and to link

the hits to a trajectory of a charged particle moving inside the magnet field was employed. The processor was independent on any FS processor and tracks found by this processor were mostly low momentum and were swept out of apparatus before they entered the forward spectrometers. The processor first found the internal line segments from each layer and used the projection to link the non-bend Z line segments into a straight line. A straight-line fit was performed once the projection was complete. If the fit passed the test, then the Z line was used for testing the combinations of hits from bending views, U and V, which must be consistent with a parabolic path. A minimum requirement of at least 2 bending views which has at least 3 line segments each, consistent with the Z line, was required before the whole path was considered as an acceptable track.

The final step of VDC PRTF is the VD processor which used the tracks found by VB processor and swam them through the CVM to the first and last plane of the PCV's. The extrapolated parameters at the first plane of the PCV were used for searching hits inside the PCV's. To search for hits left in the forward spectrometers, the track parameters at last plane of PCV were used as the starting parameters. A linear extrapolation from the starting point was used for searching the hits in PC's and the RAY TRACE method was used to extrapolate the track to the detectors which located inside or downstream of the CCM. If more than four hits have been picked up from PCV, PC, PCF, and PSC then the original VDC only track was extended to a complete spectrometer track. The track fitting was applied for the new line and if the χ^2/NDF passed the test then the track was saved.

3.5 Muon Matching

The Muon Matching matched the tracks found in the forward spectrometer and the muon tracks found in the muon detector behind the hadron absorber, to identify the muon tracks in the event. Forward tracks used for the matching were required to have hits from detectors located downstream of CCM magnet (usually the DC's or PSA was required). A straight-line projection was used to extend the FS tracks to the upstream face of the absorber, meanwhile the

muon tracks behind the absorber were projected to the downstream face of the absorber. The matching is performed at the downstream face of the absorber, thus the forward tracks were extrapolated through the steel absorber to the downstream face. The extrapolation errors of the position at the downstream face included the position variance due to the multiple scattering in the absorber.

A χ^2 test based on the track parameters (positions, slope, errors) at intercept was used for both Y and Z view for determining which muon track was associated with which forward spectrometer track. Each FS track can only associated with a muon projection in each view determined by the value of the χ^2. On the other hand, each muon projection could be associated with more than one FS tracks. This was left for the Vertex Finding processor to determine which was the best match for the muon[49].

For RUN90, the major failures for the Muon Matching were due to some PSA planes which failed during part of data taking [50]. To avoid this problem, a modified matching procedure, the "Rescue" muon matching, was made[51]. It used the last half of the PCF's detectors as the starting point for extrapolation if tracks contained no DC or PSA hits.

3.6 Vertex Fitting

The Vertex Fitting processor determined the closest interception of the muon beam track and the scattering muon track associated with other non-muon tracks. In the muon phase of the Vertex Fitting, the muon beam track was extrapolated from the last station of the PBT beam detector to an estimated interaction position at the center of the target in X. Meanwhile, all muon tracks which defined by Muon Matching were swam from the position of the most upstream detector which had hit, through the CVM, to the estimated position. The χ^2 probability of this intersection was calculated based on the separation of the tracks at this point and the extrapolated error of tracks. If the value was acceptable, the position of the primary interaction vertex was defined, otherwise a new location was assumed and the testing

continued until an acceptable χ^2 probability was reached. The muon track with the best vertex fit was assigned to be the scattering muon. If several muon tracks had the same fits then the track with highest momentum was signed as the scattering muon. After that, the scattering angle between incoming beam muon and outgoing scattering muon at the primary vertex was constructed. Meanwhile, the event kinematics with associated errors were calculated.

After the primary interacting vertex had found, the fitted tracks other than muon were swum through CVM to this vertex position. If the χ^2 probability for fitting all tracks at the vertex was greater than a cut-off value, the track with the worst χ^2 probability was removed and the rest tracks were refitted. This processor was continued until the χ^2 probability passed the cut-off value and tracks associated with this vertex were assigned to be primary "hadron" tracks. There were two classes of primary tracks; if the closest distance from the primary vertex to the track was less than 2 cm and the closest distance over measured error of this distance was less than 4 then the track was signed as "fitted" to the vertex, otherwise it was labelled a "close" track.

The last step of the Vertex Fitting was trying to find the secondary vertex for the "close" tracks. Once the secondary vertex found, the associated tracks were assigned as "fitted" to this secondary. Those secondary vertex tracks were removed from the primary hadron and the primary vertex was refitted.

3.7 Electromagnetic Calorimeter

An additional Electromagnetic Calorimeter processor was attached at the end of PTMV. This processor used the information stored in the calorimeter and translated it into LCOR banks based on the temperature, gas composition, pressure, and electronics calibration. The LCOR banks kept the information for bitubes and pad towers, in units of GeV separately. The clustering procedure of the calorimeter was based on the information from LCOR banks of pad tower and grouped the energy which was induced by the same shower into a cluster. The

energy was apportioned based on an exponential function of the pad energy times the distance from the pad to the center of cluster if clusters overlapped[52]. The information for the cluster was stored in the LGLB.

3.8 Alignment

An important requirement for the experiment is that the position of all detectors must be known accurately. The accuracy of the position for each detector determines how well the trajectory of a track has been reconstructed, and the quality of the reconstruction of a muon track determines the precision of event kinematics. The relative position of detectors has been surveyed based on a defined X-axis, the nominal muon beam line. In addition to the survey, a package of software alignment programs was performed for determining the accurate wire position for each detector.

The alignment for the beam spectrometers was done by choosing 4 reference planes (PBT2Y2, PBT2Z2, PBT4Y1, and PBT4Z1) which were assumed absolutely determined by the survey. The beam tracks (with both NMRE was on and off) obtained from the pattern recognition were used as inputs for the alignment. The α (the wire orientation) and the Θ (the position of the first wire perpendicular to the wire orientation) of other detectors were then aligned according to the residuals between the line defined by the reference planes and the hits in the detectors.

The FS spectrometer alignment was done in four steps[53]:

- For the MWPC's (PCV, PC, PCF, PSA, PSC) alignment, the beam stations 3 and 4 were used as the reference planes. The beam track was extrapolated from PBT4 to all FS detectors and the residuals were calculated (CVM, CCM were off, NMRE were on and off).
- For DC, PTM alignment, the "HALO" PCV-PC-PCF tracks were used as the references

with both NMRE on and off (CVM, CCM were off).

- For the VDC central region alignment, the beam stations 3 and 4 were used as reference to extrapolate beam track through CVM, CCM into FS.
- For VDC wide angle alignment, the PCV-PC-PCF-DC lines were used as references and CVM, CCM magnets were on.

Alignments for each "run block" has been completed before the reconstruction of data started. Detailed description of the alignment for RUN90 can be found in [53, 54].

3.9 Generation and Simulation of Monte Carlo Events

The procedure of creating Monte Carlo events for E665 was divided into two major phases, event generation (the first stage of Monte Carlo, MC1) and detector simulation (the second stage of Monte Carlo, MC2). For RUN90 the MC1 and MC2 were combined into a MC12 package which was controlled by a set of user-defined parameters.

The purpose of the MC1 was generation the interactions of beam muon with the target and the propagation of the resulting particles through the E665 spectrometer. The MC1 was divided into three major parts, the beam generation, the kinematical generation for the muon-nucleon DIS, and the hadronic final state generation and tracking through the spectrometer.

The muon beam track parameters were read from an input beam file which was generated from experimental beam data. The beam track was extrapolated to the X positions which were randomly distributed within the target material region to determine the interacting point. For E665 RUN90, the X-position of the interaction (primary vertex) should have a flat distribution within liquid targets and equal distributions centered at the five disks of the solid targets.

The ranges of event kinematical parameters were selected from a user-defined control file. The variables, Q^2 and ν, were generated based on the DIS cross section and a particular

parameterization of parton distributions. The hadronic final states were generated based on LUND52 generator which used the versions of LEPTO 5.2 and JETSET 6.3. The LEPTO was a generator for the QED and QCD processors which created the parton distributions for the interaction. The JETSET was the string fragmentation model which used for the final state hadronizations. A new version of hadronization model , JETSET 7.3 associated with LEPTO 6.1, which contains the Bose-Einstein correlation has been published, unfortunately, due to the time limitation, the new version of LUND generator was not used for this analysis.

The resulting particles were transferred to the GEANT tracking package which swam the particles through the E665 spectrometer , taking into account the magnetic field of the CVM and CCM. When particles propagated through the spectrometer, decays and interactions with material in the apparatus were simulated. Thus this package contained several physical secondary processors such as secondary interaction, photon conversion, particle decays, multiple scattering, and bremsstrahlung. Geometrical information of tracks were stored in the defined "Key-plane" which contained the intersections of the tracks with this plane.

The second stage Monte Carlo (MC2) was a processor which used the information from the "Key-planes" as inputs and digitized the coordinates of the tracks into wire chamber hits. The active region which included the efficiency and the dead region of each detector was included in the simulation. Detailed descriptions of the first and second stage Monte Carlo and the efficiency measurement of each detector can be found in [55, 56, 57, 58].

3.10 RUN90 Filter

The RUN90 filter was used to eliminate events which were non-reconstructable or events with errors in the triggering. Events having a scattering angle greater than 0.3 mrad or energy transfer, ν, greater than 20 GeV associated with a vertex were saved and written to the output tapes. This requirement reduced the amount of data to about 36 % of total raw data. Not all raw tape was run through the filter. One of every ten raw tape was run through PTMV

without applying the filter. Events which were reconstructed without filtering were saved for other studies.

3.11 Data Reduction and Split

The data after PTMV reconstruction contained "in-target" and "off-target" interaction events, interspill and normalization events, and other useful events for analysis. The Data Reduction (DR) was a processor removed events not originating from any primary physical processes. A set of "cuts" for DR on kinematics and other event characters listed below was applied:

- Reconstructed incoming and scattering muons.
- $0.001\ GeV^2 < Q^2 < 10000\ GeV^2$, and $0\ GeV < \nu < 10000\ GeV$.
- Have primary vertex and -13.5 m $< X_{vertex} <$ -11.5 m .
- $0. < X_{bj} < 100$ and $0. < Y_{bj} < 10.$
- $\delta X_{bj}/X_{bj} < 1.$, $\delta Y_{bj}/Y_{bj} < 1.$ and $\delta\nu/\nu < 1.$

After DR, the physics data was reduced to about 17 % (51 8mm tapes) of total PTMV/Filter reconstructed data. An additional separation criteria, the split, was performed for various physical analyses. The "one-hadron" sub-sample which was used for this analysis had the following additional requirements:

- More then one charged FS track associated with the scattered muon.
- The track had defined momentum (1/P > 0.0001 1/GeV).

Figure 3.2 shows the flow chart for E665 RUN90 production[59].

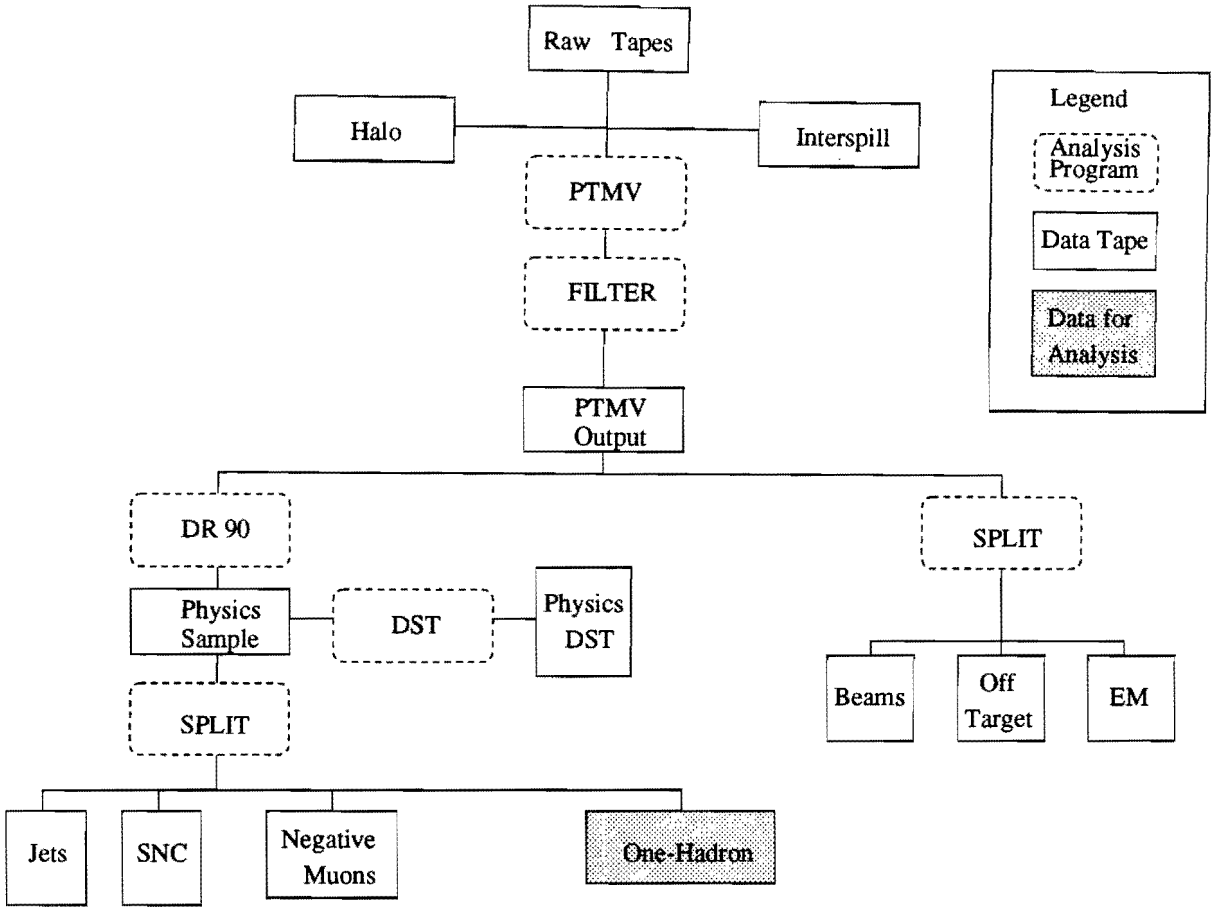

Figure 3.2: Flow chart for E665 RUN90 production

4. DATA ANALYSIS

This chapter describes the event and track selection criteria for the data recorded during the Fermilab E665 fixed target run in 1990. The event kinematics depend mainly upon the incoming and scattered muons and since hadron production is not strongly dependent on the trigger condition, data collected with both physics triggers, SAT and LAT, were used for this analysis.

The Bose-Einstein correlation measures the correlation between two bosons (mainly pions in this experiment) from DIS events. Other events which originated from non-interacting beam muons, muon-electron elastic scattering, or from other electromagnetic processes (muon bremsstrahlung) were eliminated from the sample. Described in the first part of this chapter are the event selection criteria which were used to eliminate events without produced hadrons or not originating from a muon scattering off a target nucleon. In the second part, track selection criteria which were used to select the reconstructed primary hadron tracks and reject false identical tracks during reconstruction are described. Monte Carlo studies for the track acceptance as functions of different kinematic variables, the particle contamination in the hadron sample, and pattern reconstruction effects are described in the third part. At the end of this chapter the reconstruction efficiency of two charged tracks (like-sign and unlike-sign) as function of q, the 4-momentum difference of two tracks, and the final samples for this analysis are presented.

4.1 Event Selection

The data sample used for the Bose-Einstein correlation analysis is a sub-sample of DIS events, the "one-hadron" sub-sample described in the previous chapter. Table VI shows the number of tapes ("one-hadron" split) and events for each alignment run period. In total, the RUN90 data contains 9 alignment periods; data from the first alignment period (mostly trigger and detector studies) were not used.

TABLE VI: ONE-HADRON TAPES AND EVENTS FOR EACH RUN PERIOD

Alignment period (run block)	number of tapes (8mm)	number of events (all targets)
II (12052-12453)	13(XICD08-12) (XICD17-25)	447955
III (12504-12565)	2(XICD35-36)	82973
IV (12613-12734)	6(XICD40-45)	215669
V (12757-12772)	1(XICD50)	40883
VI (12800-12865)	3(XICD55-57)	99689
VII (12877-12931)	4(XICD60-63)	114559
VIII (12938-12981)	1(XICD70)	30890
IX (13172-13266)	6(XICD75-80)	152220
Total	36	1184838

4.1.1 Event Kinematics and Reconstruction Quality Cuts

The event kinematic cuts for selecting "well" reconstructed DIS events were:

- one and only one intime beam and no out-of-time beam; 300 $GeV < E_{beam} < 650\ GeV$.
- has primary vertex and $-13.5m < X_{pri.\ vertex} < -11.5m$
- $-0.04\text{m} < \text{Y}_{\text{ver.}} < 0.02\text{m}$ and $-0.02\text{m} < \text{Z}_{\text{ver.}} < 0.02\text{m}$.

- $0.1\ (GeV/c)^2 < Q^2 < 1000\ (GeV/c)^2$
- $40\ GeV < \nu < 600\ GeV$
- $\delta\nu/\nu < 0.2$ and $\delta Q^2/Q^2 < 0.2$
- $0.0 < Y_{bj} < 0.8$
- $0.0007 < x_{bj} < 1.0$
- at least three forward charged tracks.

The first three cuts require events to have one and only one incoming muon interacting with the target nucleon and have a primary vertex which has been reconstructed inside the target's physical region. Figure 4.1 shows the X position and Y versus Z position of primary vertex for liquid and solid targets. The Q^2 minimum cut removes events which have low acceptance and the ν minimum cut removes events with reconstruction errors on the scattering muon. The cuts of $\delta\nu/\nu < 0.2$ and $\delta Q^2/Q^2 < 0.2$ restricts events to have good reconstruction quality. The values of $\delta\nu/\nu$ and $\delta Q^2/Q^2$ are strong functions of ν and Q^2 as seen in Figure 4.2.(a) and (b). The two bands structure at Figure 4.2.(b) originated from the scattered muon was found with or without PSA detector, events which have smaller $\delta Q^2/Q^2$, distributed at lower band, indicate the scattered muon of events was found with PSA detector. The acceptance as function of $log(Q^2)$ is shown in Figure 4.2.(c) ; events with $Q^2 < 0.1\ GeV^2/c^2$ were eliminated.

Figure 4.3 shows the distributions of Y_{bj}, x_{bj}, E_{cal}/ν, and multiplicity for the event which passed the cuts described above. A clear bump of bremsstrahlung events at value of Y_{bj} greater 0.8, (a), and a significant μ-e peak in the $\log(x_{bj})$ distribution, (b), at $x_{bj} = 0.0005$ are observed. From Y_{bj} versus $log(x_{bj})$ plot in Figure 4.3.(c), most of the electromagnetic events are distributed at the values of large Y_{bj} and small x_{bj} indicated as "excluded region" in the plot. Calorimeter information can also help to remove the contamination of electromagnetic events. An electromagnetic event deposits a large fraction of transfer energy (ν) in the calorimeter. As seen from the ratio of total energy deposited in the calorimeter and the energy transfer (E_{cal}/ν)

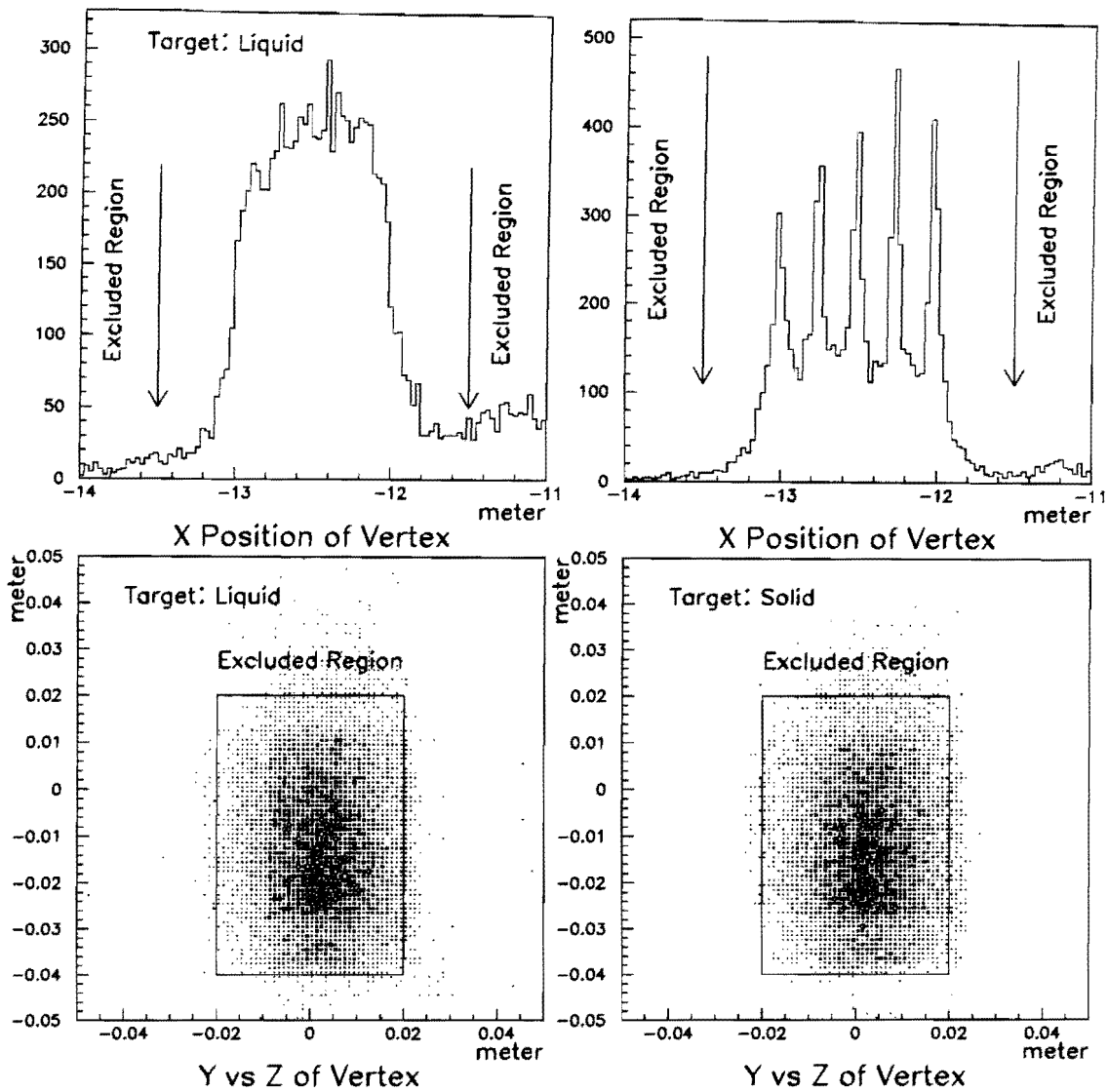

Figure 4.1: X-position and Y versus Z position of primary vertex for liquid and solid targets before cuts. The lines and the "excluded region" indicate the cuts.

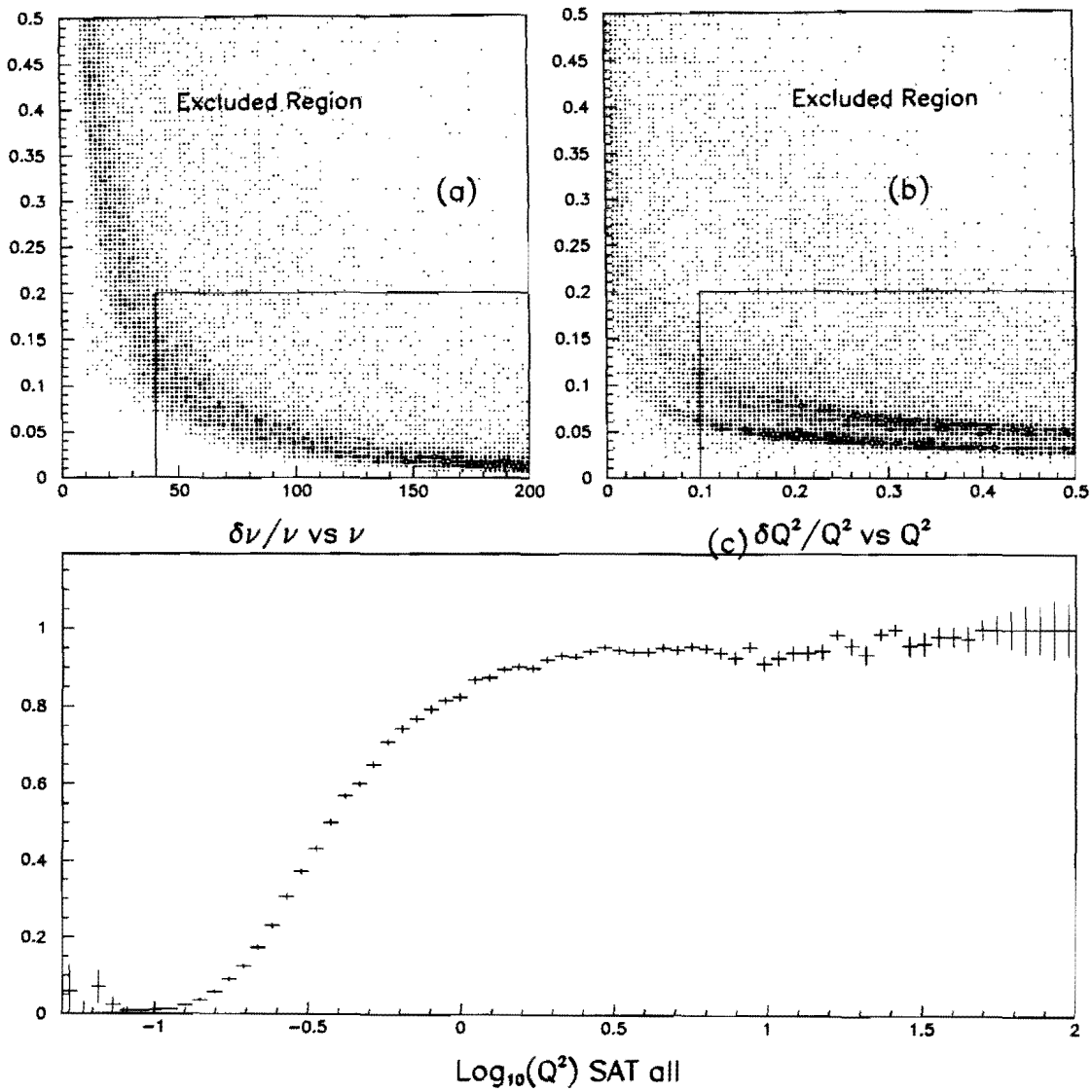

Figure 4.2: Plots of $\delta\nu/\nu$ versus ν, $\delta Q^2/Q^2$ versus Q^2, and the acceptance of SAT versus $log(Q^2)$ for all targets before cuts.

versus $log(x_{bj})$ plotted in Figure 4.3.(d), most of the $\mu - e$ events occur with $E_{cal}/\nu > 0.35$ and most of the bremsstrahlung events distributed at the value of E_{cal}/ν between 0.55 and 0.35. Figure 4.3.(e) shows the cut of $E_{cal}/\nu < 3.5$ removed most of the $\mu - e$ events at the value of $0.3 < Y_{bj} < 0.8$ at plot of Y_{bj} versus $log(x_{bj})$. Figure 4.3.(f) shows the plot of E_{cal}/ν versus $log(x_{bj})$ after required $Y_{bj} < 0.8$, most of the bremsstrahlung events distributed at value of $0.35 < E_{cal}/\nu < 0.55$ have been removed. The distribution of E_{cal}/ν in Figure 4.3.(g) shows the electromagnetic events distributed at a value of $E_{cal}/\nu > 0.35$.

The minimum requirement of at least two hadron tracks in each event for boson interference can help to reduce the contamination from electromagnetic processes. The Y_{bj} distribution after application all other cuts except Y_{bj}, as seen in Figure 4.4.(a), shows the cut at the value of $Y_{bj} = 0.8$ can remove the bremsstrahlung events. As seen in Figure 4.4.(b), the $log(x_{bj})$ distribution after application all other cuts except x_{bj} cut, the cut at $x_{bj} = 0.0007$ remove most of the $\mu - e$ scattering events. In order to reduce the electromagnetic events which survive from the Y_{bj}, x_{bj}, and multiplicity cuts, a cut on the value of $E_{cal}/\nu < 0.5$ is imposed as indicated in Figure 4.4.(c).

The distributions of Q^2, ν, $log(x_{bj})$, Y_{bj}, E_{cal}/ν, and the multiplicity are shown in Figure 4.4, (d) to (i), for events which passing all selection criteria. This Figure shows that events with low values of Q^2 high values of ν and an excess at high E_{cal}/ν, which mostly originated from electromagnetic processes, are removed by the event selection.

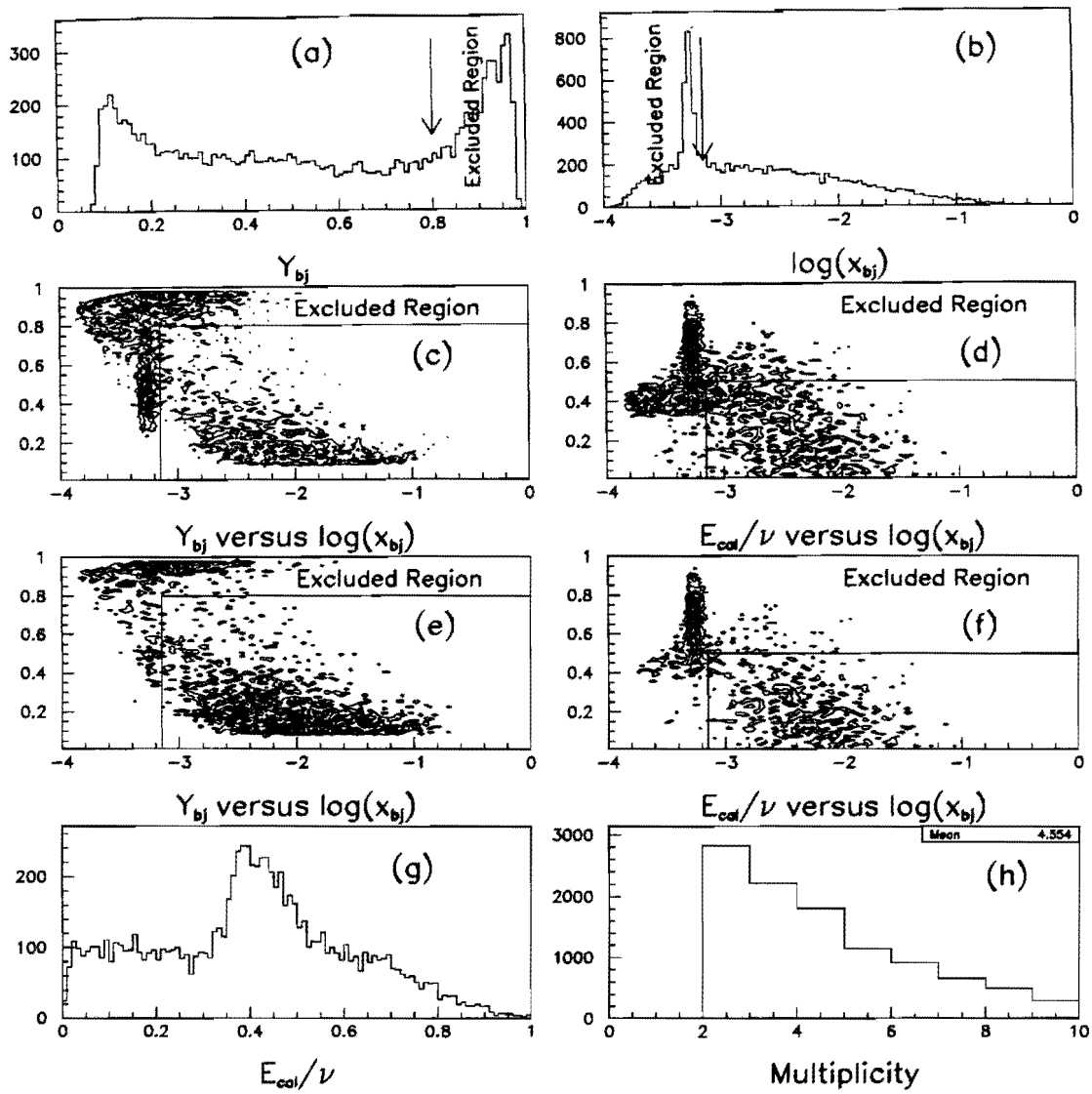

Figure 4.3: Plots for Y_{bj}, $log(x_{bj})$, Y_{bj} versus $log(x_{bj})$, , E_{cal}/ν versus $log(x_{bj})$, E_{cal}/ν, and the multiplicity for events passing the first six cuts. The "excluded region" indicates events in this region are excluded.

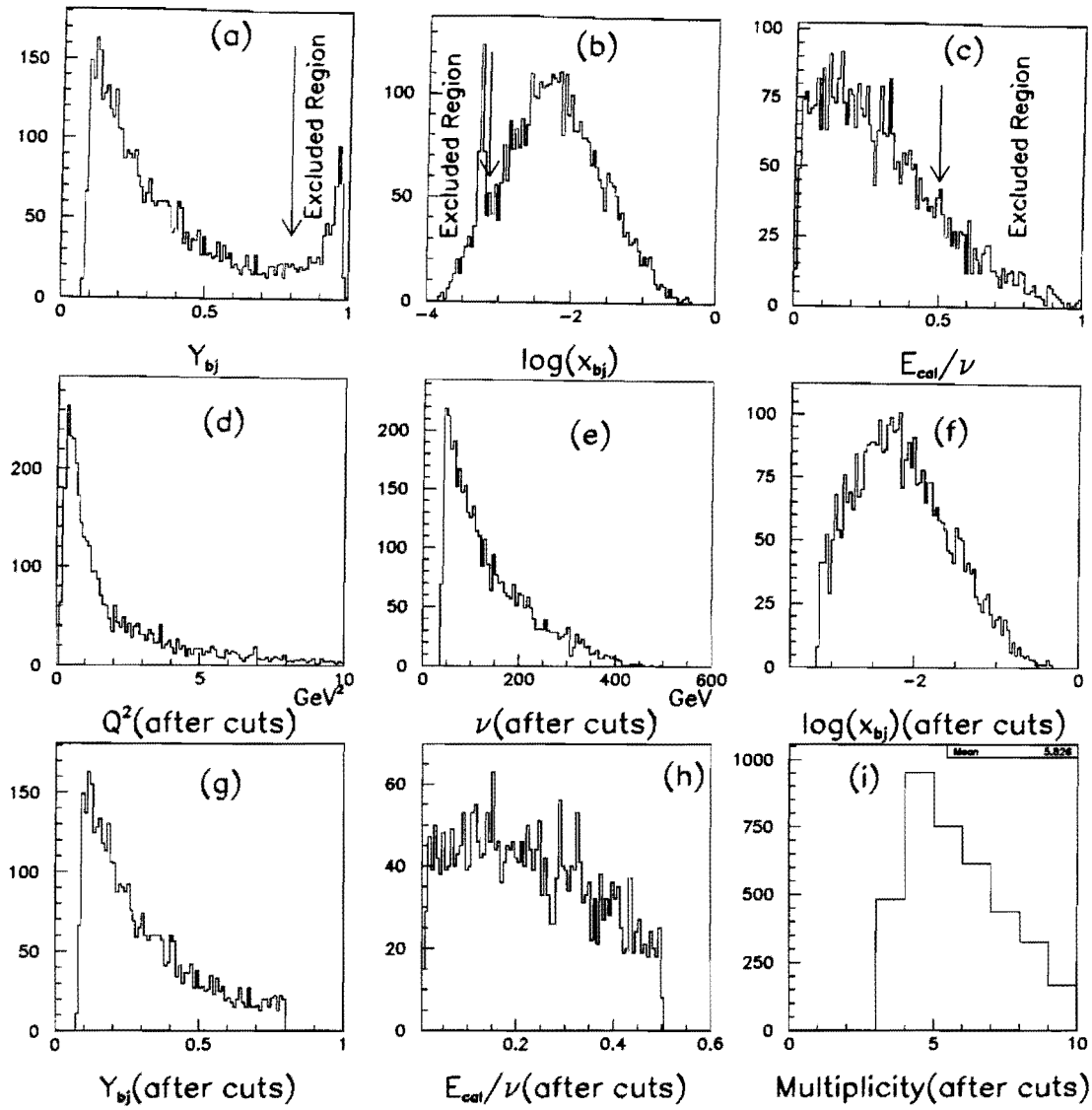

Figure 4.4: Distributions of Y_{bj}, $log(x_{bj})$, and E_{cal}/ν for events passing all cuts except the cut on the variable shown, (a) to (c). Events yield as function of Q^2, ν, $log(x_{bj})$, Y_{bj}, E_{cal}/ν, , and the multiplicity after all cuts, (d) to (i).

4.1.2 The Rejection of Events Containing Exclusively Produced Mesons

Exclusive diffractive meson production from μ^+-nucleon interactions, $\mu^+P(N) \rightarrow \mu^+\pi^+\pi^-P(N)$ or $\mu^+\pi^+\pi^-\pi^+N(\pi^-P)$, produces opposite sign hadron pairs more preferentially than like sign pairs [52]. If an event has two and only two oppositely charged tracks(excluding the muon track) the fraction of total energy carried by the two tracks compared to ν (Z_{total}) is calculated. Those events might have originated from exclusively produced meson decays (ρ, ϕ, etc.). Therefore the invariant masses calculated using pion masses and kaon masses should reflect this. Figure 4.5 shows the Z_{total} distributions for these events, and the (Z_{total}) distributions as a function of invariant masses of the pairs.

As indicated(block) in Figure 4.5, (b) and (c), a significant number of events have Z_{total} greater than 0.85, and have invariant masses in the region of the ρ and ϕ masses, 0.77 GeV and 1.02 GeV respectively. In order to investigate these exclusive production events and eventually exclude them from the event samples, the following study is performed: if the Z_{total} of events is greater than 0.85, the invariant masses are calculated with π and K masses as shown in Figure 4.6. A one-Gaussian fit centered at the ρ mass was performed for $M_{\pi\pi}$ distribution and at ϕ mass for M_{KK} distribution, (b) and (c).

If the invariant mass, calculated with pion masses, is within the range of ρ^o mass(0.770 $\pm$ 0.15 GeV) the event is considered as an exclusive ρ^o event which decayed to $\pi^+\pi^-$ and is rejected. If the invariant mass, calculated with kaon masses, is within the ϕ mass(1.020 $\pm$ 0.02 GeV) then this event is considered as a $\phi \rightarrow K^+K^-$ event and is rejected. About 3.5% of the total events which passed the event selections are removed. Table VII is a listing of one-hadron split events which passed all event selection criteria for 5 different targets.

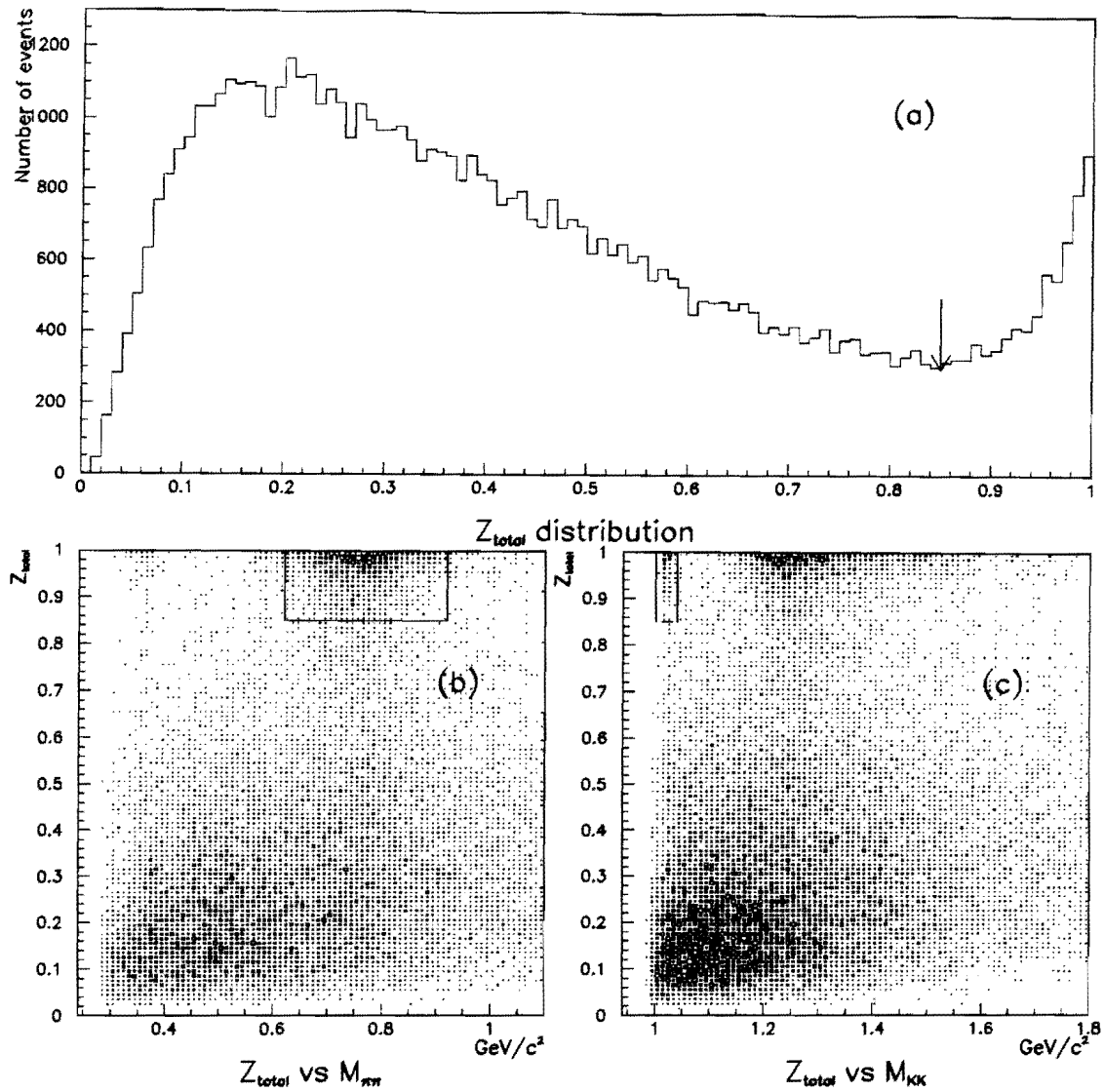

Figure 4.5: Z_{total} plot for two oppositely charged tracks events and the Z_{total} versus invariant masses of these two tracks. The plot at the lower-left is for Z_{total} versus invariant mass($M_{\pi\pi}$) and the lower-right is for Z_{total} versus invariant mass(M_{KK}).

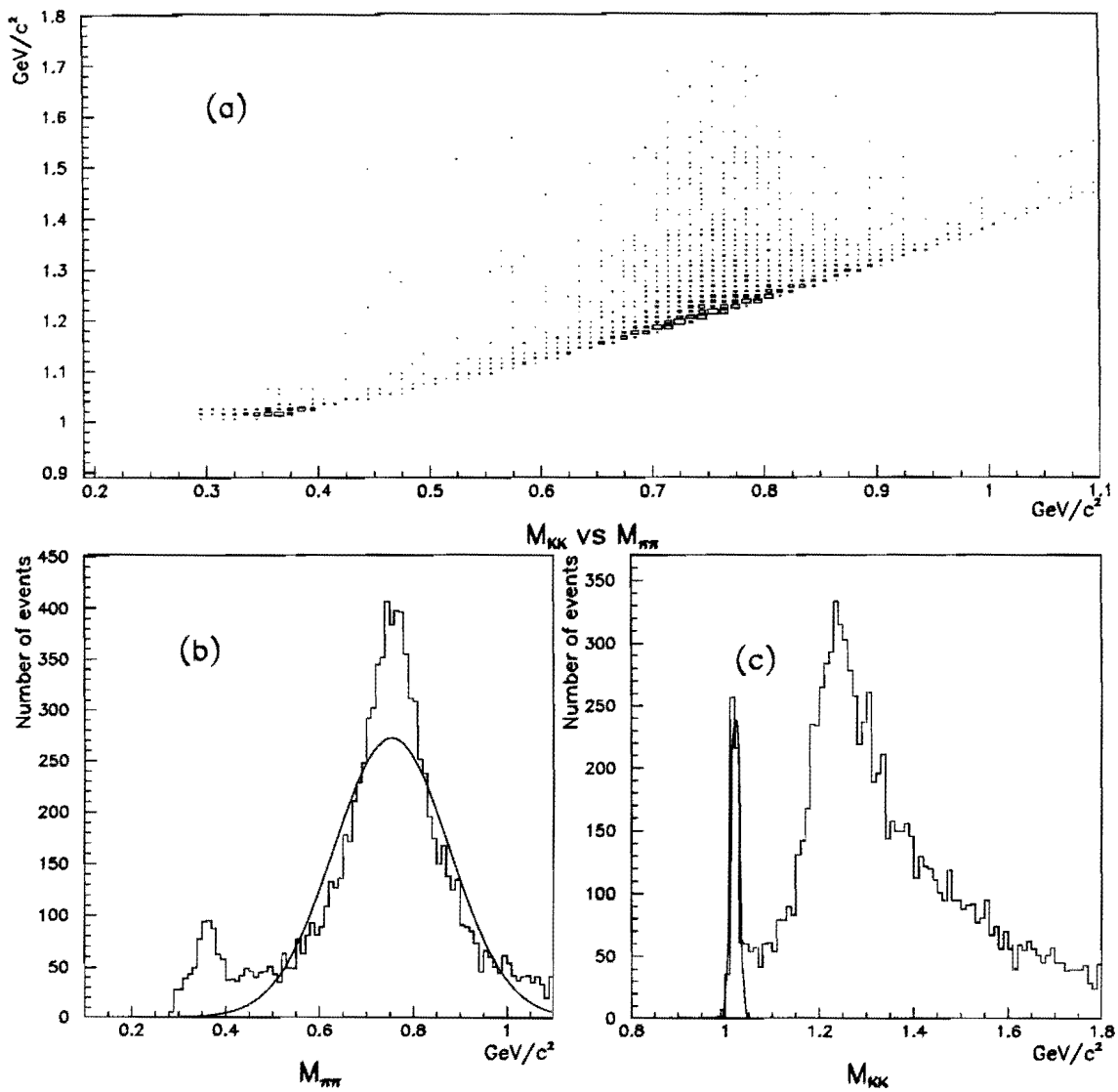

Figure 4.6: The invariant mass ($M_{\pi\pi}$, M_{KK}) distributions of exclusive two oppositely charged tracks events.

TABLE VII: EVENTS FAILED FOR EACH SELECTION REQUIREMENT

Target	H2	D2	C	Ca	Pb
Initial number of event	212290	261847	272904	267261	169711
events cut					
One intime beam and Event Kinematic cuts	152849	188529	196491	192428	122192
Bad ZEBRA structure	2	3	3	4	2
Vertex position cuts	24	30	26	26	20
Beam momentum cuts	912	1126	1173	1149	730
$E_{cal}/\nu < 0.5$	14207	17525	18265	17888	11359
Two tracks	13907	16375	17072	16715	10611
Exclusive ρ or ϕ	903	1110	1151	1132	722
Total Events left	29486	37148	38723	37919	24075

4.2 Track Selection

The goal for track selection is to select the tracks which are well reconstructed hadrons originated from primary interaction. Tracks which passed the PTMV reconstruction, as described in chapter 3, with well defined charge and momentum, are used. Following is the list of basic hadron track requirements;

- not a muon track.
- have a complete ZEBRA structure.
- have a momentum value greater than 0 and less than 1000 GeV.
- the χ^2-probability of track fitting is greater than 0.001.
- the measured displacement of track position at the primary vertex is less than 5 σ.

4.2.1 Fitted and Close Tracks

Tracks were assigned to two different categories: either "fitted" or "close" to a primary vertex as discussed in chapter 3. In order to eliminate tracks which did not originate from a primary interaction, a study of track "fitted" assignment was undertaken. The tracks which are "close" to the primary vertex but "fitted" to the secondary vertex are eliminated in this analysis. Secondary vertices should be located downstream of the primary vertex if they are due to reinteractions or decays. Figure 4.7 shows the difference of X-position between vertices, $X_{primary} - X_{second.}$, for both reconstructed Monte Carlo and data events.

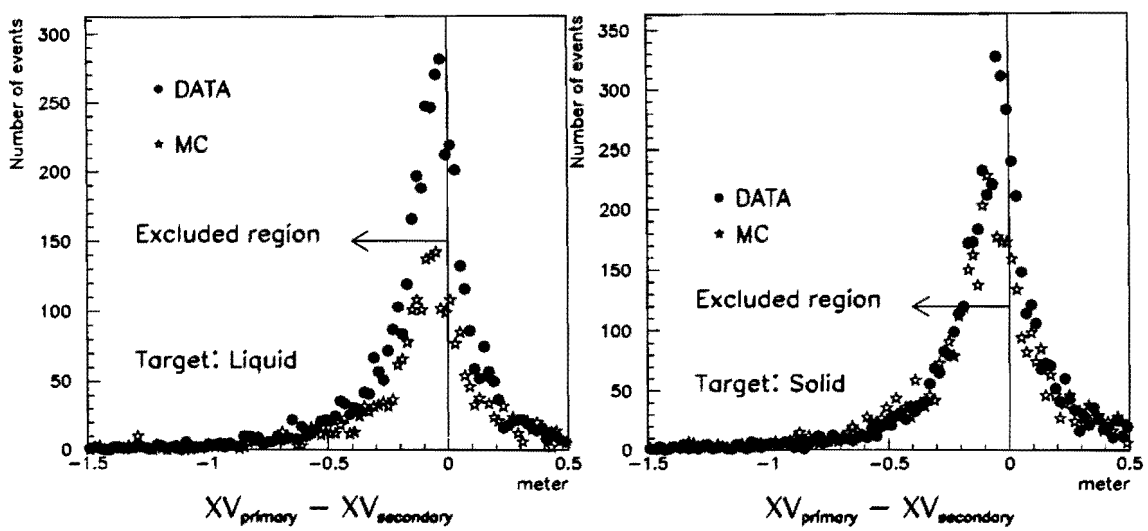

Figure 4.7: X-position difference between primary and secondary vertices for tracks which "fitted" to the secondary vertex. The negative value of difference indicates the primary vertex has been reconstructed upstream of the secondary vertex.

Hadron tracks which are "fitted" to any secondary vertex with the secondary vertex located downstream of the primary vertex, indicated as "excluded region" in Figure 4.7, originated mainly from reinteractions($\sim$ 12 %) or decays($\sim$ 50 %) and are eliminated. About 15% of total secondary tracks have secondary vertices located upstream of primary vertex, these may be due to the fluctuation of reconstruction, are kept for the next examination.

The distance of closest approach of a track from the primary vertex is defined as the distance between the extrapolated location of the track at the X-position of the primary vertex and the primary vertex itself. For a "fitted" track, the minimum distance from the vertex, d, was required to be less than 2 cm and the d/σ_d (σ_d is the minimum distance error) was required to be less than 4 as described in chapter 3. Other tracks not satisfying those requirements are termed "close" tracks. Figure 4.8, (a) and (b), show the distributions of minimum distance and d/σ_d for "all", "fitted", and "close" tracks. Figure 4.8.c shows the minimum distance for all track("fitted" and "close" tracks) were less than 2 cm after required $d/\sigma_d > 4$. On the other hand, as shown in Figure 4.8.d, the d/σ_d contribution had a tail exceeding 4 after required d < 2 cm for "close" tracks. Small contamination of "close" track which satisfied the "fitted" definition are mainly originated from secondary vertex tracks with secondary vertex upstream of primary vertex. In order to use all tracks for this analysis(including "fitted" and "close" tracks), a requirement of d < 2 cm and $d/\sigma_d < 4$ is imposed.

Figure 4.8.(e) and (f) are the ratio of data and Monte Carlo of these two variables. A large depression at small values of d and d/σ_d. This might caused by the Monte Carlo simulation of VDC detector had better resolution. About 70 % of secondary tracks have secondary vertex located at upstream of the primary vertex are survived from this cut.

4.2.2 Identical Track Remove and Track Quality Cuts

A possibility exists that a single track was reconstructed as two separate tracks. This will give a fake signal at very small four-momenta difference, q. In order to remove such tracks, hits from the PC-PCF detectors and VDC detector (for VDC-only) tracks have been checked. If more than 50 % of PC-PCF (VDC) planes contributed to two tracks simultaneously, and if more than 50 % out of those hits were identical, tracks were considered to be identical. The track which had worse χ^2 probability was eliminated. Less than 1% of tracks were rejected due to sharing hits.

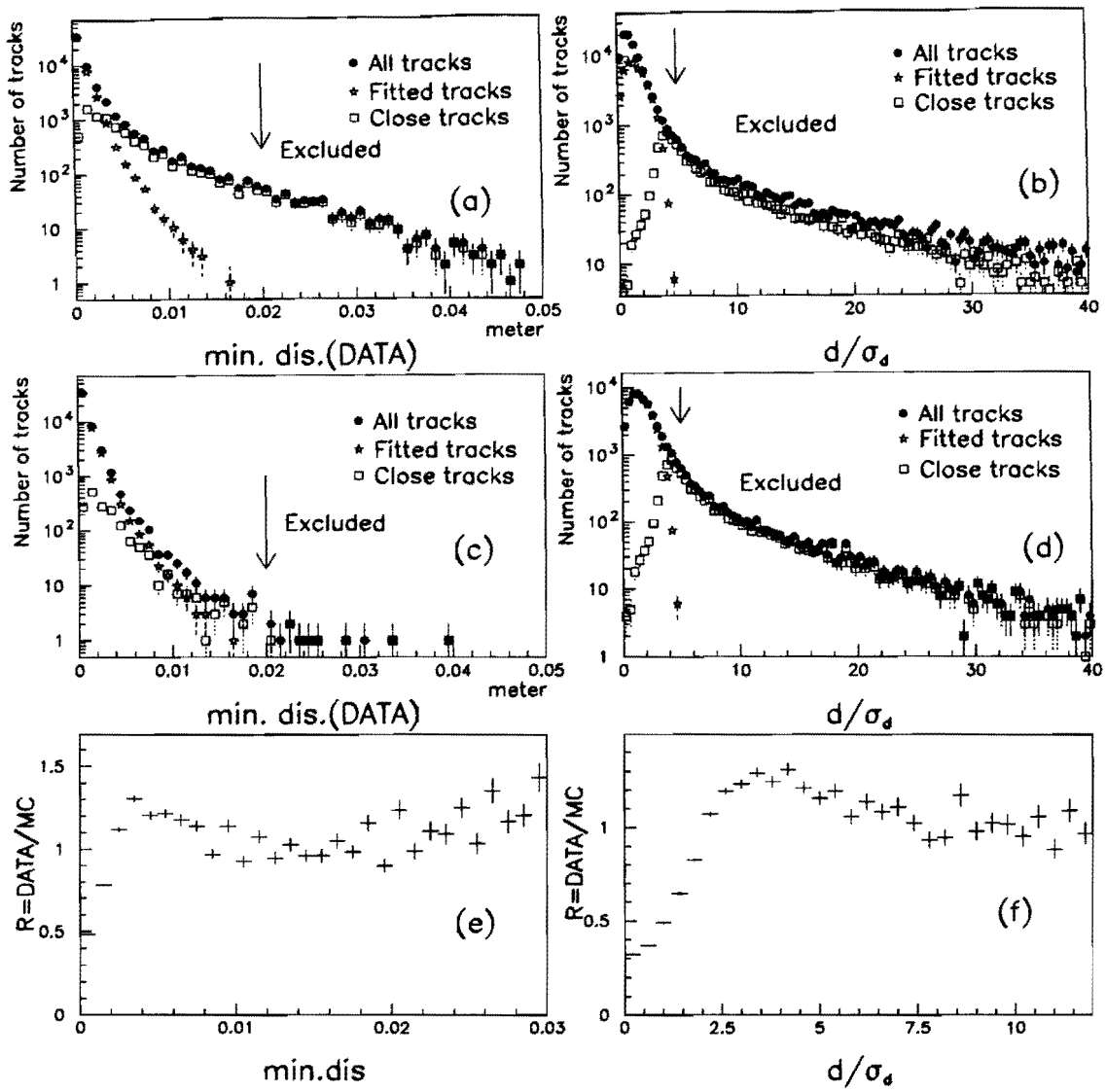

Figure 4.8: Minimum distance(d) and d/σ_d distributions for all, "fitted", and "close" tracks and R=DATA/MC distribution as functions of d and d/σ_d.

Another mechanism by which the geometrical properties of tracks are similar arise when a track reconstructed by the FS is not matched to any VDC's. Later it is also reconstructed as a separate VDC-only track. In order to avoid this problem, there was an additional requirement for VDC-only tracks: VDC-only tracks which had a momentum greater than 12 GeV and dY/dX and dZ/dX measured at the vertex < 20 mrad were rejected. This requirement intends to remove the VDC-only tracks which indeed traversed the forward spectrometers. Figure 4.9 shows the momentum dependence of dY/dX and dZ/dX measured at the vertex for forward spectrometer(FS) tracks and VDC-only tracks for both data and reconstructed Monte Carlo events. The VDC only tracks inside the regions bounded by the lines were excluded.

Additional track quality requirements were imposed to ensure high quality tracks for analysis. The curvature of a track which is proportional to $1/P$, is a purely geometrical quantity. It is a function of the track length, the number of hits on the track and the hit resolutions only. In particular, it is not an explicit function of momentum. Therefore a study of the error on the curvature which is $\delta P/P^2$ reveals the variation in track length and the number of hits on the track. Figure 4.10 shows the distribution of $\delta P/P^2$ for FS and VDC-only tracks. Both plots indicate that there are two distributions in each plot, this is presumably due to some tracks been longer than others. In order to test this hypothesis, these distributions are plotted again after the tracks are required to intersect certain key planes(PCF3) and are required to have minimum number of VDC hits (40) for VDC-only track. This ensure a minimum track length. The comparison of the distributions of $\delta P/P^2$ before and after the cuts described above (Figure 4.11) shows that the cut removes most of the tracks with large error on the curvature. The fractional momentum resolution($\delta P/P$) of each track is proportional to $\delta P/P^2$, $\delta P/P = deltaP/P^2 \cdot P$, for a track with $\delta P/P > 0.02$ was rejected. The Y, Z positions of track measured at primary vertex are required to be inside the target material region as in Figure 4.12, $-0.04m < Y < 0.02m$ and $-0.02m < Z < 0.02m$.

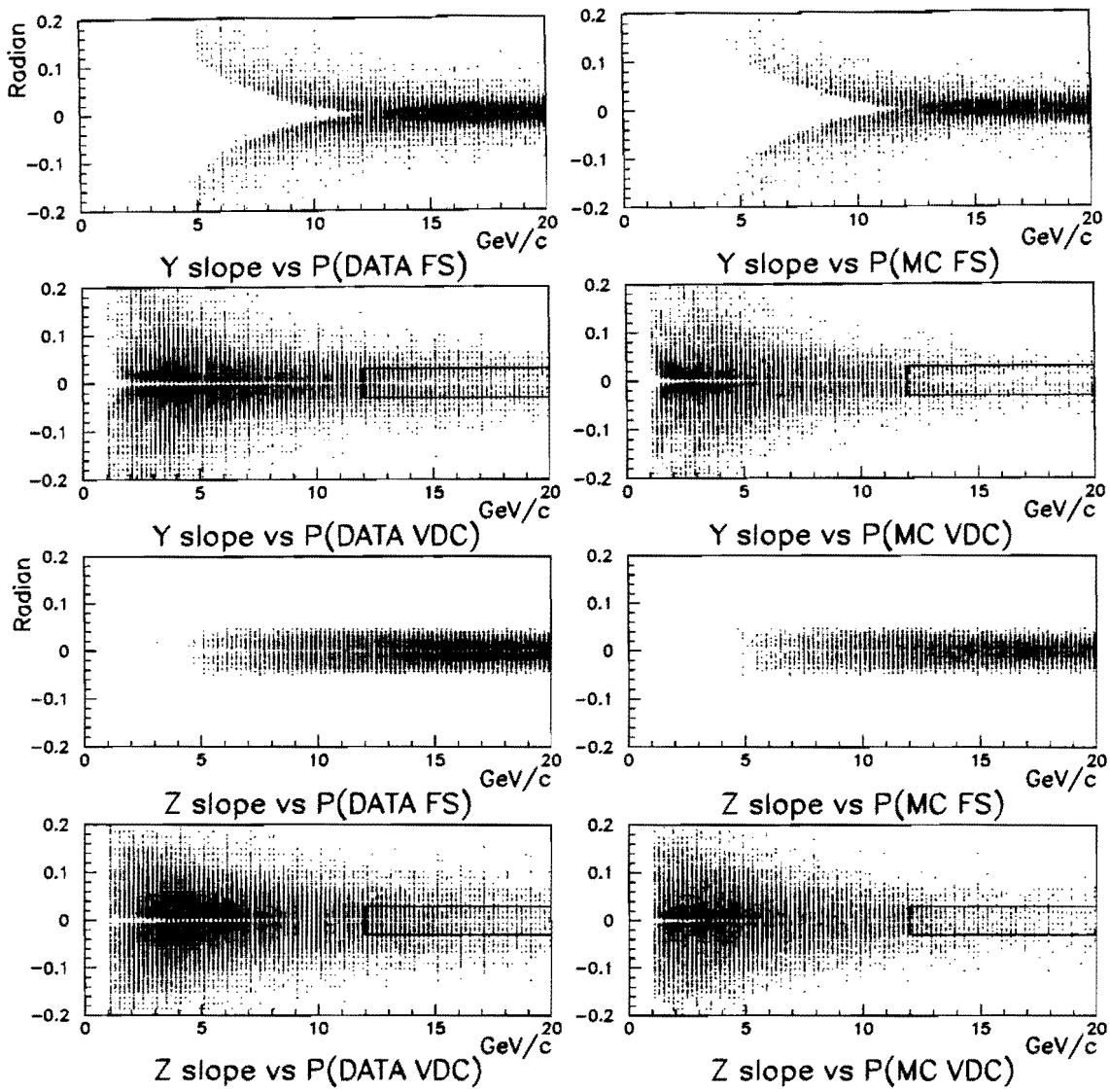

Figure 4.9: The momentum dependence of the Y and Z slopes measured at the vertex for Forward Spectrometer (FS) and VDC-only tracks. Plots on the left are data and plots on the right are Monte Carlo events. The bounded regions indicate the rejection area of tracks.

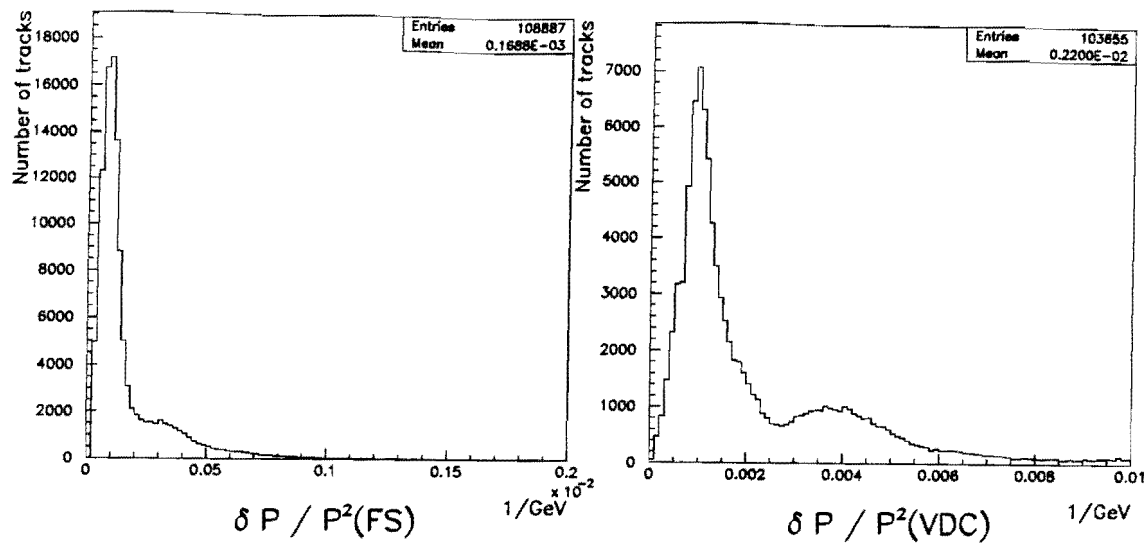

Figure 4.10: $\delta P/P^2$ distributions for forward spectrometer (FS) and VDC-only tracks.

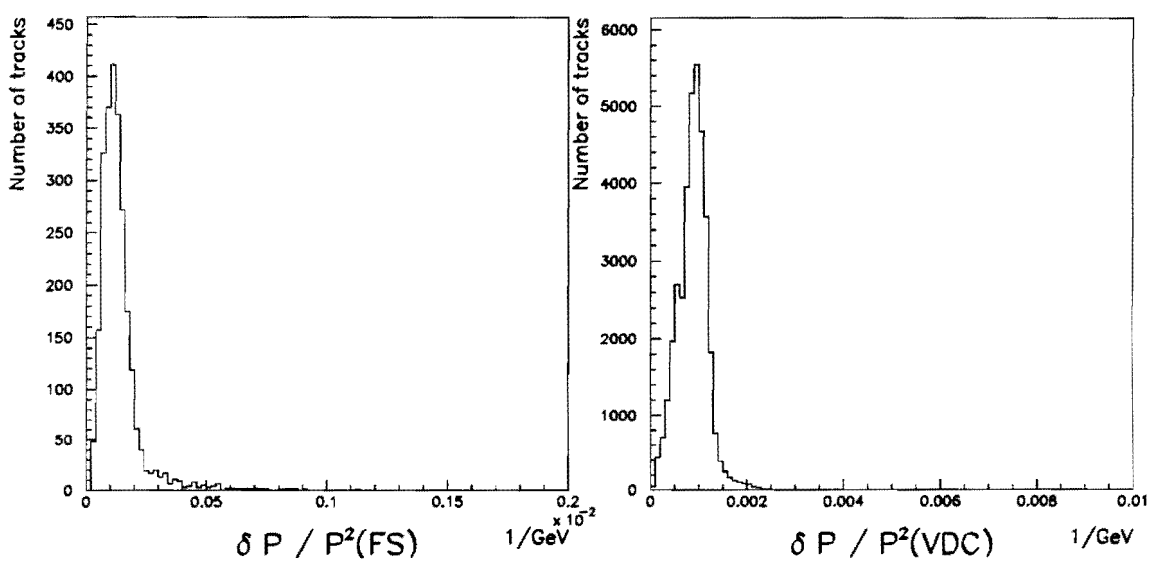

Figure 4.11: $\delta P/P^2$ distributions for forward spectrometer (FS) and VDC-only tracks after track length cut.

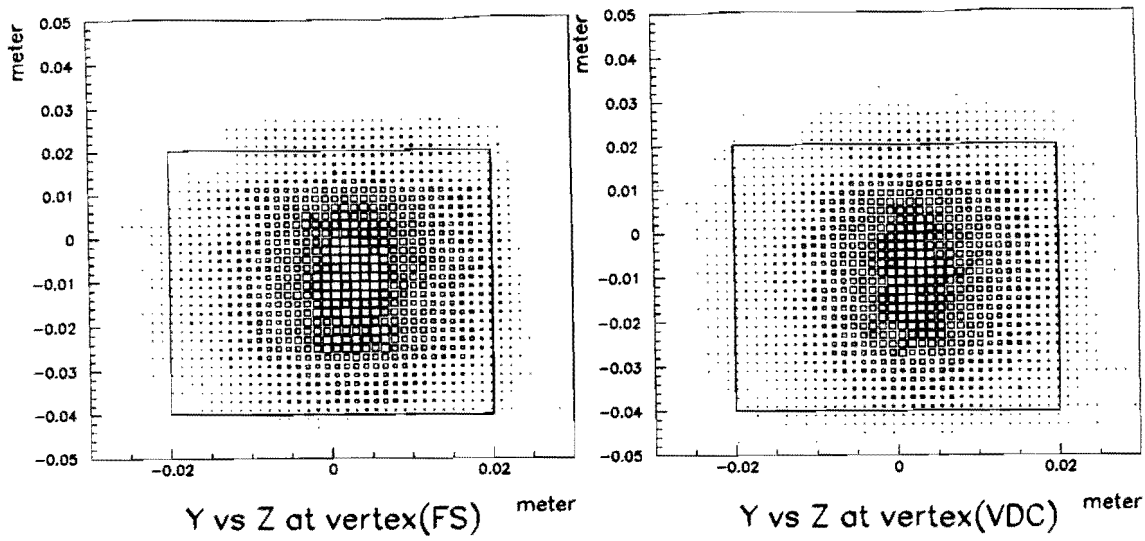

Figure 4.12: Y versus Z position of track at the primary vertex for forward spectrometer (FS) and for VDC only tracks.

4.3 The Monte Carlo Study

All particles created during the collision are not fully detected due to the acceptance of experimental apparatus and the efficiency of the reconstruction. The Monte Carlo technique provides information to understand the reconstruction capability and the experimental acceptance. In this section, the results of studies of the efficiency for reconstructing tracks as a function of track variables are described.

Events generated from the Monte Carlo are referred to as "TRUE" and the Monte Carlo events which passed the same reconstruction package (PTMV) as data are labeled as "MC REC".

4.3.1 Acceptance and Reconstruction Efficiency

The full acceptance of the experiment is defined as the fraction of "MC REC" / "TRUE". The full acceptance is based on two factors of the experiment: the geometrical acceptance and the reconstruction efficiency. Not all generated "TRUE" tracks can propagate through the whole experimental geometry apparatus. Thus, the geometrical acceptance is defined as the fraction of the "TRUE" tracks which entered the electronically active region of the apparatus. The reconstruction efficiency is defined as the fraction of these tracks which were reconstructed. The chamber efficiency, overlapping tracks and PR algorithms all contribute to this value. The full acceptance described in this section represents the combination of these two effects, the geometrical acceptance and reconstruction efficiency.

A charged particle is defined as geometrically accepted if it went through VDC4 and VDC10 located in the gap of CVM magnet, this requirement insure the minimum number of VDC hits for reconstruction. The geometrical acceptance was calculated as the ratio of two true distributions: geometrically accepted tracks over all generated tracks. Figure 4.13 to Figure 4.18 show the geometrical acceptance, reconstruction efficiency, and overall full acceptance of tracks as a function of P, Y position, Z position, dY/dX, and dZ/dX measured at primary vertex in the liquid target. Each distribution was divided into positive and negative tracks and the ratio(positive/negative) was shown in the plot(c, f, i). The full acceptance distribution as a function of P is similar for positive and negative track but for positive tracks is about 10 % higher than negative tracks at P $\sim$ 30 GeV/c, the PR in the DC dead region surrounding the beam contributed to this difference. Figure 4.13.(g) and (h) show the full acceptance drops sharply at low momentum, below 4 GeV/c, because these tracks are neither able to enter the apparatus nor able to "fire" enough detectors to be reconstructed , as shown in the geometrical acceptance in (a) and (b).

In Figure 4.14, plot shows that when momentum increases the VDC's reconstruction efficiency rises and the full acceptance reaches a plateau around 35 % at P $\sim$ 4 GeV/c. At this plateau, the full acceptance is dominated by the VDC chambers. When the momentum

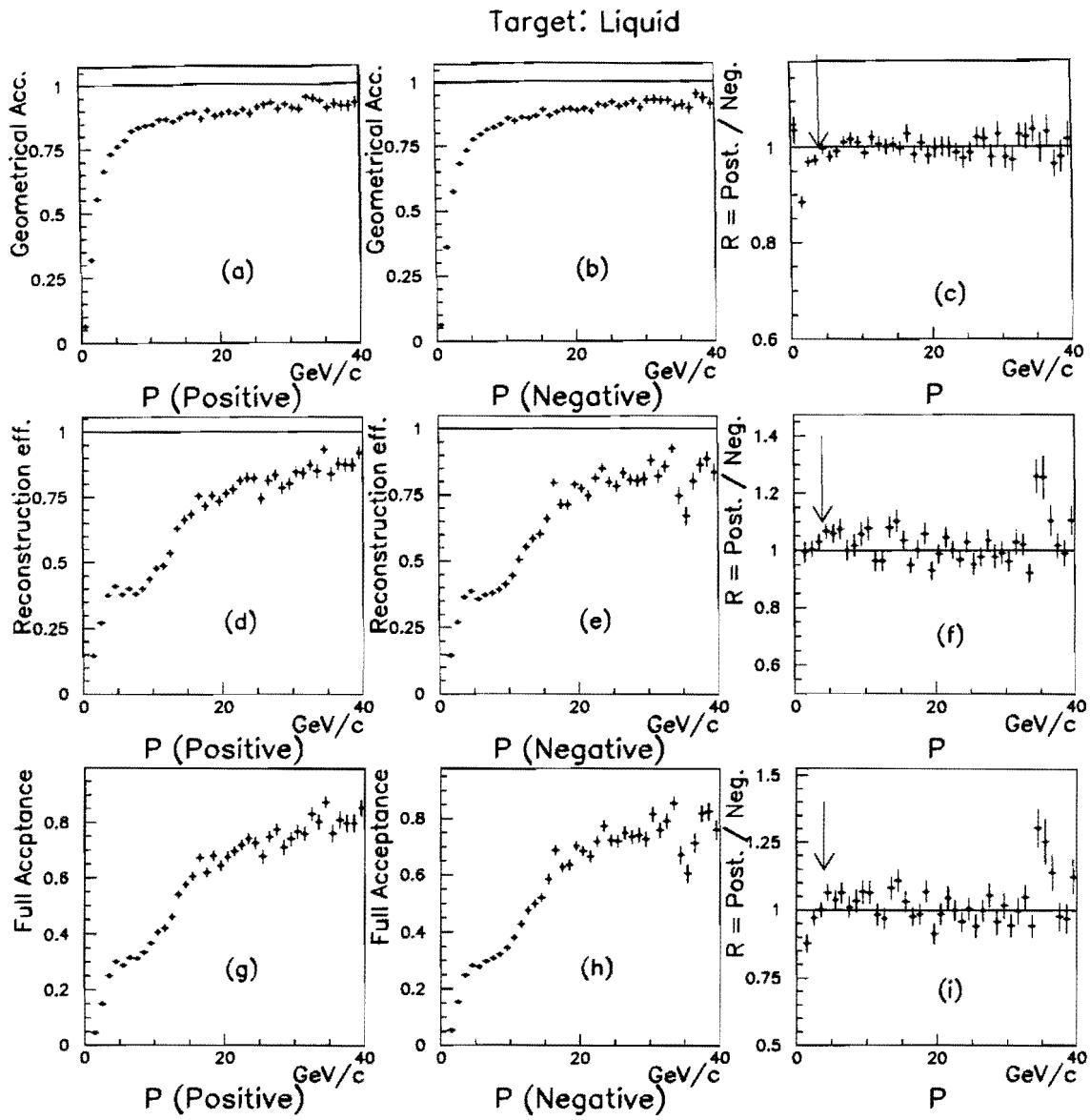

Figure 4.13: Geometrical acceptance, reconstruction efficiency, and full acceptance, as a function of momentum for positive and negative tracks. The arrow indicate the value of cut on momentum(4 GeV/c).

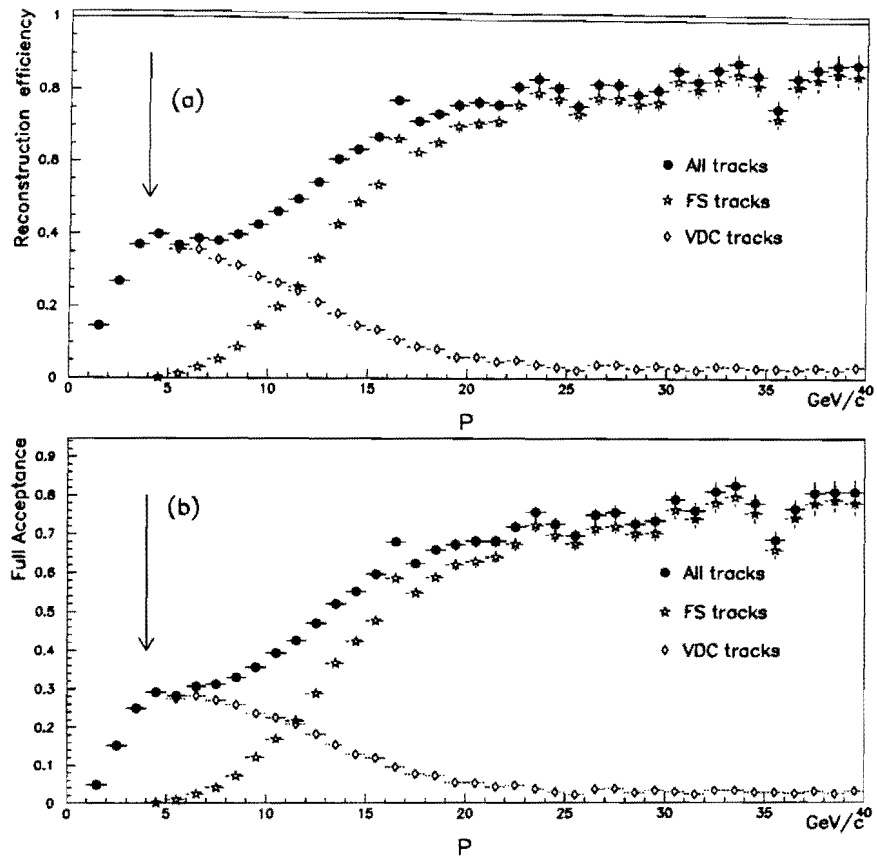

Figure 4.14: The momentum dependence of reconstruction efficiency (a) and full acceptance (b) for all, FS-only, and VDC-only tracks. The arrow indicate the value of cut on momentum(4 GeV/c).

increases to above 8 GeV/c, the tracks start entering the forward spectrometer and the full acceptance increases with momentum to another plateau around 80 % when momentum reaches 20 GeV/c.

Due to the magnet field bends charged particles in the Y direction only. Plots in Figure 4.15 and Figure 4.17 show that the geometrical acceptance and reconstruction efficiency were strongly dependent on the Y position and dY/dX measured at primary vertex for different charged tracks. No charge dependence on the Z-position and dZ/dX at primary vertex as shown in Figure 4.16 and Figure 4.18. The sharply cut off in the acceptance as function of Y and Z position measured at the primary vertex was due to the beam size, -3 cm $<$ Y $<$ 1 cm and -2 cm $<$ Z $<$ 2 cm. The distribution outside this region was the acceptance for tracks which were not originated from the primary interaction. The low efficiency in reconstructing close tracks at small Y and Z open angle introduced the central dip structure in the full acceptance as function of Y and Z slope.

Figure 4.19, (a) and (b), shows the momentum dependence of full acceptance for liquid and solid targets, and the ratio (solid/liquid) is shown in Figure 4.19.c. Figure 4.20 and Figure 4.20 show the same plots for full acceptance as a function of Y, Z, dY/dX, and dZ/dX measured at primary vertex. The full acceptance for solid target is consistent with liquid target except a higher acceptance for solid target at P $<$ 4 GeV/c. This enhancement indicates that the solid target can generate more low momentum tracks than liquid. The ratio of full acceptance of solid/liquid targets does not depend on the Y and Z positions of primary vertex. The ratio of full acceptance of solid/liquid targets does seem to depend on the Y and Z slopes of the tracks at the primary vertex. To make the acceptance for both liquid and solid targets are consistent, cuts on track momentum(P) $>$ 4 GeV/c and -3 cm $<$ Y $<$ 1 cm and -2 cm $<$ Z $<$ 2 cm and abs(Y', Z') $<$ 100 mrad are imposed.

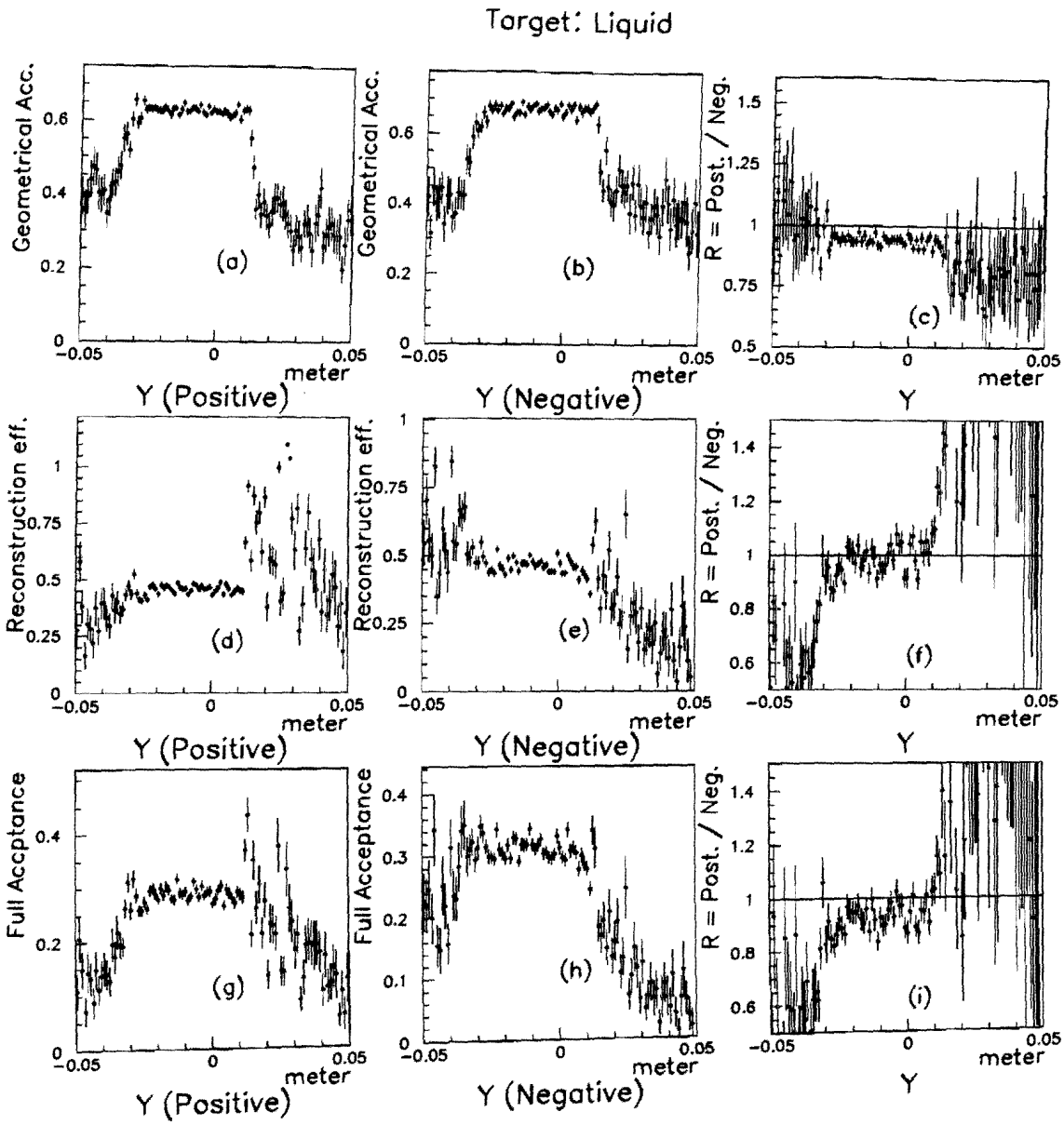

Figure 4.15: Geometrical acceptance, reconstruction efficiency, and full acceptance as a function of Y position measured at primary vertex for positive and negative tracks.

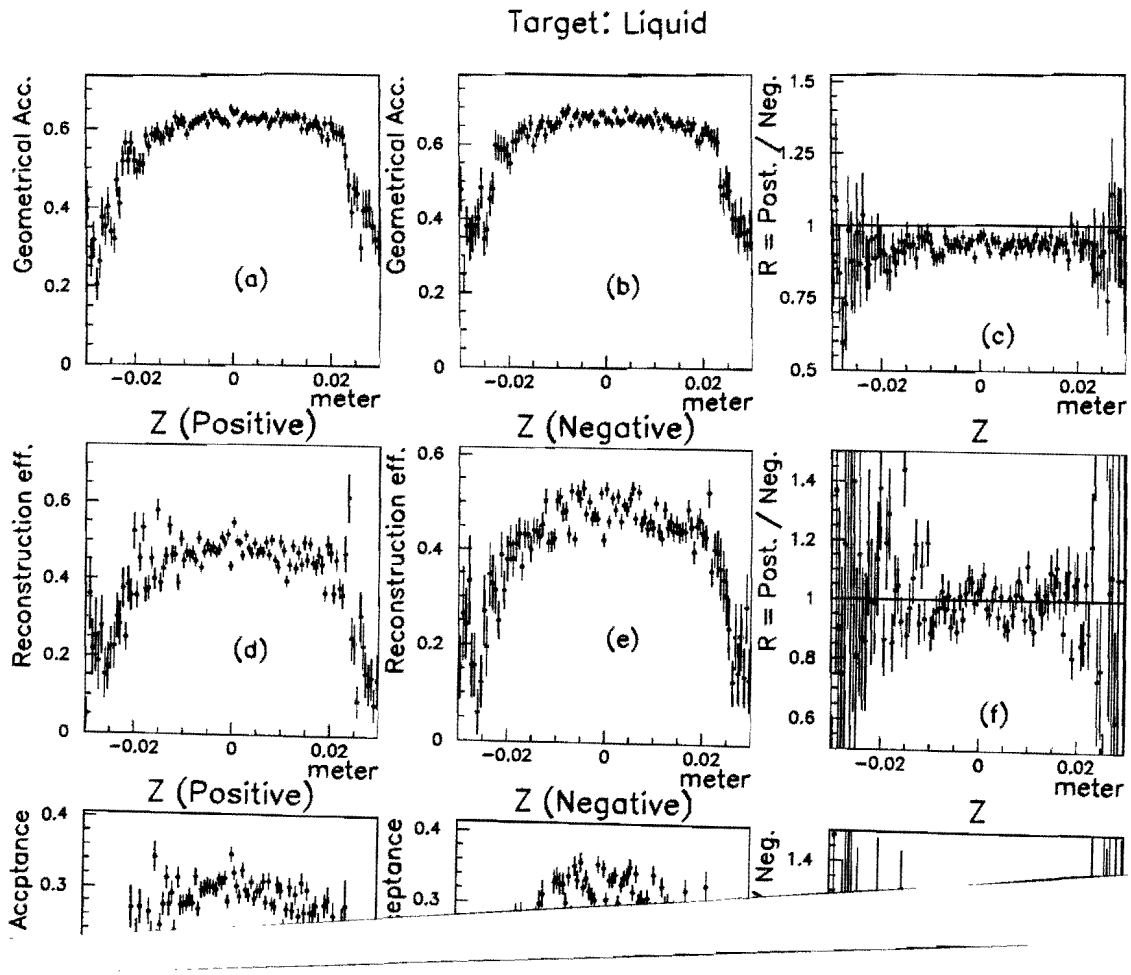
Target: Liquid
Geometrical Acc.
(a)
meter
Z (Positive)
Geometrical Acc.
(b)
meter
Z (Negative)
R = Post. / Neg.
(c)
meter
Z
Reconstruction eff.
(d)
meter
Z (Positive)
Reconstruction eff.
(e)
meter
Z (Negative)
R = Post. / Neg.
(f)
meter
Z
Accptance
Z (Positive)
Z (Negative)
Z

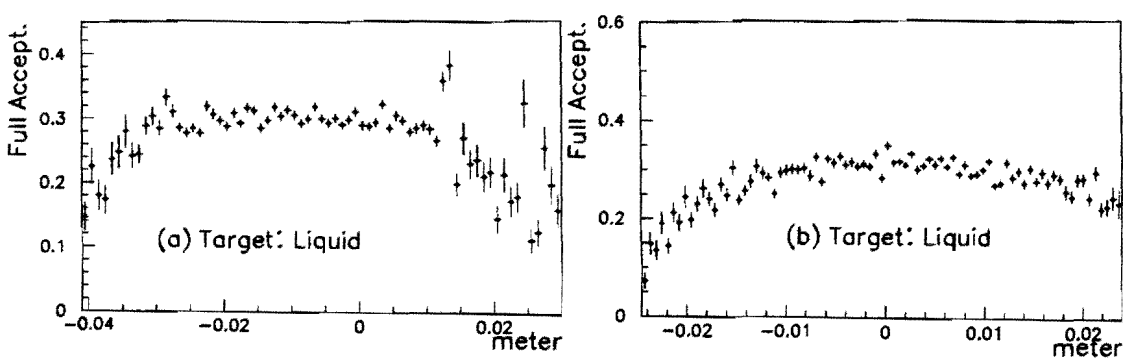
Full Accept.
(a) Target: Liquid
meter
Full Accept.
(b) Target: Liquid
meter

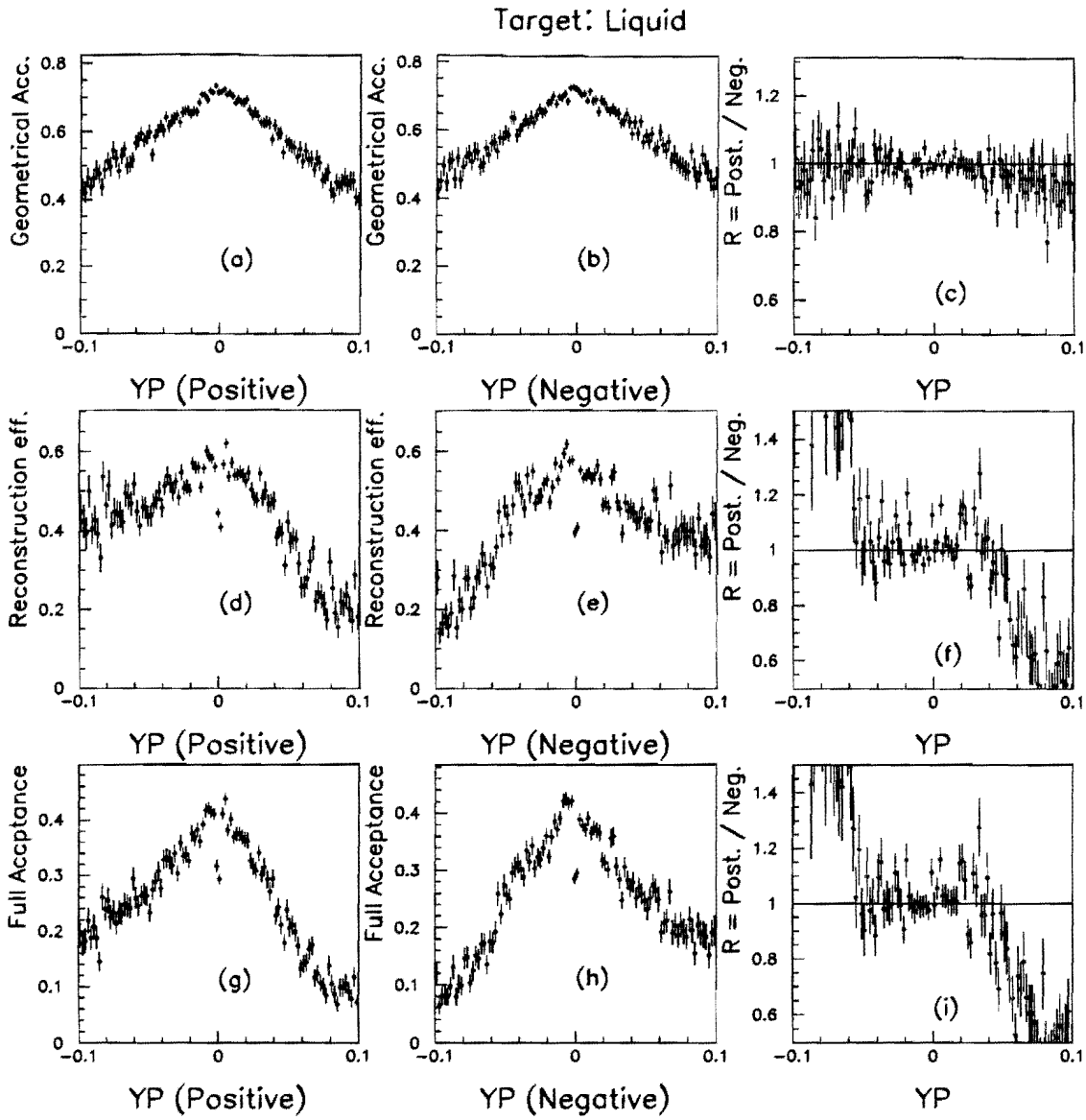

Figure 4.17: Geometrical acceptance, reconstruction efficiency, and full acceptance as a function of dY/dx measured at primary vertex for positive and negative tracks.

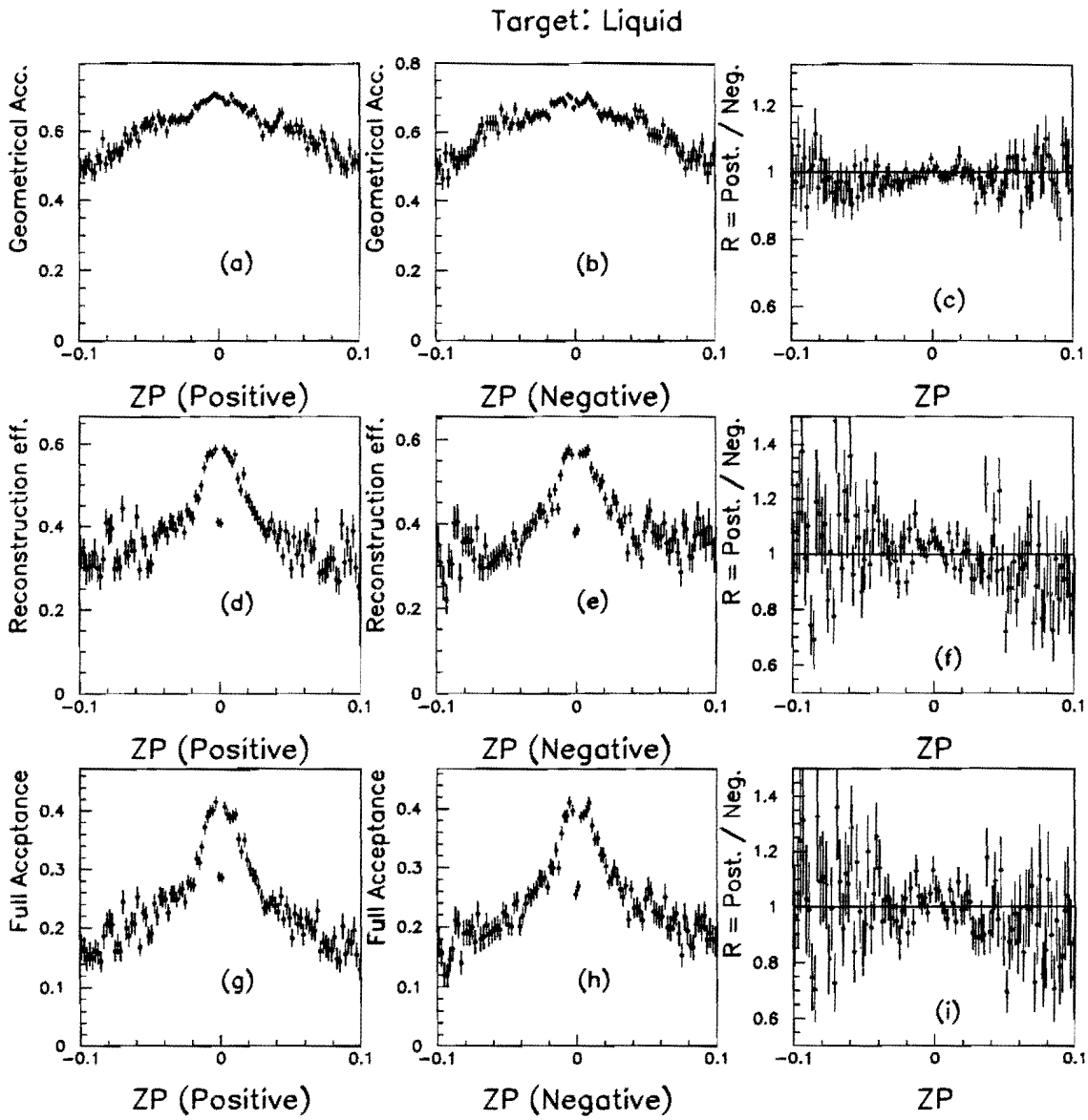

Figure 4.18: Geometrical acceptance, reconstruction efficiency, and full acceptance as a function of dZ/dx measured at primary vertex for positive and negative tracks.

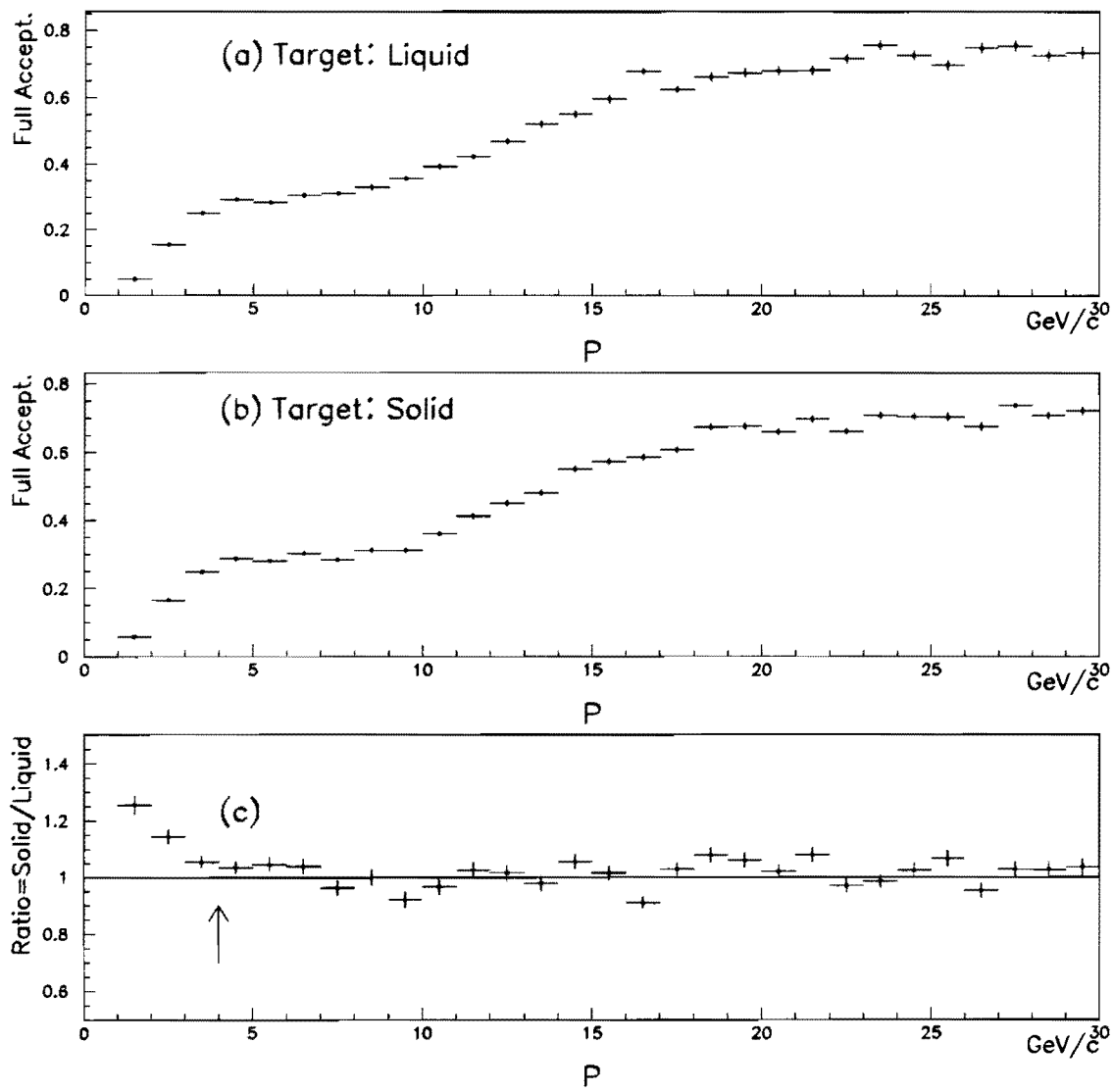

Figure 4.19: The momentum dependence of full acceptance for liquid and solid targets, (a) and (b). The ratio of solid and liquid target for full acceptance is shown in (c).

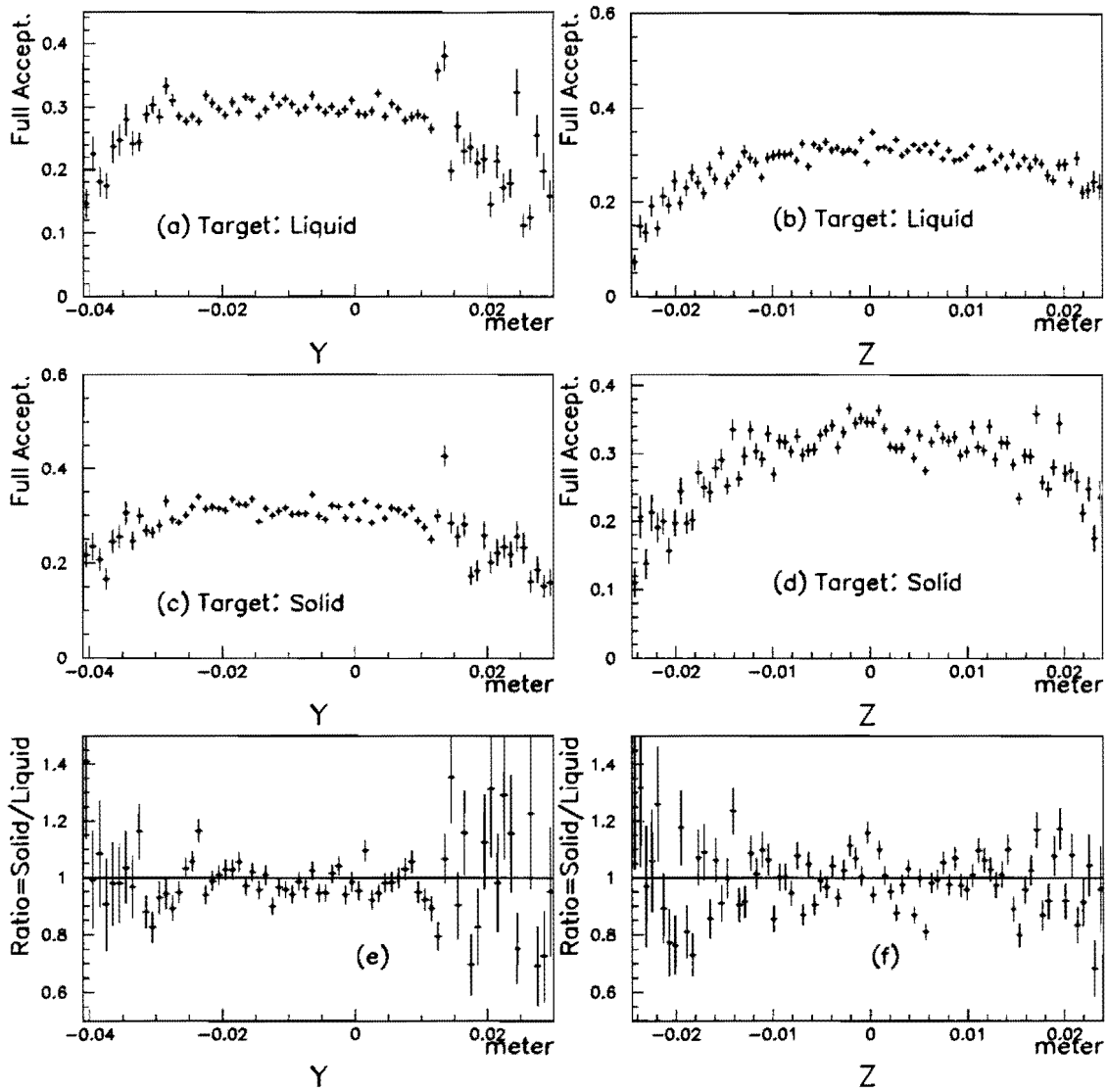

Figure 4.20: The full acceptance as a function of Y and Z position measured at primary vertex for liquid and solid targets, (a) and (b). The ratio of solid and liquid target for full acceptance is shown in (c).

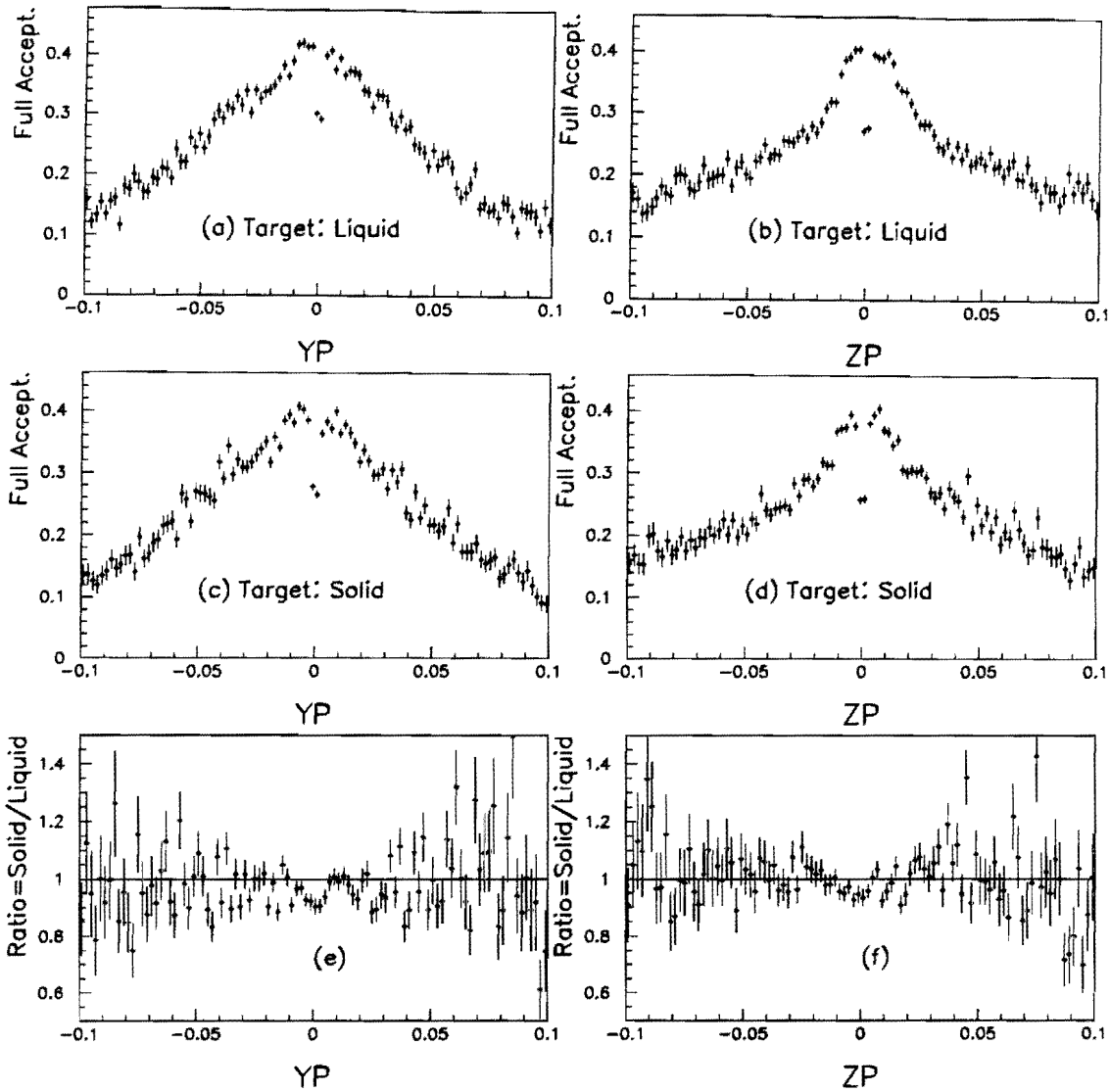

Figure 4.21: The full acceptance as a function of dY/dX and dY/dX measured at primary vertex for liquid and solid targets, (a) and (b). The ratio of solid and liquid target for full acceptance is shown in (c).

A summary of the final track selection criteria, based on the studies described above, as follow;

- non-muon tracks with complete ZEBRA structure
- the χ^2 probability of track fitting greater than 0.001
- the measured resolution of tracks (Y, Z, Y slope, and Z slope) at primary vertex is less than 20 %
- secondary tracks with vertex located downstream of primary vertex are rejected
- satisfy the "fitted" definition
- VDC only tracks should have more than 40 hits and if P greater than 12 GeV/c should have $|Y'|$ and $|Z'| > 20$ mrad
- $P > 4$GeV/c and $\delta P/P < 0.02$
- - 100 mrad $< Y', Z'$ at vertex $<$ 100 mrad
- -3.0 cm $<$ Y at vertex $<$ 1 cm and -2 cm $<$ Z at vertex $<$ 2 cm.
- remove tracks with $|Y'| = 0$ and $|Z'| = 0$
- $E_{cal}/P < 0.8$ if track has non-zero calorimeter energy

The last requirement is needed to eliminate electrons. Approximately 97 % electrons (positrons) originate from photon conversions. The calorimeter can help to remove these electrons if their momentum are large enough to reach the calorimeter (greater than 10 GeV/c). If the electron reaches the calorimeter and deposits its energy in the calorimeter, and if the deposited energy cluster is greater than 2 GeV, then the ratio of cluster energy over momentum of the track is checked. If the ratio is greater than 0.8 then the track is assumed to be an electron and is eliminated from the sample[60].

The full acceptance as a function of P, Y′, Z′, and Y and Z position of tracks measured at the primary vertex provides overall experimental reconstruction efficiency for tracks. In order to make the study more relevant to the tracks which used in this analysis, selections of the "TRUE" and "MC REC." tracks were imposed. A "modified" full acceptance measurement was made as follow: The "TRUE" tracks were required to originate from the primary vertex with momentum greater than 4 GeV/c. The "MC REC." tracks were required to pass the "good" tracks cuts described in the previous sections. Then the ratio of "MC REC."/"TRUE" was measured.

Figures 4.22 to 4.24 show the "modified" full acceptance as a function of P, Y position, Z position, dY/dZ and dZ/dX of tracks measured at the primary vertex for both solid and liquid targets. The ratio of solid/liquid targets for "modified" full acceptance as function of P is consistently flat at the value of 0.98. The ratios of solid/liquid targets for "modified" full acceptance as a function of Y and Z position at primary vertex are flat, with some fluctuations, at values 0.93 and 0.99. The ratios of solid/liquid targets for "modified" full acceptance as a function of Y and Z slopes at the primary vertex are flat at values 0.98 and 0.99.

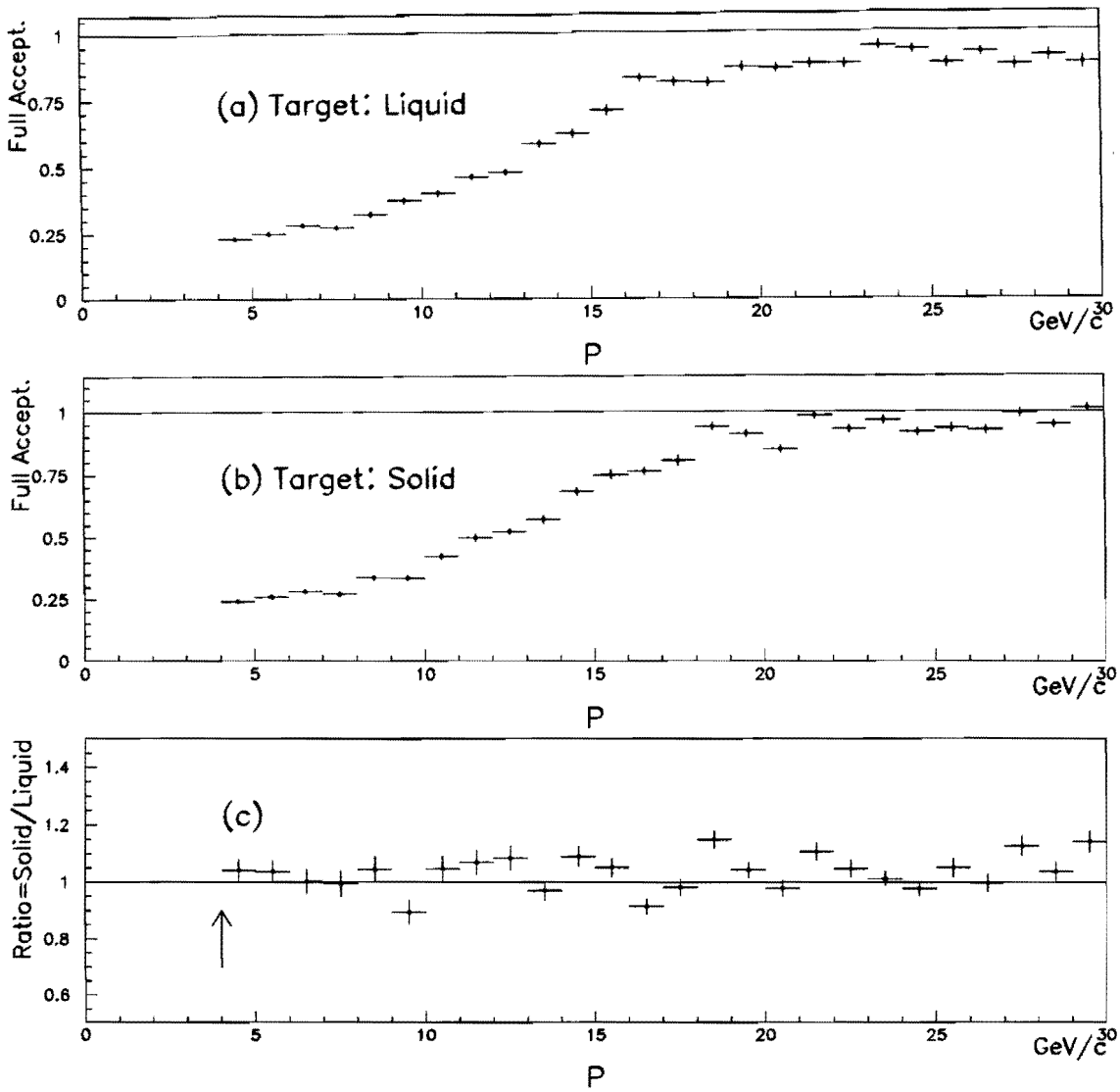

Figure 4.22: The "modified" momentum dependence of full acceptance for liquid and solid targets, (a) and (b). The ratio of solid and liquid target for full acceptance is shown in (c).

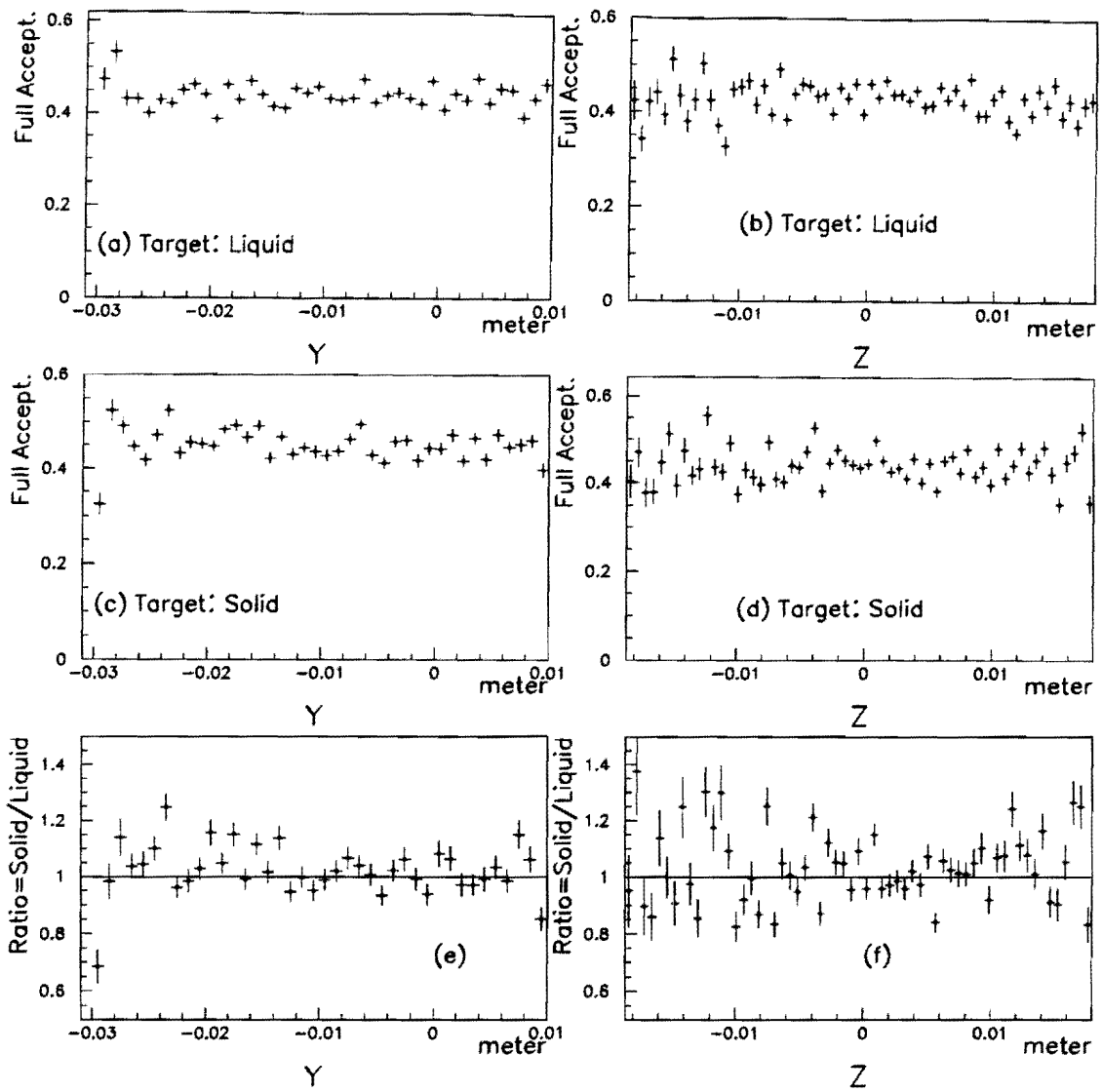

Figure 4.23: The "modified" full acceptance as function of Y and Z position measured at primary vertex for liquid and solid targets, (a) and (b). The ratio of solid and liquid target for full acceptance is shown in (c).

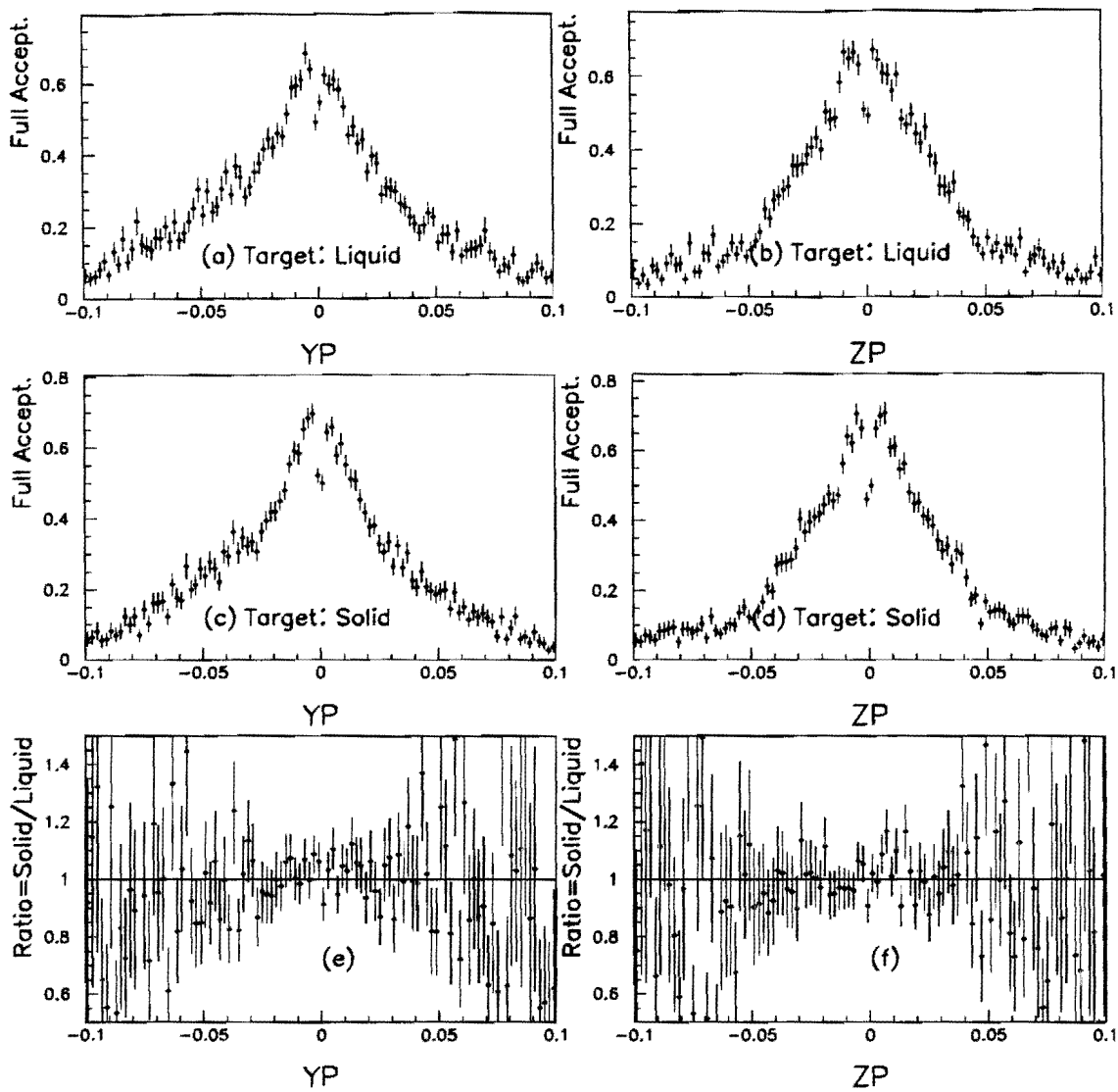

Figure 4.24: The "modified" full acceptance as function of dY/dX and dY/dX measured at primary vertex for liquid and solid targets, (a) and (b). The ratio of solid and liquid target for full acceptance is shown in (c).

4.3.2 The Reconstruction of Physical Origins and Particle Types

To understand the reconstruction effects of the particle origin and the particle type contaminations, a study between the Monte Carlo "TRUE" and "MC REC." is performed. Table VIII shows the fractions of the particles physical origins of "TRUE" and "MC REC." for both solid(Ca) and liquid(D2) targets. The "MC REC." tracks were required to have originated from the primary vertex.

TABLE VIII: FRACTIONS OF PHYSICAL ORIGINS FOR "TRUE" AND "MC REC."

Physical Origin	TRUE(D2) %	MC REC.(D2) %	TRUE(Ca) %	MC REC.(Ca) %
scattered muon	0	0.4	0	0.3
pri. particles	42.1	81.7	47.6	83.5
decay products	8.4	5.8	8.2	5.2
sec. interactions	31.7	8.9	20.5	1.7
γ conversions	17.8	3.1	23.7	9.3

As seen in Table VIII, the "TRUE" secondary interaction has a higher fraction in the D2 than in the Ca target due to the longer interaction length for D2 targets. On the other hand, the Ca targets have higher fraction of photon conversions. After reconstruction, fractions of the primary particles are increased to about 82 % for both targets. The decrease of the other contaminations is mostly due to the momentum dependence of the acceptance and reconstruction capability. The result for H2 target is similar to D2 and the Pb target is similar Ca target, but the C target has higher secondary interactions (5.3 %) than Ca (Pb) and had similar photon conversions (8.3 %) to Ca (Pb).

Fractions of particle physical origins for tracks reconstructed as "fitted" or "close" are shown in Table IX for liquid and solid targets. Approximately 8 % of primary "fitted" tracks originate from secondary interactions in the liquid target and 7.5 % of primary "fitted" tracks

originate from photon conversion in solid target. About 57 % of reconstructed "close" tracks originate from true primary hadrons for both targets.

TABLE IX: ORIGINS FOR RECONSTRUCTED "FITTED" AND "CLOSE" TRACKS

Reconstructed Primary Hadrons(fitted)	Liquid Target %	Solid Target %
Physical Origin		
primary particles	87.2	90.2
decay products	2.2	1.8
secondary interactions	8.0	0.2
photon conversions	2.2	7.5
scattered muon	0.4	0.3
Reconstructed Primary Hadrons (close)		
Physical Origin		
primary particles	58	57.2
decay products	21	16.6
secondary interactions	12	1.8
photon conversions	9	24.4

Figure 4.25 shows the fraction of primary particle contamination (π, K, P and electron) as a function of particle momentum for liquid and solid targets. The plots show a sharp rise in the fraction of electrons when momentum < 4 GeV/c. The minimum momentum requirement $P > 4.0 GeV/c$ reduces the electron (positron) contaminations. Primary protons and kaons or kaons originating from short lived decays, such as $\phi \rightarrow K^+K^-$, are not distinguished from pions. They form a background for the Bose-Einstein correlation. Kaons are also expected to have a Bose-Einstein effect and introduce a smaller source size as mentioned in chapter 1. The effect will decrease the value of parameter λ.

Table X shows the final particle types for the samples which passed all track selections as mentioned above.

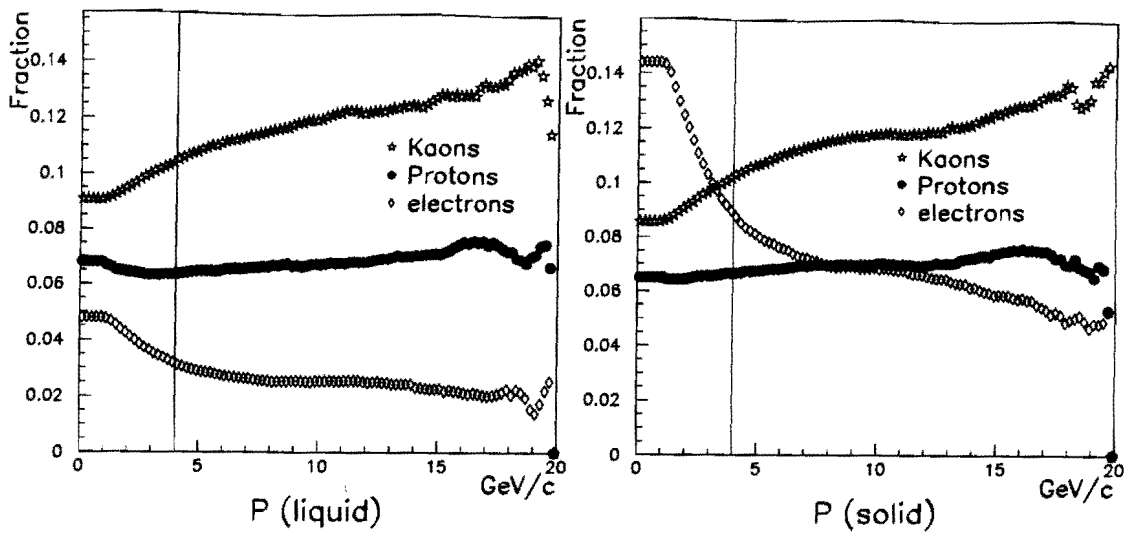

Figure 4.25: Fraction of particle contamination as a function of P.

4.3.3 The Reconstruction of Two Charged Tracks

The Bose-Einstein correlation is sensitive to the reconstruction of two charged tracks in the events. In this section, a study of two-charged track reconstruction efficiency as a function of Y and Z slope difference(ΔYP and ΔZP) measured at the vertex and the 4-momentum difference, q, is performed. The results are used for the "Monte Carlo correction" to eliminate the reconstruction effect on the Bose-Einstein correlation. The reconstruction efficiency of two charged tracks for each distribution is determined as the ratio of two "MC REC." charged tracks over two "TRUE" charged tracks. The "MC REC." tracks are required to passed the cuts described in the preview section and the " MTRU" tracks are required to be acceptable primary tracks.

Figure 4.26 and Figure 4.27 show the reconstruction efficiency for two like-charged and two unlike-charged tracks for solid and liquid target versus these three variables. The reconstruction efficiency as a function of ΔYP is similar for like-charged and unlike-charged pair (consistently flat over the region) but has a depression at small value of $\Delta ZP < 0.002$. The depression in ΔZP measured at vertex of two charged track was due to the inability of the VDC to resolve

TABLE X: PHYSICAL ORIGINS AND PARTICLE TYPES AFTER CUTS

Reconstructed Primary Hadrons(after cuts)	Liquid Target %	Solid Target %
Physical Origin		
primary particles	88	91.4
decay products	4.4	4.5
secondary interactions	6.4	0.8
photon conversions	2.1	3.2
scattered muon	0.1	0.03
Particle Content		
pions	79.7	75.6
protons	7.4	7.6
kaons	10.1	11.0
electrons(positrons)	2.5	5.6
muons	0.3	0.2

two tracks that have small separation in the Z view. The VDC pattern recognition relies on finding the tracks in the Z view first, so that when the tracks are not resolve in the Z view the track finding fails. This inefficiency in finding two close track in Z view results a depression of reconstruction efficiency at small q ($q < 0.5$GeV).

Figure 4.28 shows the ratio (solid/liquid) of reconstruction efficiency as function of these variables for both like and unlike charged pairs. Plots show that the reconstruction efficiency is consistent for both liquid and solid target(ratios are consistently flat at value ~ 1).

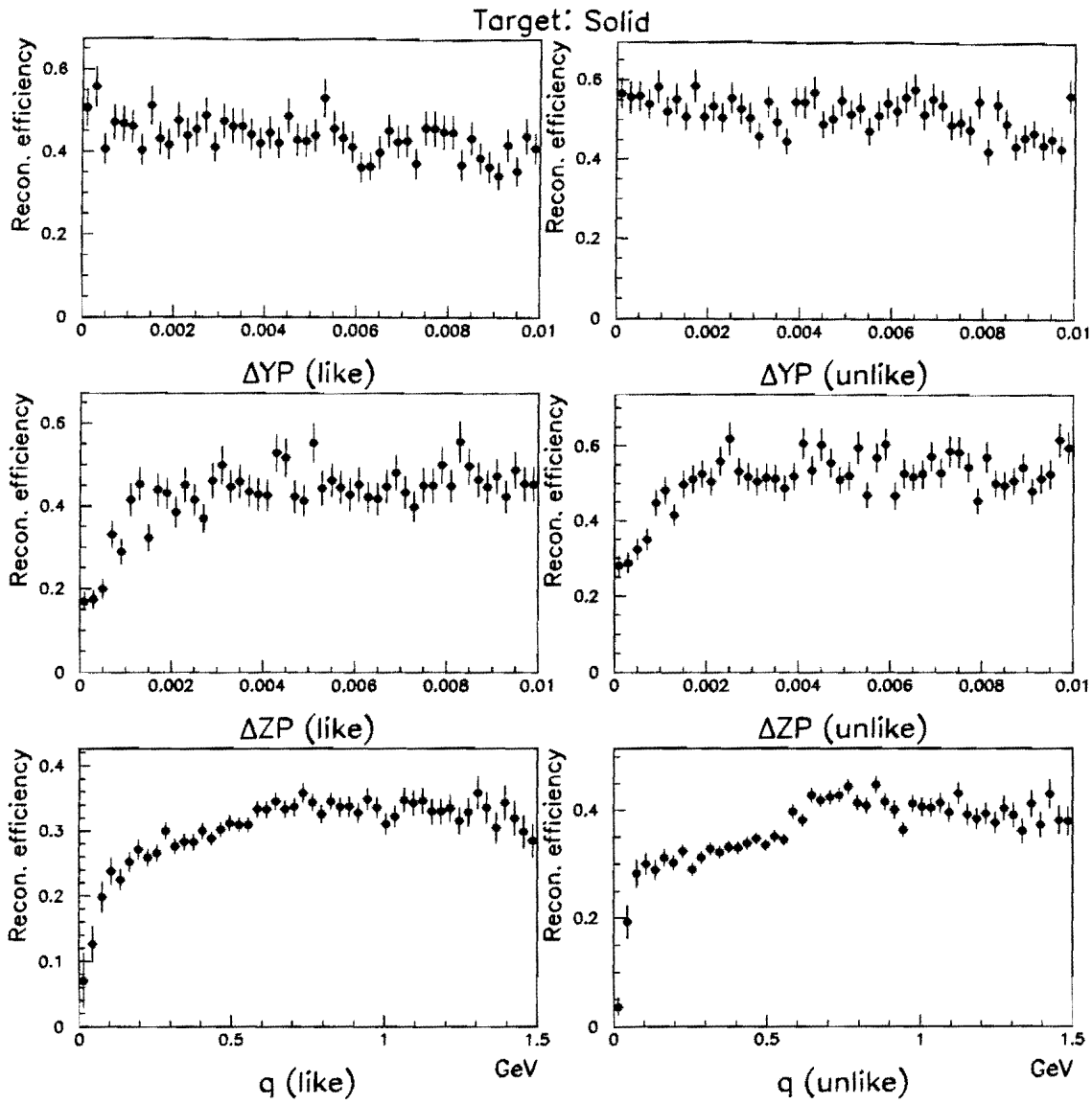

Figure 4.26: Reconstruction efficiency as a function of ΔYP, ΔZP, and q for two like-charged and unlike-charged tracks(Solid).

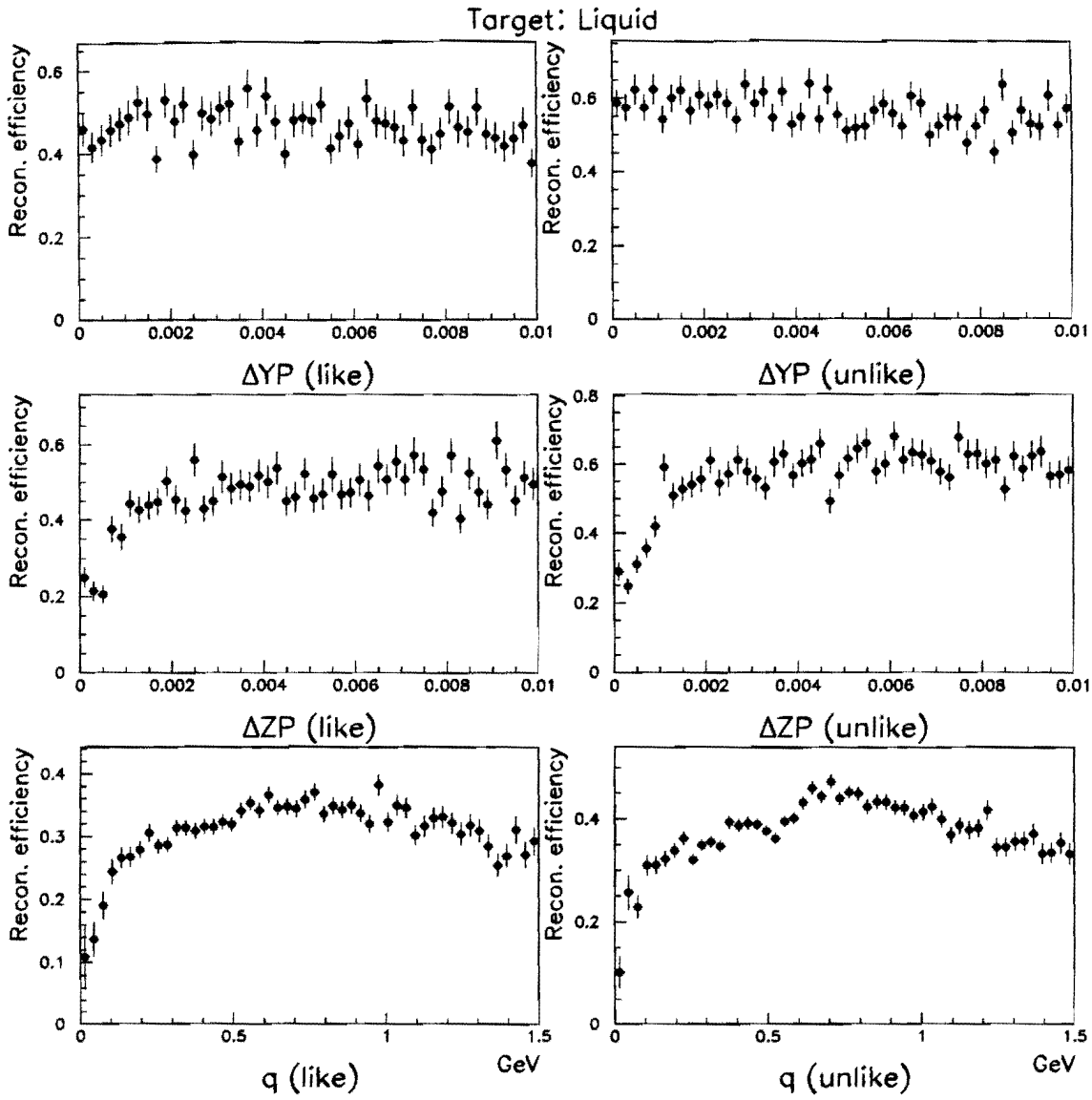

Figure 4.27: Reconstruction efficiency as a function of ΔYP, ΔZP, and q for two like-charged and unlike-charged tracks(Liquid).

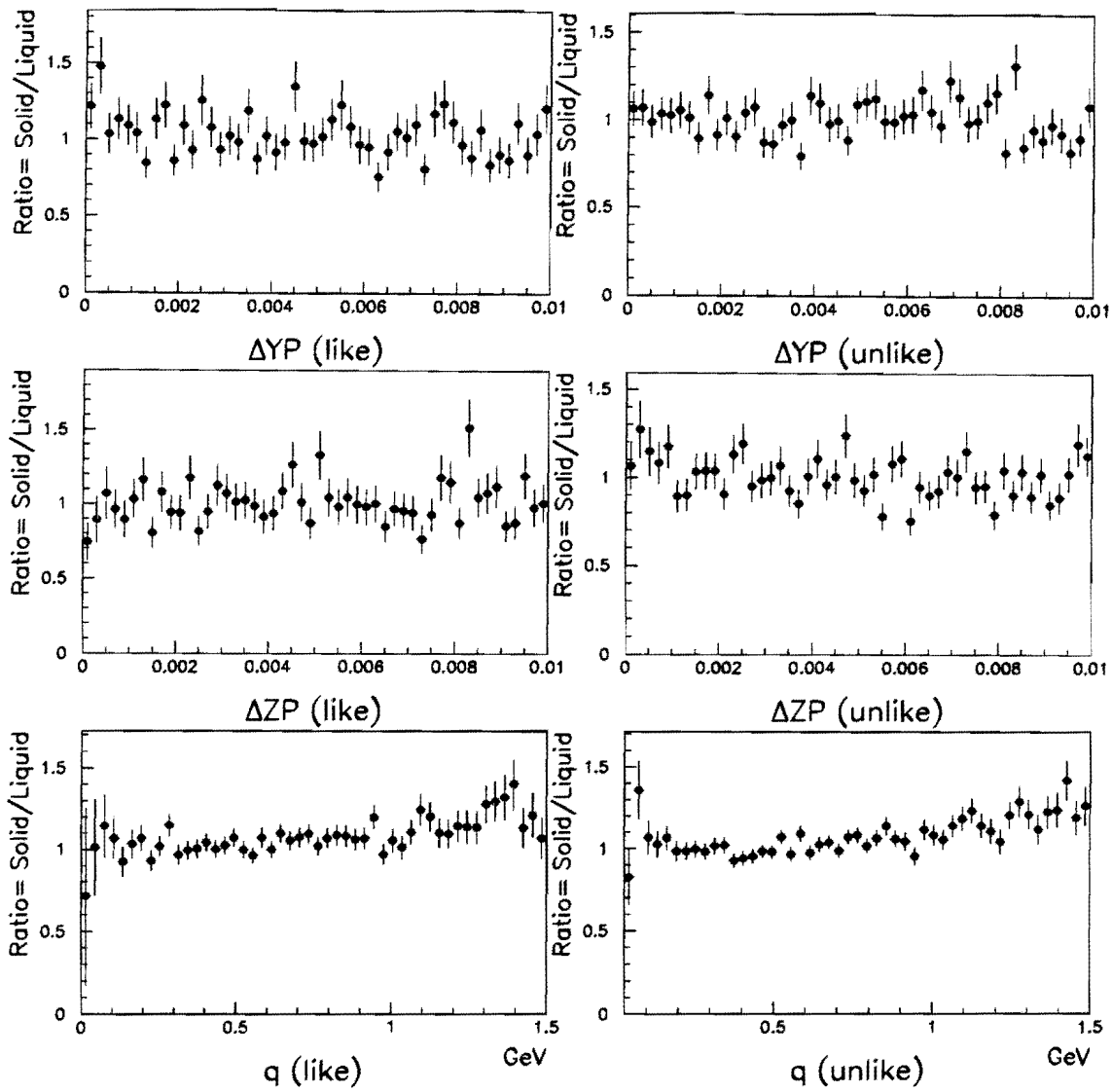

Figure 4.28: Ratio (Solid/Liquid) of Reconstruction efficiency as a function of ΔYP, ΔZP, and q for like-charged and unlike-charged pairs.

4.4 The Final Statistics and The Comparison of Data and Monte Carlo

At least two "hadron" tracks passing all selection criteria are required in each event for the final analysis. The total number of events and tracks which passed selection criteria for data and Monte Carlo are shown in Table XI. The data are divided into four sub-samples, the light target (H2 and D2), the C target, the Ca target, and Pb target for the Bose-Einstein analysis.

TABLE XI: EVENTS AND TRACKS PASSED ALL SELECTION CRITERIA

Target	Events	Tracks	MC events	MC tracks
H2+D2	67003	207709	49615	145436
C	28130	84390	18980	58838
Ca	33529	103940	23262	72990
Pb	21460	66525	25584	79310

To demonstrate that the model of the Monte Carlo simulation used for this analysis is of sufficient accuracy, data and Monte Carlo distributions are compared in more detail. The data and reconstructed Monte Carlo samples for this comparison have had the same selection criteria applied, and the targets used for the comparison are separated into liquid(H2 and D2) and solid(C, Ca, and Pb). Figure 4.29 to Figure 4.31 show the plots of event kinematics comparisons between data and Monte Carlo, with each histogram is normalized to the number of entries. Only X-position of primary vertices are shown separately for liquid and solid targets, other kinematics distributions are shown together for both targets because they are not significantly different.

Small deviations at event kinematics distributions between data and reconstructed Monte Carlo are observed in Figure 4.30. The data combined events from SAT and LAT triggers but no exact match of the ratio was sought in MC, resulting in a Q^2 discrepancy. The X-position of primary vertex for solid target as shown in Figure 4.31.b has different distributions between

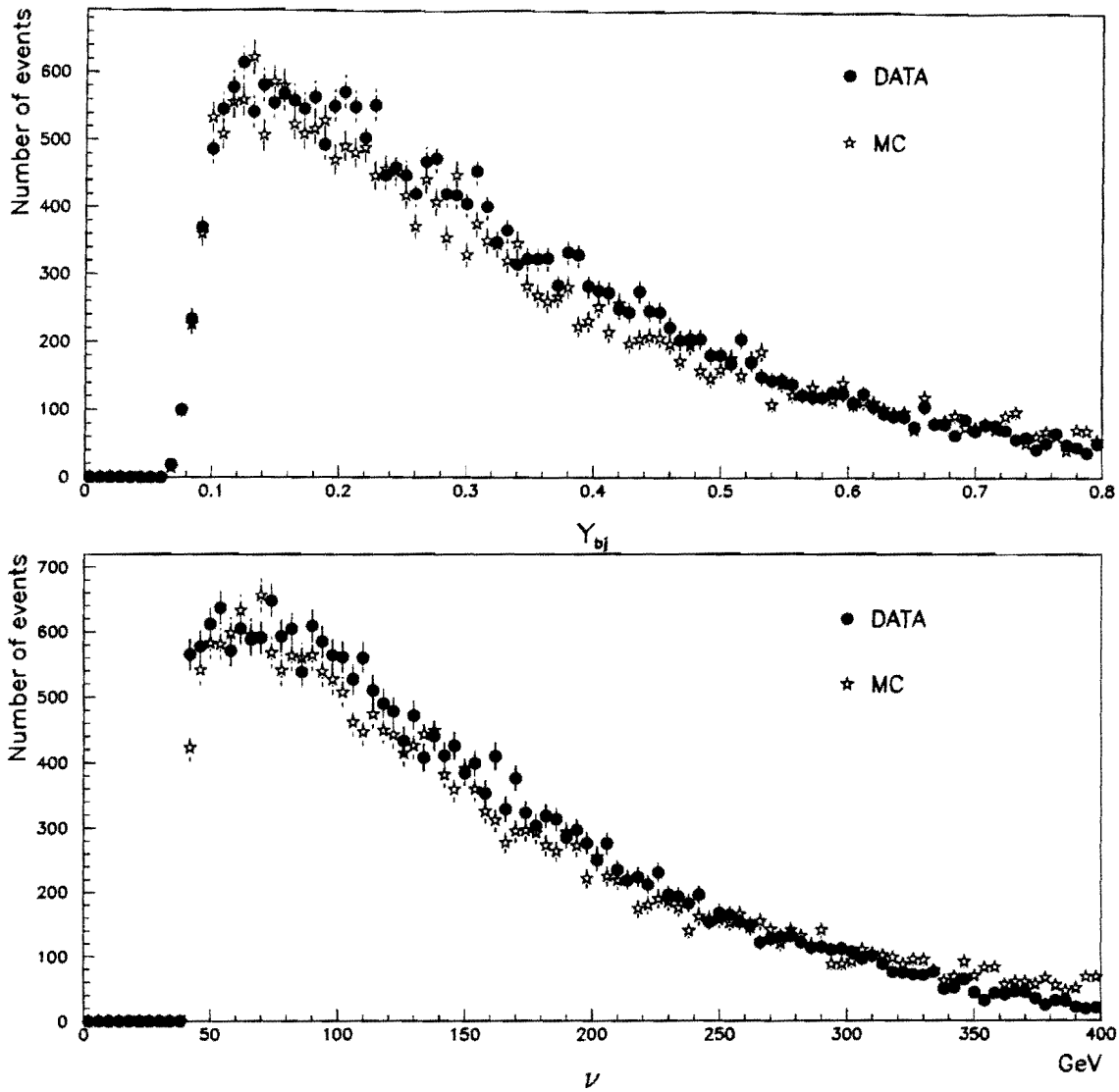

Figure 4.29: Y_{bj} and ν distributions for data and reconstructed Monte Carlo events.

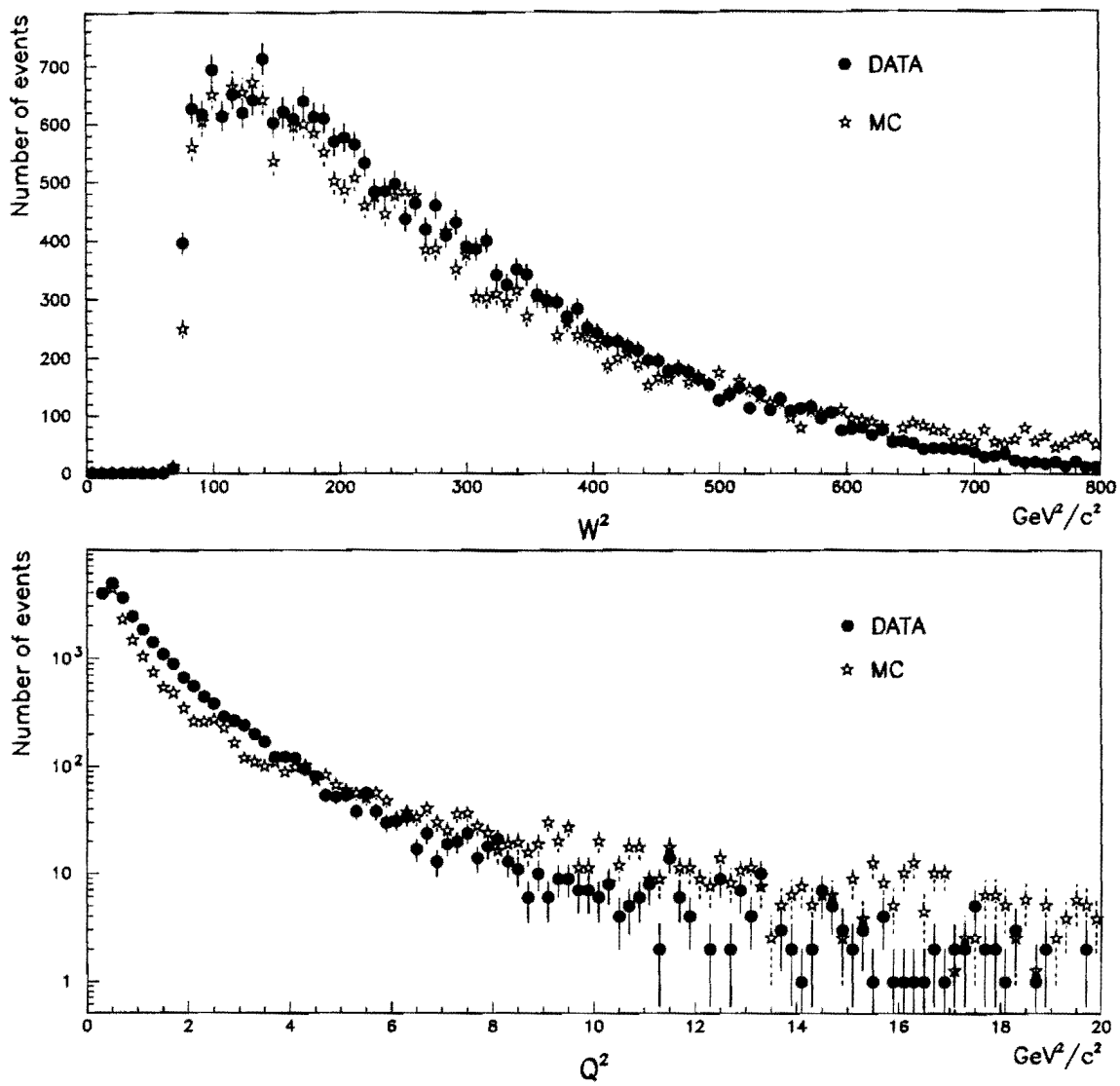

Figure 4.30: W^2 and Q^2 distributions for data and reconstructed Monte Carlo events.

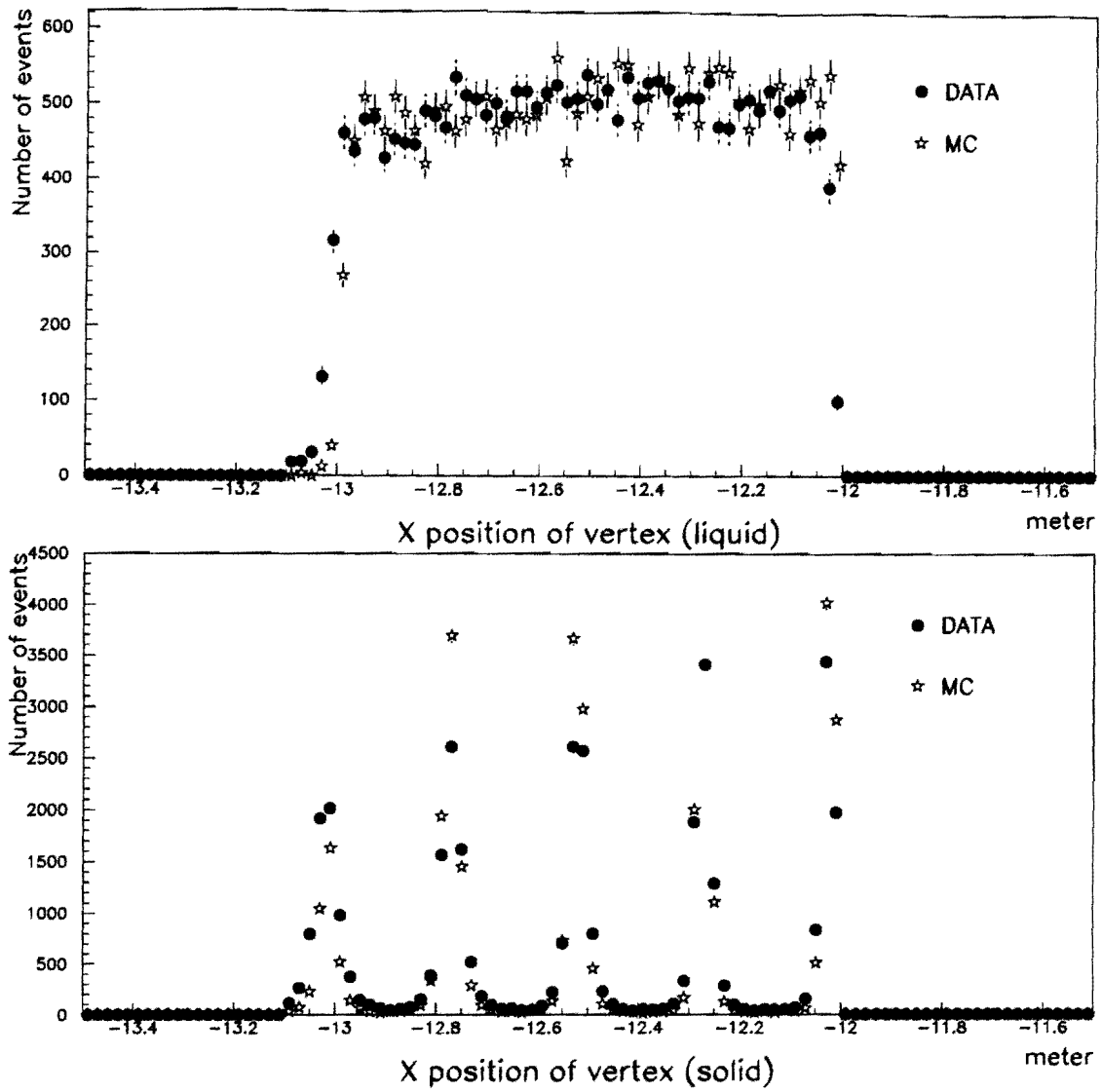

Figure 4.31: X-position of primary vertex for data and reconstructed Monte Carlo events. The plot on the top is for liquid target and at the bottom is for solid target.

data and reconstructed Monte Carlo. The detector simulation for Monte Carlo had assumed slightly better vertex resolution than data due to VDC resolution (see section 4.2.2).

The event kinematics provide the information to persuade oneself that the events are from DIS from target, and small deviations of X-position of primary vertex in the comparison will not affect the selection of events. However, the Bose-Einstein correlation is measuring the correlate effects between two tracks, so the similarity of track properties for data and reconstructed Monte Carlo is much more important.

Figure 4.32 to Figure 4.33 show the comparisons of track variables between data and reconstructed Monte Carlo. The plots combine data from liquid and solid targets because there were similar within statistical error. No significant differences between data and Monte Carlo distributions are observed as shown in (b), (d), (f) of Figure 4.32 and Figure 4.33.

The "double bump" structure in the laboratory frame momentum distribution, Figure 4.32.a, is caused by the domination of VDC acceptance at low momentum and FS acceptance at high momentum.

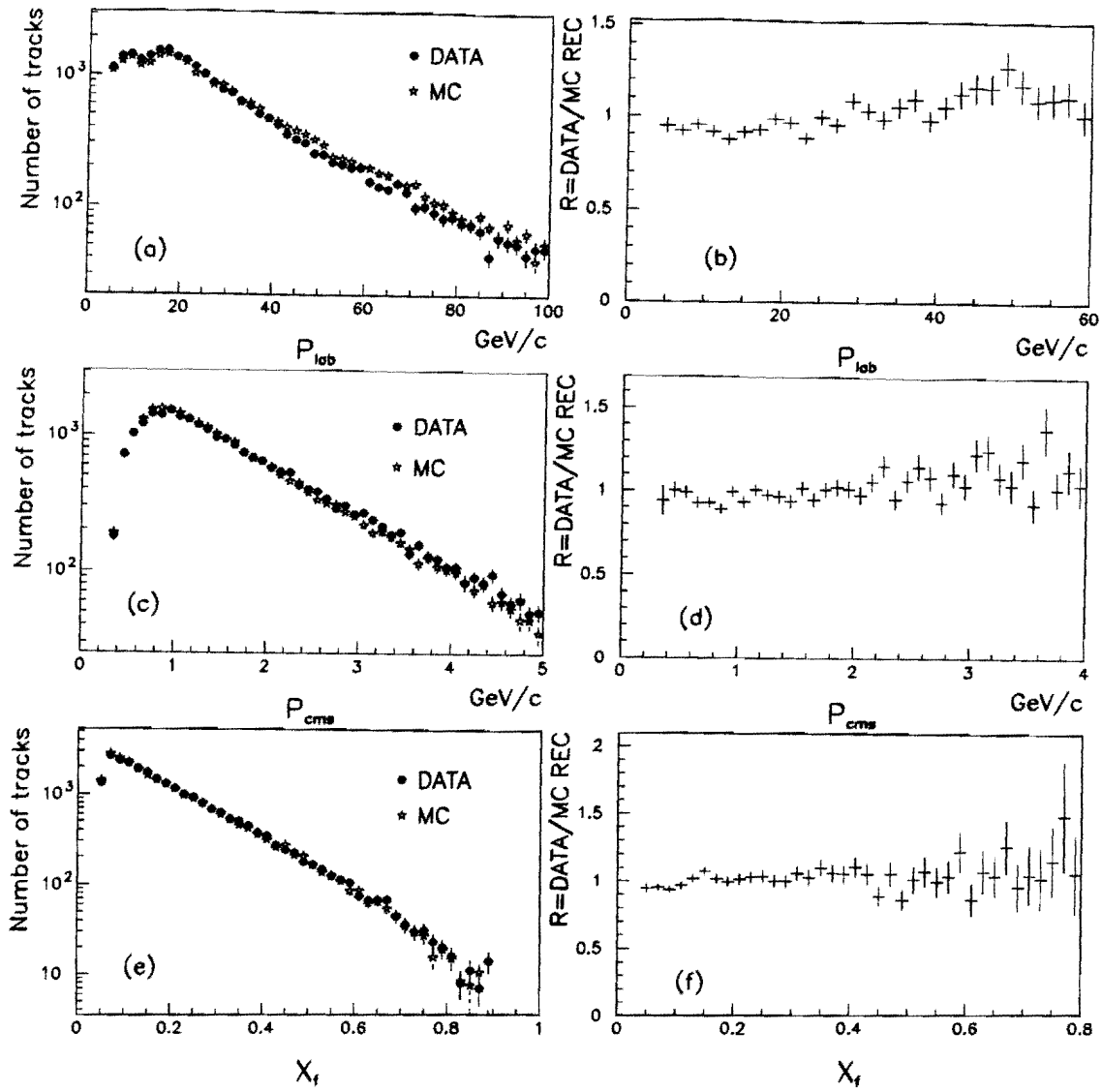

Figure 4.32: Data and MC REC comparisons for momentum at lab. frame, the momentum in photon-proton C.M.S. frame, and the X_f distributions. (b), (d), (f) are the ratio of DATA/MC REC.

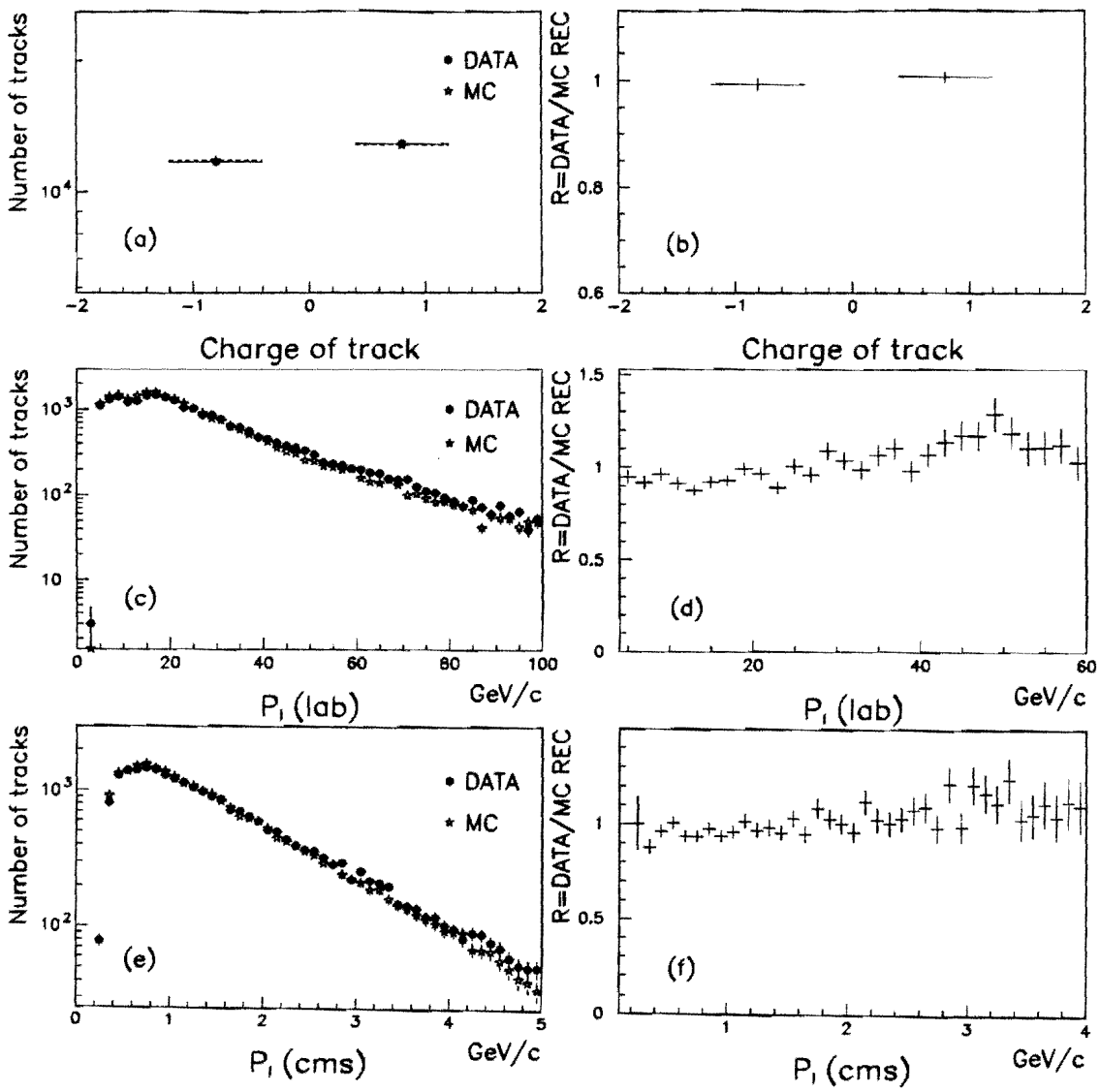

Figure 4.33: Data and MC REC comparisons for charge of track, longitudinal momentum related to virtual photon direction of lab and CMS frame. (b), (d), (f) are the ratio of DATA/MC REC.

5. THE BOSE-EINSTEIN CORRELATION ANALYSIS

This chapter describes the analysis procedure and results from Bose-Einstein correlation studies for both data and Monte Carlo. The data are divided into four target groups. H2+D2, C, Ca and Pb, as was stated in the previous chapter. The plots text and equations in this chapter are labeled "DATA" for data after PTMV, "MC REC." for Monte Carlo simulated data after PTMV, "MC TRUE" for Monte Carlo truth data, and "DATA CORR." for experimental data after Monte Carlo correction has been applied. The Monte Carlo correction is defined as:

$$F_{DATA\ \ CORR.} = \frac{F_{MC\ \ TRUE}}{F_{MC\ \ REC.}} \cdot F_{DATA} \tag{5.1}$$

where F is any distribution. The same event and track selection criteria are applied to "DATA" and "MC REC.". For "MC TRUE" all the charged tracks are required to originate at the primary vertex and to have the momentum greater than 4 GeV/c. The "DATA CORR." events thus should have the same characteristics as " MC TRUE" events except for Bose-Einstein correlations.

5.1 The Reference Samples

In this analysis, the unlike-sign charged track pairs from events (unlike reference sample) and the mixed like-sign charged track pairs from different events which have similar event kinematics (mixed reference sample) are used as the reference samples.

5.1.1 Unlike-Sign Charged Pairs

The effects of resonance decays on the reference sample obtained by using unlike-sign charged pairs in the events were described in chapter 1. The exclusive meson production event were rejected by our event selection cuts but the decays from inclusive short-lived mesons are contained in the reference sample. Since tracks from short-lived decays have similar properties as primary tracks, it is impossible to distinguish them from the primary tracks. Their resonance decays cause depressions in the (like-sign pairs)/(unlike-sign pairs) versus q plot at values of q related to masses of the resonances. Such dips can affect fits and the extraction of Bose-Einstein correlation parameters.

Figure 5.1 shows the q distributions for unlike-sign charged and like-sign charged pairs from data, reconstructed Monte Carlo, and Monte Carlo true samples. In the plots, a bump in unlike-sign charged pairs q distributions at the value of around 0.72 GeV for all three samples is seen. The average invariant masses of these $\pi^{\pm}$ pairs, $M_{\pi\pi}=\sqrt{q^2+4m_{\pi}^2}$, are around 0.77 GeV. This indicates that a large fraction of the unlike-sign charged pairs in this range originated from ρ decays. The effects of decays of other short-lived particles such as K^{*0}, ω, η, and η' which decay into multiple pions are more spread out. Another bump is seen around the value of 0.25 GeV in true Monte Carlo unlike-sign charged q distribution. This is due to decays from ϕ to K^+K^- with the kaons misidentified as pions. The ϕ bump is less pronounced in the "MC REC." plot and is almost absent in the "DATA" plots due to the track resolution.

A study of the correlation effect from these short-lived particles was imposed. Figure 5.2, (a) to (f), shows the MTRU q distributions of two unlike-charged tracks both are originated from same decay in the event. Plots (g) and (h) show the total effect (exclude and include the ρ decay) from decays for the unlike-charged pairs as a function of q. To reconstruct the q, all particles are assumed to be pions. As mentioned above, three significant bumps distributed at $q \sim 0.25GeV$, $q \sim 0.4GeV$, and $q \sim 0.7GeV$ separately are observed in (h). The ρ^0 dominates the bump centered at $q \sim 0.7GeV$. Figure 5.3.(a) shows the comparison of all unlike-charged pairs and unlike-charged pairs from decays as a function of q. Figure 5.3.(b) shows the q

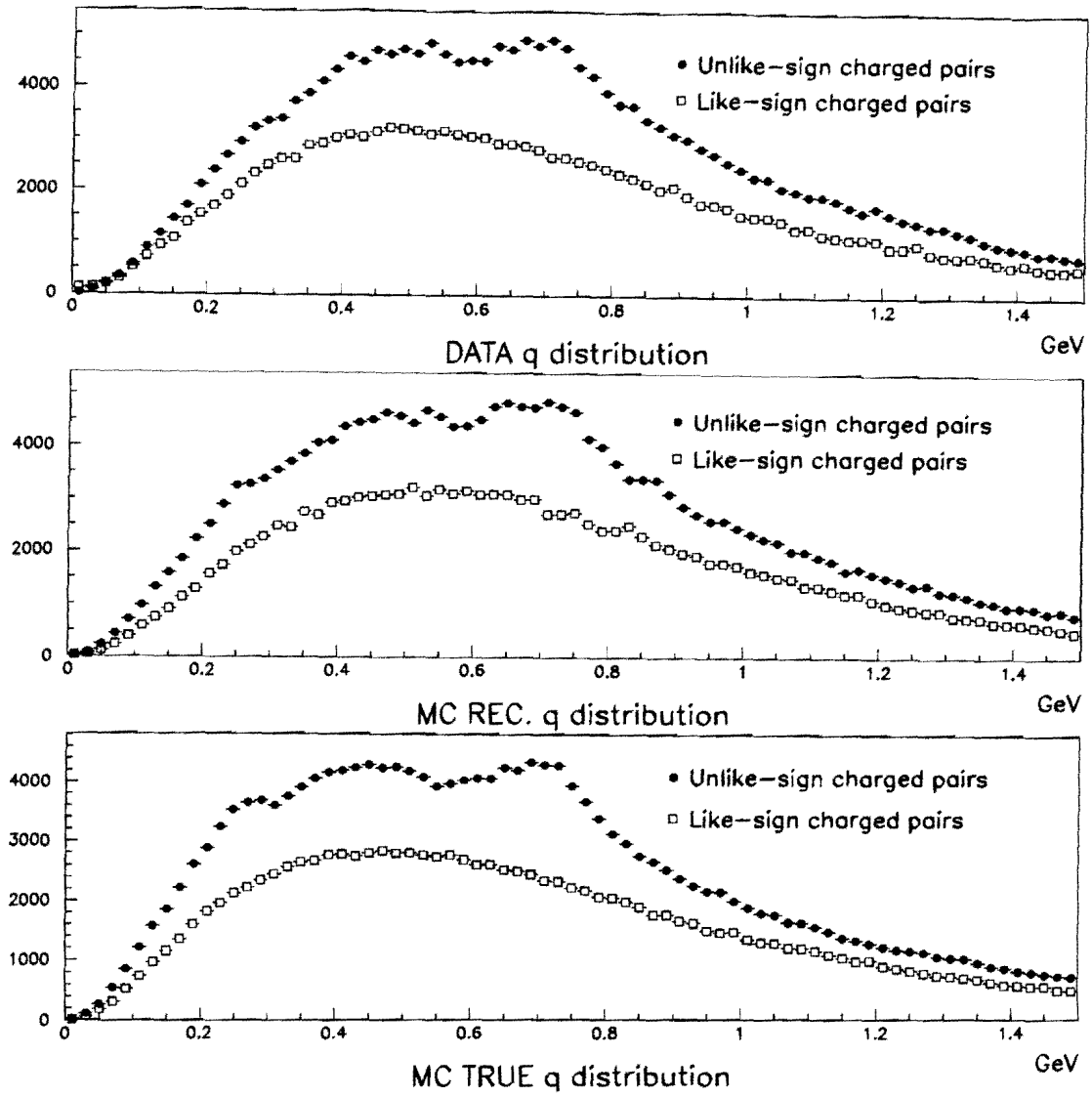

Figure 5.1: Number of entries versus q distribution of like-sign charged pairs and unlike-sign charged pairs from events for data, reconstructed Monte Carlo, and Monte Carlo truth samples.

distribution of unlike-charged and like-charged pairs after removed the particles from decays, and (c) shows the same distribution except the ρ^0 decays are included. Both (b) and (c) are used for the Monte Carlo correction(MC TRUE) for the Bose-Einstein correlation result.

Same plots as in Figure 5.2 for reconstructed Monte Carlo events are shown in Figure 5.4. The shape of total q distribution for all decays are similar to MTRU distribution except some discrepancy due to the reconstruction efficiency. The resonance decays have not been removed in the MC REC and will used as the correction for the data.

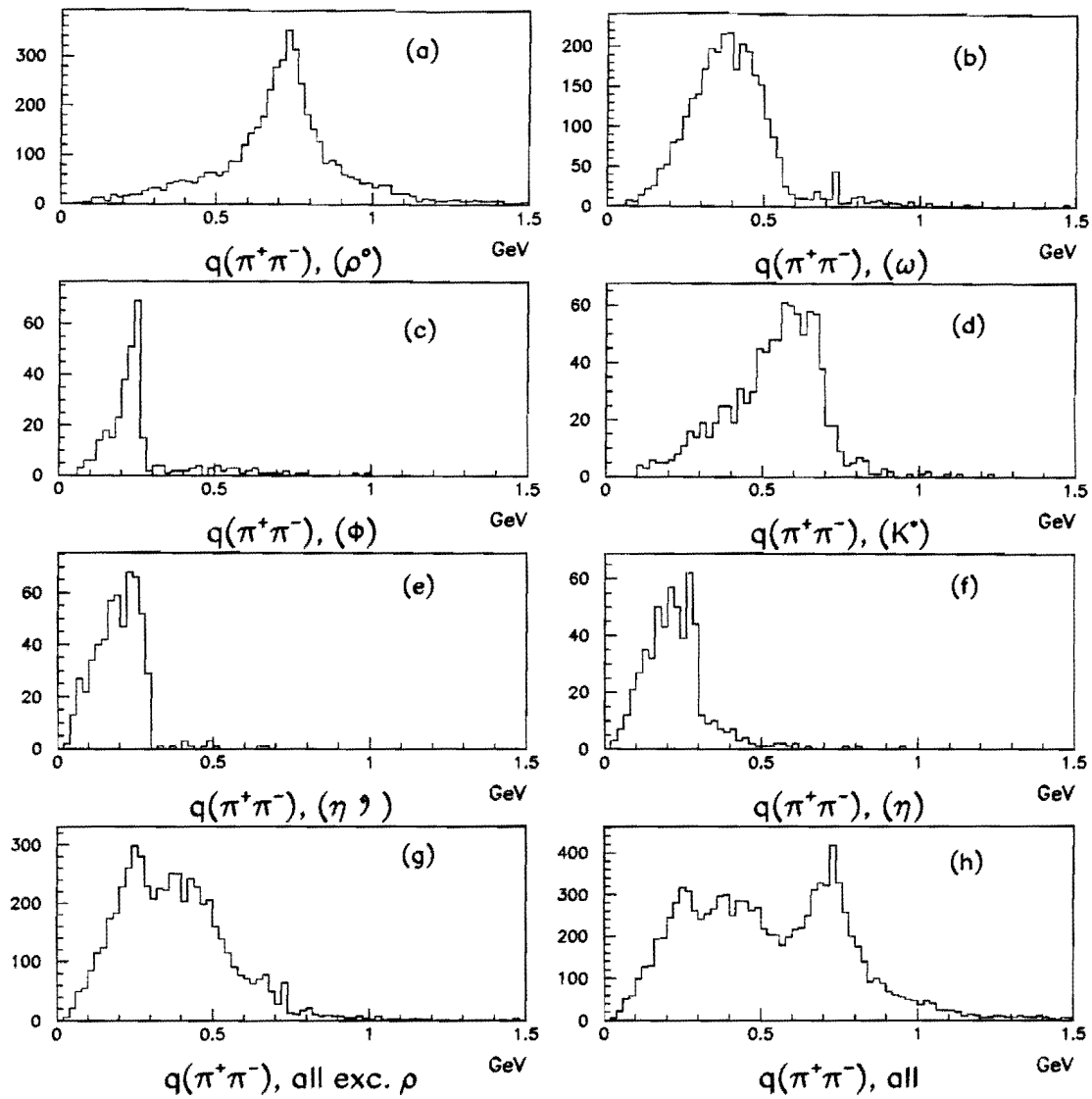

Figure 5.2: MTRU q distributions for inclusive decays, (a): ρ^0, (b): ω, (c): ϕ with pion masses, (d): K^{*0} with pion masses, (e): η', and (f): η. Plot (h) is sum of all decays and (g) is the sum excluding ρ^0 decay.

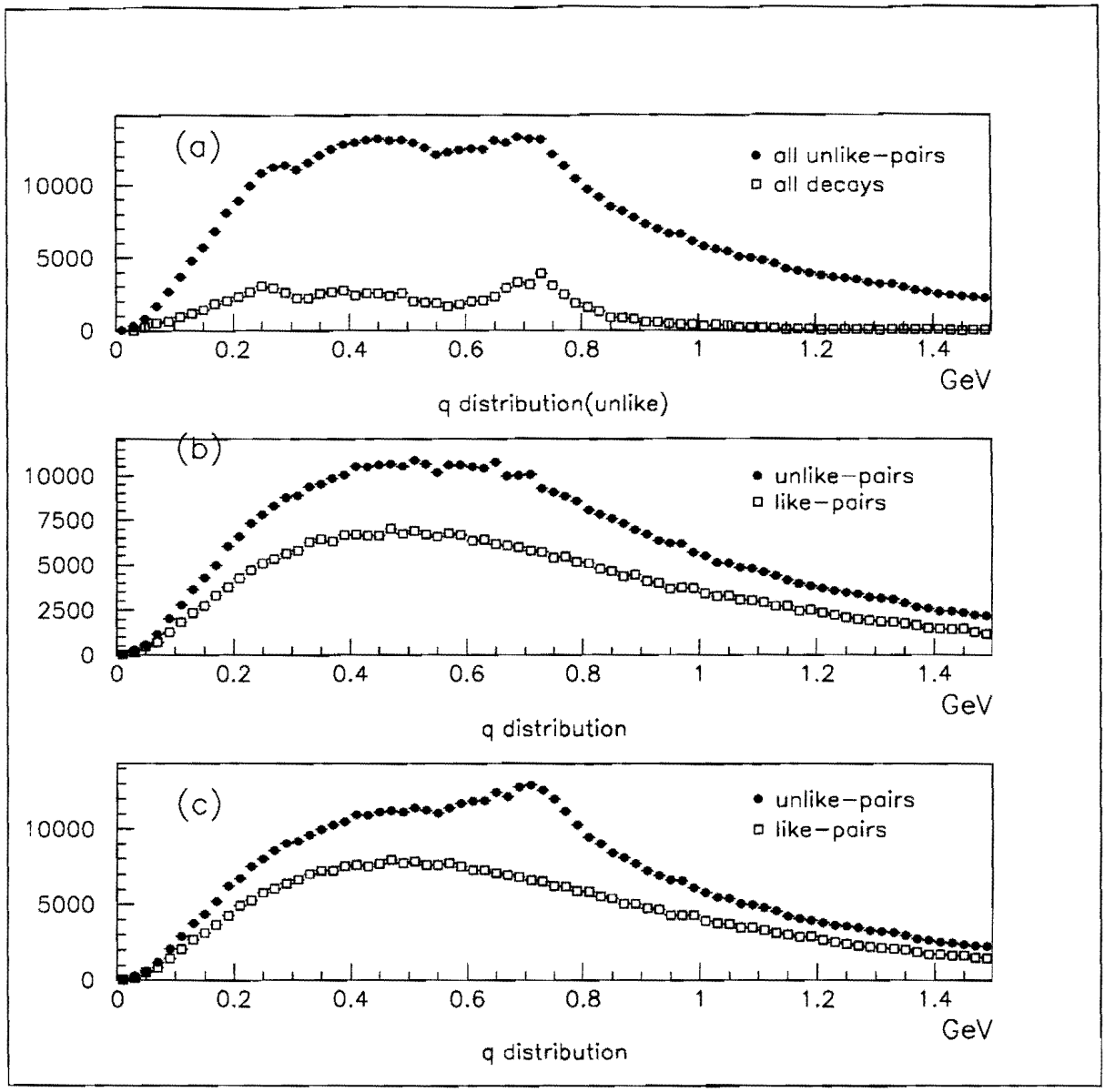

Figure 5.3: q distributions of (a): all unlike charged pairs and unlike charged pairs from all decays. (b): unlike charged pairs and like charged pairs after removed all decays. (c): same as (b) but include ρ^0 decays.

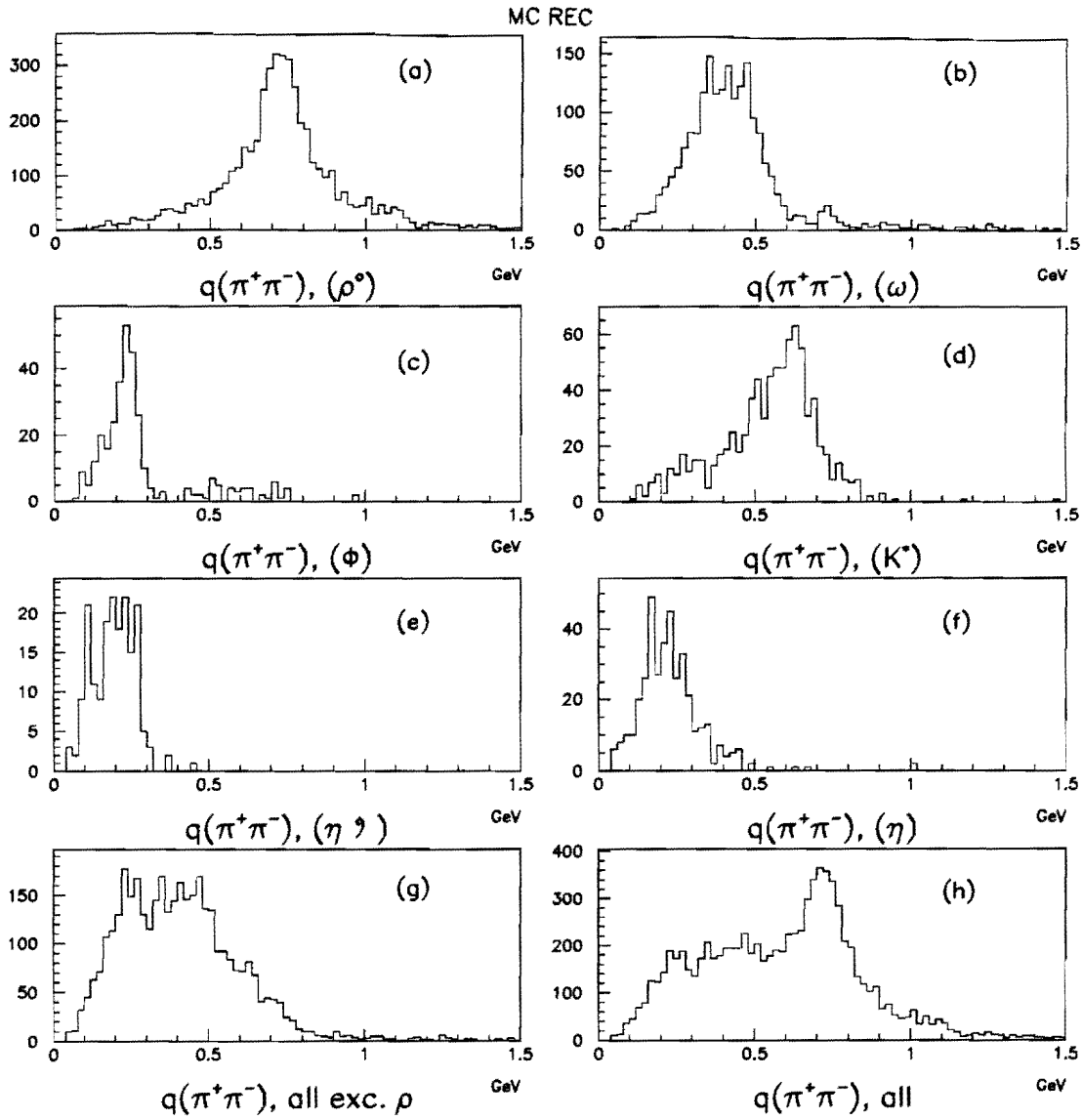

Figure 5.4: MC REC q distributions for inclusive decays, (a): ρ^0, (b): ω, (c): ϕ with pion masses, (d): K^{*0} with pion masses, (e): η', and (f): η. Plot (h) is sum of all decays and (g) is the sum excluding ρ^0 decay.

5.1.2 Mixed Charged Pairs

The advantage of using the mixed like(unlike)-sign charged pairs as the reference sample is that the resonance effects present in the unlike-sign charged reference sample q distributions are removed. However, since the tracks in such a sample are chosen from different events, the kinematic properties of mixed like-sign charged pairs may differ from than of like(unlike)-sign charged pairs. In order to minimize this effect, the "mixed" samples are chosen from events where invariant mass of the hadronic state, W, differs < 1 GeV and have identical multiplicity. In addition, before mixing the like(unlike)-sign charged tracks from different events, each event is boosted into the virtual photon-nucleon center of momentum frame with the virtual photon pointing along the X axis. Figure5.5 shows the comparison of the track momentum (p, p_l, and p_t) in CMS frame between event and mixed event for both DATA and MC REC. The ratio of track momenta between event/mixed events are consistently flat at 1 and this indicates that the mixed momentum distributions are similar to the distribution of events.

A study of the "mixed" background is performed as follow. Charged tracks (like-sign or unlike-sign) from different events should not show any BE correlation; the ratio of mixed like-sign charged paris to mixed unlike-sign charged pairs should be structureless. Any structure would be a consequence of the apparatus, acceptance or track reconstruction. Plots of q distribution for mixed like and unlike-sign charged pairs and plots of the ratio for mixed like-sign pairs over mixed unlike-sign pairs as a function of q for "MC TRUE", "MC REC.", "DATA", and "DATA CORR." are shown separately in the Figure 5.6 and Figure 5.7.

Figure 5.7 shows the ratio of mixed like-sign charged over mixed unlike-sign charged pairs has an enhancement at q less than 0.15 GeV for "DATA" and "MC REC." events but is consistently flat for "MC TRUE". This indicates that the enhancement does not introduced by the mixed method, instead it might originate from reconstruction effects. The bottom plot shows that most of the enhancement has been removed after applying the Monte Carlo correction, the ratio versus q distribution is consistently flat except for a depletion in the lowest 4 bins.

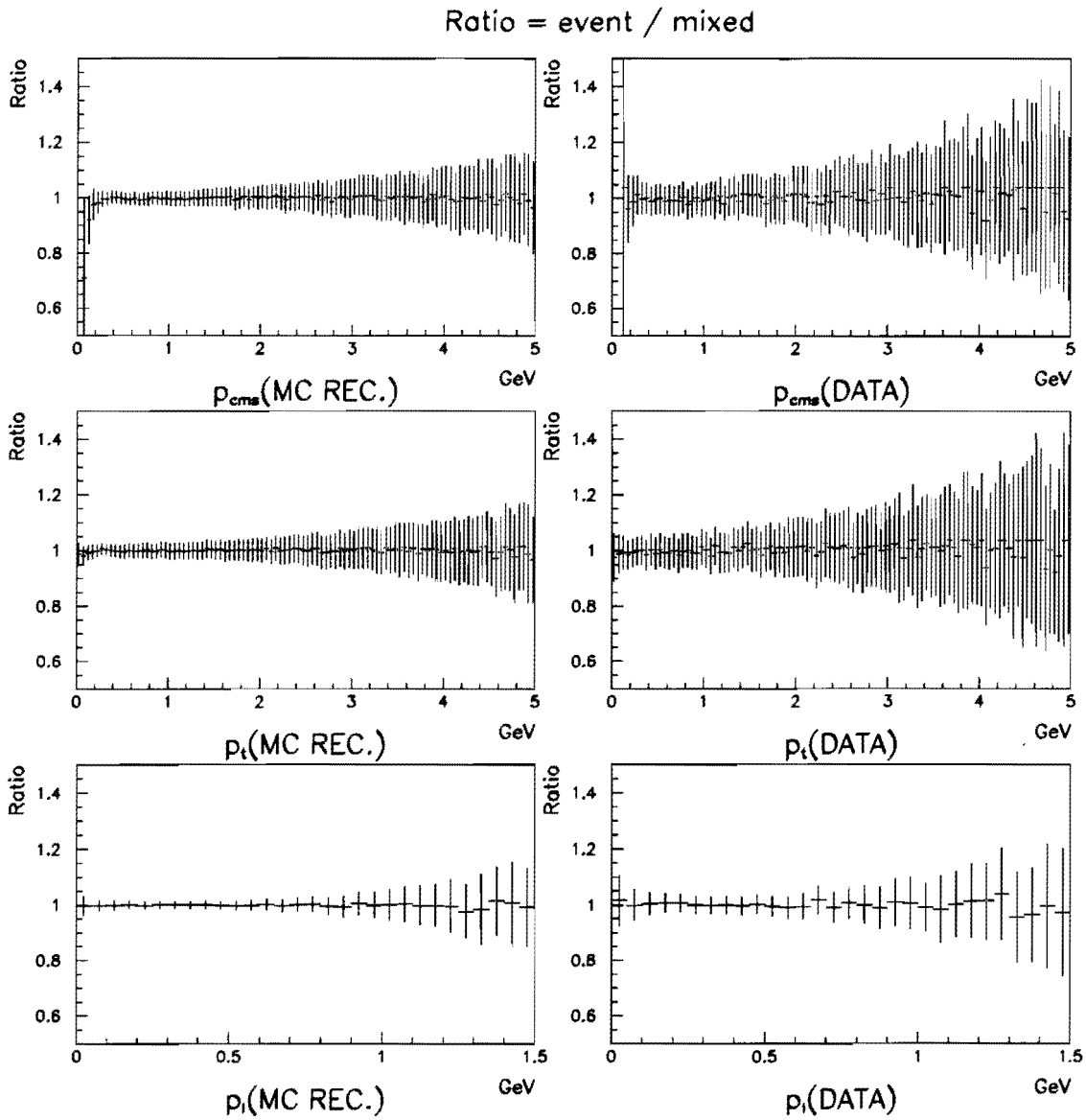

Figure 5.5: Ratio of track momenta distribution between event and mixed event. The momenta are calculated in the CMS frame.

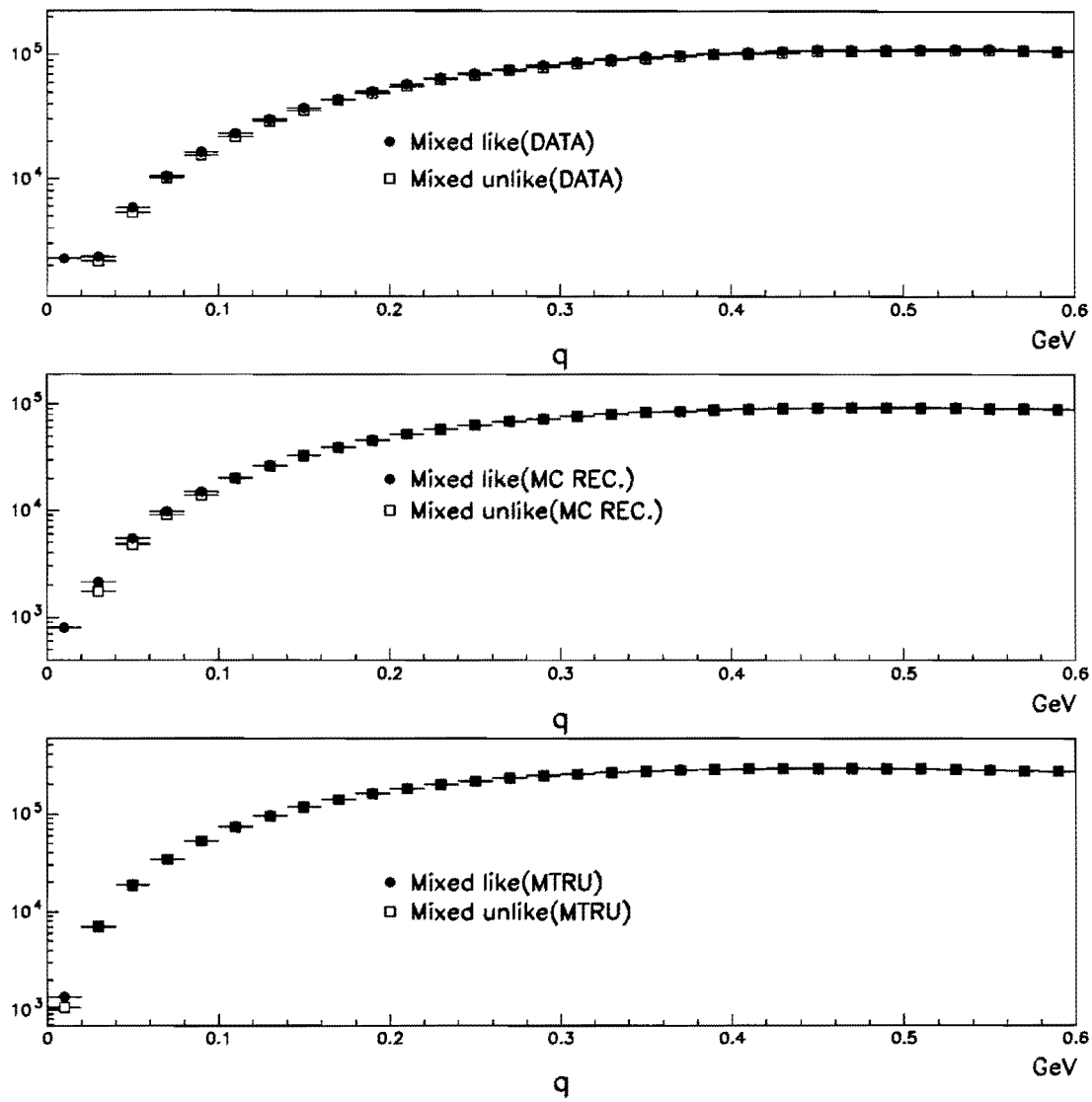

Figure 5.6: Number of entries versus the q distribution of mixed like-sign charged pairs and mixed unlike-sign charged pairs for "DATA", "MC REC", and "MC TRUE" events.

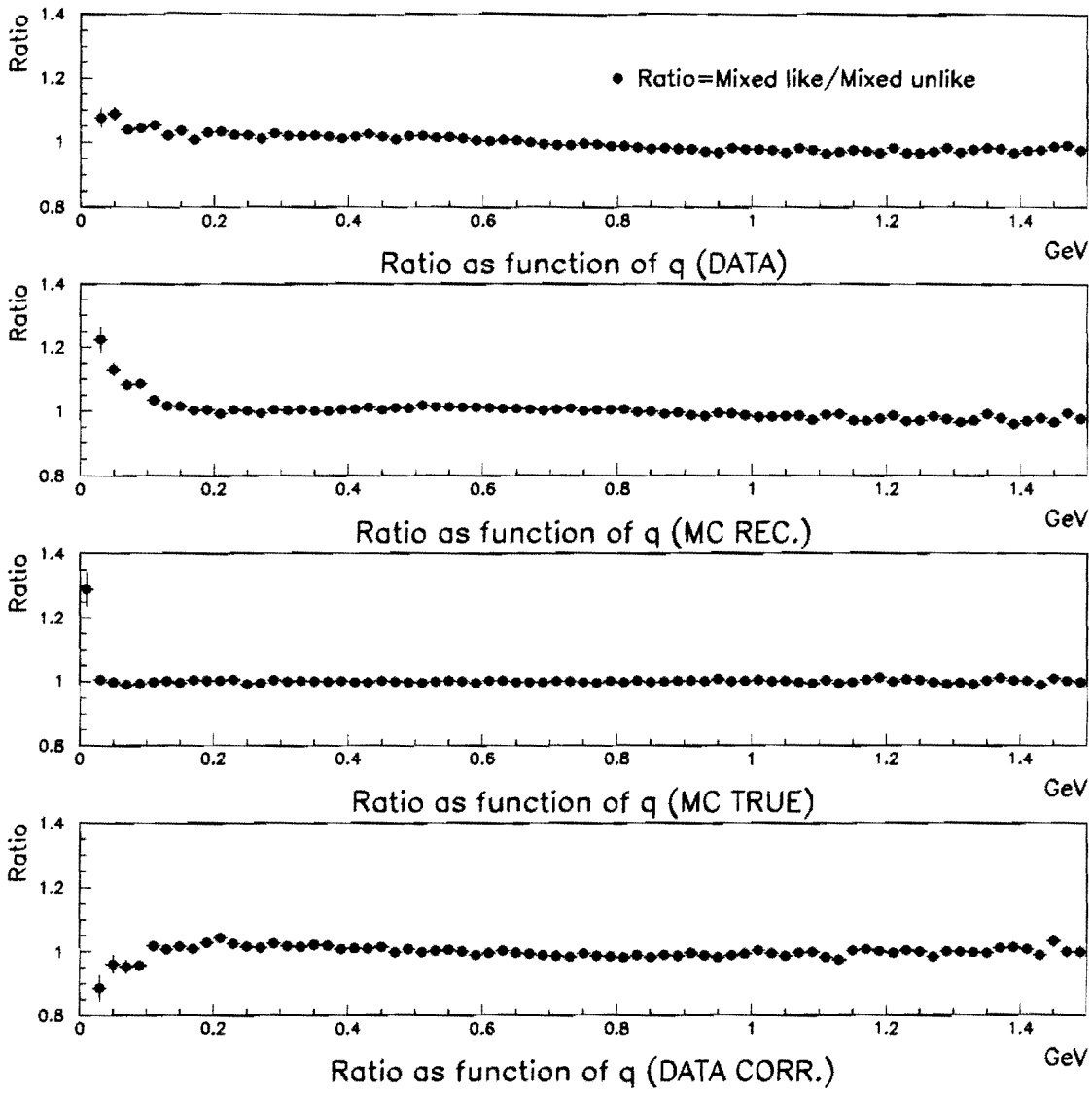

Figure 5.7: Ratios of mixed like-sign charged pairs over mixed unlike-sign charged pairs versus q distributions for "DATA", "MC REC.", "MC TRUE" samples. The bottom plot shows the ratio for data after correction from Monte Carlo has been applied.

To investigate the enhancement of (mixed like)/(mixed unlike) as a function of q seen for "MC REC" events , studies for the reconstruction effect as a function of q for mixed like-sign and mixed unlike-sign pairs are performed. The ratio of "MC REC."/ "MC TRUE" for mixed like-sign pairs and mixed unlike-sign pairs as a function of q are plotted in Figure 5.8. The ratio of "MC REC."/"MC TRUE" for mixed like-sign pairs is fairly flat as a function of q except for a small dip around $q = 0.15GeV$, on the other hand ratio of "MC REC."/"MC TRUE" for mixed unlike-sign pair has a large depression for $q < 0.2GeV$.

This indicates that the enhancement of (mixed like)/(mixed unlike) at small q in Figure 5.7 is dominated by the depression of the "MC REC."/"MC TRUE" of mixed unlike-sign pairs. For systematic consistency, the mixed like-sign pairs and the mixed unlike-sign pairs are both used as the reference sample in this analysis.

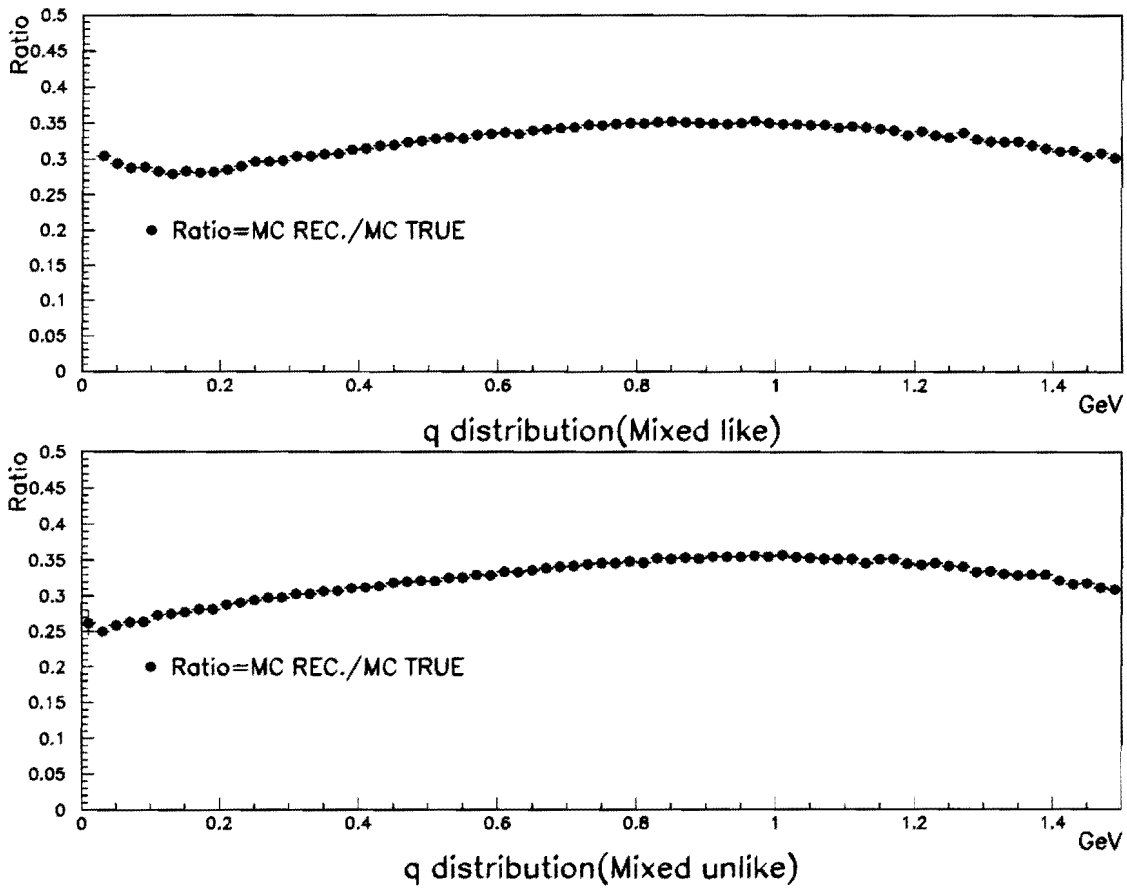

Figure 5.8: Ratio of "MC REC."/"MC TRUE" versus q for mixed like-sign charged and mixed unlike-sign charged pairs.

5.2 The Correlation Function $R(q)$

The correlation function $R(q)$ is calculated by taking the ratio of measured q distributions of the like-sign charged and the reference samples. The inputs in this section will include correlation functions for the "DATA", "MC REC.", "MC TRUE", and the "DATA CORR.". The data are corrected using the equation given below;

$$R(q)_{DATA\ CORR.} = \frac{R(q)_{MC\ TRUE}}{R(q)_{MC\ REC.}} \cdot R(q)_{DATA} \tag{5.2}$$

Figure 5.9 to 5.12 show the ratios of like-sign pairs/references as a function of q for all targets, here data from different target have been combined. The ratio distribution of "DATA CORR" obtained by using unlike-sign charged pairs as reference has significant dip structures at 0.2 GeV $< q <$ 0.9 GeV, along with a significant Bose-Einstein enhancement at $q <$ 0.5 GeV. As mentioned in the previous section, these dips are believed have originated from the $\phi \rightarrow K^+K^-$, ω, K^{*0}, η', η, and ρ^0 as indicated in Figure 5.9.(d). The same ratio plot of "DATA CORR" after removed all decays from MTRU distribution and the plot only include the ρ decay are shown in Figure 5.10, (c) and (d). The decay effect at 0.2 GeV $< q <$ 0.9 GeV for unlike-sign charged pairs was removed after applied Monte Carlo correction.

The "DATA CORR." ratio plots obtained by using the mixed like-sign pairs and mixed unlike-sign charged pairs as references exhibit a Bose-Einstein enhancement below a q value of 0.6 GeV. The large depression at the value of $R(q) <$ 0.5 for "MC REC.", Figure 5.11.(b) and Figure 5.12.(b), is due to the reconstruction inefficiency of two charged particles in the events as shown in Figure 4.26. The inefficiency of the reconstruction gives same effects for both "DATA" and "MC REC.", after applied the Monte Carlo correction this effect is removed and the Bose-Einstein enhancement is observed.

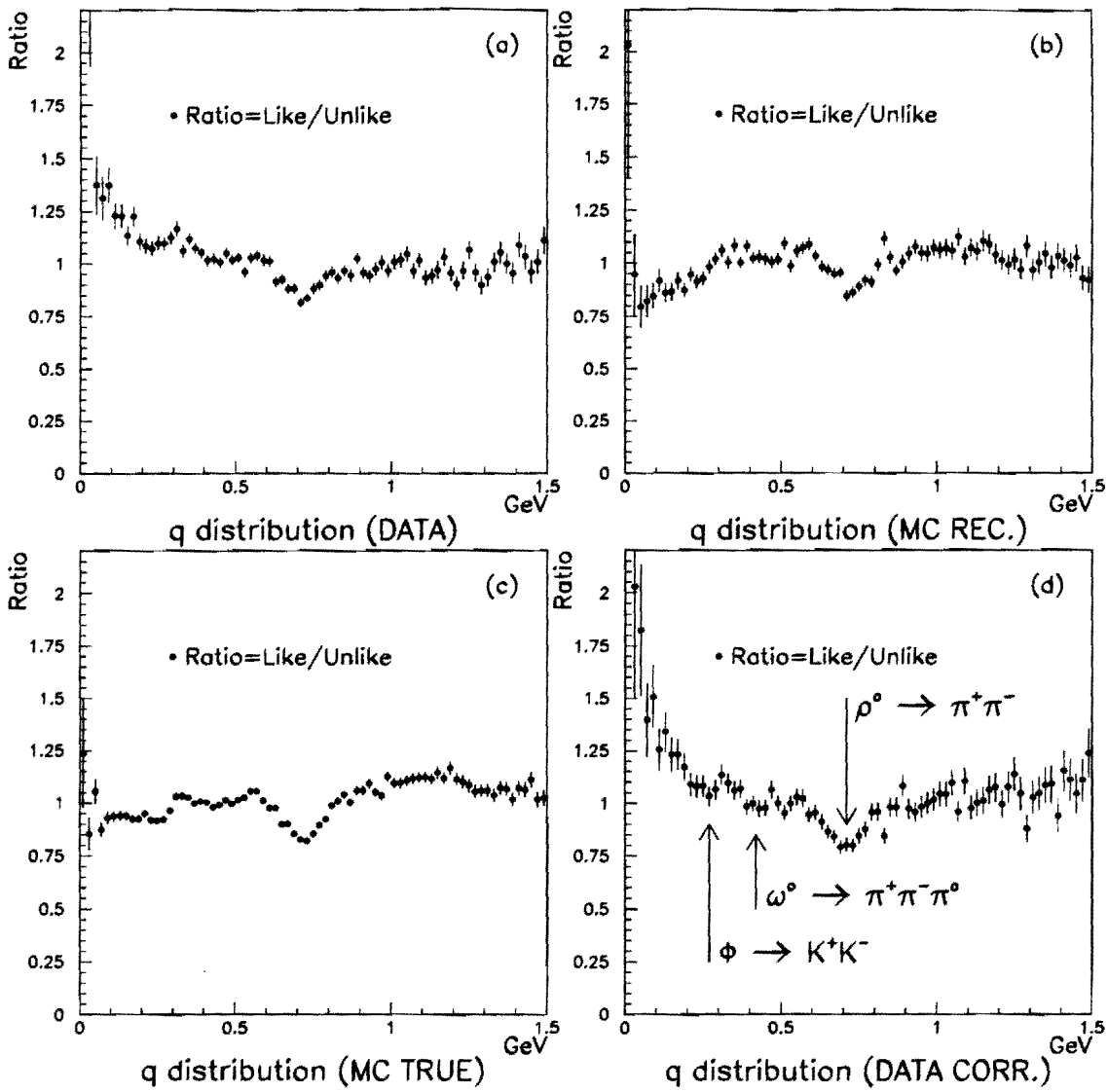

Figure 5.9: The ratio of like-sign/unlike-sign charged pairs versus q, $R(q)$, from events for all "DATA", "MC REC.", "MC TRUE", and "DATA CORR.".

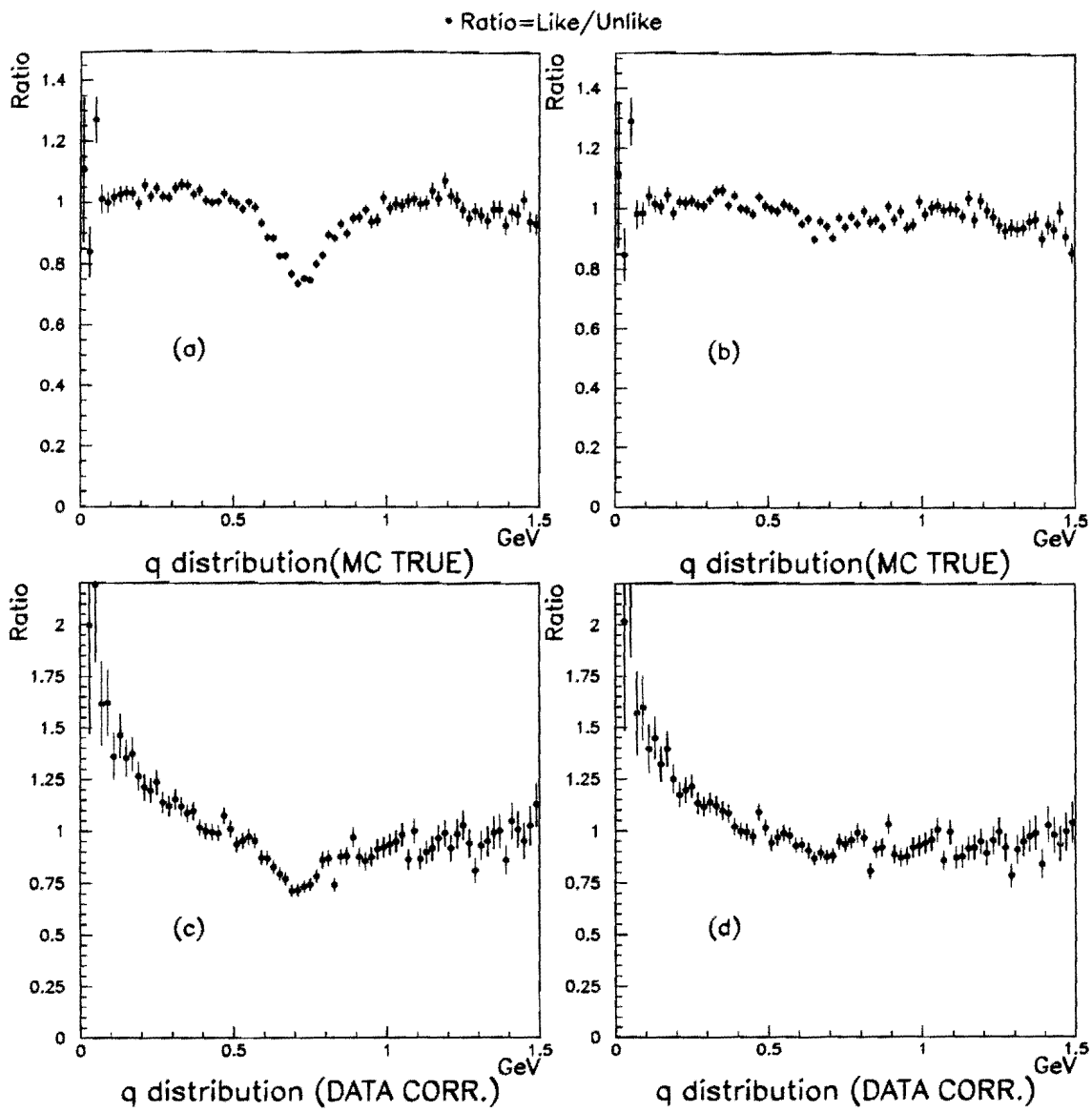

Figure 5.10: The ratio for like-sign/unlike-sign charged pairs versus q, $R(q)$, for "MC TRUE" and "DATA CORR." after removed all decays, (b) and (d). In (a) and (c) shows the $R(q)$ after removed all decays other than ρ^o decay.

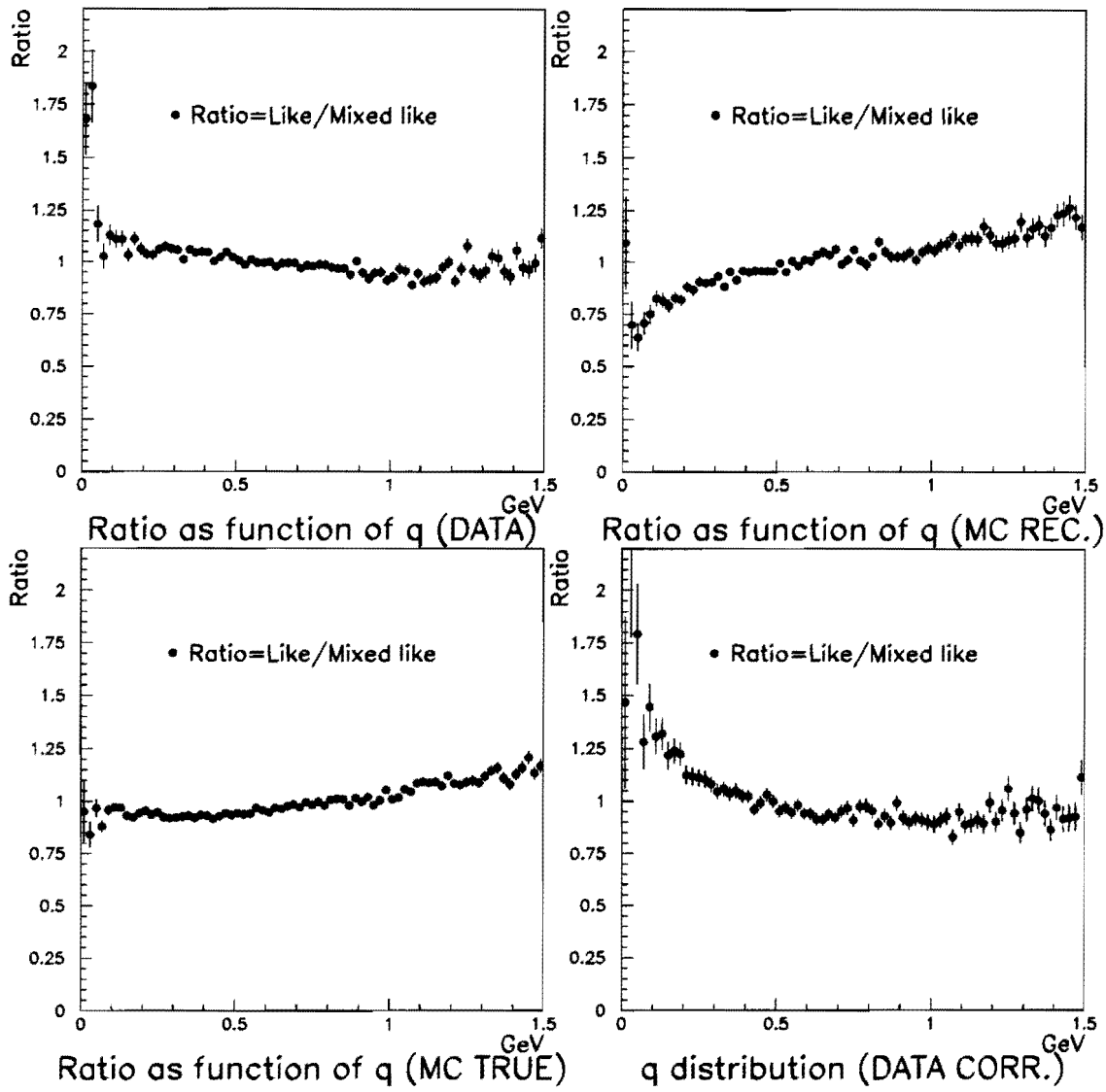

Figure 5.11: The ratio for like-sign/mixed like-sign charged pairs versus q, $R(q)$, for all "DATA", "MC REC.", "MC TRUE", and "DATA CORR.".

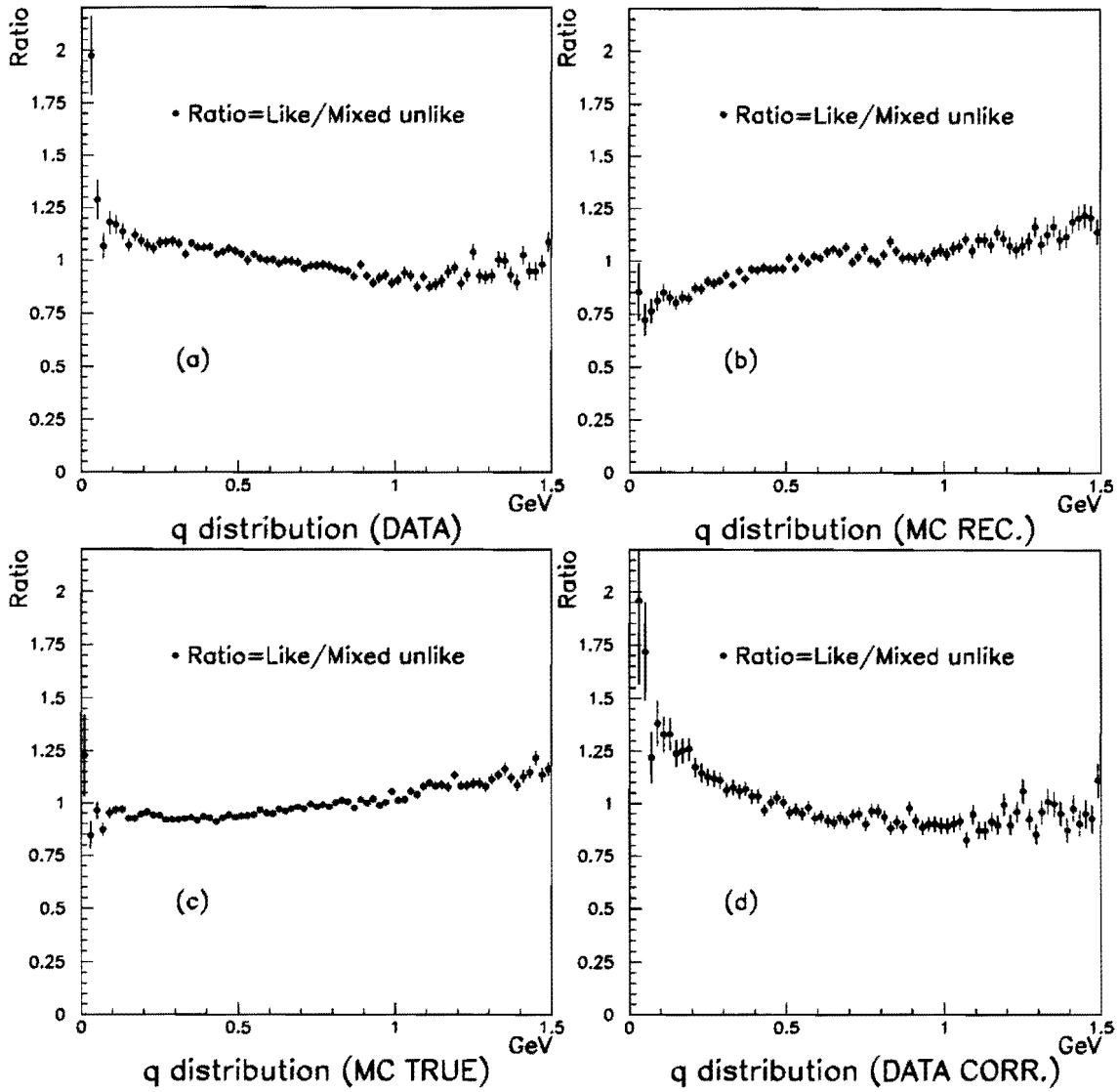

Figure 5.12: The ratio for like-sign/mixed unlike-sign charged pairs versus q, $R(q)$, for all "DATA", "MC REC.", "MC TRUE", and "DATA CORR.".

5.2.1 The Goldhaber Parametrization

The correlation function $R(q)$ can be fitted using a modified Goldhaber Parametrization based on equation (1.23). The equation is given by:

$$R(q) = \gamma + \lambda exp(-\beta^2 q^2). \tag{5.3}$$

The fit parameters are the normalization γ, the chaoticity λ, and the spatial dimension of the pion source β. β is related to the radius of the source by $r_g = 0.197\beta fm$ where r_g is measured in fermi and β is measured in GeV^{-1}. Some experiments in addition use a linear correction term $1 + \delta q$ in order to take into account the behavior of $R(q)$ when using the unlike-sign charged pairs as references. No strong arguments about the particular form for this variation correction exist. As shown in Figure 5.10, in this analysis the $R(q)$ distribution obtained using the unlike-sign charged pairs as reference has no strong variation at large q. Therefore the linear variation correction, $1 + \delta q$, has not been applied on the fits.

I). Mixed Reference

Figure 5.13.a shows the ratio (like/reference) obtained by using mixed like-sign charged pairs as reference and fitted with equation (5.3) , a single Gaussian distribution. It shows that the fit with one Gaussian distribution can well describe the data except for the lowest few bins($q < 0.1GeV$) where the data is higher than the fit. This small q enhancement is associated with long range correlations, which have been observed by several other experiments [28, 14, 20]. A two-Gaussian fit for the ratio distribution $R(q)$,

$$R(q) = \gamma + \lambda exp(-{r_s}^2 q^2) + \lambda_2 exp(-{r_l}^2 q^2) \tag{5.4}$$

is shown in Figure 5.13.b.

Plots (c) and (d) of Figure 5.13 show the ratio obtained by using mixed unlike-charged pairs as reference and fitted with same equations as (a) and (b). The fitted results and the χ^2/NDF of fits are shown in Table XII. The smaller radius obtained from two-Gaussian fit is consistent with the radius obtained from one-Gaussian fit (within error) and is able to represent the pion

source size. The large size is believed to be the combination of the source size and the path length of the $\rho \rightarrow \pi\pi$ decay (the cτ of the ρ^o is 1.3 fm) as shown in Figure 1.3 [28, 61].

Figure 5.14.(a) shows the results of one-Gaussian fit from this analysis along with the results from other lepton scattering experiments. The radius extracted by using mixed like and mixed unlike charged pairs as reference are the same within errors. This indicates that the reconstruction effect at mixing like and mixing unlike charged pairs does not affect the reference selection and is a good description of the data. The average radius of pion emission source, r_g, of this analysis (E665 RUN90) is slightly bigger than previous experiment result (E665 RUN87) but smaller than ν-P(N) experiments. Figure 5.14.(b) shows the two-Gaussian fitted results for using mixed like and mixed unlike as references and results from E665(RUN87) results.

TABLE XII: RESULTS FROM FITS FOR $R(q)$("MIXED" REFERENCE)

Ref.	Mix-Like	Mix-Like	Mix-Unlike	Mix-Unlike
Fit	1-Gauss.	2-Gauss.	1-Gauss.	2-Gauss.
γ	0.928±0.006	0.923±0.006	0.918±0.006	0.91±0.006
λ	0.386±0.03	0.27±0.05	0.40±0.03	0.33±0.048
r_g(fm)	0.63±0.04	0.51±0.06	0.57±0.03	0.51±0.05
p4		(λ_2)0.37±0.11		(λ_2)0.25±0.11
p5		(r_l)1.53±0.39 fm		(r_l)1.45±0.4 fm
χ^2/NDF	1.04	0.93	1.04	0.998

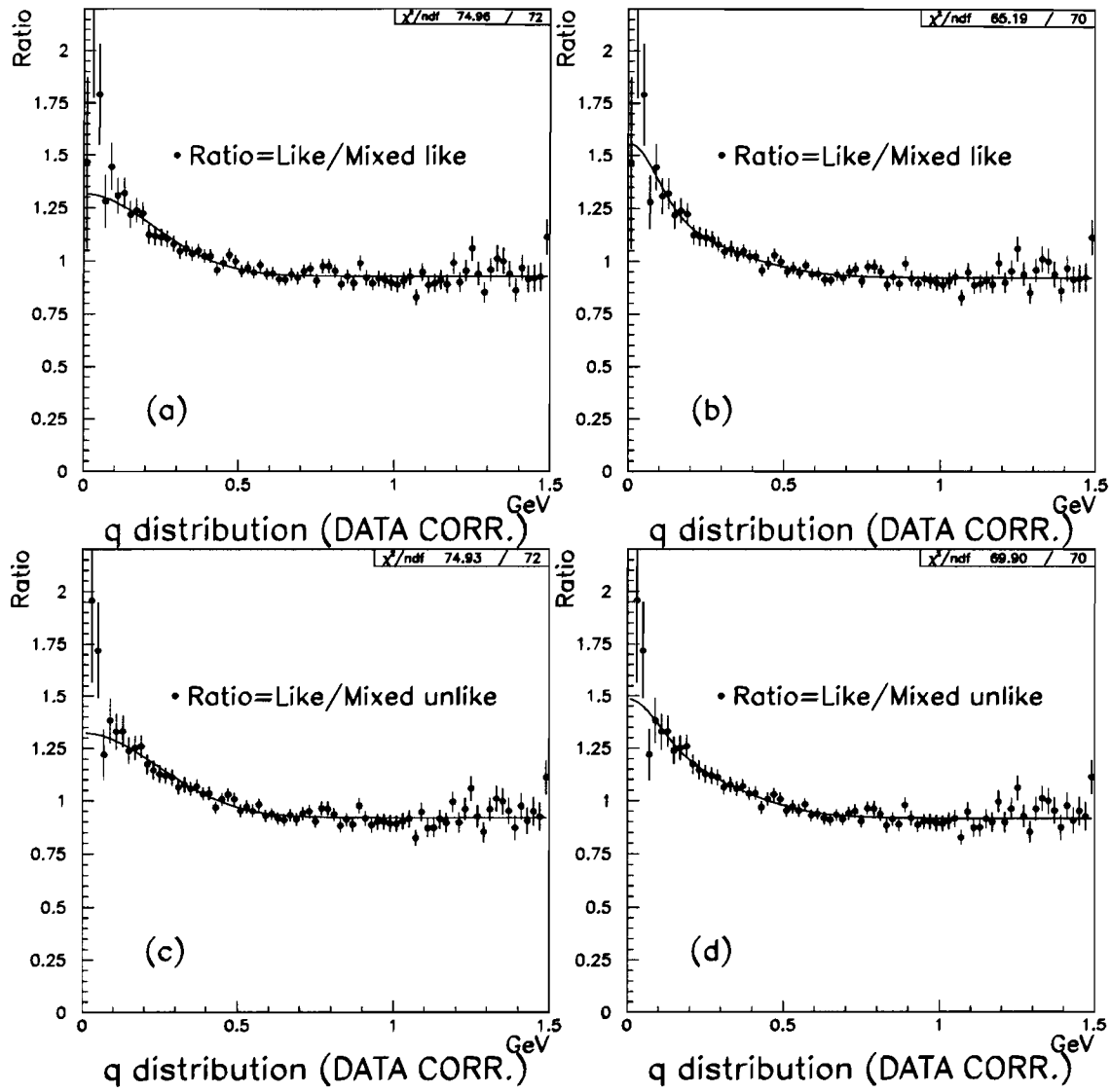

Figure 5.13: Goldhaber Parametrization fit for the ratio, $R(q)$, which obtained by using mixed like-sign, (a) and (b), and mixed unlike-sign, (c) and (d), charged pairs as references. (a), (c) are fitted with 1-Gaussian and (b), (d) are fitted with 2 Gaussian.

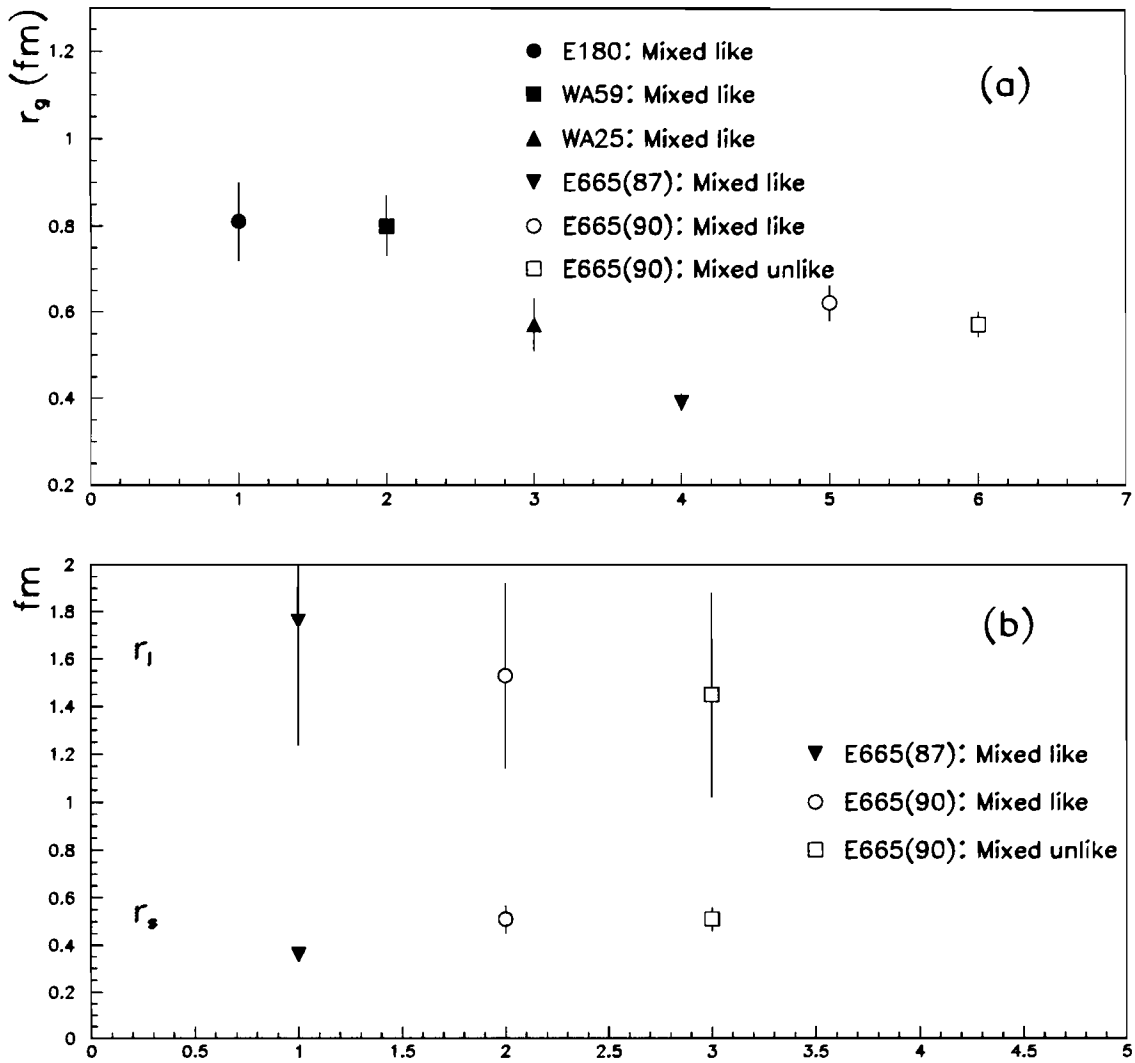

Figure 5.14: Comparison of radius (r_g) extracted from the fit for different experiments which used the mixing method as reference. (a): one-Gaussian fit, (b): two-Gaussian fit.

II). Unlike-Sign Charged Reference

The $R(q)$ distribution obtained from using unlike-sign charged pairs as references has structures from resonances as shown in Figure 5.9.d. Since the Bose-Einstein correlation measures the effects in the small q region so the resonances which distributed in this region will affect the fit results. As shown in Figure 5.10.c and d, the decay effect at $q < 0.5GeV$ have been removed after subtracted the decays from the MTRU distribution and these two distributions will used for the fit.

Several fits using different functions have been performed and shown in Figure 5.15. The Figure 5.15.a is the fitting result obtained by using equation (5.3) for the distribution after removed all decays. The result of the two-Gaussian fit, using equation (5.4), for the same distribution is shown in Figure 5.15.b. Motivated by the observation, a modified parametrization which includes equation (5.3) and an additional explicitly Gaussian distribution around the ρ decay region, $0.6GeV < q < 0.8GeV$,

$$R(q) = \gamma + \lambda exp(-\beta^2 q^2) + \eta * exp(-0.5((q-\mu)/\Gamma)^2) \tag{5.5}$$

has been fitted with the result shown in Figure 5.15.c. In the equation above, η, μ, Γ, are the depth, mean, and the width of the resonance respectively. This fit gives a invariant mass of $M_{\pi\pi} = 0.7702 \pm 0.007GeV$ for the mean value of the ρ dip. The χ^2/NDF of the fit is 75.17/69 and is a good description of the data. The fit in Figure 5.15.d is a two-Gaussian fit, equation (5.4), and includes the ρ decay. The χ^2/NDF of the fit is 67.3/67 and the ρ invariant mass is identical to that obtained in Figure 5.15.c. Table XIII shows the results from the fits for Figure 5.15.

The extrapolated source size from one-Gaussian fit for the "unlike" reference sample , including or excluding the ρ decays, is identical to which obtained from using the "mixed"(like and unlike) as reference. The two-Gaussian fits for all reference methods(mixed like, mixed unlike ,and unlike) have similar small and large source sizes(within error).

A check for the consistency of fits with or without the lowest 4 bins in the q distribution,

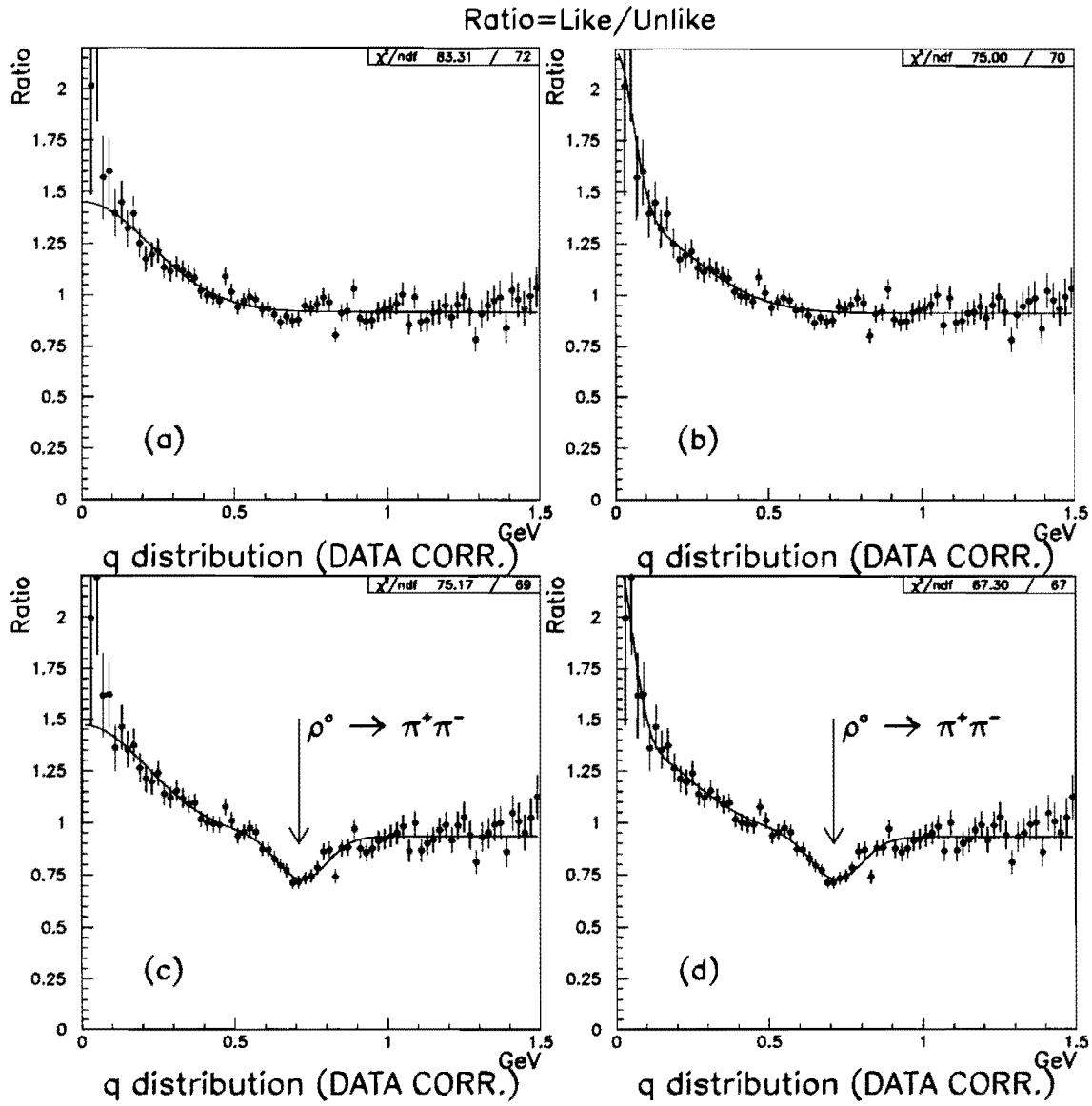

Figure 5.15: Goldhaber Parametrization fits of $R(q)$ which obtained from using unlike-sign charged pairs as references. The fitting parameters are detailed in Table XIII. (a) and (c) are one-Gaussian fit, (b) and (d) are two-Gaussian fit.

TABLE XIII: RESULTS FROM FITS FOR $R(q)$ ("UNLIKE" REFERENCE)

Fit	1 Gau.	2 Gau.	1 Gau. + ρ	2 Gau. + ρ
γ	0.91±0.005	0.91±0.008	0.93±0.01	0.93±0.011
λ	0.54±0.045	0.41±0.05	0.54±0.05	0.47±0.06
r(fm)	0.617±0.037	0.57±0.04	0.64±0.04	0.59±0.46
p4		(λ_2)0.81±0.44	(η)-0.2±0.016	(λ_2)0.90±0.49
p5		(r_l)2.46±0.77 fm	(μ)0.720±0.007 GeV	(r_l)2.67±0.84 fm
p6			(Γ)0.082±0.01GeV	(η) -0.2±0.017
p7				(μ)0.718±0.007
p8				(Γ)0.082±0.01GeV
χ^2/NDF	1.1	1.07	1.08	1.0

which under the effects from the fluctuation of reconstruction. Same fits (exclude the lowest 4 bins) as Figure 5.13 and Figure 5.15 have been applied. Figure 5.16 and 5.16 show the plots of the fit along with the χ^2/NDF of the fit. The comparison of the fitting results between fit all and exclude lowest 4 q bins is given in Figure 5.18 and Table XIV. Results show that the radius of pion emission source extracted from single Gaussian distribution for both references are identical, $\sim 0.6fm$, and independent of including or excluding the lowest 4 bins. The two Gaussian source distribution extracted from fitting all like/unlike distribution has bigger r_l with large error. The fluctuation at lowest 4 bins contributed this as expected. The two Gaussian fit excluded lowest 4 bins for like/unlike distribution has identical r_s and r_l as using mixed references(like and unlike).

Results show that the radius of pion emission source is independent on the reference method. For the studies carried out in the following sections, the result obtained by the one-Gaussian fit using the "mixed like" reference sample are used. The results from using unlike-sign charged pairs as reference will be used only for the systematical cross checking.

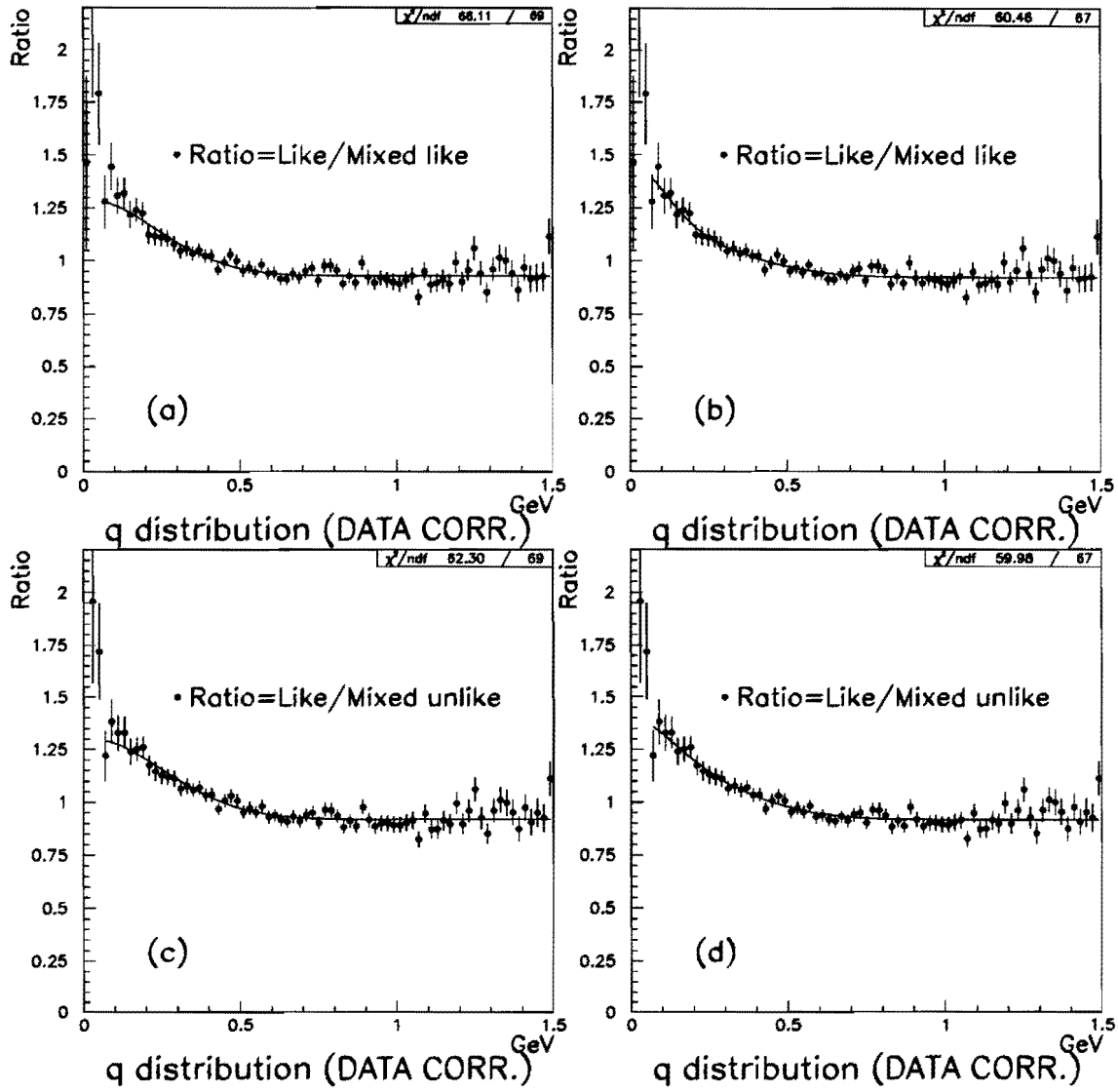

Figure 5.16: Same fits as Figure 5.7 for $R(q)$ with excluding the lowest 4 q bins.

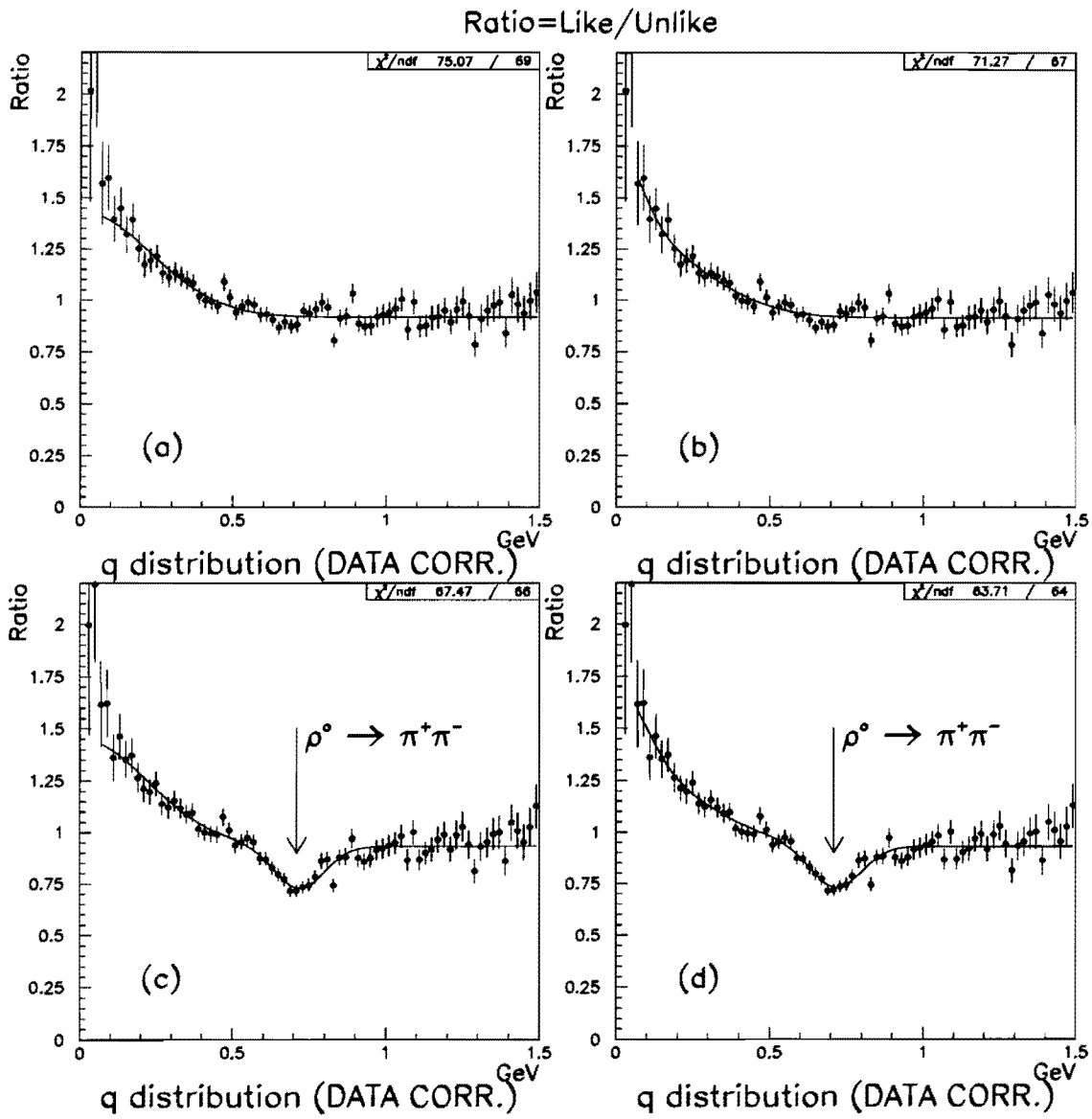

Figure 5.17: Same fits as Figure 5.7 for $R(q)$ with excluding the lowest 4 q bins.

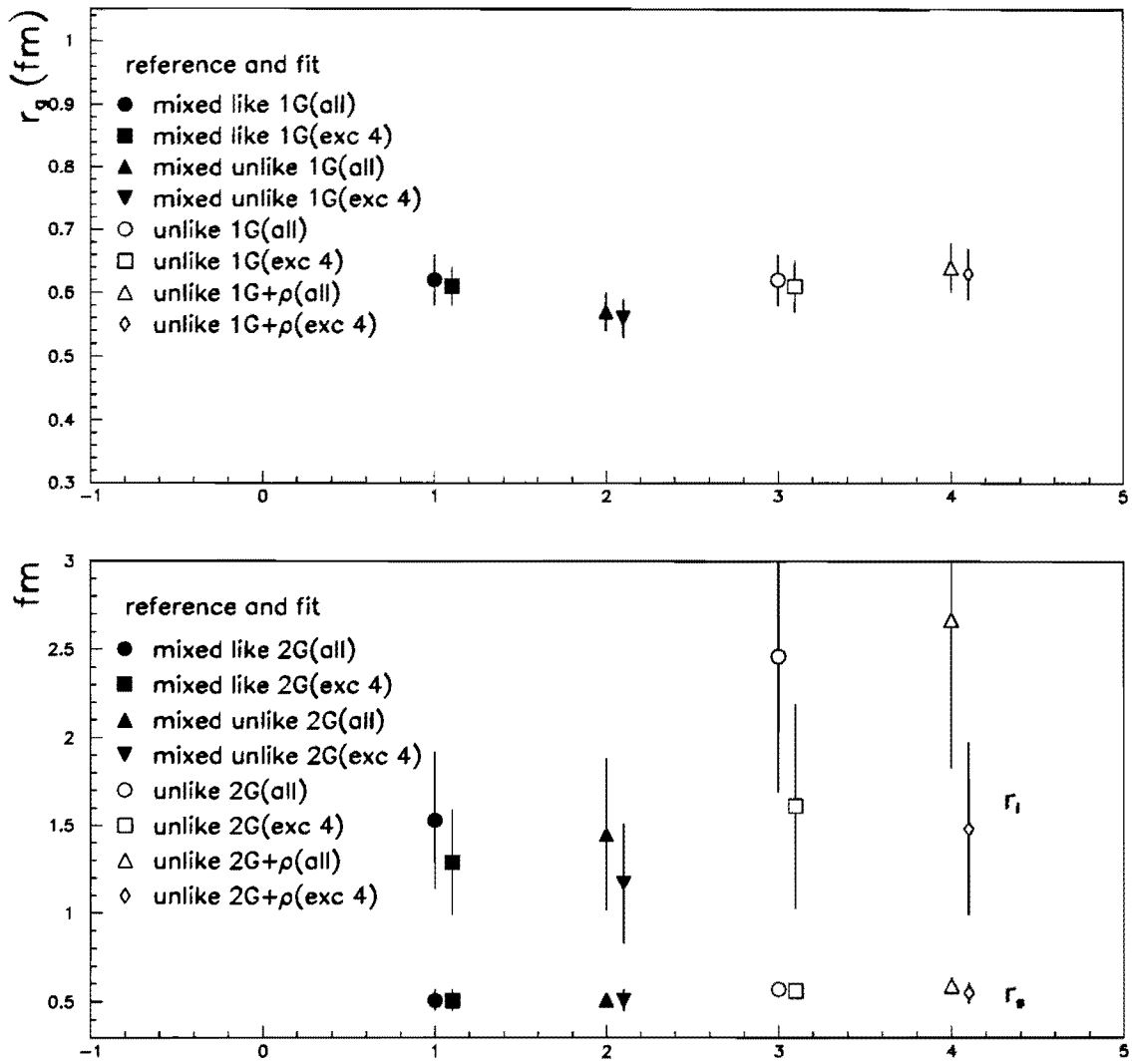

Figure 5.18: Comparison of the radius extracted from fitting all bins(all) and fitting without lowest 4 bins(exc 4) for both references. 1G: one Gaussian fit, 2G: two Gaussian fit, 1G+ρ: one Gaussian plus ρ fit. 2G+ρ: two Gaussian plus ρ fit. for $R(q)$ with excluding the lowest 4 q bins.

TABLE XIV: RESULTS OF FITS WITH (WITHOUT) THE LOWEST 4 q BINS

Fit	γ	λ	r_g(fm)	λ_2	r_l fm	χ^2/NDF
1G(m-li.)	0.93(0.93)	0.39(0.37)	0.62(0.60)			1.04(0.96)
2G(m-li.)	0.92(0.92)	0.27(0.25)	0.51(0.51)	0.37(0.31)	1.53(1.29)	0.93(0.90)
1G(m-unl.)	0.92(0.92)	0.40(0.39)	0.57(0.56)			1.04(0.95)
2G(m-unl.)	0.91(0.91)	0.33(0.31)	0.51(0.51)	0.25(0.22)	1.45(1.17)	0.99(0.92)
1G (unl.)	0.91(0.91)	0.54(0.51)	0.62(0.61)			1.07(1.06)
2G (unl.)	0.91(0.91)	0.41(0.44)	0.57(0.56)	0.81(0.45)	2.46(1.61)	1.04(1.02)
1G+ρ(unl.)	0.93(0.93)	0.54(0.52)	0.64(0.63)			1.06(1.01)
2G+ρ(unl.)	0.93(0.93)	0.47(0.39)	0.59(0.55)	0.70(0.37)	2.67(1.51)	1.0(0.99)

5.3 The Kopylov-Podgoretskii Parametrization $R(q_t, q_0)$

The Kopylov-Podgoretskii (KP) parametrization, as described in chapter 1, dictated searching for the Bose-Einstein effect at small q_0. In order to investigate the q_t dependence of KP parametrization for Bose-Einstein correlation, the data are separated into three q_0 ranges, $q_0 < 0.24GeV$, $0.24GeV < q_0 < 0.42GeV$, and $q_0 > 0.42GeV$. A similar procedure is adopted to study the q_0 dependence for correlation function in ranges of q_t, $q_t < 0.3GeV$, $0.3GeV < q_t < 0.5GeV$, and $q_t > 0.5GeV$.

The correlation function $R(q_t,q_0)$ for like-sign charged pairs over mixed like-sign charged pairs is shown in Figure 5.19. Plots show an enhancement at small q_t for the interval of $q_0 < 0.24GeV$ and no enhancement for other q_0 intervals. The correlation function obtained by using unlike-sign charged as references has similar results, however only mixed references results are shown. For q_0 dependence, an enhancement is observed at small q_0 at the ranges of $q_t < 0.5GeV$ and flat beyond $q_t > 0.5GeV$. Results show that the 2 dimensional correlation function $R(q_t, q_0)$ of KP parametrization has Bose-Einstein correlation at small values of q_t and q_0 (0.5 GeV and 0.24 GeV respectively).

To extract the source size dependence on q_t and q_0 for the Kopylov-Podgoretskii parame-

terization, an equation

$$R(q_t, q_0) = \gamma + \lambda e^{(\frac{-r_k}{2}^2 q_t^2)} e^{-\tau^2 q_0^2} \tag{5.6}$$

is applied for q_t at $q_0 < 0.24GeV$ and q_0 at $q_t < 0.5GeV$ individually. Where $q_t = |\vec{q} \times \vec{p}|/|\vec{p}|$ and $q_0 = |E_1 - E_2|$ with $\vec{q} = \vec{p}_1 - \vec{p}_2$, $\vec{p} = \vec{p}_1 + \vec{p}_2$. The fit parameters are shown in Table XV. A larger pion source size (r_k) is observed. As mentioned in chapter 1, at $q_0 \approx 0$ the source size extrapolated from KP (r_k) is about twice the source size from Goldhaber (r_g); this is also observed from the result (within error). The source size extracted from the q_0 dependence (τ) is similar to the Goldhaber radius r_g. These results confirm that both parametrizations are similar and are able to describe the Bose-Einstein correlation at small q_t and q_0 (small q). Similar result was found at π^+p-Interaction at 250 GeV/c [20].

TABLE XV: FIT RESULTS FOR Kopylov-Podgoretskii PARAMETRIZATION

	γ	λ	r_k(fm)	τ(fm)	χ^2/ndf
$R(q_0), q_t < 0.5GeV$	0.947±0.017	0.34±0.051		0.748±0.18	1.23
$R(q_t), q_0 < 0.24GeV$	1.040±0.03	0.27±0.12	1.8±0.72		1.79

5.4 The Goldhaber and Kopylov-Podgoretskii Parametrizations

The one dimensional fits to the ratio distributions of both Goldhaber and Kopylov-Podgoretskii parametrizations showed the Bose-Einstein effects at small q. Therefore to distinguish the two parametrizations one should look at the two dimensional dependence of the Bose-Einstein effect. The two dimensional correlation function of Goldhaber parametrization can be expressed from equation (5.3) as

$$R(q_v, q_0) = \gamma + \lambda e^{-r_g^2 q_v^2} e^{r_g^2 q_0^2} \tag{5.7}$$

where q_v presents the 3-vector momentum difference. Comparing equation (5.7) with equation (5.6), one can see that the difference between these two equations is the opposite sign of the q_0 term. for small value of q_0, these two parametrizations are similar. On the other hand, when

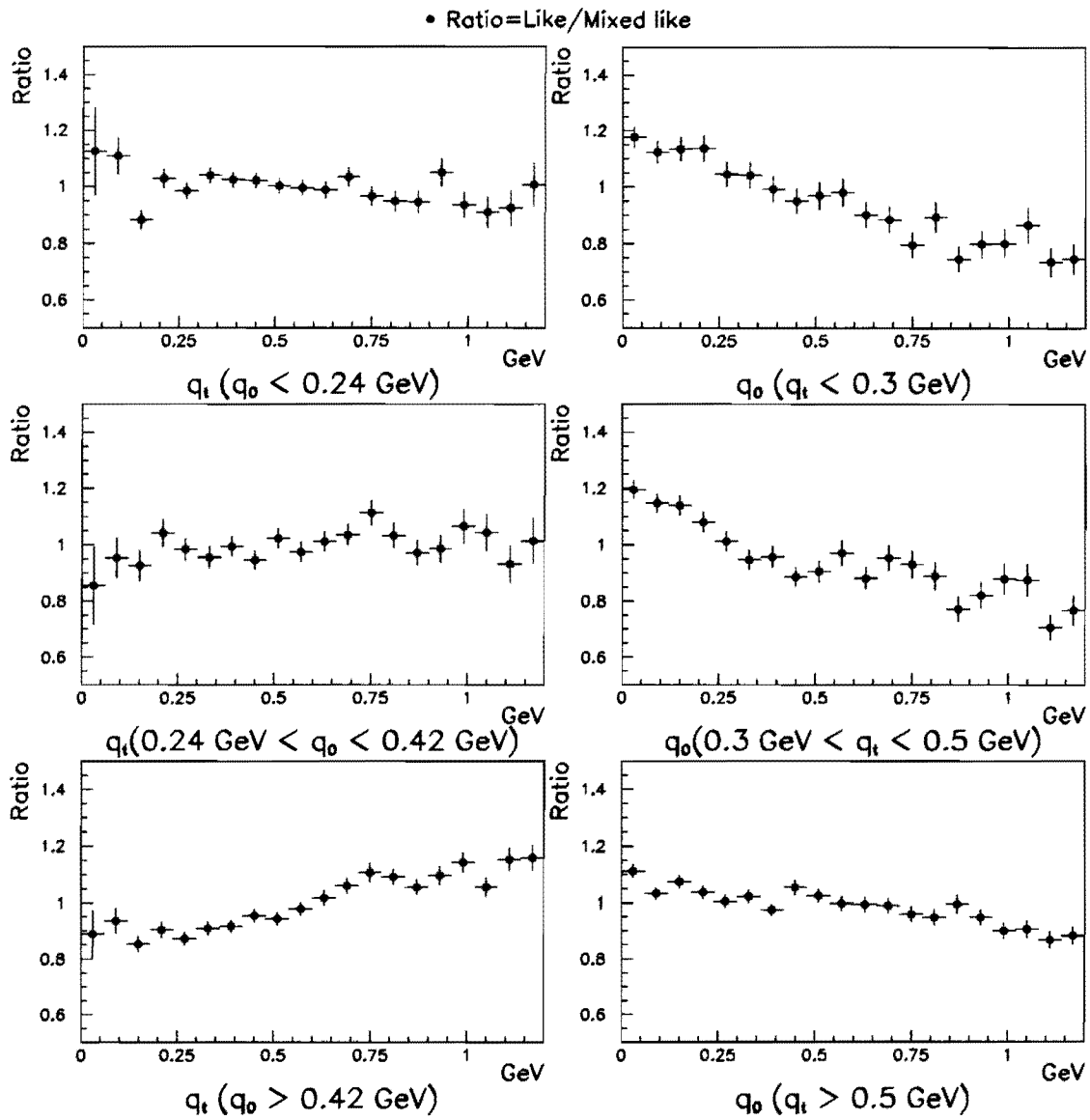

Figure 5.19: The ratio versus q_t and q_0 distributions for three q_0 and q_t regions. Plots on the left are as a function of q_t a nd plots on the right are as a function of q_0.

q_0 is large, these two parametrizations are significantly different. The correlation functions in two dimensional space are shown in Figure 5.20.

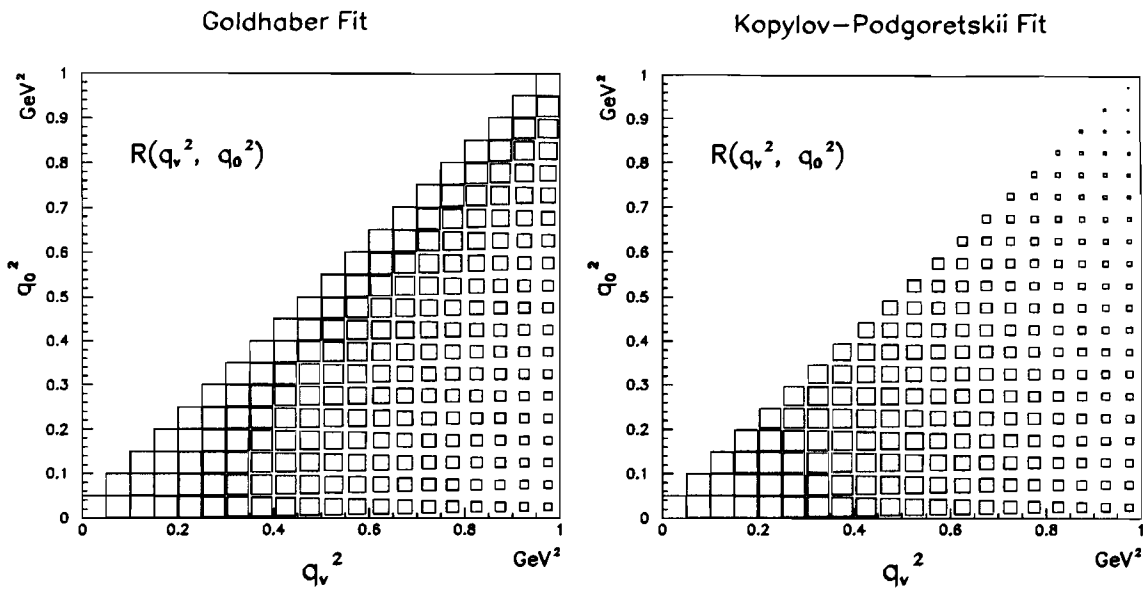

Figure 5.20: Schematic representation of the q_v^2 and q_0^2 dependence of the correlation function R as given by equations (5.7) and (5.6) with $\gamma = 1$ and $\lambda = 1$. The area of the boxes is proportional to the value of $R(q_v^2, q_0^2)$.

The corresponding two-dimensional plots for data after Monte Carlo correction are shown in Figure 5.21. The data plots in Figure 5.21 show the enhancement do go along the diagonal direction up to large q_v^2 and q_0^2, and this enhancement along the diagonal, $q_v^2 \approx q_0^2$ (small q^2), indicate that the invariant variable $q^2 = q_v^2 - q_0^2$ is a good description for the data. On the other hand, the Kopylov-Podgoretskii fit in Figure 5.20.b gives enhancements only along the diagonal to the value of $q_0^2 = 0.5GeV^2$ which is inconsistent with the data. From above one can conclude that the Goldhaber parameterization describes the data of this experiment better since the correlation persists at large q_0^2 and q_v^2. This result is consistent with the results from [28, 27, 26].

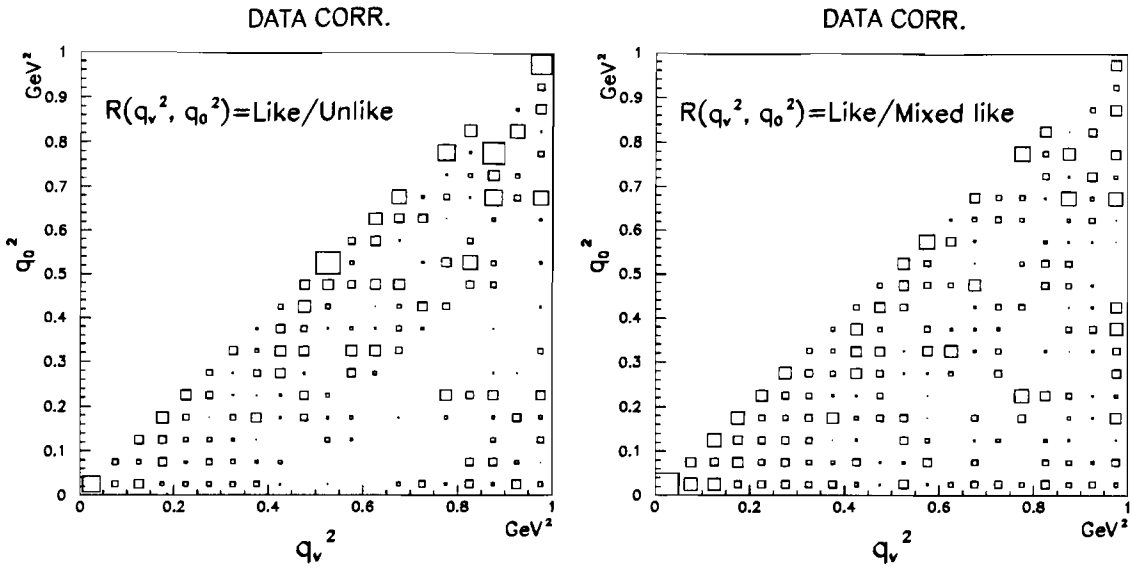

Figure 5.21: Schematic 2-dimensional representations of the correlation function $R(q_v^2, q_0^2)$ for "DATA CORR." The area of the boxes is proportional to the value of $R(q_v^2, q_0^2)$= Like/references.

5.5 The A-Dependence of Bose-Einstein Correlation

To study the A-dependence on the Bose-Einstein correlation, data are separated into four target groups H2+D2, C, Ca, and Pb. The ratio as a function of q, $R(q)$ = Like/Mixed like, of four target groups are shown in Figure 5.22. The one-Gaussian Goldhaber parametrization fits are presented. To check the systematical consistency of the effect, the same plots using unlike-sign charged pairs as references, excluding all possible decays from MTRU, are shown in Figure 5.23 along with the one-Gaussian Goldhaber fits. Source size (r_g) and chaoticity parameter (λ) versus atomic mass are plotted in Figure 5.24. No significant dependence on target atomic mass is seen for both source size and chaoticity. The result is the same as from 38 GeV π-nuclei interactions[62], no dependence of the Bose-Einstein correlation on the atomic mass.

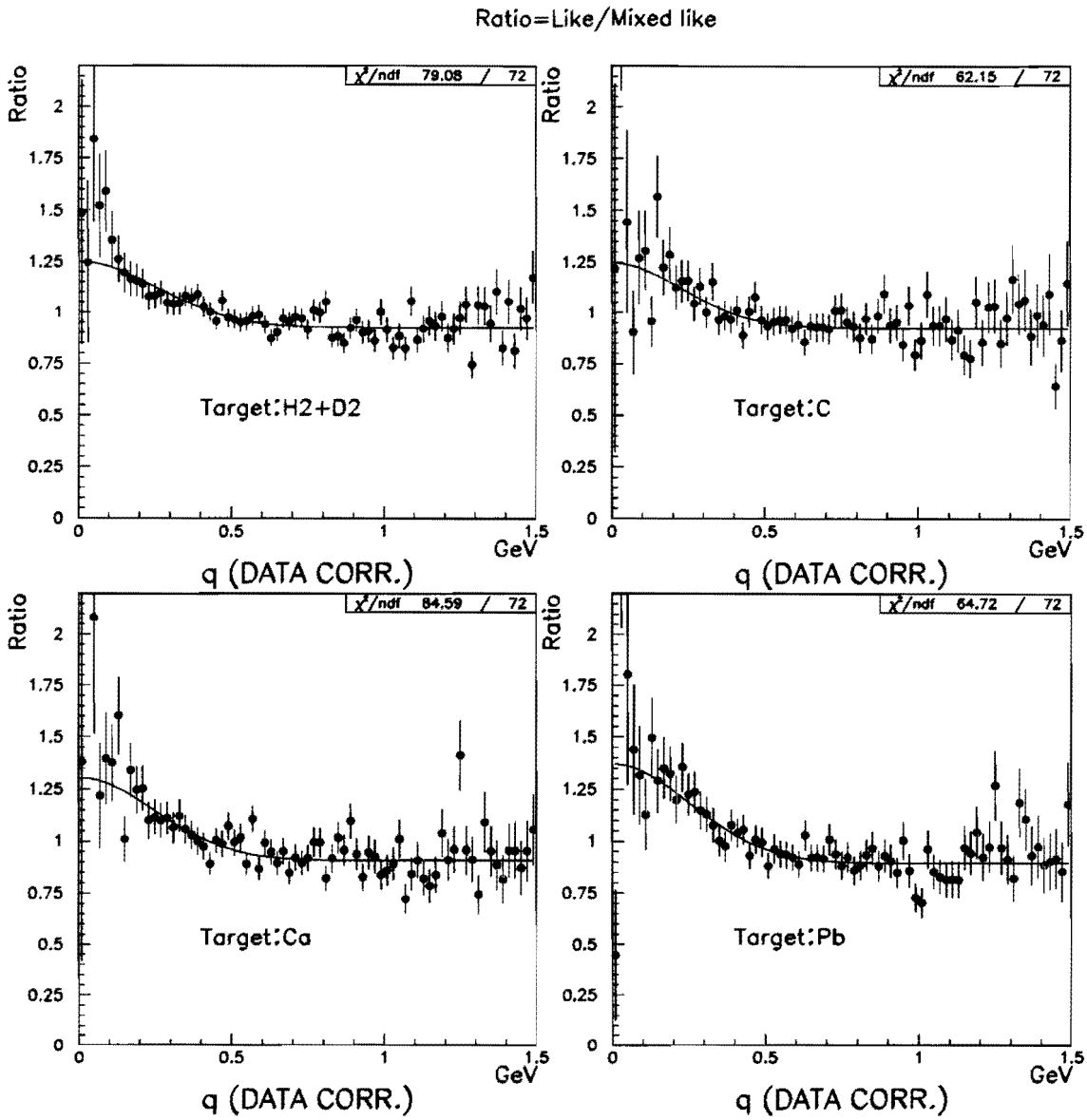

Figure 5.22: Ratio (Like/Mixed like) as a function of q for four targets with one-Gaussian Goldhaber parametrization fit.

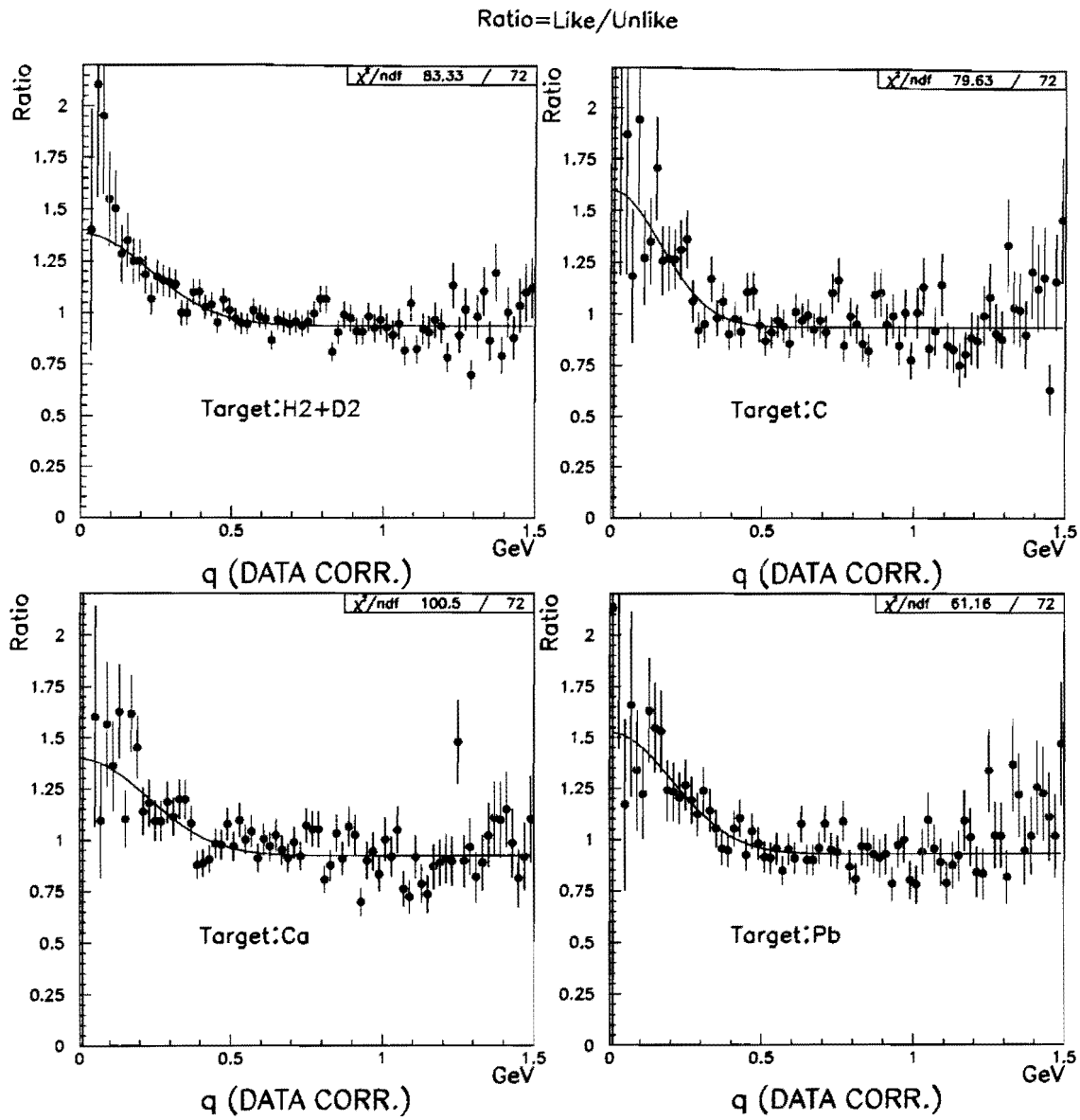

Figure 5.23: Ratio (Like-Unlike) versus q distributions for four targets with one-Gaussian Goldhaber parametrization fit. The decays effect are removed in the MTRU.

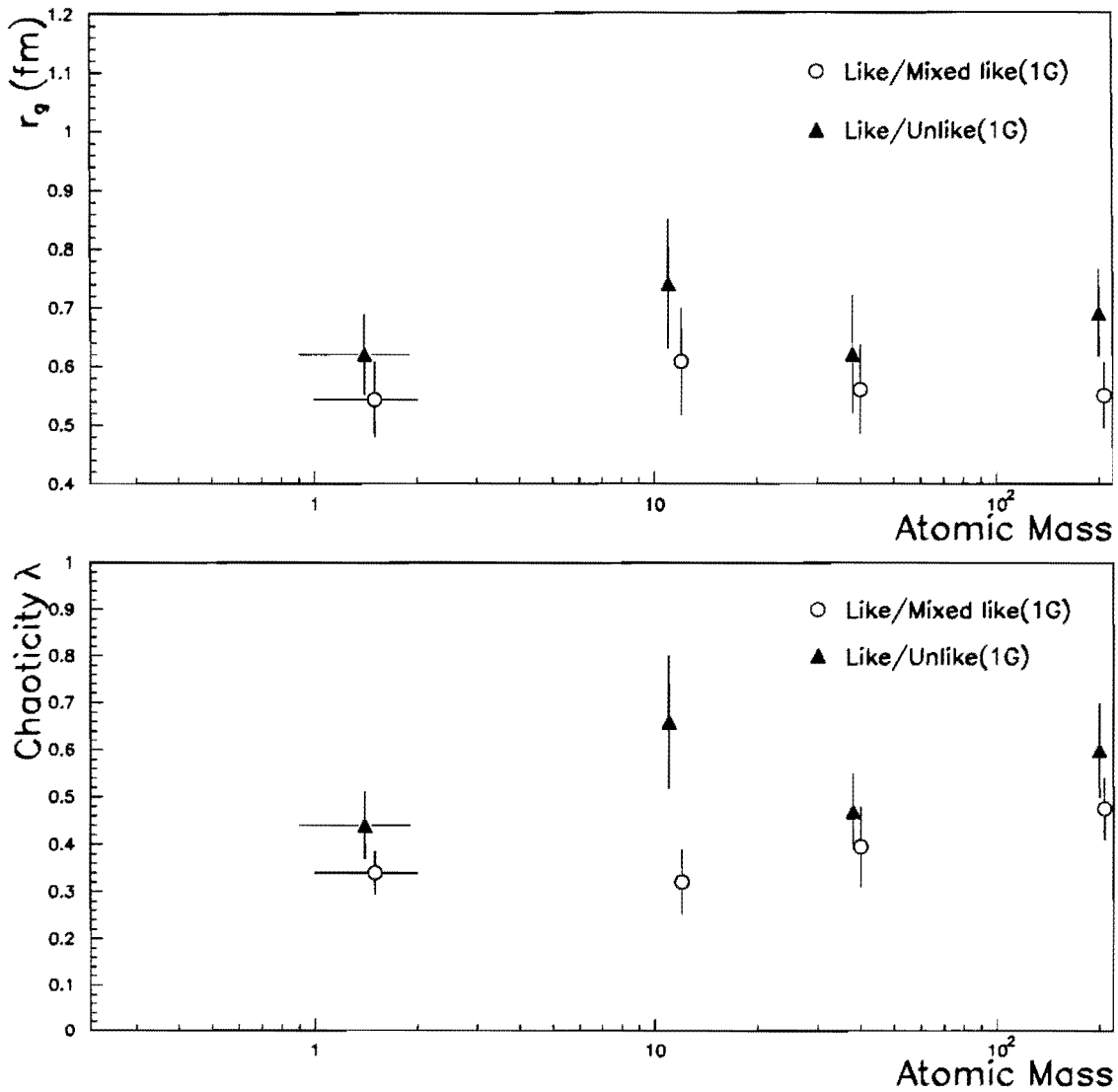

Figure 5.24: Schematic plots of radius(r_g) and chaoticity(λ) versus target atomic mass obtained from the fits of $R(q) = Like/reference$.

5.5.1 A-Dependence of the Shape of the Pion Emission Source

The source parameter associated with the Bose-Einstein effect derived from the q correspond to the size of the pion source averaged over all directions. However, it is possible that the emission region is non-spherical as postulated by the string models[63]. In order to investigate the shape of the pion emission region, a study of the dependence on two separate variables, q_l and $q_\top$, of the Bose-Einstein effect instead of the single variable q is performed. As mentioned in chapter 1, q_l is the longitudinal component of momentum difference along the virtual photon direction in the center of collision frame, $q_l^2 = q_z^2 - q_0^2$, and $q_\top^2 = q_x^2 + q_y^2$ is the transverse component of the momentum difference.

The ratio $R(q_l, q_\top)$ is binned in a two-dimensional array of the variables q_l and $q_\top$ in three intervals based on the number of entries. They are $q_l \leq 0.2GeV$, $0.2GeV < q_l \leq 0.4GeV$, and $q_l > 0.4GeV$,$q_\top \leq 0.15GeV$, $0.15GeV < q_\top \leq 0.3GeV$, and $q_\top > 0.3GeV$ respectively. The ratio R versus q_l, for each bin of $q_\top$, and ratio R versus $q_\top$ for each bin of q_l are shown in Figure 5.25. The data show an enhancement of ratio at small q_l for $q_\top \leq 0.15GeV$ and relatively flat for $q_\top > 0.3GeV$. On the other hand, data also show an enhancement of ratio at small $q_\top$ for $q_l \leq 0.2GeV$ and flat for other q_l intervals.

This indicates that the Bose-Einstein effects presents at low $q_\top$ when q_l is small and at low q_l when $q_\top$ is small, ie when $q = \sqrt{q_l^2 + q_\top^2}$ is small. A fit using the equation $R = \gamma + \lambda exp(-r_l^2 q_l^2)$ was made for the q_l distribution at $q_\top \leq 0.15GeV$, and a fit using the equation $R = \gamma + \lambda exp(-r_\top^2 q_\top^2)$ was made for the $q_\top$ distribution at $q_l \leq 0.2GeV$. Figure 5.25.a and Figure 5.25.b show the fitted results of q_l and $q_\top$ for all targets. The fitted results give $r_l = 0.68 \pm 0.056$ fm and $r_\top = 1.75 \pm 0.38$ fm with χ^2/NDF equal 0.91 and 0.89 respectively.

The correlation functions R versus q_l and $q_\top$ for separate targets are shown in Figure 5.26 and Figure 5.27. The source sizes in longitudinal and transverse relative to the virtual photon direction, r_l and $r_\top$, for all targets are shown in Figure 5.28 along with the chaoticity parameters. The χ^2/NDF of the fits are within the range of 1.0 ± 0.2. No significant dependence of r_l

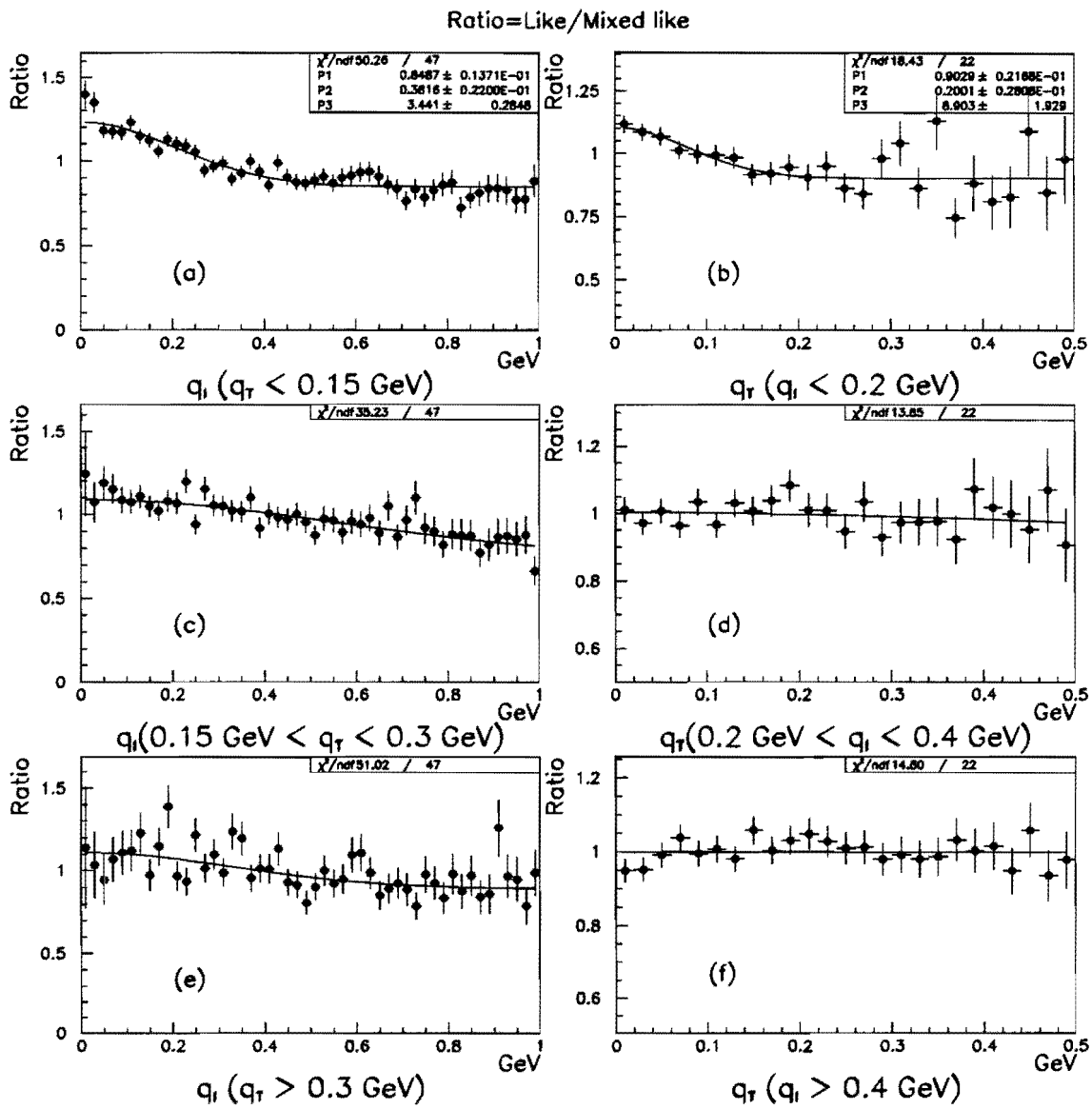

Figure 5.25: Ratio versus $q_l(q_T)$ distributions for each individual $q_T(q_l)$ interval.

($r_\top$) and λ_l ($\lambda_\top$) on the target atomic mass is observed .The transverse sizes are clearly bigger than longitudinal sizes for each target as seen when data from different target are combined.

In the hadronic system, if the $\pi\pi$ system moves mostly longitudinally to the virtual photon direction, the radius in the longitudinal direction is smaller due to the Lorentz booster in this direction. On the other hand if the $\pi\pi$ system moves mainly transverse to the virtual photon direction then it should have a larger longitudinal size with a prolate shape. The results from this analysis point to a larger transverse size than longitudinal size, an oblate shape is concluded. This can in fact be expected understanding that most $\pi\pi$ systems in this analysis move along the virtual photon direction.

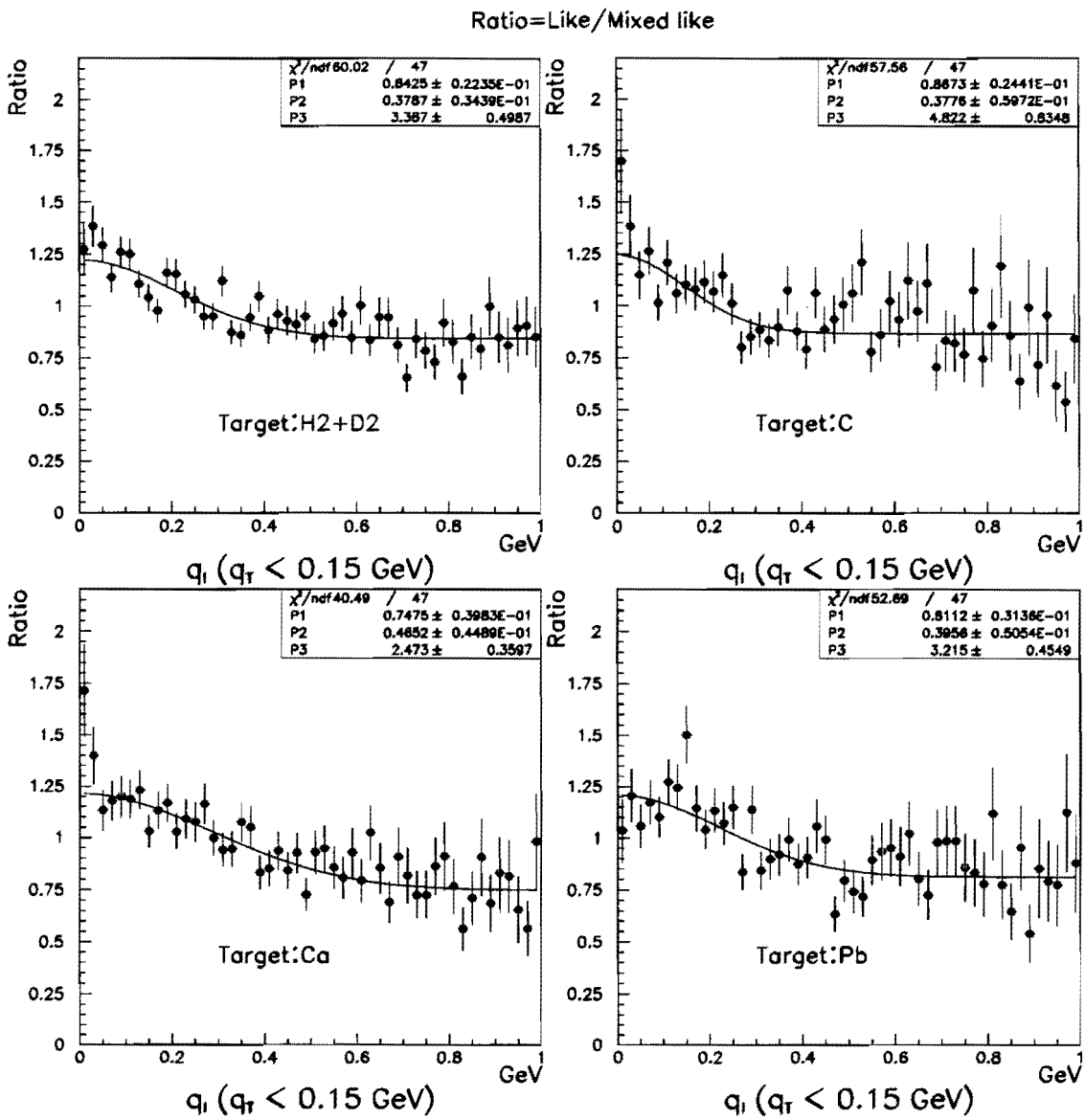

Figure 5.26: Ratio versus q_l distributions at $q_T \leq 0.15 GeV$ for all targets. The plots are fitted with the function $R = \gamma + \lambda exp(-r_l^2 q_l^2)$.

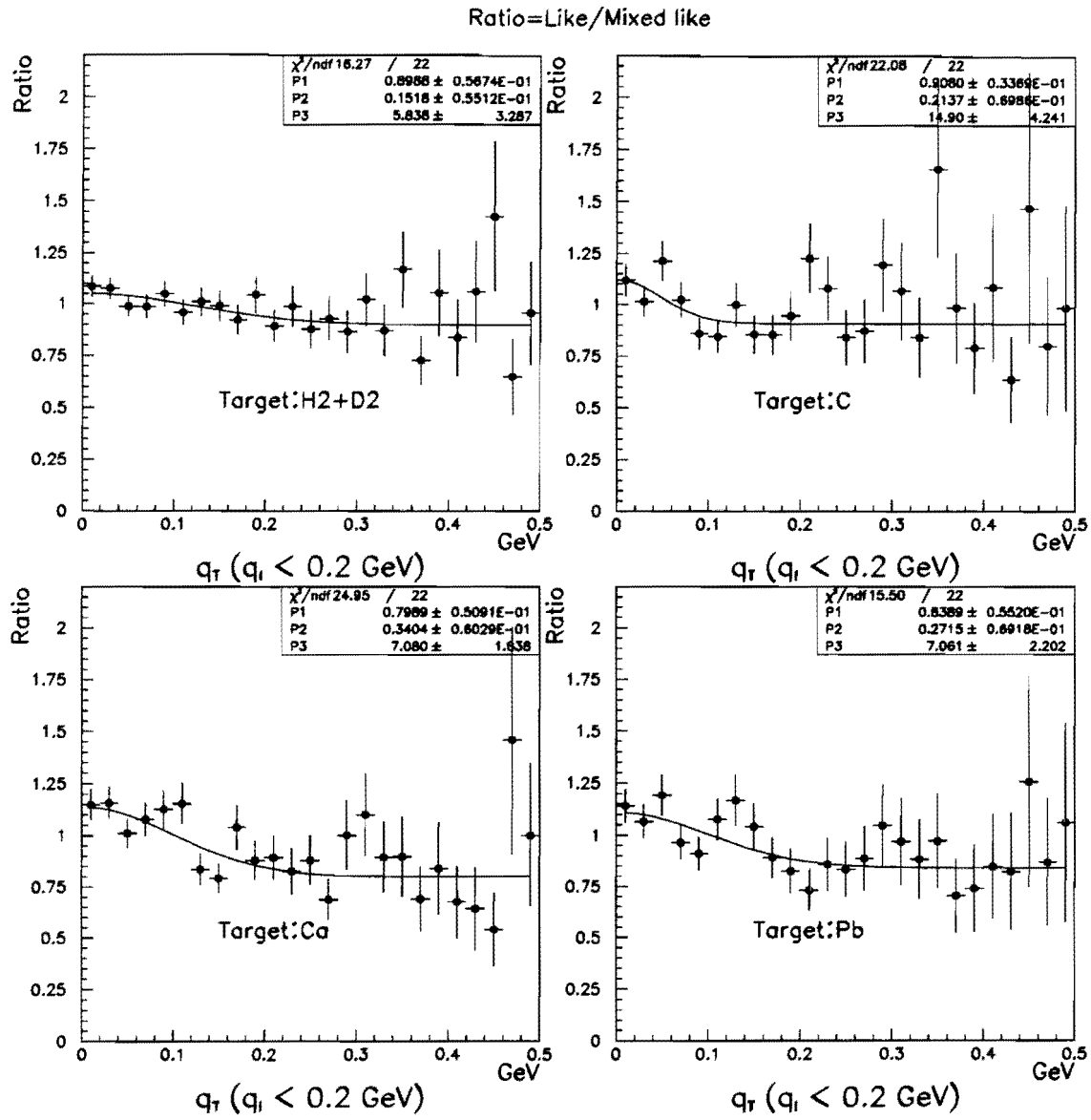

Figure 5.27: Ratio versus q_T distributions at $q_l \leq 0.2GeV$ for all targets. The plots are fitted with the function $R = \gamma + \lambda exp(-r_T^2 q_T^2)$.

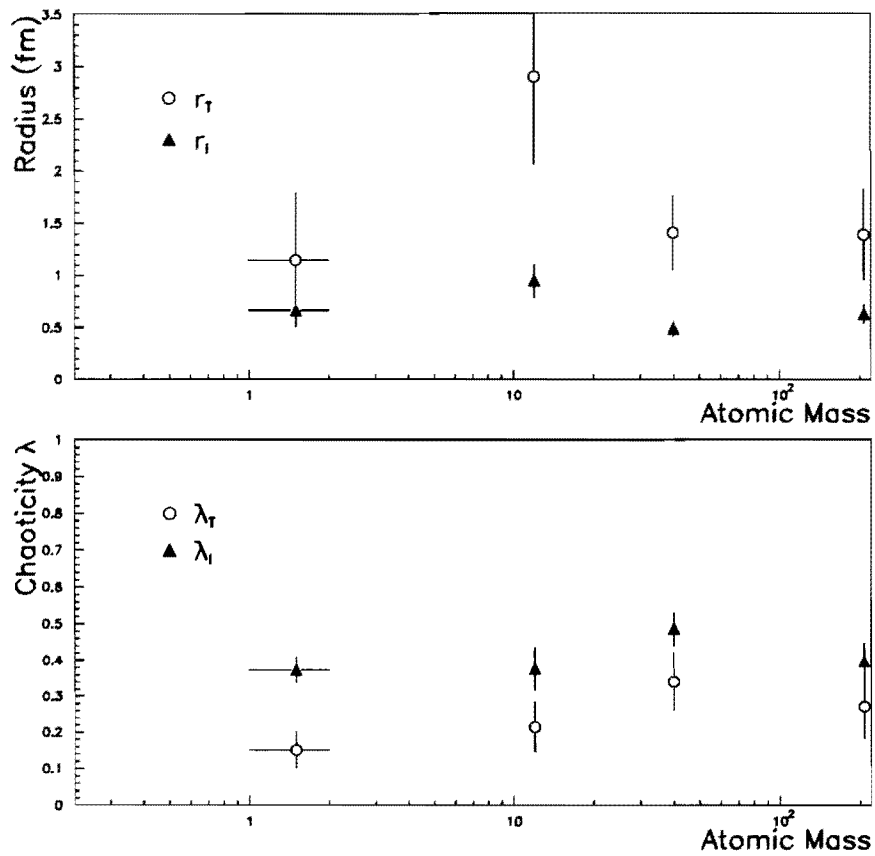

Figure 5.28: The A-dependence of the "radius" and chaoticity "λ" in longitudinal and transverse directions.

5.6 The Dependence on the Event Kinematical Variables

A study of the dependence of the radius r_g and chaoticity parameter λ on the deep inelastic kinematical variables x_{bj}, W^2, ν and Q^2 has been performed. For statistical reasons, the data were divided into three regions for each kinematical variable. Due to possibility that the hadronizations from nuclear targets in various kinematical regions were different an additional study for A-dependence in three regions is attached. Data are separated into two parts, data from D2 and H2 were grouped as "light" targets and Ca and Pb were grouped as "heavy" targets.

5.6.1 The x_{bj} Dependence

Most events of E665 data were in the low-x_{bj} regions , $x_{bj} \leq 0.01$, events with x_{bj} below this value are divided into two regions based on the number of entries. Events having x_{bj} greater than 0.01 are grouped into one bin. Figure 5.29 shows the ratio versus q distributions for All, D2+H2, and Ca+Pb targets in three different x_{bj} bins. The solid lines in the plots were obtained by fitting with the Goldhaber parametrization, the χ^2/NDF of each fit is also displayed in the plots. The radius of pion source(r_g) and the chaoticity(λ) of the measurements for All, D2+H2, and Ca+Pb targets which were obtained from these fits are plotted in the Figure 5.30. The ratios of r_{Ca+Pb}/r_{D2+H2} and $\lambda_{Ca+Pb}/\lambda_{H2+D2}$ for three x_{bj} intervals are also plotted in Figure 5.30.

A noticeable decrease for the radius in the last x_{bj} bin along with a decreasing measurement chaoticity(λ) were observed. Also from the plots for separated targets we can observe the same reduction of radius. The ratio plots for the radius (r_{Ca+Pb}/r_{H2+D2}) and chaoticity ($\lambda_{Ca+Pb}/\lambda_{H2+D2}$) show no obvious dependence on x_{bj}.

In order to check the consistency of the results which were obtained from both "mixed" and "unlike" methods, the same study of x_{bj} dependence was performed for "unlike" method

as well. Figure 5.31 and Figure 5.32 show the same results for the "unlike" method. The same decrease of r_g with x_{bj} increase was observed as from the "mixed" method.

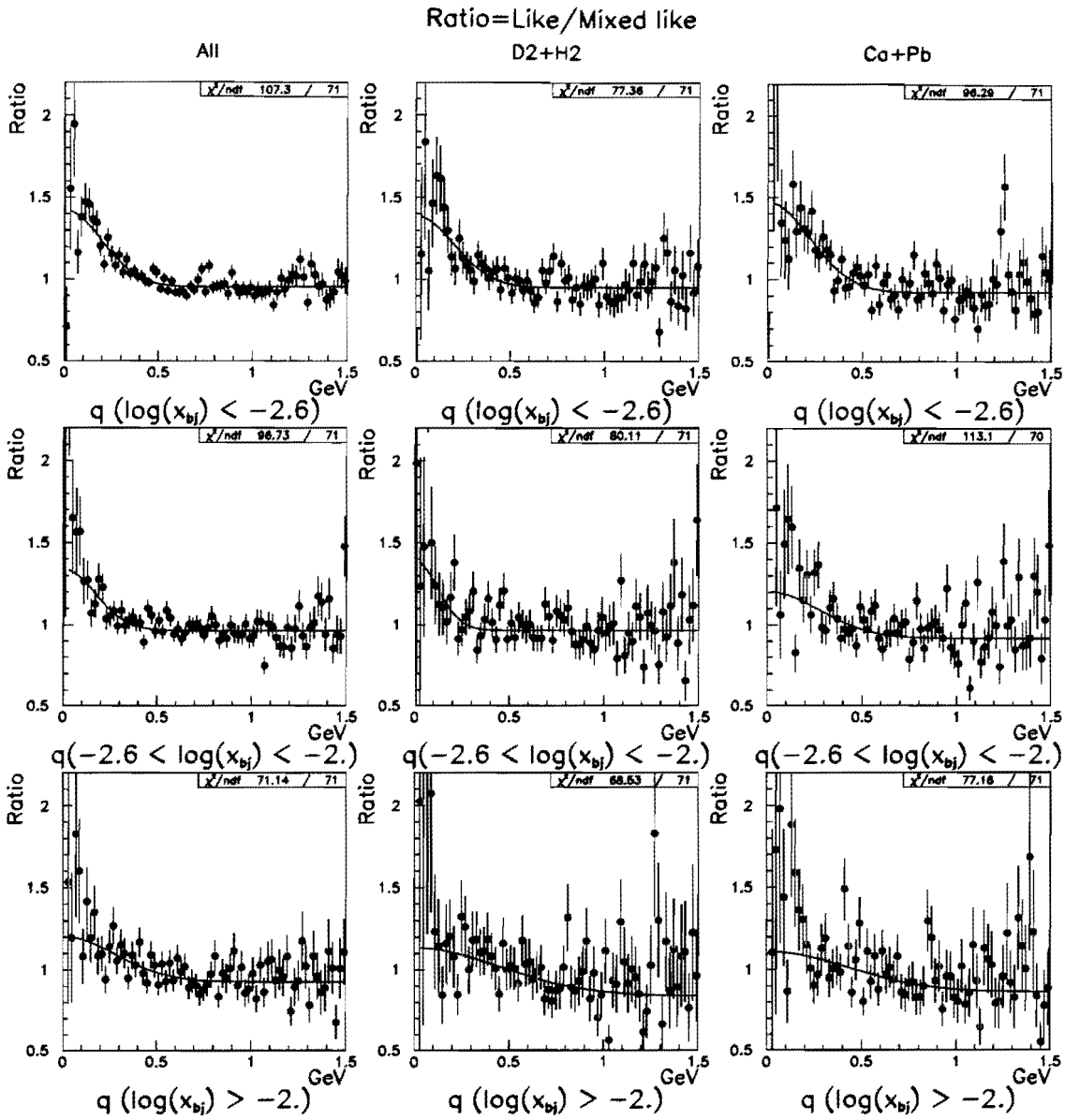

Figure 5.29: Ratios of like-sign pairs over mixed like-sign versus q in three different x_{bj} intervals for All(includes C), D2+H2, and Ca+Pb target.

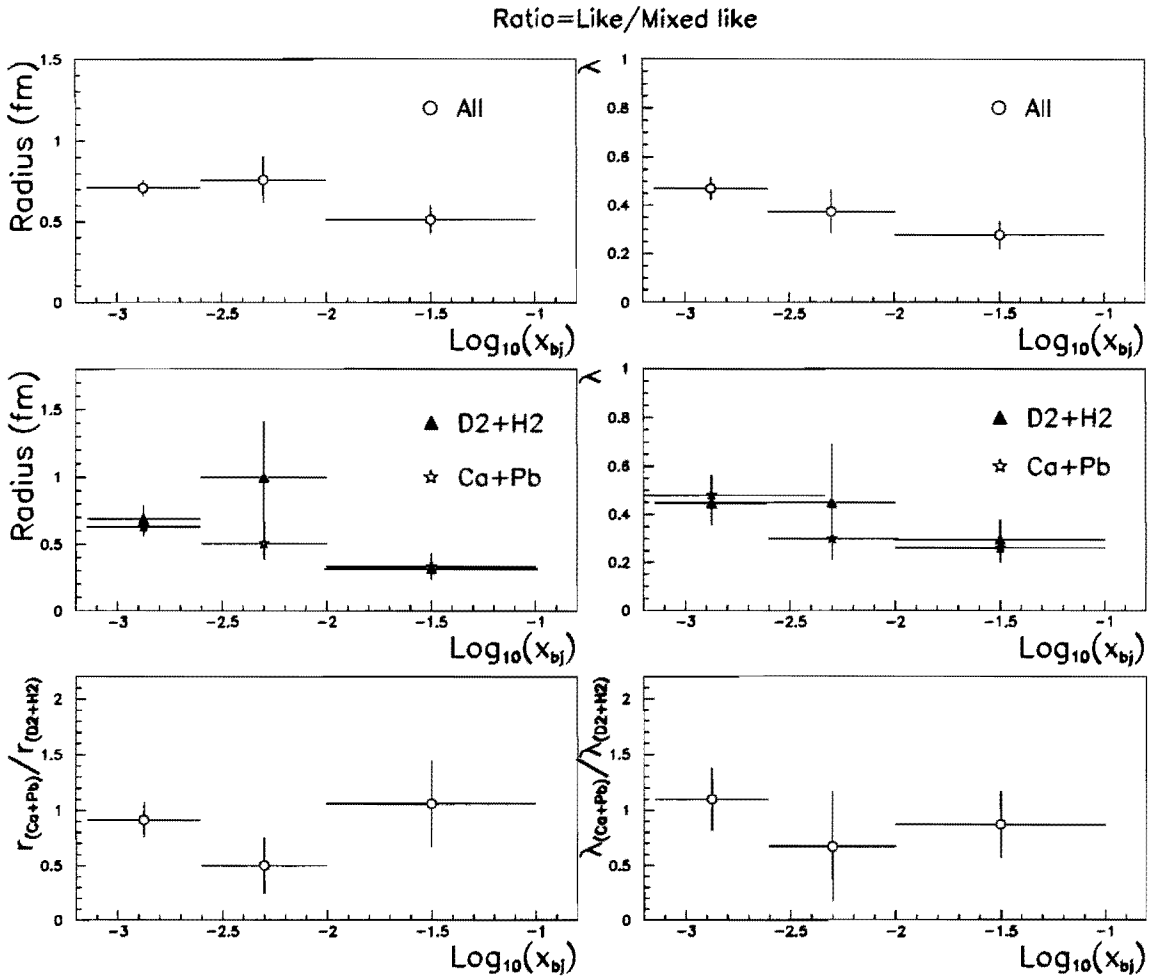

Figure 5.30: Plots for r_g and λ obtained from the fit of plots in previous figure for three x_{bj} intervals. The bottom two plots are the ratio of r_g and λ of "heavy" target over "light" target.

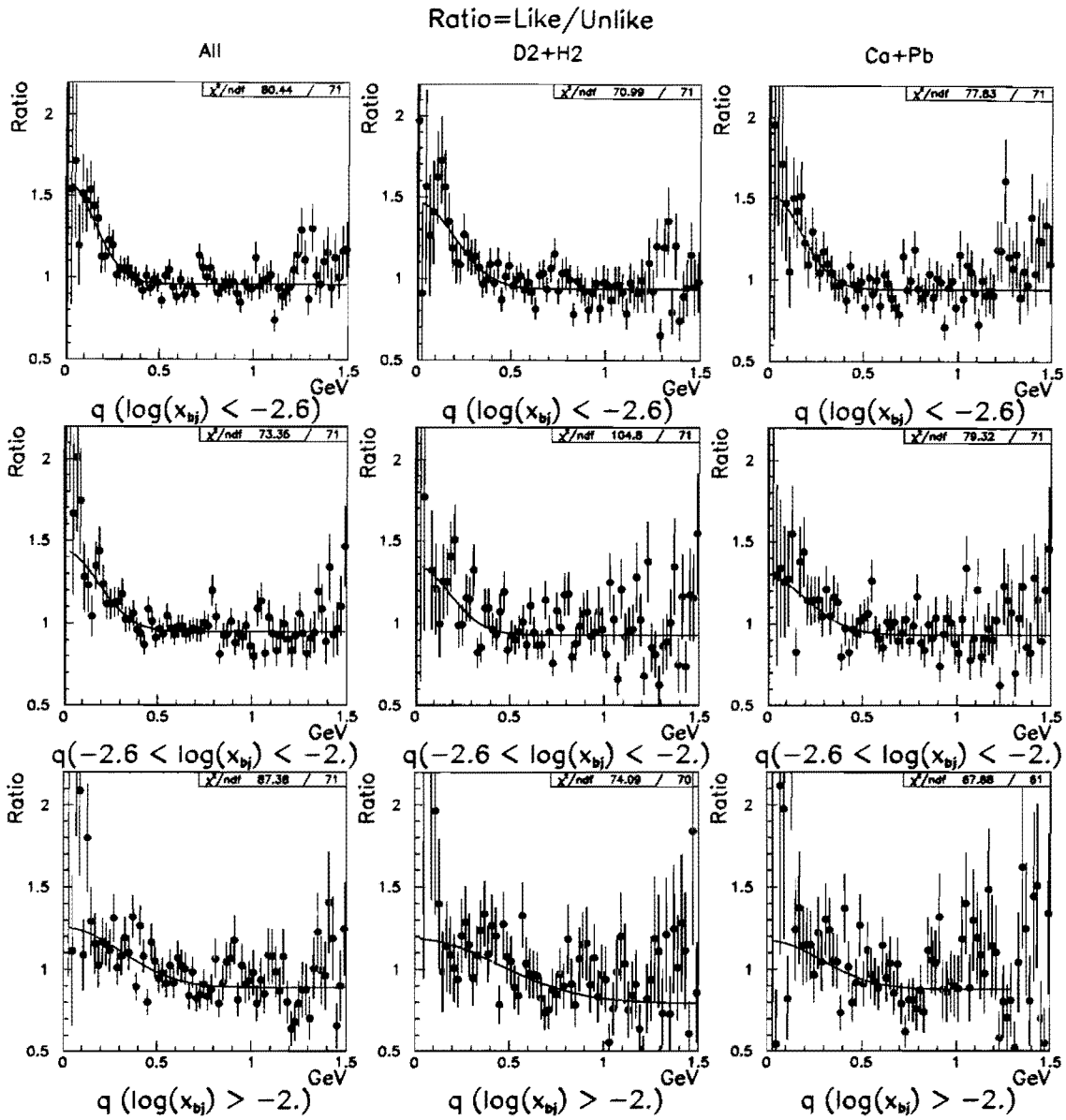

Figure 5.31: Ratios (like/unlike) as function of q in three different x_{bj} intervals for All, D2+H2, and Ca+Pb target.

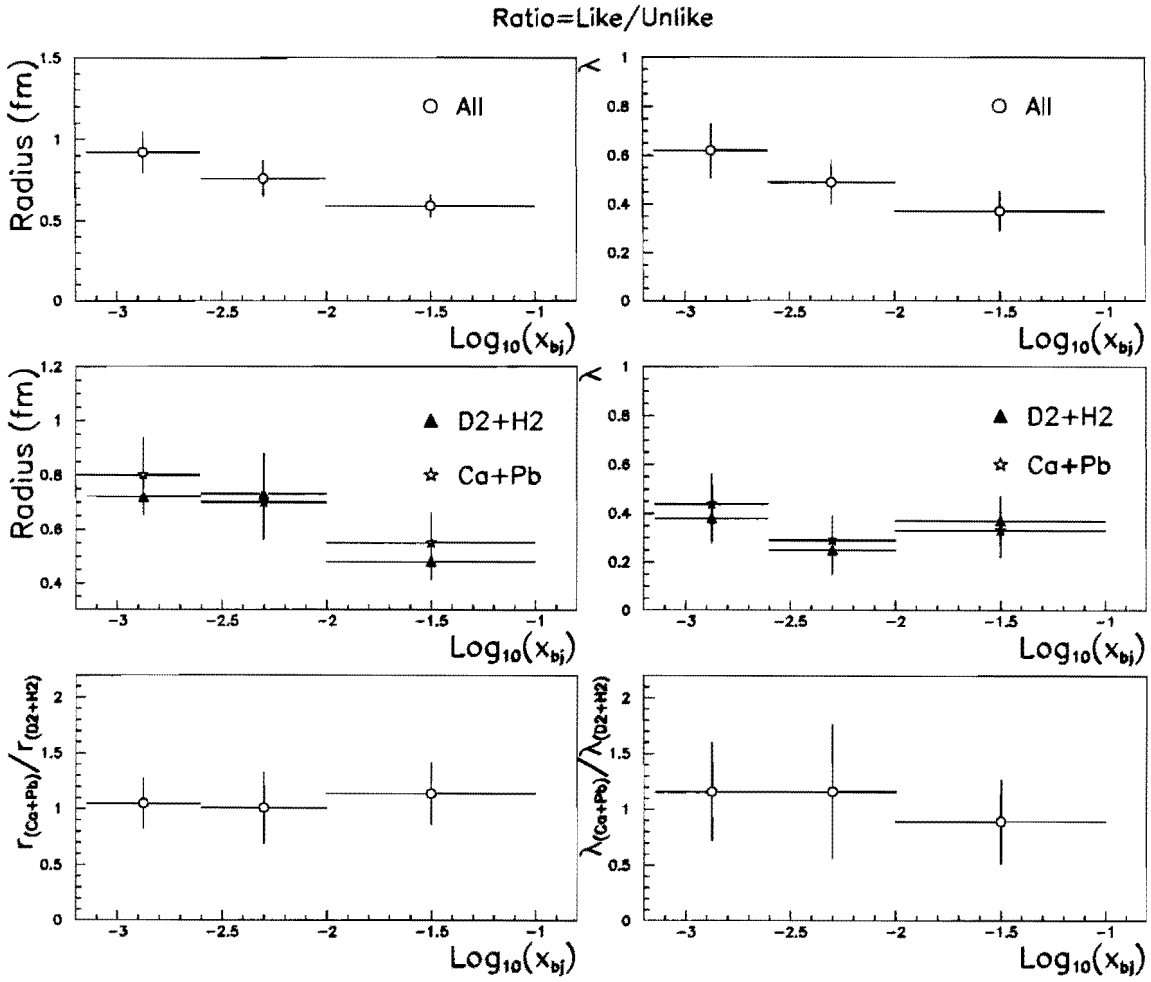

Figure 5.32: Plots for the r_g and λ obtained from the fit of previous plots in three x_{bj} intervals. Plots (e) and (f) are the ratios of heavy/light target for "radius(r_g)" and "λ".

5.6.2 The W^2 Dependence

For this study, the data were divided into three W^2 intervals 40-180 GeV^2, 180-300 GeV^2, and 300-800 GeV^2. In each W^2 bin the ratio as a function of q is plotted in Figure 5.33 along with the Goldhaber parametrization fit for "light" and "heavy" targets. The radius and chaoticity are calculated from the parameters of the fits. Figure 5.34 shows the radius and chaoticity for each W^2 bin for All, "light", and "heavy" targets. Also the ratios of radius and chaoticity for "heavy" over "light" targets are attached on the bottom of the Figure. No significant dependence on W^2 for either the radius or chaoticity is observed , also the ratio plots of both parameters for "heavy" over "light" target are consistent with 1.

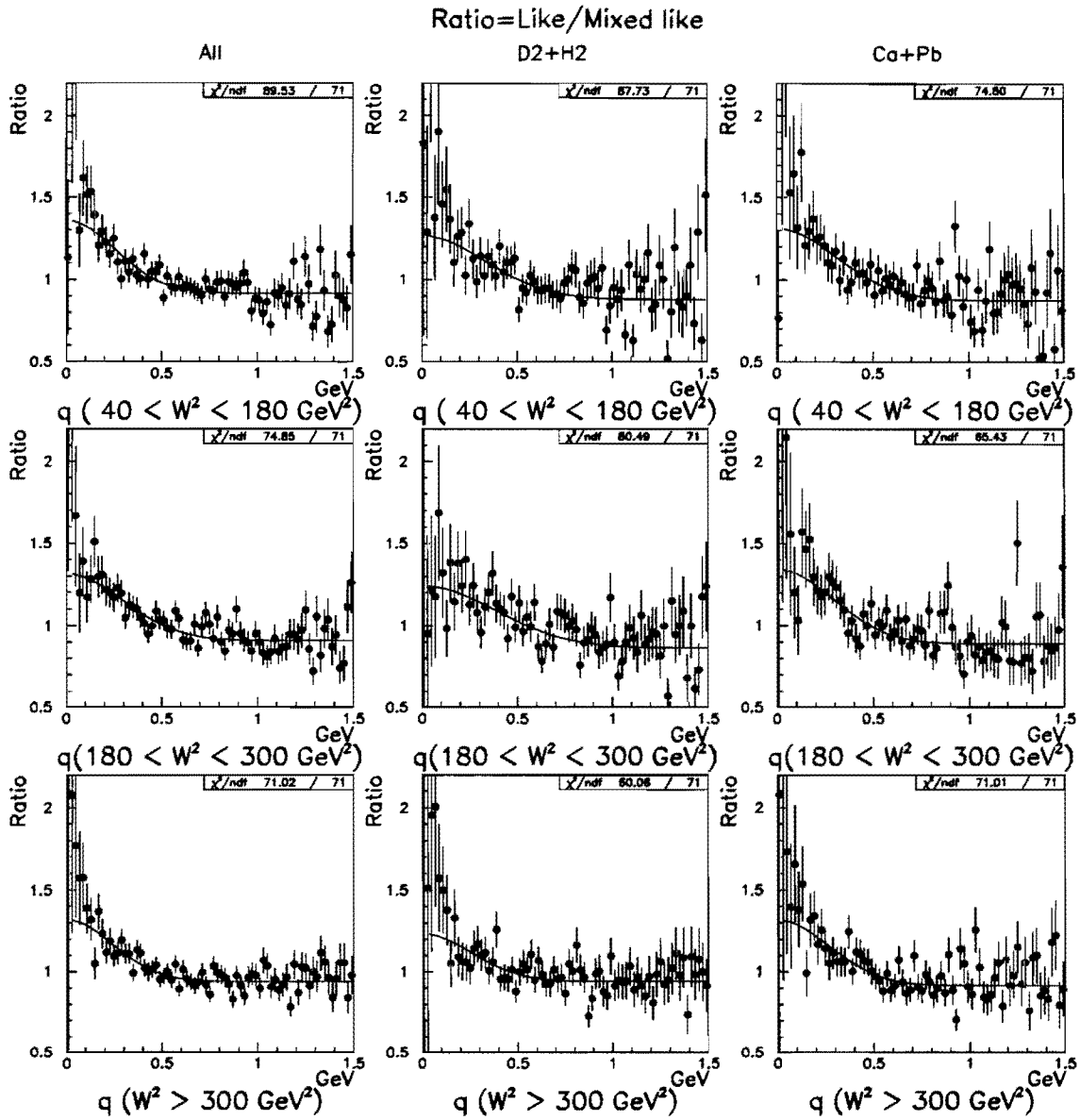

Figure 5.33: Ratios (like/mixed) as function of q in three different W^2 intervals for All(includes C), D2+H2, and Ca+Pb target.

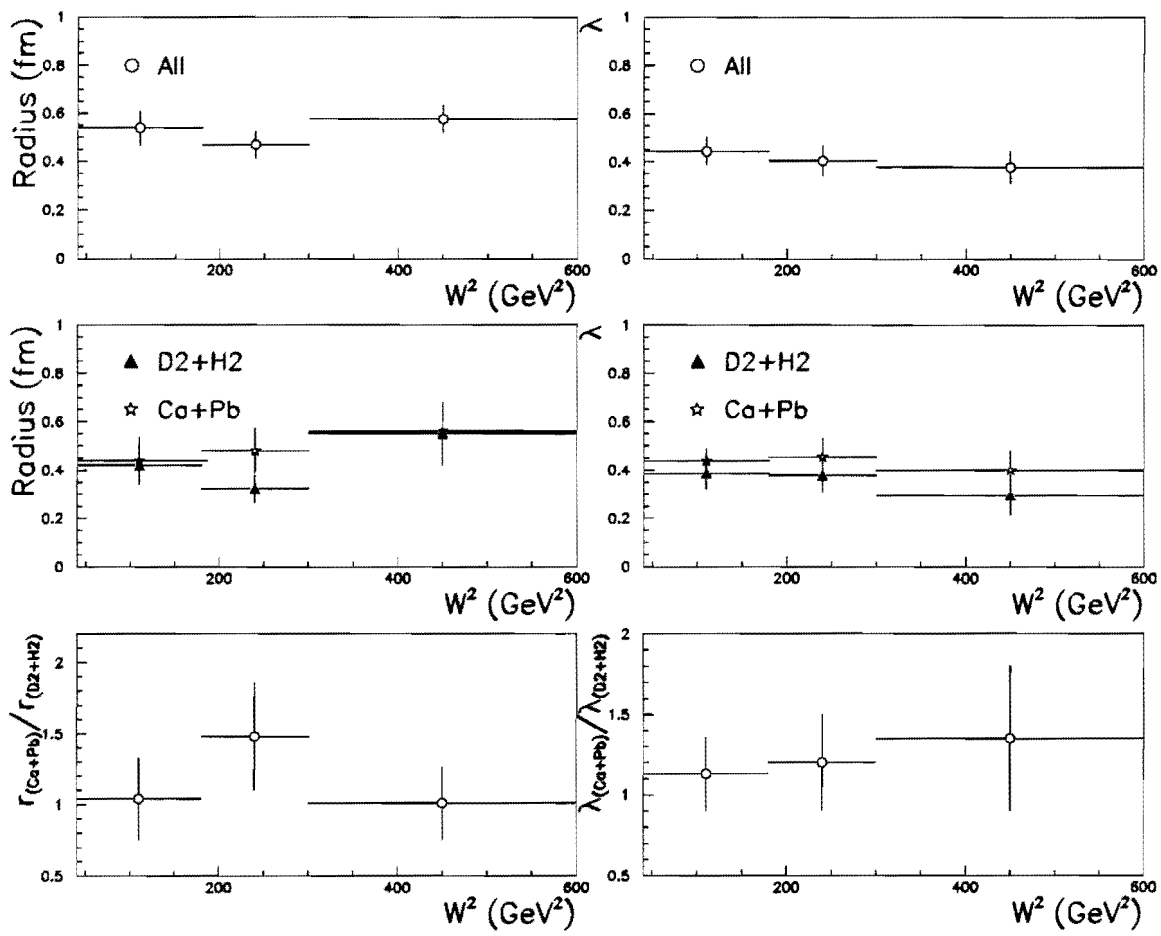

Figure 5.34: Radius and chaoticity "λ" obtained from the fit to the q plots in three W^2 intervals. Plots (e) and (f) are the ratios of heavy/light target for "radius(r_g)" and "λ".

5.6.3 The ν Dependence

In order to study the ν dependence of the nuclear effects in the radius and chaoticity, the data are divided in three ν intervals 40-80 GeV, 80-120 GeV and 120-200 GeV. Figure 5.35 and Figure 5.36 show the ratio versus q for each ν bin and the fitted parameters (r and λ) of each ν bin for both "light" and "heavy" targets. No obvious variation of radius or λ is seen as a function of ν. The ratio plot of the radius for nuclear target shows a an increase as ν increase. The effect should not be ignored but is also consistent with 1 within error.

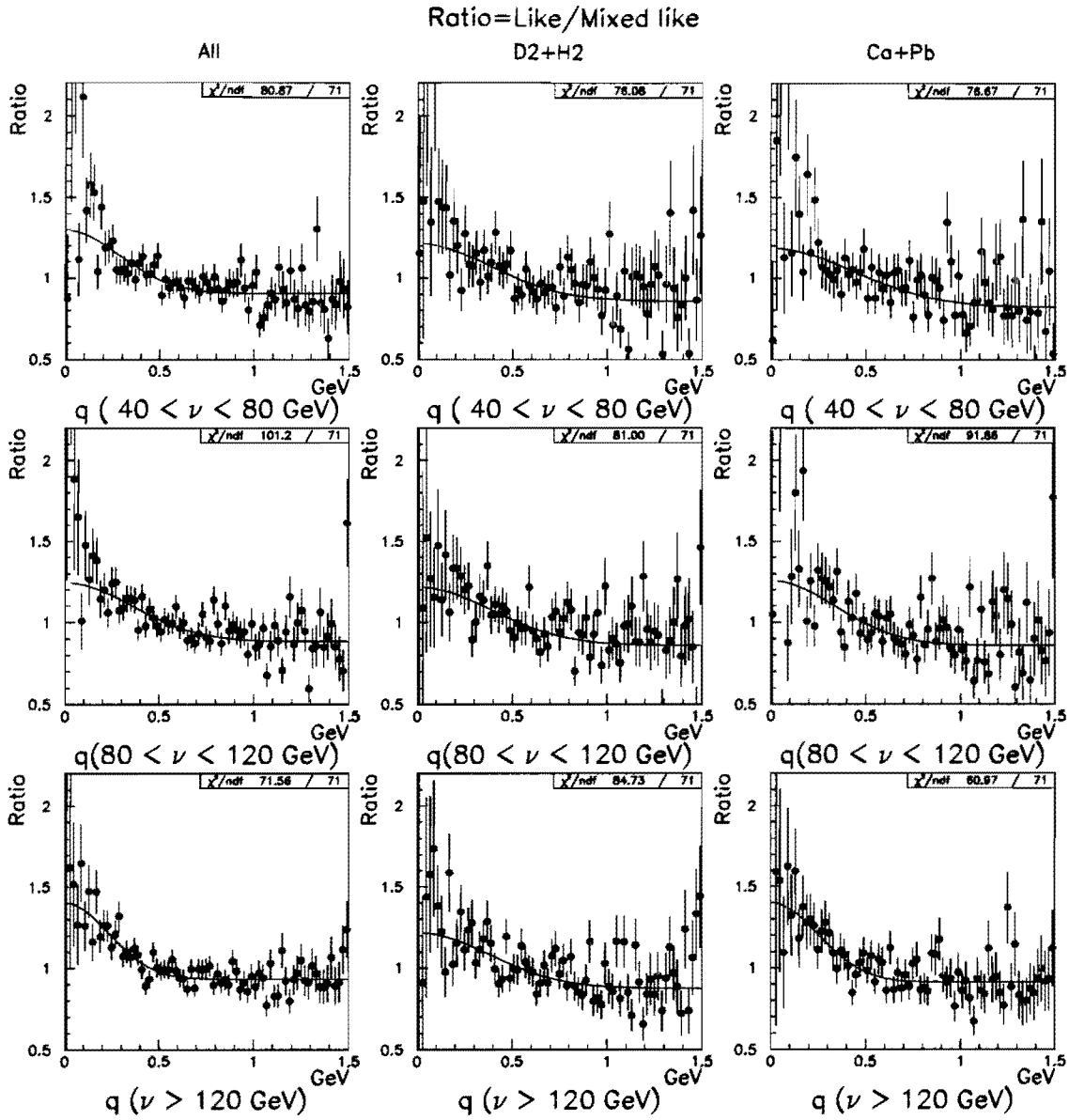

Figure 5.35: Ratios (like/mixed) as function of q in three different ν intervals for All(includes C), D2+H2, and Ca+Pb target.

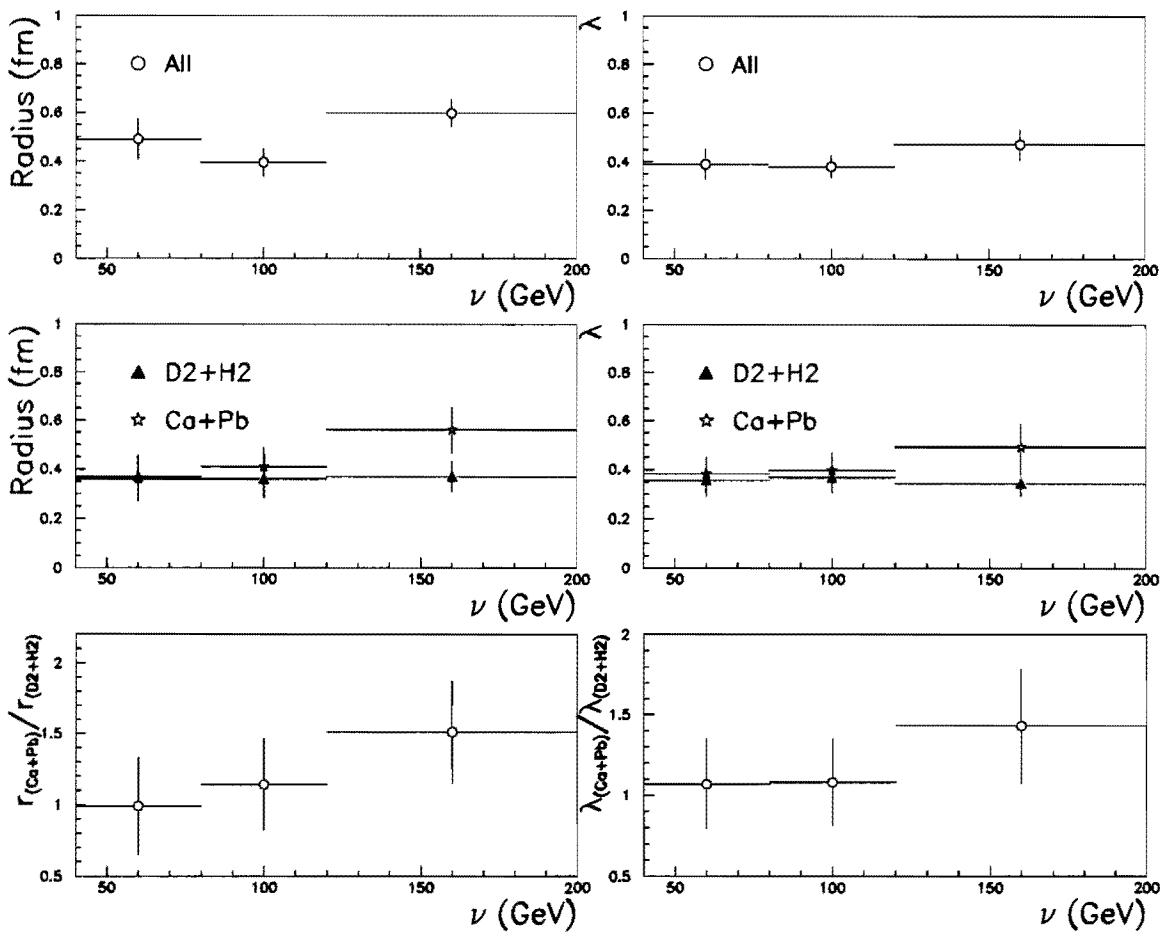

Figure 5.36: Radius and chaoticity "λ" obtained from the fit to the plots in three ν intervals. Plots (e) and (f) are the ratios of heavy/light target for "radius(r_g)" and "λ".

5.6.4 The Q^2 Dependence

To investigate further the bigger size at large ν for the nuclear target, the data have been divided in three Q^2 ranges $Q^2 \leq 0.5GeV^2$, $0.5 < Q^2 \leq 2GeV^2$, and $Q^2 > 2GeV^2$. Figure 5.37 and Figure 5.38 show the ratio plots for different Q^2 intervals and the fitted parameters, r_g and λ, of different Q^2 intervals for both targets . A noticeable decrease of the radius when Q^2 increases has been observed. The ν dependence plot does not show this decrease but it does appear in the x_{bj} dependence plot. No obvious nuclear effect on the radius and chaoticity for Q^2 dependence has been observed.

Figure 5.39 and 5.40 plot the dependence of source size(r_g) on the kinematics variables (x_{bj}, W^2, ν, and Q^2) for this study and results from other lepton-nucleon experiments[17].

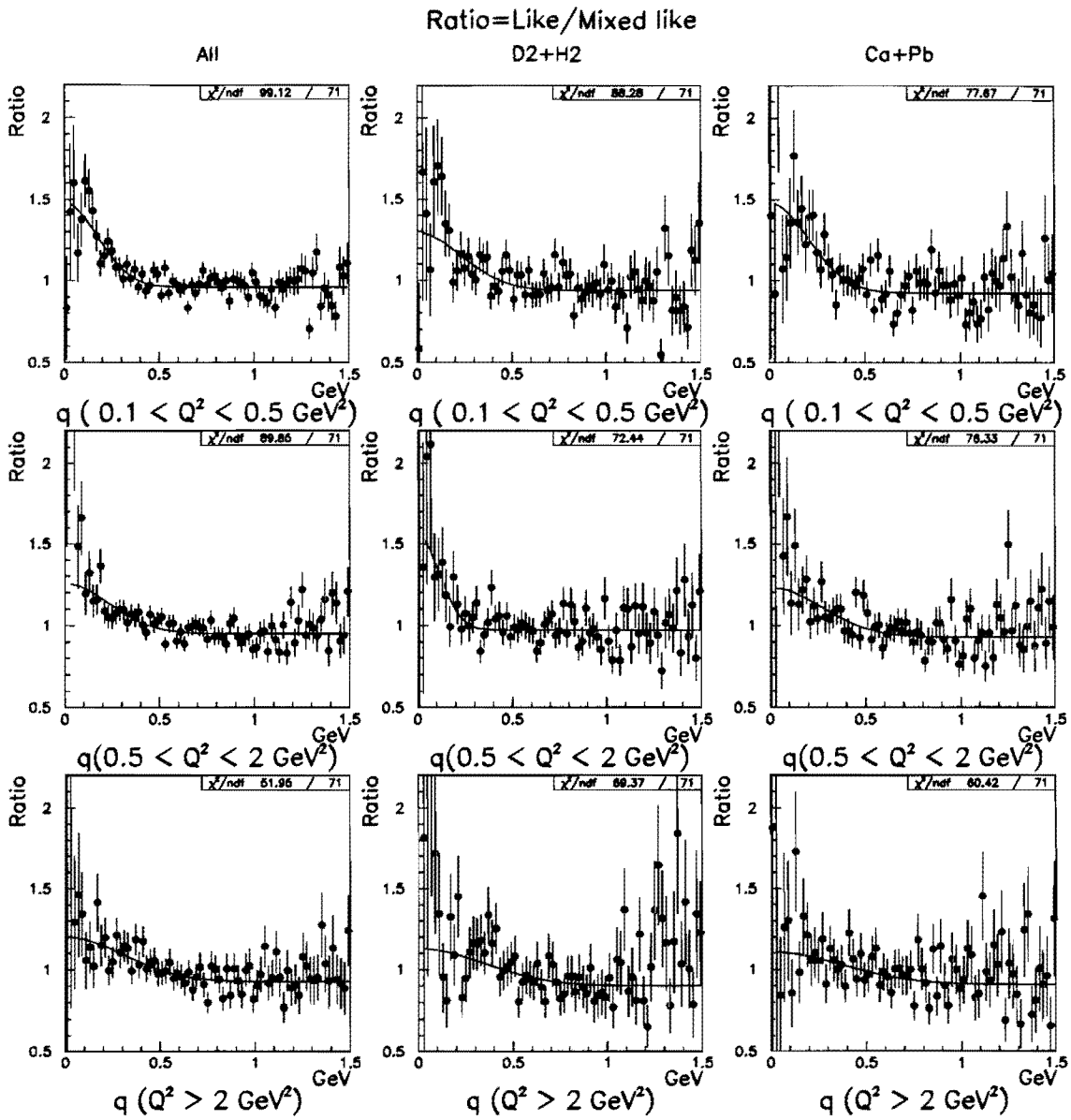

Figure 5.37: Ratios (like/mixed like) as function of q in three different Q^2 intervals for All(includes C), D2+H2, and Ca+Pb target.

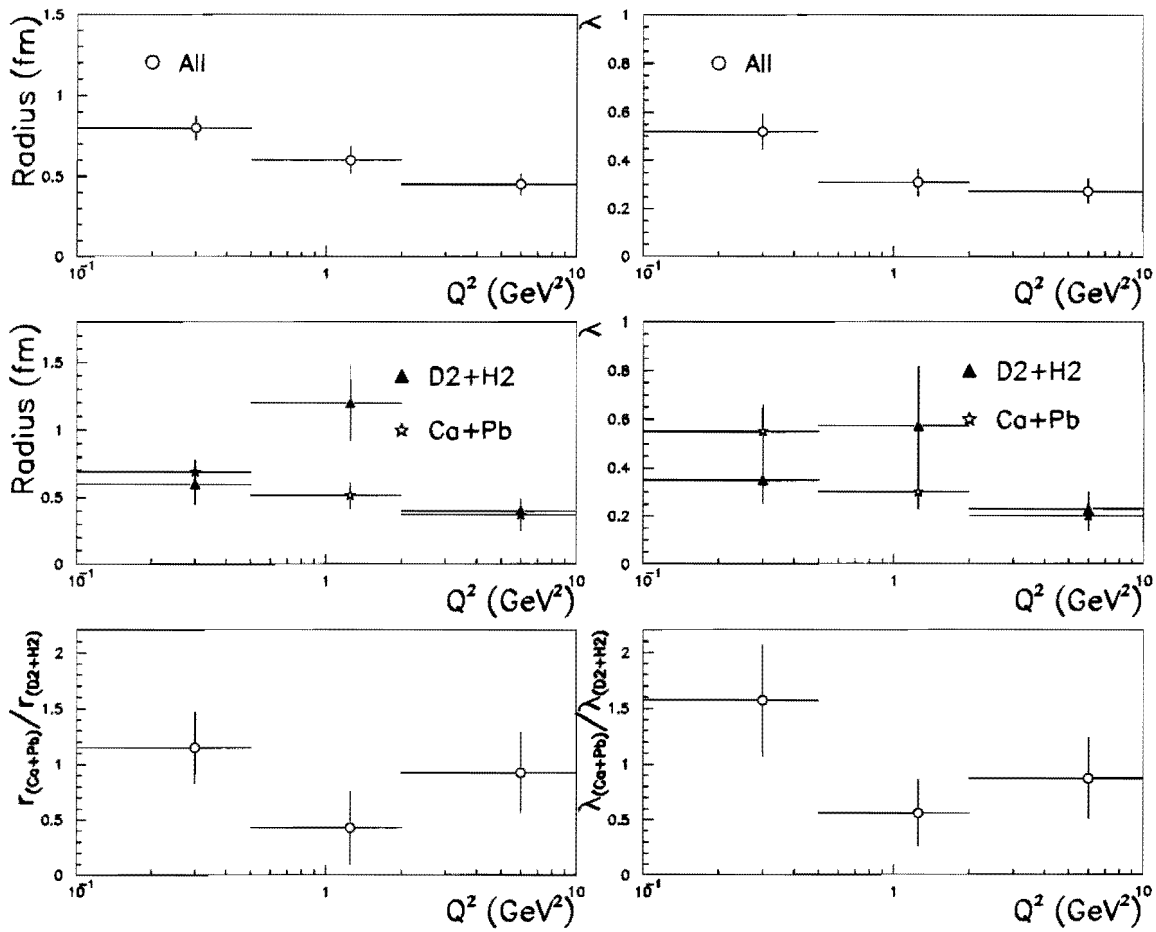

Figure 5.38: "Radius" and chaoticity "λ" obtained from the fit to the plots in Q^2 intervals. Plots (e) and (f) are the ratios of heavy/light target for "radius(r_g)" and "λ".

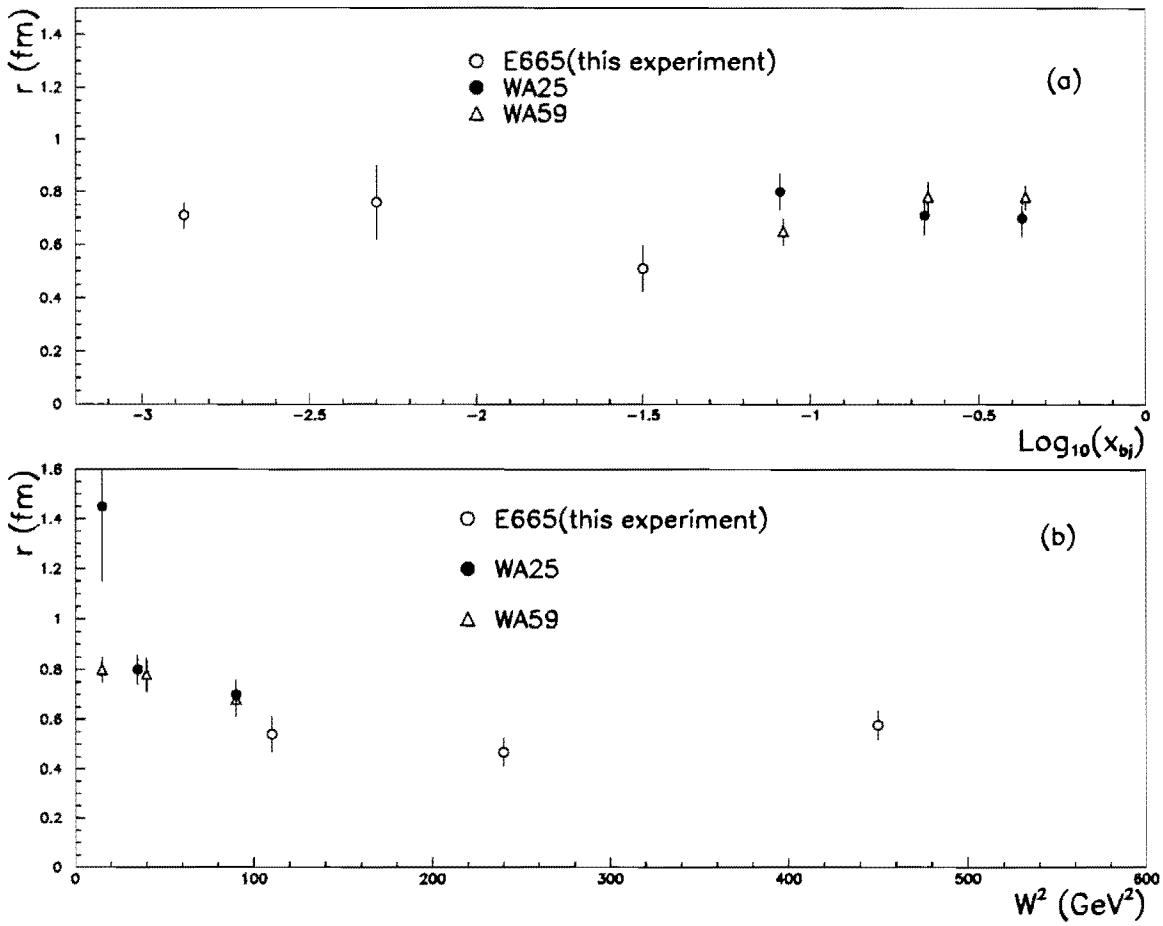

Figure 5.39: Radius(r_g) as a function of x_{bj} (a) and W^2 (b) for this analysis and other lepton-nucleon experiments.

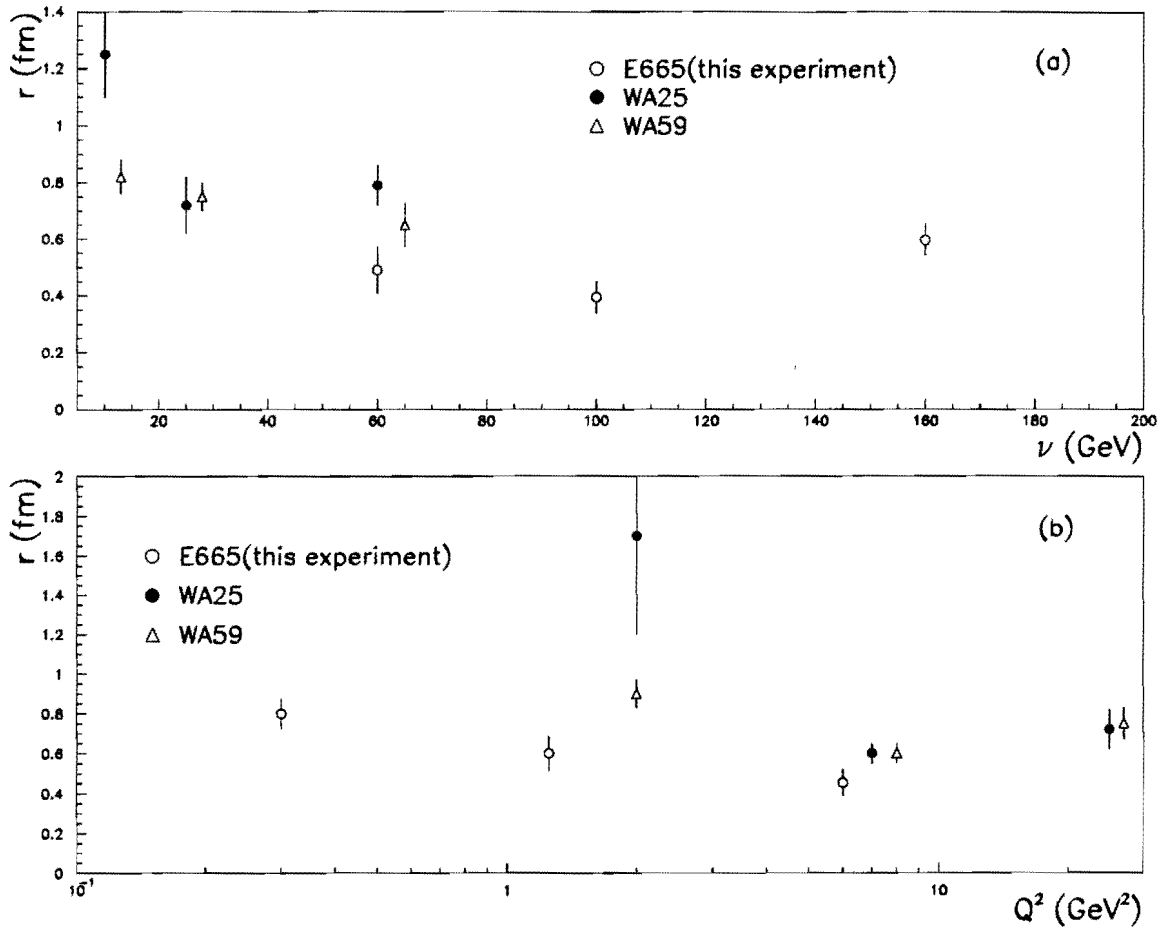

Figure 5.40: Radius(r_g) as a function of ν (a) and Q^2 (b) for this analysis and other lepton-nucleon experiments.

5.7 Conclusion

The Bose-Einstein correlations between two like-sign charged pions have been observed in 465 GeV μ-nucleon and μ-nucleus deep inelastic scattering. Two reference methods, the "mixed" and the "unlike", have been studied and used for the analysis. The consistency of the references used in this analysis, the "mixed like", the "mixed unlike" and the "unlike" charge pairs, are studied. The results of this study show the radius of pion emission source is independent on the reference ssample.

The radius of pion emission source region (r_g) extracted from Goldhaber parametrization fit (single Gaussian) were 0.63 $\pm$ 0.04 fm, 0.57 $\pm$ 0.03 fm and 0.62 $\pm$ 0.04 fm obtained by using "mixed-like", "mixed-unlike", and "unlike" (excluding all resonance decays) as reference samples respectively. A double source size distribution has been observed with a smaller first source size ("wide enhancement") of 0.51 $\pm$ 0.06 $\pm$ 0.04 fm and the bigger second source size ("narrow enhancement") of 1.53 $\pm$ 0.39 $\pm$ 0.28 fm. The first error is the statistical error and the second error is the systematic error estimated from the differences between the results of the two reference methods("mixed" and "unlike").

The fit of the two-dimensional Kopylov-Podgoretskii parametrization in terms of q_t and q_0, yielded r_k = 1.8 $\pm$ 0.72 fm and for the pion source lifetime τ= 0.75 $\pm$ 0.18 fm which are consistent with other experimental results [17, 65]. The radius extracted from Kopylov-Podgoretskii fit (r_k) is approximately twice as big as r_g from the Goldhaber fit, as expected. From the E665 experimental results, the two-dimensional Goldhaber parametrization, $R(q_v^2, q_0^2)$, gives a better description of the data.

The A-dependence of Bose-Einstein correlation has been studied from four target materials, liquid(H2+D2), C, Ca, and Pb, by using both reference methods. No nuclear effects on the parameters of Bose-Einstein correlation , radius(r_g) and chaoticity(λ), have been observed. The transverse source size($r_\top$) in the photon-nucleon collision c.m.s. was found to be 1.75 $\pm$ 0.4 fm and the longitudinal source size(r_l) was 0.68 $\pm$ 0.05 fm respectively. An oblate shape

of the pion source distribution as viewed from the hadronic c.m.s. for this analysis was found. In addition, the source sizes (both in longitudinal and transverse directions) and the source shape have shown no dependence on the target atomic mass.

The dependence of Bose-Einstein parameters, r_g and λ, on event kinematical variables x_{bj}, W^2, ν, and Q^2 along with the nuclear effects of BE correlation on these variables were studied. A decrease in the source size r_g as x_{bj} increased when using unlike-sign charged pairs as reference sample was seen, and a smaller source size (r_g) in the region of $x_{bj} > 0.01$ for both reference methods was observed. A significant decrease of λ when x_{bj} increased was also observed. The results from $\nu(\bar{\nu})$ interactions with nucleons [17] have not seen any change in the source size in the $x_{bj} > 0.01$ region but there is no data for lower x_{bj} region. This analysis is the first measurement of BE correlation at the region of $x_{bj} < 0.01$ and is able to extend the measurement of parameters to lower x_{bj} values.

Similar decrease of r_g and λ when Q^2 increased was also observed but did not show any dependence on the variables ν and W^2. The dependence on kinematic variables was the same for all targets except a noticeable increasing of the radius for nuclear target as ν increase.

CITED LITERATURE

[1] Miller, G., Bloom, E. D., Buschhorn, G., Coward, D. H., Destaebler, H., Drees, J., Friedman, J. I., Hartmann, G., C., Jordan, C. L., Kendall, H., Mo, L. W., Taylor, R. E., and Verdier, R., "Inelastic electron-proton scattering at large momentum tranfers and the inelastic structure functions of the proton", Phys. Rev. D, 5(3): 528, 1972.

[2] Field, R. D., and Feynman, R. P., "Quark elastic scattering as a source of high-transerse-momentum mesons", Phys. Rev. D, 15(9): 2590, 1977.

[3] Bjorken, J. D, "Asymptotic Sum Rules at Infinite Momentum", Phys. Rev. 179: 1547, 1969.

[4] Hanbury-Brown R. and Twiss, R. Q., "The Question of Correlation Between Photons in Coherent Light Rays", Nature 178: 1046; 1447, 1956.

[5] Golbhaber, G., Golbhaber, S., Lee, W., and Pais, A., " Influence of Bose-Einstein Statistics on the Antiproton-Proton Annihilation Process", Phys. Rev. 120: 300, 1960. LBL Report, LBL-13291(1981).

[6] Deutschmann, M., Kostka, P., Nahnhauer, R., Bockmann, M., Cocconi, V.T., Morrison, D. R., Bartke, J., Coghen, T., Figiel, J., Stopa, P., Barnham, K. J., Pollock, B., Para, A., and Wroblewski, A. K., "A Study of Second-Order Interference for Pions Produced in Various Hadronic Interactions" Nucl. Phys. B204, 333, 1982.

[7] Gyulassi, M., Kauffmann, S. K., and Wilson, Lance W., "Pion Interference of Nuclear Collisions. I. Theory", Phys. Rev. C20: No. 3, 2267, 1979.

[8] Suzuki, M., Phys. Rev. D35: 3359, 1987.

[9] Bowler, M. G., Z. Phys. C Particles and fields 39: 81, 1988.

[10] Heinz, U., Lee, K. S., and Rhoades-Brown, M. J., Phys. Rev. Lett. 58: 2292, 1987.

[11] Heinz, U., Lee, K., and Schnedermann, E., Z. Phys.C48: 525, 1990.

[12] Bolz, J., Orink, U., Plumer, M., Schlei, B. R., and Weiner, R. M., "Interferometry of Pions and Kaons in High Energy Collisions", G. S. I. preprint GSI-92-74, 1992.

[13] Kopylov, G. T. and Podgoretskii, M. I., "Correlation of Identical Particles Emitted by Highly Excited Nuclei", Sov. J. Nucl. Phys. 15: 219, 1972.
Sov. J. Nucl. Phys. 18: 336, 1974.

[14] Akesson, T., Albrow, M. G., Almehed, S., Benary, O., Boggild, H., Botner, O., Breuker, H., Burkert, V., Carter, A., Carter, J., Cleland, W., Dagan, S., Dahl-Jensen, E., Dahl-Jensen, I., Damgaard, G., Fabjan, C., Goerlach, U., Hansen, K., Hedberg, V., Jarlskog, G., Kroeger, R., Kulka, K., Lissauter, D., Lorster, B., Markou, A., Mccubbin, N., Moller, R., Molzon, W., Nielsen, B., Olsen, L., Oren, Y., Stumer, I., Sullivan, M., Thompson, J., Vella, E., Williamson, J., Willis, W., and Zajc, W., "Evidence for a Directional Dependenc of Bose-Einstein Correlations at the CERN Intersecting Storage Rings", Z. Phys. C-Particles and Fields 36: 517, 1987.

[15] Bailly, J. L., Banerjee, S., Caso, C., Chiba, Y., Dibon, H., Epp, B., Ferrando, A., Fontanelli, F., Gemesy, T., Gurtu, A., Hamatsu, R., Hirose, T., Hrubec, J., Iga, Y., Ivanyshenkov, Yu., Khalatyan, N., Kistenev, E., Kitamura, S., Kubik, V., MacNaughton, J., Matsumoto, S., Mittra, I. S., Montanet, L., Neuhofer, G., Pinter, G., Porth, P., Rodrigo, T., Singh, J., Squarcia, S., Takahashi, K., Tikhonova, L. A., Trevisan, U., Yamagata, T., Zholobov, G., and Zotkin, S. A., "Rapidity Dependence of Multiplicity distributions in Proton-Nucleus Collisions at 360 GeV/c", Z. Phys. C- particles and Field 40: 215, 1988.

[16] Arneodo, M., Arvidson, A., Aubert, J.J., Badelek, B., Beaufays, J., Bee, C.P., Benchouk, C., Berghoff, G., Bird, I.G., Blum, D., Bohm, E., Bouard, de X., Brasse, F.W., Braun, H., Broll, C., Brown, S.C., Bruck, H., Calen, H., Chima, J.S., Ciborowski, J., Clifft, R., Coignet, G., Combley, F., Coughlan, J., d'Agostini, G., Dahlgren, S., Derado, I., Dreyer, T., Drees, J., Duren, M., Eckardt, V., Edwards, A.W., Edwards, M., Ernst, T., Eszes, G., Favier, J., Ferrero, M.I., Figiel, J., Flauger, W., Foster, J., Gabathuler, E., Gajewski, J., Gamet, R., Geddes, N., Grafstrom, P., Gustafsson, L., Haas, J., Hagberg, E., Hasert, F.J., Hayman, P., Heusse, P., Jaffre, M., Jacholkowska, A., Janata, F., Jansco, G., Johnson, A.S., Kabuss, E.M., Kellner, G., Kruger, A., Kruger, J., Kullander, S., Landgraf, U, Lanske, D., Loken, J., Long, K., Matthews, M., Maire, M., Malecki, P., Manz, A., Maselli, S., Mohr, W., Montanet, F., Montgomery, H.E. Nagy, E., Nassalski, J., Norton, P.R., Oakham, F.G., Osborne, A.M., Pascaud, C., Pawlik, B., Payre, P., Peroni, C., Peschel, H., Pessard, H., Pettingale, J., Pietrzyk, B., Poensgen, B., Potsch, M., Renton, P., Ribarics, P., Rith, K., Rondio, E., Sandacz, A., Scheer, M., Schlagbohmer, A., Schiemann, H., Schmitz, N., Schneegans, M., Scholz, M., Schouten, M., Schroder, T., Schultze, K., Sloan, T., Stier, H.E., Studt, M., Taylor, G.N., Thenard, J.M. Thompson, J.C., Torre, A. de la, Toth, J., Urban, L., Urban, L., Wallucks, W., Whalley, M., Wheeler, S., Williams, W.S.C., Wimpenny, S.J., Windmolders, R., Wolf, G., ,"The Bose-Einstein Correlation in Deep Inelastic ν p Interaction at 280 GeV", Z. Phys. C32: 1, 1986.

[17] Korotkov, V. A., Guy, J., Venus, W., Ammosov, V. V., Andryakov, A. D., Asratyan, A. E., Coghen, T., Erriquez, O., Gapienko, G. S., Gapienko, V. A., Jones, G. T., Kaftanov, V. S., Krutchinin, S. P., Kubantsev, M. A., Makhlueva, I. V., Marage, P., Morrison, D.R. O., Neveu, M., Sacton, J., Varvell, K. E., Willocq, S., Wittek, W., Zaetz, V. G., "Bose-Einstein Correlations in Neutrino and antineutrino Interactions with nucleons", Z. Phys. C60: 37, 1993.

[18] Neumeister, N., Gajdosik, T., Buschbeck, B., Dibon, H., Markytan, M., Bocquet, G., Norton, A., Karimaki, V., Kinnunen, R., Pimia, M., Tuominiemi, J., Albajar, C., Revol, J. P., Sphicas, P., Sumorok, K., Tan, C. H., Tether, S.," Higher Order Bose-Einstein Correlation in *ppbar* Collisions at $\sqrt{s}$=630 and 900 GeV", Phys. Lett. B275: 186, 1992.

[19] Aguilar-Benitez, M., Allison, W. W., Batalov, A. A., Castelli, E., Checchia, P., Colino, N., Contri, R., De Angelis, A., De Roeck, A., De Seriis, N., De Wolf, E., Duboc, J., Endler, A., Ermolov, P., Falciano, S., Fisyak, Y. V., Fontanelli, F., Ganguli, S., Gasparini, U., Gurtu, A., Hernandez, J., Holmgren, S., Hrubec, J., Iori, M., Johansson, K., Kageya, T., Kistenev, E., Kitamura, S., Mazzucato, M., Michalon, A., Montanet, L., Monge, R., Nguyen, H., Novak, H., Oliveira, L., Pilette, P., Poropat, P., Poppleton, A., Rohringer, H., Salicio, J., Saran, S. Sessa, M., Shabalina, E. K., Simonetto, F., Sotnikova, N., Stopchenko, V., Trevisan, U., Troncon, C., Vebeure, F., Yarba, J., Zumerle, G., " Bose-Einstein Correlation in pp Collisions at 400 GeV/c", CERN-PPE/91-102, June 1991.

[20] The LEBC-EHS (NA22) Collaboration, Agababyan, N. M., Ajinenko, I. V., Atayan, M. R., Bottcher, H., Botterweck, F., Charlet, M., Chliapnikov, P. V., DeWolf, E. A., Dziunikowska, K., Endler, A. M., Garutchava, Z. C., Gulkanyan, H. R., Hakobyan, R., Kisielewska, D., Kittel, W., Mehrabyan, S. S., Olkiewicz, K., Shabalina, E. K., Smirnova, L. N., Tikhonova, L. A., Tomaradze, A., and Verbeure, F., " Influence of Multiplicity and Kinematical Cuts on Bose-Einstein Correlation in π^+p-Interaction at 250 GeV/c", Nijmegen Preprint, HEN, 341, 1993.

[21] Alexopoulos, T., Allen, C., Anderson, E. W., Balamurali, V., Banerjee, S., Beery, P. D., Bhat, P., Bishop, J. M., Biswas, N. N., Bujak, A., Carmony, D. D., Carter, T., Choi, Y., Cole, P., DeBonte, R., DeCarlo, V., Erwin, A. R., Findeisen, C., Goshaw, A. T., Gutay, L. J., Hirsch, A. S., Hojvat, C., Jennings, J. R., Kenney, V. P., Lindsey, C. S., Loomis, C., LoSecco, J. M., McMahon, T., McManus, A. P., Morgan, N. K., Nelson, K., Oh, S. H., Porile, N. T., Reeves, D., Rimai, A., Robertson, W. R., Scharenberg, R. P., Stampke, S. R., Stringfellow, B. C., Thompson, M. A., Turkot, F., Walker, W. D., Wang, C. H., Warchol, J., Wesson, D. K., Zhan, Y. H.,"A Study of Source Size in $p\bar{p}$ Collisions at $\sqrt{s}$ =1.8 TeV Using Pion Interferometry",WISC-EX-92-327 March, 1993.

[22] Boal, D. H., Gelbke, C.K., and Jennings, B., "Intensity Interferometry in Subatomic Physics", Reviews of Modern Physics, Vol. 62: No.3, 553-602, 1990.

[23] Zajc, W. A.," Bose-Einstein Correlation, from Statistics to Dynamics, in Hadronic Multiparticle Production", World Scientific Press, P. Carrathers ed., 1988.

[24] The Mark II Callaboration., Juricic, I., Goldhaber, G., Gibal, G., Abrams, G., Amidei, D., Baden, A., Boyer, J., Butler, F., Carthers, W., Gold, M., Golding, L., Haggerty, J., Derrup, D., Kadyk, J. A., Levi, M., Nelson, M., Rowson, P. C., Schellman, H., Schmidke, W. B., Sheldon, P. D., Trilling, G., Wood, D., Barklow, T., Boyarski, A., Mreidenbach, M., Burchat, P., Burke, D., Cords, D., Dorfan, J., Feldman, G., Gladney, L., Hanson, G., Hayes, K., Hitlin, D., Hollebeek, R., Innes, W., Jaros, J., Karlen, D., Klein, S. R., Lankford, A., Larsen, R., LeClairs, B., Lockyer, N. S., Luth, V., Ong, R., Perl, M., Richter, B., Riles, K., Ross, M. C., Schindler, R., and Yelton, J., "Bose-Einstein Correclation in e^+e^- Collision", Phys. Rev. D39: 1, 1989.

[25] Acton, P.D., Alexander, G., Allison, J., Allport, P.P., Anderson, K.J., Arcelli, S., Armitage, J.C., Ashton, P., Astbury, A., Axen, D., Azuelos, G., Bahan, G.A., Baines, J.T.M., Ball, A.H., Banks, J., Banker, G.J., Barlow, R.J., Batley, J.R., Beaudoin, G. Beck, A., Becker, J., Behnke, T., Bell, K.W., Bella, G., Bethke, S., Biebel, O., Binder, U., Bloodworth, I.J., Bock, P., Boden, B., Bosch, H.M., Bougerolle, S., Brabson, B.B., Breuker, H., Brown, R.M., Brun, R., Buijs, A.,Burckhart, H.J., Capiluppi, P., Carnegie, R.K., Carter, A.A., Carter, J.R., Chang, C.Y., Charlton, D.G., Chrin, J.T.M., Clarke, P.E.L., Cohen, I., Collins, W.J., Conboy, J.E., Cooper, M., Couch, M., Coupland, M., Cuffiani, M., Dado, S., Dallavalle, G.M., De Jone, S., Debu, P., Del Pozo, L., Deninno, M.M., Dieckmann, A., Dittmar, M., Dixit, M.S., Duchovni, E., Duckeck, G., Duersoth, I.P., Dumas, D.J.P., Eckerlin, G., Elcombe, P.A., Estabrooks, P.G., Etzion, E., Fabbri, F., Fincke-Keeler, M., Fischer, H.M., Fong, D.G., Fukunaga, C., Gaidot, A., Ganel, O., Gary, J.W., Gascon, J., McGowan, R.F., Geddes, N.I., Geich-Gimbel, C., Gensler, S.W., Gentit, F.X., Giacomelli, G., Gibson, V., Gibson, W.R., Gillies, J.D., Goldberg, J., Goodrick, M.J., Gorn, W., Grandi, C., Grant, F.C., Gross, E., Hagemann, J., Hanson, G.G., Hansroul, M., Hargrove, C.K., Harrison, P.F., Hart, J., Hattersley, P.M., Hauschild, M., Hawkes, C.M., Herflin, E., Hemingway, R.J., Heuer, R.D., Hill, J.C., Hillier, S.J., Hinshaw, D.A., Ho, C., Hobbs, J.D., Hobson, P.R., Hochman, D., Holl, B., Homer, R.J., Hou, S.R., Howarth, C.P., Hughes-Jones, R.E., Humbert, R., Igo-Kemenes, P., Ihssen, H., Imrie, D.C., Janissen, L., Jawahery, A., Jeffreys, P.W., Jeremie, H., Jimack, M., Jobes, M., Jones, R.W.L., Jovanovic, P., Karlen, D., Kawagoe, K., Kawamoto, T., Keeler, R.K., Kellogg R.G., Kennedy, B.W., Kleinwort, C., Klem, D.E., Kobayashi, T., Kokott, T.P., Komamiya, S., Kopke, L., Kowalewski, R., Kreutzmann, H., Krogh, J. Von, Kroll, J., Kuwano, M., Kyberd, P., Lafferty, G.D., Lamarche, F., Larson, W.J., Layter, J, G., Le Du, P., Leblanc, P., Lee, A.M., Lehto, M.H., Lellouch, D., Lennert, P., Leroy, V., Lessard, L., Letts, J., Levegrun, S., Levinson, L., Lloyd, S.L., Loebinger, F.K., Lorah, J.M., Lorazo, B., Losty, M.J., Lou, X.C., Ludwig, J., Mannelli, M., Marcellini, S., Maringer, G., Martin, A.J., Martin, J.P., Mashimo, T., Mattig, P., Maur, U., Mckenna, J., McMahon, T.J., McNutt, J.R., Meijers, F., Menszner, D., Merritt, F.S., Mes, H., Michelini, A., Middleton R.P., Mikenberg, G., Mildenberger, J., Miller, D.J., Milstene, C., Mir, R., Mohr, W., Moisan, C., Montanari, A., Mori, T., Moss, M.W., Mouthuy, T., Nellen, B., Nguyen, H.H., Nozaki, M., O'Neale, S.W., O'Neill, B.P., Oakham, F.G., Odorici, F., Ogg, M., Ogren, H.O., Oh, H., Oram, C.J., Oreglia, M.J., Orito,S., Pansart,J.P., Panzer-Steindel, B., Paschievici, P., Patrick, G.N., Pawley, S.J., Pfister, P., Pilcher, J.E., Pinfokd, J.L., Plane, D.E., Poffenberger, P., Poli, B. Pouladdej, A., Prebys, E., Pritchard, T.W.,Przysiezniak, H., Quast, G., Redmond, M.W., Rees, D.L., Riles, K., Robins, S.A., Robinson, D., rollnik, A., Roney, J.M., Ros, E., Rossberg, S., Rossi, A.M., Routenburg, P., Runge, K., Runolfsson, O., rust, D.R., Sanghera, S., Sasaki, M., Schaile, A.D., Schaile, O., Schappert, W., Scharff-Hansen, P., Schenk, P., Schmitt, H. von der, Schreiber, S., Schwarz, J., Scott, W.G., Settles, M., Shen, B.C., Sherwood, P., Shypit, R., Simon, A., Singh, P., Siroli, G.P., Skuja, A., Smith, A.M., Smith, T.J., Snow, G.A., Sobie, R., Springer, R.W., Sproston, M., Stephens, K.,Stier, H.E., Strohmer, R., Strom, D., Takeda, H., Takeshita, T., Taras, P., Tarem, S., Teixeira-Dias, P., Thackray, N.J., Transtromer, G., Tsukamoto, T., Turner, M.F., Tysarczyk-Niemeyer, G., Van den plas, D., Van Kooten, R., VanDalen, G.J., Vasseur, G., Virtue, C.J., Wagner, A., wahl, C., Walker, J.P., Ward, C.P., Ward, D.R., Watkins,P.M., Watson, A.T., Watson N.K., Weber, M., Weber, P., Weisz, S., Wells, P.S., Wermes, N., Weymann, M., Whalley, M.A., Wilson, G.W., Wilson, J.A., Wingerter, I., Winterer, V-H., Wood, N.C., Wotton, S., Wyatt, T.R., Yaari, R., Yang, Y., Yekutieli, G., Zacharov, I., Zeuner, W., Zorn, G.T.," A Study of Bose-Einstein Correlation in e^+e^- Annihilations at LEP", CERN-PPE/91-110, July, 1991.

[26] The ALEPH Collaboration., Decamp, D., Deschizeaux, B., Goy, C., Lees, J-P., Minard, M., Alemany, R., Crespo, J., Delfino, M., Fernandes, E., Gaitan, V., Garrido, Ll., Mir, Ll., Pacheco, A., Catanesi, D., Palma, M., Farilla, A., Iaselli, G., Maggi, G., Maggi, M., Natali, S., Nuzzo, S., Ranieri, A., Raso, G., Romano, F., Ruggieri, F., Selvaggi. G., Silvestri, L., Tempesta, P., Zito, G., Gao, Y., Hu, H., Huang, X., Lin, J., Lou, J., Qiao, C., Ruan, T., Wang, T., Xie, Y., Xu, D., Xu, R., Zhang, J., Zhao, W., Atwood, W., Bird, F., Blucher, E., Bonvicini, G., Bossi, F., Burnett, T., Drevermann, H., Forty, R., Grab, C., Hagelberg, R., Haywood, S., Hilgard, J., Jost, B., Kasemann, M., Lacourt, A., Lancom, E., Lehrausm, I., Lohse, T., Lusiani, A., Marchioro, A., Martinez, M., Mato, P., Menary, S., Meyer, T., Minten, A., Miotto, A., Miquel, R., Moser, H., Nash, J., Palazzi, P., Ranjard, F., Redlinger, G., Rolandi, L., Roth, A., Rothberg, J., Saich, M., Schlatter, D., Schmelling, M., Tejessy, W., Wachsmuth, H., Wasserbaech, S., Wiedenmann, W., Witzeling, W., Wotschack, J., Ajalouni, Z., Badaud, F., Bardadin-Otwinowska, M., Bencheick, A., Fellous, R., Falvard, A., Gay, P., Guicheney, C., Henrard, P., Jousset, J., Michel, B., Pallin, D., Perret, P., Pietrzyk, B., Proriol, J., Prulhiere F., Stimple, G., Hansen, J., Hansen, J. R., Hansen, P., Mollerud, R., Nilsson, B., Efthmiopoulos, I., Simopoulu, E., Vayaki, A., Badier, J., Blondel, A., Bonneaud, G., Fouque, G., Gamess, A., Harvey, J., Orteu, S., Rosowsky, A., Rouge, A., Rumpf, M., Tanaka, R., Videau, H., Candlin, D., Veitch, E., Moneta, L., Parrini, G., Corden, M., Ikeda, M., Lannutti, J., Mermikides, M., Sawyer, L., Antonelli, A., Baldini, R., Bencivenni, G., Bologna, G., Campana, P., Capon, G., Cerutti, F., Chiarella, V., Felici, G., Laurelli, P., Mannocchi, G., Murtas, G., Murtas, F., Passlcqua, L., Picchi, P., Zografou, P., Altoon, B., Boyle, O., Colrain, P., Halley, A., Have, I., Lynch, J., Maitland, W., Morton, W., Raine, C., Scarr, J., Smith, K., Thompson, A., Turnbull, R., Braun, O., Geiges, R., Geweniger, C., Hanke, P., Hepp, V., Maumary, Y., Putser, A., Stahl, A., Wunsch, M., Belk, A., Binnie, D., Cameron, W., Cattaneo, M., Dornan, P., Dugeay, S., Greene, A., Hassaed, J., Lieske, N., Patton, S., Payne, D., Phillips, M., Sedgbeer, J., Taylor, G., Tomalin, I., Wright, A., Girtler, P., Kuhn, D., Rudolph, G., Bowdery, C., Finch, A., Foster, F., Hughes, G., Keemer, N., Nuttall, M., Patel, A., Sloan, T., Snow, S., Whelan, E., Raab, J., Renk, B., Roehn, S., Schmidt, H., Steeg, F., Walthex, S., Wolf, B., Aubert, J., Benchouk, C., Carr, J., Coyle, P., Etinne, F., Payre, P., Qian, Z., Tably, M., Adlung, S., Becker, H., Blum, W., Brown, D., Cowan, G., Dietl, H., Dydak, F., Jahn, A., Lange, E., Lauber, J., Luts, G., Manner, W., Pan, Y., Richter, R., Schroder, J., Schwars, A., Settles, R., Stiegler, U., Denis, R., Thomas, J., Wolf, G., Bertin, V., Callot, O., Chen, X., Cordier, A., Davier, M., Heusse, Ph., Janot, P., Kim, D., LEFRANCOIS, J., LUTS, A., SCchune, M., Veillet, J., Zhang, Z., Zomer, F., Carter, J., Green, M., March, P., Quasi, I., Strong, J., West, L., Wildish, T., Botterill, D., Clifft, R., Edgecock, T., Edwards, M., Fisher, S., Jones, T., Norton, P., Salmon, D., Thompson, J., Colas, P., Locci, E., Loucatos, S., Peres, P., Perlas, J., Perrier, F., Rander, J., Roussarie, A., Schuller, J., Vallage, B., Ashman, J., Booth, C., Buttar, C., Carney, R., Cartwright, S., Combley, F., Dorgru, M., Martin, J., Parker, D., Thompson, L., Barberio, E., Brandt, S., Grupen, C., Mirabito, L., Seywerd, H., Ganis, G., Giannini, G., Gobbo, B., Ragusa, F., Bellantoni, L., Cinabro, D., Conway, J., Cowen, D., Feng, Z., Ferguson, D., Gao, Y., Grahl, J., Harton, J., Jared, R., Johnson, R., LeClaire, B., Lishka, C., Pan, Y., Pater, J., Saadi, Y., Sharma, V., Shi, Z., Tang, Y., Walsh, A., Wear, J., Weber, F., Whitney, M., Wu, S., Zobernig G., " A Study of Bose-Einstein Correlations in e^+e^- Annihilation at 91 GeV", Z. Phys. C - Particles and Fields 54: 75, 1992.

[27] The TASSO Callaboration., Althoff, M., Braunschweig, W., Kirschfink, F., Martyn, H., Rosskamp, P., Eisrnmann, J., Fischer, H., Hartmann, H., Jocksch, A., Knop, G., Kolanoski, H., Kuck, H., Mertens, V., Wedemeyer, R., Foster, B., Wood, A., Bernardi, E., Eskreys, A., Fohrmann, R., Gather, K., Hultschig, H., Joes, P., Klima, B., Kotz, U., Kowalski, H., Ladage, A., Lohr, B., Luke, D., Mattig, P., Notz, D., Revel, D., Trines, D., Wolf, G., Zeuner, W., Hilger, E., Kracht, T., Krasemann, H., Poelz, G., Posnecker, K., Binnie, D., Dornan, P., Garbutt, D., Jenkins, C., Jones, W., Sedgbeer, J., Thomas, J., Su, D., Wan Abdullah, W., Barreiro, F., Labarga, L., Ros, E., Bowler, M., Bull, P., Cashmore, R., Dauncey, P., Hawkes, C., Heath, G., Mellor, D., Ratoff, P., Lloyd, S., Forden, D., Hart, J., Hasell, D., Saxon, D., Brandt, S., Dittmar, M., Holder, M., Kreutz, G., Neumann, B., Eisenberg, Y., Montag, A., Mikenberg, G., Mir, R., Ronat, E., Yekutieli, G., Baranko, G., Caldwell, A., Cherney, M., Izen, J., Mermikides, M., Ritz, S., Storm, D., Takashima, M., Wicklund, E., Wu., S. L., Zobernig, G., " Bose-Einstein Correlations Observed in e^+e^- Annihilation at a Centre of Mass Energy of 34 GeV", Z. Phys. C - Particles and Fields 30: 355-369, 1986.

[28] Adams,M.R., Aid, S., Anthony, P.L., Baker, M.D., Bartlett, J., Bhatti, A.A., Braun, H.M, Busza, W., Carroll T.J., Conrad, J.M., Coutrakon, G., Davisson, R., Derado, I., Dhawan, S.K., Dougherty, W., Dreyer, T., Dziunikowska, K., Eckardt, V., Ecker, U., Erdmann, M., Eskreys, A., Fang, G., Figiel, J., Gebauer, H.J., Geesaman, D.F., Gilman, R., Green, M.C., Hass, J., Halliwell, C., Hanlon, J., Hantke, D., Hughes, V.W., Jackson, H.E., Jaffe, D.E., Jansco, G., Jansen, D.M, Kaufman, S., Kennedy, R.D, Kirk, T., Kobrak, H.G.E, Krzywdzinski, S., Kunori, S., Lord, J.J., Lubatti, H.J., McLeod, D., Magill, S., Malecki, P., Manz, A., Melanson, H., Micheal, D., Mohr, W., Montgomery, H.E., Morfin, J.G., Nickerson, R.B., O'Day, S., Olkiewicz, K., Osborne, L., Papavassiliou, V., Pawlik, B, Pipkin, F.M., Ramberg, E.J., Roser, A., Ryan, J.J., Salgado, C., Salvarani., A., Schellman, H., Schmitt, M., Schmitz, N., Schuler, K.P., Seyerlien, H.J, Skuja., A., Snow, G.A., Soldner-Rembold, S., Stienberg, P.H., Stier, H.E., Stopa, P., Swanson, R.A., Talaga, R., Tentindo-Repond, S., Trost, H.J., Venkataramania, H., Vidal, M., Wilhelm, M., Wilkes, J., Wilson, R., Wittek, W., Wolbers, S.A. and Zhao, T., " An Investigation of Bose-Einstein Correlations in Muon-Nucleon Interactions at 490 GeV", Phys. Lett. B308; 418, 1993.

[29] De Marzo, C., De Palma, M., Distante, A., Favuzzi, C., Lavopa, P., Maggi, G., Posa, F., Ranieri, A., Selvaggi, G., Spinelli, P., Waldner, F., Eskreys, A., Eskreys, K., Kisielewski, D., Madeyski, B., Malecki, P., Olkiewicz, K., Pawlick, B., Stopa, P., Fry, J. R., Houlden, M., Moreton, A., Wong, S. L., Antic, M., Dengler, F., Derado, I., Eckardt, V., Fent, J., Freund, P., Gebauer, H. J., Kahl, T., Manz, A., Miller, K., polakos, P., Shiers,J., Vranic, D., Wolf, G., Crijns, F., Metzger, W. J., Pols, C., and Spuijbrock, T., Phys. Rev. D29: 363, 1984.

[30] Bayukov, Yu. D., Gavrilov, V. B., Degtyarenko, P., Zaitsev, Yu. M., Leksin, G. A., and Suchkov, D. A., "Correlations Between the Identical Pions Produced in $\pi - A$ Collisions at 3.7 GeV/c", Sov. J. Nucl. Phys. 33: 377, 1981.

[31] Ryan, J. J., "Particle Production in Deep Inelastic Muon Scattering", Ph.D. Thesis, Mass. Inst. of Tech., 1990.

[32] Michael, D. G., "A Study of Transverse Momentum and Jets Using Forward Hadron and Photons in Deep Inelastic Scattering at 490 GeV/c", Ph.D. Thesis, Harvard University, 1990.

[33] Fenker, H., " A standard Beam PWC for Fermilab", Technical Report, TM-1179, 2557, Fermilab, 1983.

[34] Adams,M.R., Aid, S., Anthony, P.L., Baker, M.D., Bartlett, J., Bhatti, A.A., Braun, H.M, Busza, W., Carroll T.J., Conrad, J.M., Coutrakon, G., Davisson, R., Derado, I., Dhawan, S.K., Dougherty, W., Dreyer, T., Dziunikowska, K., Eckardt, V., Ecker, U., Erdmann, M., Eskreys, A., Fang, G., Figiel, J., Gebauer, H.J., Geesaman, D.F., Gilman, R., Green, M.C., Hass, J., Halliwell, C., Hanlon, J., Hantke, D., Hughes, V.W., Jackson, H.E., Jaffe, D.E., Jansco, G., Jansen, D.M, Kaufman, S., Kennedy, R.D, Kirk, T., Kobrak, H.G.E, Krzywdzinski, S., Kunori, S., Lord, J.J., Lubatti, H.J., McLeod, D., Magill, S., Malecki, P., Manz, A., Melanson, H., Micheal, D., Mohr, W., Montgomery, H.E., Morfin, J.G., Nickerson, R.B., O'Day, S., Olkiewicz, K., Osborne, L., Papavassiliou, V., Pawlik, B, Pipkin, F.M., Ramberg, E.J., Roser, A., Ryan, J.J., Salgado, C., Salvarani., A., Schellman, H., Schmitt, M., Schmitz, N., Schuler, K.P., Seyerlien, H.J, Skuja., A., Snow, G.A., Soldner-Rembold, S., Stienberg, P.H., Stier, H.E., Stopa, P., Swanson, R.A., Talaga, R., Tentindo-Repond, S., Trost, H.J., Venkataramania, H., Vidal, M., Wilhelm, M., Wilkes, J., Wilson, R., Wittek, W., Wolbers, S.A. and Zhao, T., Nucl. Instrum. Methods A291: 533, 1990.

[35] Kinney, E., "Target Control Software User's Guide, V 2.1", E665 Internal Report OL031: Batavia, Il, June 1990.

[36] Schellman, H. and Baller, B., "Final Design for Vertex Tracking System", E665 Internal Report VS024: Batavia, Il, May, 1989.

[37] De Palma M.," A System of Large Multiwire Proportional Chambers for High Intensity Experiment", Nuclear Instruments and Methods 217: 137-139, 1983.

[38] Bratzler, U., "Desogn, Fabrication and Testing of a Low-Mass, High Resolution, MWPC System for E665 at Fermilab", Master Thesis, University of Washington, 1991.

[39] Melanson, H., "E665 DC Calibration, Pass 1", E665 Internal Report FS027: Batavia, Il, June, 1988.
"E665 DC Calibration, Pass 2", E665 Internal Report AN059: Batavia, Il, July, 1989.

[40] Melanson, H., "E665 Analysis Meeting", Batavia, Il, June, 1992.

[41] Jaffe, D.," The Small Angle Scintillator (SSA)", E665 Internal Report FS033: Batavia, Il, Sep., 1990.

[42] Kotwal, A., "RUN90 Calorimeter Alignment", E665 Internal Report AN172, AN173: Batavia, Il, August, 1993.

[43] Kotwal, A.,"Summary of Reconstruction of RUN90 EM Calorimeter Calibration Data", E665 Internal Report AN166, AN175: Batavia, Il, August, 1993.

[44] Kennedy, R. D., " Measurement of the Ratio of the Neutron and Proton Structure Functions F_2 in Inelastic Muon Scattering" Ph.D. Thesis, University of California at San Diago, 1992.

[45] Jaffe, D. E., "The 1990 Small Angle Trigger" E665 Internal Report BT087: Batavia, Il, Sepember, 1989.

[46] Carroll, T. J. and Adams, M., "SAT Trigger Processor Users Guide" E665 Internal Report, Batavia, Il, August, 1993.

[47] Guo, R.," FS Pattern Recognition Studies", E665 Internal Report AN144: Batavia, Il, June, 1992.

[48] Salvarani, A. F.," Forward Hadron Productin in Muon Deep Inelastic Scattering at 490 GeV from Deuterium and Xenon", Ph.D. Thesis. University of California at San Diego, 1991.

[49] Anthony, P. A.," Bose-Einstein Correlation in Deep-Inelastic Muon Scattering", Ph.D. Thesis, Mass. Inst. of Tech., 1990.

[50] Guo, R., "PSA Time Line Data", E665 Internal Report AN074: Batavia, Il, November, 1990.

[51] Carroll, T. J.," Using TRASTF to Improve the Muon Matching Efficiency", E665 Internal Report SW185: Batavia, Il, February 1992.

[52] Schmitt, M., "A Modification to Nickerson's Pad Clustering Routine", E665 Internal Report EM017: Batavia, Il, March, 1991.

[53] Spentzouris, P.," Beam Alignment", E665 Internal Report AN167: Batavia, Il, October, 1992.

[54] Spentzouris, P., "FS Alignment", E665 Internal Report AN169: Batavia, Il, December, 1992.

[55] Kunori, S., Aid, S.," E665 Monte Carlo Program", E665 Internal Report MC012: Batavia, Il, October, 1986.

[56] Salgado, C., W.," E665 Stage 1 Monte Carlo", E665 Internal Report MC039: Batavia, Il, February, 1991.

[57] Wolbers, S.," The E665 Second Stage Monte Carlo; Version 5.0", E665 Internal Report MC010: Batavia, Il, February, 1991.

[58] Ryan, J. J, Schmitt, M., Bhatti, A.," Chamber Efficiency", E665 Internal Report AN081: Batavia, Il, December, 1990.

[59] Wolbers, S.," E665 Production", E665 Collaboration Meeting, Batavia, Il, July, 1993.

[60] Kotwal, A., "Calorimeter Calibration" E665 Collaboration Meeting, Batavia, Il, July, 1993.

[61] Lorstad, B.,"Boson Interferometry at High Energy", Lund Unversity Report: Lund, Sweden, June, 1990.

[62] The RISK-Spectrometer Serpukhov: Bayukov, Yu.D., Garvrilov, V.B., Degtyarenko, P. V., Zaitsev, Yu., M., Leksin, G. A., and Suchkov, D. A., "Correlations Between the Identical π Mesons Produced in $\pi^- A$ Collision at 3.7 GeV/c" Sov. J. Nucl. Phys. 33(3): 377, 1981.

[63] Andersson, B. and Hofmann, W., Phys. Lett. 169B: 364, 1986.
Artru, X. and Bowler, M. G., Z. Phys C37: 293, 1988.

[64] Bowler, M. G., Z. Phys. C- particles and Field 29: 617, 1985.

[65] The TPC collaboration: Aihara, H., Alson-Garnjost, M., Bakken, J., Barbaro-Galtieri, A., Barnes, A., Barnett, B., Bengtsson, H., Blumenfeld, B., Bross, A., Buchanan, C., Chambwelain, O., Chein, C-Y., Clark, A., Cordier, A., Dahl, O., Day, C., Derby, K. A., Eberhard, P., Fancher, D., Fujii, H., Fujii, T., Gobioud, B., Gary, J., Gorn, W., Hadley, N., Hauptman, J., Hofmann, W., Huth, J., Hylen, J., Kamae, T., Kaye, H., Kenny, R., Kerth, L., Koda, R., Kofler, R., Kwong, K., Layter, J., Lindsey, C., Loken, S., Lu, X., Lynch, G., Madansky, L., Madaras, R., Maruyama, K., Marx, J., Matthews, A., Melnikoff, S., Moses, W., Nemethy, P., Nygren, D., Oddone, P., Park, D., Pevsner, A., Robrish, P., Ronan, M., Ross, R., Rouse, F., Sauerwein, R., Shapiro, G., Shen, B., Slater, W., Stevenson, M., Stork, D., Ticho, H., Toge, N., VanDalen, G.J., VanTyen, R., Wang, E., Wayne, M., Wenzel, W., Yamamoto, H., Yamauchi, M., and Zhang, W-M., "Study of Bose-Einstein correlation in $e^{\pm}$ annihilation at 29 GeV", Phys. Rev. D31: 996, 1985.

VITA

NAME:	Rurngsheng Guo
EDUCATION:	B.S., Physics, National Kaohsiung Normal University, Kaohsiung, Taiwan, 1978.
	M.S., Physics, Northern Illinois University, Dekalb, Illinois, 1989.
	Ph.D., Physics, University of Illinois at Chicago, Chicago, Illinois, 1994
WORK EXPERIENCE:	Physics Teacher of Junior High, Taiwan, 1980-1983.
	Teaching Assistant, Department of Physics, National Kaohsiung Normal University, Kaohsiung, Taiwan, 1983-1986.
	Research Assistant, Department of Physics, Northern Illinois University, DeKalb, IL., 1987-1988.
	Teaching Assistant, Department of Physics, University of Illinois, Chicago, IL., Sep. 1988 - Jan. 1990.
	Research Assistant, Fermilab E665 Collaboration, University of Illinois, Chicago, IL., Jan. 1987 - Present.
PUBLICATIONS:	Kaplan, D. M., Alde, D. M., Bare, H. W., Carey, T. A., Garvey, G. T., Klein, A., Lee, C., Leitch, J., Liilberg, J. M., McGaughey, P. L., Mishra, C. S., Moss, J. M., Peng, J. C., Brown, C. N., Cooper, W. E., Hsinng, Y. B., Adams, M. R., Guo, R., McCarthy, R. L., Danner, G., Wang, M. J., Barlett, M. L., and Hoffman, G. W., "Production of Low-Mass Dihadrons in 800 GeV pW Interactions", Phys. Rev. D41: 2334, 1990.
	Guo, R., Alde, D. M., Bare, H. W., Carey, T. A., Garvey, G. T., Klein, A., Lee, C., Leitch, J., Liilberg, J. M., McGaughey, P. L., Mishra, C. S., Moss, J. M., Peng, J. C., Brown, C. N., Cooper, W. E., Hsinng, Y. B., Adams, M. R., Kaplan, D. M., McCarthy, R. L., Danner, G., Wang, M. J., Barlett, M. L., and Hoffman, G. W., "Improved Limit on Axion Production in 800 GeV Hadronic Showers.", Phys. Rev. D41: 2924, 1990.

VITA(continued)

Alde, D. M., Bare, H. W., Carey, T. A., Garvey, G. T., Klein, A., Lee, C., Leitch, J., Liilberg, J. M., McGaughey, P. L., Mishra, C. S., Moss, J. M., Peng, J. C., Brown, C. N., Cooper, W. E., Hsinng, Y. B., Adams, M. R., Guo, R., Kaplan, D. M., McCarthy, R. L., Danner, G., Wang, M. J., Barlett, M. L., and Hoffman, G. W., "Nuclear Dependence of Dimuon Production at 800 GeV/c.", Phys. Rev. Lett. 64: 2479, 1990.

Alde, D. M., Bare, H. W., Carey, T. A., Garvey, G. T., Klein, A., Lee, C., Leitch, J., Liilberg, J. M., McGaughey, P. L., Mishra, C. S., Moss, J. M., Peng, J. C., Brown, C. N., Cooper, W. E., Hsinng, Y. B., Adams, M. R., Guo, R., Kaplan, D. M., McCarthy, R. L., Danner, G., Wang, M. J., Barlett, M. L., and Hoffman, G. W., "A Dependence of J/Psi and Psi' Production at 800 GeV/c.", Phys. Rev. Lett. 66: 133, 1991.

Alde, D. M., Bare, H. W., Carey, T. A., Garvey, G. T., Klein, A., Lee, C., Leitch, J., Liilberg, J. M., McGaughey, P. L., Mishra, C. S., Moss, J. M., Peng, J. C., Brown, C. N., Cooper, W. E., Hsinng, Y. B., Adams, M. R., Guo, R., Kaplan, D. M., McCarthy, R. L., Danner, G., Wang, M. J., Barlett, M. L., and Hoffman, G. W., "Nuclear Dependence of the Production of Upsilon Resonances at 800 GeV.", Phys. Rev. Lett. 66: 2285, 1991.